Kelemen, P.B., Kikawa, E., Miller, D.J., et al., 2004
Proceedings of the Ocean Drilling Program, Initial Reports Volume 209

5. Site 1270[1]

Shipboard Scientific Party[2]

OPERATIONS SUMMARY

Transit to Site 1270

Site 1270 is the southernmost of all sites occupied during Leg 209, 16 nmi southeast of Site 1269. Originally planned as an alternate site, this location is on the ridge flank at the eastern limit of the axial valley. The site survey dive tapes reveal an exposed fault surface, and samples of mylonitic peridotite were recovered during the dive, together with less deformed peridotite and gabbroic rocks. We chose to occupy this site as a result of poor hole conditions and low recovery, including only basalt, at Site 1269.

Hole 1270A

On 28 May 2003, we arrived at the Global Positioning System (GPS) coordinates of a position along the dive track of *Shinkai* 6500 Dive 425 (Figs. F1, F2), just upslope of where serpentinized peridotite had been sampled from a large outcrop (sample R007). A six-collar bottom-hole assembly (BHA) (nominally 130 m long) was lowered with the drill string, and the subsea camera was deployed. After a ~3.5-hr survey (Fig. F1) during which we recognized several intervals of bare rock exposure, we selected a drilling target ~150 m west of our camera survey starting position.

Hole 1270A was initiated with slow rotation and low bit weight at 0500 hr on 29 May. The upper guide horn was removed to allow us to keep the subsea camera near the seafloor as we started the hole to ensure the bit did not track downslope. After 3 m of penetration, the camera was retrieved and coring continued through Core 4R (0.0–26.9 meters below seafloor [mbsf]) (Table T1). Core 4R contained fault gouge, and our attempt to deepen the hole was hampered by erratic

F1. Bathymetry of survey tracks and hole locations, p. 50.

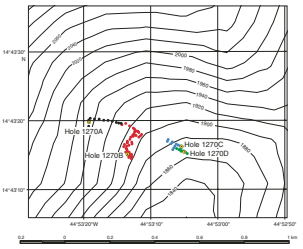

F2. Track of *Shinkai* Dive 425, hole location, and bathymetric section for Site 1270, p. 51.

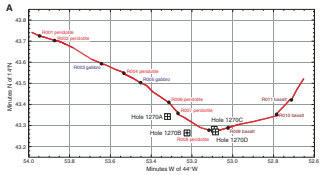

T1. Coring summary, p. 173.

[1]Examples of how to reference the whole or part of this volume.
[2]Shipboard Scientific Party addresses.

torque on the drill string and wall collapse, which filled the borehole. After hole cleaning attempts failed, we pulled clear of the seafloor at 1600 hr on 29 May, ending Hole 1270A.

Hole 1270B

We returned to our original camera survey position, redeployed the subsea camera, and began a survey upslope in search of a new drilling location on a bare rock exposure. We moved 100 m east along an azimuth of ~120° over the path followed by *Shinkai* 6500 Dive 425 and then turned south to follow a depth contour where outcrop was evident in the dive videotape. After completing a rectangular box survey pattern, we located an extensive exposure of bare rock ~230 m southeast of Hole 1270A and initiated Hole 1270B.

Coring began in Hole 1270B as in Hole 1270A (at 0200 hr on 30 May) by advancing the bit with slow rotation and low bit weight to 3 mbsf while observing the operation with the subsea camera. After retrieving the camera, we cored to a depth of 45.9 mbsf (Cores 1R to 10M). As we began our third coring interval, the bit would not advance past 13.5 mbsf (1 m deeper than the top of Core 2R). At that depth, coring continued as if we had not already drilled the interval between 13.5 and 17.4 mbsf. Core 3M represents rock recovered in the same general interval as Core 2R (13.5–17.4 mbsf) but contains >1 m of cut core cylinders. When the same blockage was encountered at virtually the same depth on our next coring attempt (13.5 mbsf), we cored beyond the bottom depth of Cores 2R and 3M, to 22 mbsf. Since we redrilled the upper part of the interval, the recovered core was curated as Core 4M. Normal coring curation and nomenclature was resumed with Core 5R, when we were sure we were coring a new interval from the beginning of the cored interval. Coring progressed steadily with improving recovery until Core 9R. Hard fill in the bottom of the hole prevented advancement and caused high and erratic torque. Since we were still operating with a reduced-length BHA, we chose not to risk getting the pipe stuck and abandoned the hole at 1205 hr on 31 May.

Hole 1270C

We began our third camera survey (Fig. **F1**) at the GPS coordinates of sample R008 from *Shinkai* 6500 Dive 425 (Fig. **F2**) where mylonitinized peridotite had been sampled. Unlike outcrops at our two previous holes (bare rock free of talus), the dive videotape revealed this outcrop was littered with what appeared to be slabs of rock, albeit more or less in place. We selected this location upslope from our two previous holes, surmising that if the fault gouge encountered at depth in Hole 1270A was a result of incipient landsliding, this older, more weathered outcrop might yield better drilling conditions. After a 2.5-hr survey, we selected a drilling target ~240 m east of Hole 1270B.

Hole 1270C was initiated at 1735 hr on 31 May in a manner similar to our two previous holes. Coring only progressed to 18.5 mbsf (Cores 1R and 2R) before the hole began to fill, restricting circulation. No advancement was possible on our third coring interval, even after 2.5 hr of rotation, so the core barrel was recovered (curated as Core 3M) and the hole was abandoned at 0300 hr on 1 June.

Hole 1270D

The survey for Hole 1270D began over the position of Hole 1270C. We moved only a short distance (~30 m east) and selected a drilling target in bare rock. At 0730 hr on 1 June, Hole 1270D was initiated while we watched the operation with the subsea camera. We cored to 3 mbsf before the camera cable appeared to start wrapping around the drill string. While recovering the camera (without rotating the pipe) the driller became concerned when he was required to advance the pipe to maintain a minimum weight on bit. Upon lowering the camera back to the seafloor, the camera image showed that the bit had slid off the outcrop and embedded in sediment. A second hole initiation (at 0934 hr on 1 June) was successful to 3 mbsf, so the camera was retrieved and coring continued to 57.3 mbsf. After recovering Core 11R, hole conditions deteriorated to the point that no further advance was possible. The bit was pulled clear of the seafloor, ending operations at Site 1270 at 1445 hr on 2 June. Rate of penetration at Site 1270 varied from 3 to 7 m/hr.

IGNEOUS AND MANTLE PETROLOGY

Four holes were drilled at Site 1270; three of these recovered predominantly mantle peridotite and the last recovered almost exclusively oxide-rich gabbronorites. Here we discuss each of the holes separately and then combine these observations to compare the variations within Site 1270 and then between Sites 1270 and 1268.

Hole 1270A

Lithology and Stratigraphy

The predominant rock type in this hole is serpentinized harzburgite (88 vol%) with minor serpentinized dunite (7 vol%), gabbro (3 vol%), and breccia (1 vol%) (Fig. F3). There are two major gaps in the downhole stratigraphy. The first gap in recovery (9.5 m) is located at the transition between the first two sections of core. The second gap (9.5 m) corresponds to two intervals where no rock was recovered between the second and third (4.75 m) and third and fourth cores (4.16 m). All of Core 209-1270A-3R (0.34 m) is serpentinite fault gouge and small pebbles of peridotite that are too altered to identify the protolith more completely. The percentage recovery is so limited that statistical analysis of the observations and the construction of a stratigraphy may not be meaningful. Nevertheless, we observe consistency in the modal variation of the harzburgite that forms the three recovered portions of Hole 1270A. In these rocks, the modal proportions of orthopyroxene decrease from ~30% at the top of the cored interval to ~10% at the bottom. In addition, the (apparent) grain size in the harzburgite protoliths of the three units decreases downhole and they have undergone different extents of high-temperature deformation. Dunite is most abundant in the upper part of Section 209-1270A-1R-1 and in the gabbros in the lower half of Section 2R-1. Based on these observations, we define three lithologic units (Fig. F3).

F3. Lithostratigraphic summary, Hole 1270A, p. 53.

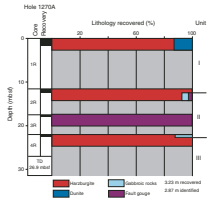

Unit I

Interval: Sections 209-1270A-1R-1 through 2R-1
Depth: 0–12.12 mbsf
Lithology: orthopyroxene-rich harzburgite/dunite

Unit I is characterized by orthopyroxene-rich harzburgite with dunite bands, orthopyroxene-rich bands, and a single thin crosscutting orthopyroxenite. Orthopyroxene constitutes 23%–30% of this coarse-grained harzburgite, which contains olivine and orthopyroxene as large as 2 cm, although 1.5 cm is the most common size (Fig. F4). Relict orthopyroxene is kinked and recrystallized into relatively coarse subgrains, defining a protogranular porphyroclastic texture. The top of Section 209-1270A-1R-1 is a mixture of dunite and harzburgite pebbles, and we identified four dunites that are 2–5 cm wide in the first meter of core. This section also contains several (five were identified) thin (<1 cm thick), boudinaged pyroxene-rich bands characterized by coarse recrystallized orthopyroxene crystals intergrown with large spinel. At Section 209-1270A-1R-1 (Piece 2, 5 cm), the orthopyroxenite is in contact with dunite. Sections 209-1270A-1R-2 and 2R-1 down to 12 mbsf are the continuation of the same harzburgite, but no dunite or orthopyroxenite is present. At the top of Section 209-1270A-1R-2, the harzburgite is strongly deformed but the deformation intensity decreases with depth. The harzburgite at the top of Section 209-1270A-2R-1 is little deformed but contains two intervals of harzburgitic pebbles and sand.

F4. Coarse-grained orthopyroxene-rich harzburgite, p. 54.

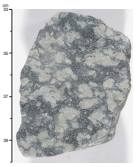

Unit II

Interval: Sections 209-1270A-2R-1 through 4R-1
Depth: 12.2–22.03 mbsf
Lithology: harzburgite with gabbro

Unit II is harzburgite with gabbroic intervals. The harzburgite contains 15–20 vol% orthopyroxene. With respect to the Unit I harzburgite, the Unit II harzburgite is poorer in orthopyroxene and has smaller grains; the original size is estimated to be ~1 cm. The top of the unit (Section 209-1270A-2R-1 [Piece 17]) is strongly deformed with significant grain size reduction, but the texture changes to porphyroclastic in Pieces 18–21 then to protogranular/porphyroclastic in Pieces 21–27 to the bottom of the unit. The harzburgite is cut by two gabbro layers, 2–3 cm thick, in intervals 209-1270A-2R-1, 81–85 cm, and 113–117 cm, and by breccia in interval 2R-1, 101–104 cm. Brown amphibole-rich veins, a few millimeters wide, are common in the breccia and the harzburgite underneath it. In Section 209-1270A-4R-1, the Unit II harzburgite is cut by a 6-cm-thick gabbro. However, the bottom of Section 209-1270A-2R-1 and the top of Section 4R-1 are separated by 28 cm of serpentinite and altered ultramafic fault gouge (the protolith is not identifiable). This fault gouge constitutes all of Section 209-1270A-3R-1. The base of Unit II is more strongly deformed and has porphyroclastic textures.

Unit III

Interval: Section 209-1270A-4R-1
Depth: 22.03–26.9 mbsf
Lithology: harzburgite/dunite

Unit III is characterized by a peridotite that has ~10 vol% orthopyroxene and so is classified at the harzburgite/dunite boundary. This harzburgite, forming the lowermost 37 cm of the core in Hole 1270A, has a porphyroclastic texture. It is crosscut by millimeter-wide bands of amphibole-bearing ultramafic rock in Section 209-1270A-4R-1 (Pieces 14 and 15) (Fig. F5).

F5. Amphibole vein or dike crosscutting harzburgite, p. 55.

Lithologic Characterization

The harzburgites are highly altered (>99%), so reconstruction of the high-temperature mineral assemblages is based on the nature of the alteration and pseudomorphs. In many samples, the grain boundaries between the primary olivine and pyroxene grains are preserved and provide information on the microstructure and texture, allowing us to roughly estimate their modal proportions. Partially fresh clinopyroxene is present in a thin section (Sample 209-1270A-4R-1, 54–56 cm) from Unit III, suggesting that this sample had ~2% modal clinopyroxene. In the other harzburgite thin sections, altered pyroxenes with similar character could be interpreted as former clinopyroxene. There may have been relatively large clinopyroxene grains (up to 2 mm) in the orthopyroxene-rich harzburgites of Unit I. The amount of former clinopyroxene, estimated based on the geometry of the grain boundaries and the nature of the serpentinization (pseudomorphs of thin, regular exsolution lamellae), is as high as 3–4 vol% in Sample 209-1270A-1R-1, 139–141 cm. This amount of clinopyroxene is not atypical for harzburgites containing ~70 vol% olivine like those in Unit I. However, the other three thin sections from Unit I do not include anything that we interpret as having been clinopyroxene. The bulk of the Unit I harzburgite thus appears to be an unusual harzburgite characterized by high orthopyroxene contents (23–30 vol%) but low clinopyroxene and spinel (2 vol%) contents. Unit II harzburgite is poorer in orthopyroxene, with 15%–20% modal orthopyroxene, 1%–2% clinopyroxene, and 1%–3% spinel, with the remainder olivine. Unit III peridotite is even poorer in modal orthopyroxene, with 10% orthopyroxene, 2% clinopyroxene, and 1% spinel. In all three units, the texture before plastic deformation and recrystallization was protogranular. The original sizes of the primary olivine and orthopyroxene grains cannot be determined with confidence, but, based on the olivine/orthopyroxene grain boundaries, they must have been on the order of 1.5–2 cm in Unit I, 1 cm in Unit II, and 1.2 cm in Unit III.

Orthopyroxene pseudomorphs are anhedral with embayments filled with olivine (Figs. F6, F7). They tend to be equant (Fig. F6), and although they have some irregular portions interstitial to olivine grains, these irregularities are far less common than in harzburgite from Hole 1268A. Likewise, none of the amoeboidal orthopyroxene, so common in Hole 1268A, is found in the Hole 1270A harzburgites. Orthopyroxene is commonly recrystallized into relatively large subgrains of 1–5 mm size (Fig. F7), but the primary olivine is recrystallized into smaller neoblasts. Where observed, clinopyroxene is present as small (<0.5 mm) crystals at boundaries and junctions of orthopyroxene subgrains and probably results from orthopyroxene exsolution during deformation and recrystallization. Holly leaf–shaped spinel grains, as large as 1–3 mm, are commonly found as intergrowths with orthopyroxene. Smaller grains disseminated in the serpentinized olivine matrix are less common.

F6. Orthopyroxene porphyroclast, p. 56.

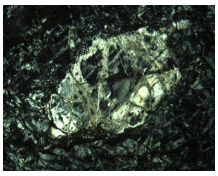

F7. Recrystallized orthopyroxene porphyroclast, p. 57.

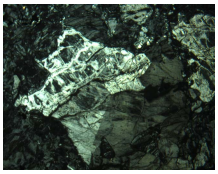

The dunites are totally altered, with 2%–5% relict orthopyroxene and 1% spinel. The original size of the olivine grains is difficult to determine but was probably on the order of 1 cm, based on the size of the orthopyroxenes.

Thin orthopyroxenites and orthopyroxene-rich bands in harzburgites are characterized by coarse primary orthopyroxene recrystallized in relatively large subgrains and intergrown with skeletal, large spinels (Fig. F8). Small interstitial grains of spinel and clinopyroxene (Fig. F8B) are interpreted as exsolution products generated by recrystallization.

A 3-mm-wide ultramafic dike or vein that cuts Unit III harzburgite (Section 209-1270A-4R-1 [Pieces 14 and 15]) is made up of 20% olivine, 20% orthopyroxene, 53% clinopyroxene, 5% magmatic interstitial brown amphibole (pargasite) (Fig. F9), and 2% oxides. This dike is intruded into a mylonitic band, and we cannot exclude the possibility that the olivine and orthopyroxene grains are derived from the harzburgite wallrock. Indeed, these minerals occur as 0.5-mm-size neoblasts, as shown in Figure F9, whereas clinopyroxene forms larger (1 mm) subhedral crystals, oriented parallel to the margins of the intrusion.

A single large piece of pegmatitic gabbro (with 20% clinopyroxene and 80% plagioclase) was recovered from Unit II (Section 209-1270A-2R-1 [Piece 20]).

F8. Recrystallized orthopyroxene with olivine and clinopyroxene, p. 58.

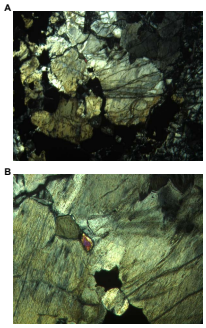

F9. Brown amphibole and iron oxides interstitial to olivine, p. 59.

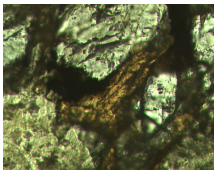

Hole 1270B

Hole 1270B was drilled to a depth of 45.9 mbsf and its 10 cores are composed of 99% oxide gabbronorite, gabbronorite, and microgabbro, with the remainder being altered harzburgite. Because of problems with drilling, three of these cores are not well located stratigraphically. These "M" cores were placed into a stratigraphic context using a combination of their reported starting depth from the driller's estimates and observed modal, textural, and lithologic variations. Most of the rocks have undergone high-temperature deformation and now are appropriately described as gabbroic gneisses. However, the original mineralogy is preserved, so in this section we characterize these rocks in terms of their igneous protolith and focus on evidence of their magmatic history.

Grain size, variations in the fraction of oxide minerals (magnetite and ilmenite), and lithologic variations were used to define seven units in Hole 1270B (Fig. F10). Units I, III, and VII compose 85.2% of the drilled interval and are predominately coarse-grained oxide gabbronorite with lesser amounts of gabbronorite. (This gabbronorite is not free of oxides but lacks the 5% modal required for the mineralogical modifier.) Units II and VI are microgabbros (4.3% of the recovered core), and Unit V is a gabbronorite (1.1% of the recovered core). Unit IV is distinct in that it contains harzburgite interpreted to be the upper mantle host rock of the gabbroic rocks. Although Unit IV makes up 9.46% of the drilled interval, it corresponds to only 2.5% of the recovered core.

F10. Modal plagioclase and estimated magnetite, p. 60.

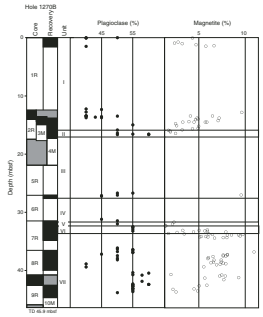

Oxide Gabbronorite Units

Unit I

Interval: Sections 209-1270B-1R-1 through 4M-2
Depth: 0–16.16 mbsf
Lithology: oxide gabbronorite

Unit III

Interval: Sections 209-1270B-4M-2 through 6R-1
Depth: 16.74–27.51 mbsf
Lithology: oxide gabbronorite

Unit V

Interval: Section 209-1270B-7R-1
Depth: 31.74–32.16 mbsf
Lithology: oxide gabbronorite

Unit VII

Interval: Sections 209-1270B-7R-1 through 10M-1
Depth: 33.63–45.9 mbsf
Lithology: oxide gabbronorite

There are three oxide gabbronorite/gabbronorite units. Unit V is similar to the gabbronorite parts of the other three units and was only designated as separate unit because of intervening lithologies. In nearly all of the units the rocks are relatively fresh with <10% alteration. This makes estimation of modal proportion of plagioclase, oxides, and pyroxene straightforward. However, both clinopyroxene and orthopyroxene are present and are very difficult to distinguish reliably. Calculation of modal proportions based on the bulk rock composition is dependent on the mineral compositions used but generally suggests that 5%–10% orthopyroxene is present. In most samples the plagioclase abundance is 40%–55% and does not vary stratigraphically in any discernable pattern.

We estimated the amount of magnetite in the samples by measuring the bulk magnetic susceptibility via a susceptibility loop on individual pieces. The susceptibility loop averages some distance along the length of the core such that pieces that are at least 7 cm in length account for ≥95% of the response curve. In the measurement procedure we considered a 7-cm piece to give a full response and estimated the size of any smaller pieces as a fraction of the volume of a 7-cm half round. In practice, no pieces smaller than an estimated 50% of this volume were measured and the raw data were adjusted upward to compensate for the smaller volumes. The raw data were corrected for the expected cross-sectional area for which the loop was designed (6.6 cm whole round). The corrected susceptibilities were then converted into volume percent estimates of the magnetite content by dividing the corrected susceptibility by 10,000 and multiplying by 3.3, corresponding to a susceptibility of magnetite of 3 million μSI units (Fig. **F11**). The amount of magnetite estimated using this susceptibility method generally agrees with visual estimates of oxide proportions in thin sections, except in Unit I where the visual estimate is much larger than the susceptibility-based estimate of magnetite proportion. These samples contain discrete ilmenite crystals and may have some TiO_2 in the magnetite, lowering its bulk susceptibility and thus causing our susceptibility-based estimates to be systematically low.

There is a variable amount of deformation in these units that decreases with depth. All the rocks in Unit I are moderately to strongly deformed. Most rocks in Unit III are moderately deformed; some are strongly deformed. Rocks in Unit VII are moderately deformed at the top of the unit, but some relatively undeformed rocks are found near the base of the core (Figs. **F12**, **F71**). The least deformed rocks are medium grained and have lath-shaped plagioclase grains that preserve both optical zonation and polysynthetic twins. These rocks have subhe-

F11. Estimation of magnetite from bulk susceptibility, p. 61.

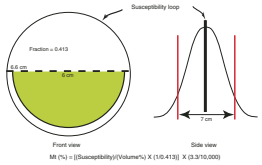

F12. Deformation of oxide gabbronorites, p. 62.

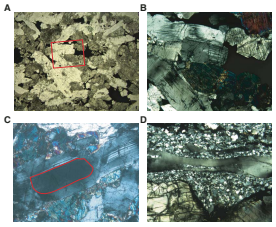

dral to euhedral clinopyroxene and orthopyroxene and interstitial oxides. Preservation of some igneous features in the more deformed rocks indicates that the original grain size in some samples was >20 mm for both clinopyroxene and plagioclase. The largest orthopyroxene grains preserved suggest that orthopyroxene had a maximum size of 10–15 mm. The crystals have been variably rounded, partially deformed, and recrystallized into small neoblasts in these coarse-grained samples. Locally, clinopyroxene grains that include euhedral oxide grains are found (Fig. F13). One example of an unstrained euhedral plagioclase crystal was also noted (Fig. F14). Clinopyroxene is mostly equant, but a few examples of large ophitic clinopyroxene crystals are preserved (Fig. F15), most notably in Section 209-1270B-10M-1 (Piece 23), in which a 70 mm × 40 mm oikocryst of clinopyroxene is found.

It has been suggested that some amount of oxide was added to the igneous protolith during the deformation process, as was proposed for some oxide gabbros recovered from Leg 118 Hole 735B. Based on the following observations, we find no compelling reason to consider that oxide addition during deformation was an important process in the genesis of the oxide-rich gabbronorites in Hole 1270B:

1. The least deformed rocks contain the same proportion of oxide as the deformed rocks.
2. Samples with igneous textures have interstitial oxide that crystallized with the surrounding silicate minerals.
3. In the most deformed rocks, euhedral oxide grains preserved in the clinopyroxene indicate that oxides were present prior to deformation.
4. We have not found accessory phases such as zircon, apatite, or titanite associated with strongly deformed, oxide-rich parts of these rocks, as might be expected if an evolved oxide-rich liquid were added.

These observations do not eliminate the possibility that the rock compositions were modified, but this process is not required to explain the observed oxide textures and proportions. However, for an alternative viewpoint, see "Structural Geology," p. 12, in the "Site 1274" chapter and Figure F24, p. 102, and accompanying text in the "Leg 209 Summary" chapter.

F13. Clinopyroxene with inclusions of euhedral oxide crystals, p. 64.

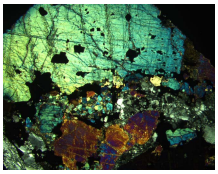

F14. Plagioclase preserved in deformed oxide gabbronorite, p. 65.

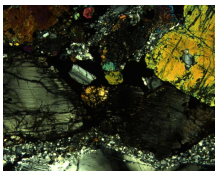

F15. Ophitic clinopyroxene crystal, p. 66.

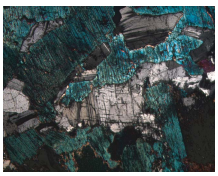

Microgabbro Units

Unit II

Interval: Sections 209-1270B-4M-2 through 4M-3
Depth: 16.16–16.74 mbsf
Lithology: microgabbro

Unit VI

Interval: Sections 209-1270B-7R-1 through 7R-2
Depth: 32.16–33.63 mbsf
Lithology: microgabbro

Units II and VI are microgabbros crystallized from a more primitive liquid that intruded the oxide gabbronorite after it cooled. This interpretation is based on the fine grain size of the rocks, their relatively low abundance of oxides, and their distinctive chemical composition compared to the gabbronorites (see "Geochemistry," p. 34; Table T4). Both

of these units have been deformed, so the observed grain size may reflect some amount of grain size reduction during recrystallization. The grain size in Unit II decreases as the lower contact is approached. The portion of Unit II near the contact is severely altered, and it is not clear if the reduction in grain size reflects more rapid cooling at the margin of the microgabbro or deformation-related recrystallization associated with the lithologic boundary.

Unit IV

Interval: Sections 209-1270B-6R-1 through 7R-1
Depth: 27.51–31.74 mbsf
Lithology: harzburgite

Unit IV contains the only ultramafic rocks in Hole 1270B. They are extremely altered but are interpreted to have originally been harzburgites. Harzburgite was recovered in three cobble-sized pieces with no lithologic contacts. The harzburgite cobbles are interspersed with coarse-grained oxide gabbronorite in the uppermost part of Section 209-1270B-6R-1. This mixture may simply be a consequence of oxide gabbronorite falling into the hole during core retrieval.

Hole 1270C

Hole 1270C consists of three cores with total drilled length of 19.8 m (recovery = 10.65%). The predominant rock type is harzburgite (79%) and dunite (21%), with minor amounts of gabbro and orthopyroxenite (Fig. F16). The core is lithologically uniform, so we have not subdivided it into units.

The harzburgite has significant variations in both texture and modal proportions. The texture of the harzburgite varies from protogranular to porphyroclastic to mylonitic (see **"Structural Geology,"** p. 21; Fig. F17). The proportion of orthopyroxene porphyroclasts (now as pseudomorphs) ranges as high as 30% and can be heterogeneously distributed, resulting in modal variations in a single piece (e.g., Fig. F18). In the orthopyroxene-rich harzburgites, a few grains of olivine, orthopyroxene, and the spinel are enclosed by orthopyroxene grains that have escaped alteration (Fig. F19). No contact between harzburgite and dunite is preserved. Alteration makes the textures of dunites difficult to recognize, but they typically contain <3% orthopyroxene and ~1% spinel.

Anastomosing gabbroic intrusions (5–10 mm thick) cut both harzburgite and dunite in eight discrete intervals in the core. These gabbros are highly deformed with asymmetric structure and irregular-shaped boundaries, probably related to localized shear deformation (Fig. F20). Gabbro intrusions consist of clinopyroxene porphyroclasts surrounded by fine-grained clinopyroxene and plagioclase with mosaic texture. Some large clinopyroxenes poikilitically enclose plagioclase, and secondary brown amphibole partially replaces clinopyroxene. The gabbros contain trace amounts of subhedral zircon. The host rock of the gabbro is brecciated and deformed at the contact, resulting in elongated lenses of fresh olivine and orthopyroxene with porphyroclastic to mylonitic texture (Fig. F21). Orthopyroxene porphyroclasts form aggregates next to the olivine matrix.

F16. Lithologic summary, Hole 1270C, p. 67.

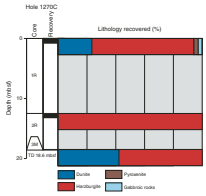

F17. Orthopyroxenes with curved grain boundaries in olivine, p. 68.

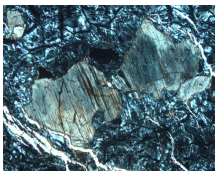

F18. Altered orthopyroxene porphyroclasts in altered harzburgite, p. 69.

F19. Vermicular spinels in orthopyroxene, p. 70.

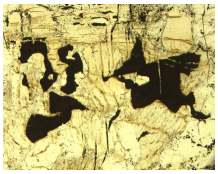

F20. Gabbroic intrusion with mylonitic texture, p. 71.

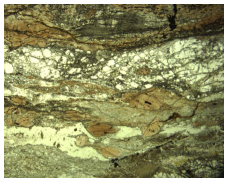

F21. Dunite lens with mylonitic texture, p. 72.

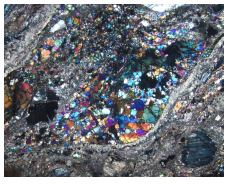

Hole 1270D

Drilling penetrated to a depth of 57.3 mbsf in Hole 1270D with a total recovery of 7.68 m (recovery = 13.4%). The core consists mainly of deformed harzburgite (98.7%) with a minor amount of dunite (1.3%) and so is treated as a single unit (Fig. F22). These peridotites are cut by pervasive small intrusions of gabbroic material prior to deformation (Fig. F23). The mixed ultramafic and gabbroic rocks are very similar to those recovered in Hole 1270C. Centimeter-scale dunites are distributed throughout the core. There is ~20%–25% orthopyroxene in the deformed harzburgite and <5% in the dunite. The strong deformation, recrystallization, and alteration of the rocks diminishes the reliability of these modal estimates. The percentage of gabbroic material cutting the harzburgites and dunites was visually estimated and compared with the natural gamma radiation (NGR) (Fig. F22). There are two peaks in the NGR in Sections 209-1270D-3R-1 and 4R-1, in which zircon and apatite were found in thin section.

Deformation in Hole 1270D is concentrated in the gabbroic intrusions, and large domains of porphyroclastic harzburgite are preserved. Microscopic observations of these domains show that the primary grain size of the host rock was 4–8 mm and texture is granular to porphyroclastic. The harzburgite clasts contain as much as 25% orthopyroxene and up to 90% fresh recrystallized olivine. Inclusions of fresh or serpentinized olivine are found in orthopyroxene. Rare interstitial clinopyroxene runs in discontinuous parallel bands cutting through a serpentinized olivine matrix (Fig. F24).

Strongly altered dunites usually occur in 1- to 3-cm-sized domains within the harzburgite but also as discrete portions of the core (pebbles) with a few bands enriched in orthopyroxene. The only primary phase that survived alteration is spinel, up to 1%–2% in abundance, whereas orthopyroxene pseudomorphs make up ≤2% of the mode. It is not possible to determine the original size of the olivine crystals because they are totally altered.

Anastomosing gabbroic intrusions, originally composed of plagioclase, clinopyroxene, and amphibole, are pervasive in the harzburgite. The plagioclase is now completely altered, but there is some relict clinopyroxene. Euhedral brown amphibole crystals (up to 2 mm in size) with well-developed 60°–120° cleavages are preserved in the sheared gabbro (Fig. F25). We interpret this amphibole to be a late magmatic phase. Zircon and apatite occur as discrete accessory minerals in these sheared gabbros (Fig. F26). They are dispersed in the gabbroic matrix and are locally included in the amphibole rims (Fig. F25).

Discussion

Three of the four holes drilled at Site 1270 are fundamentally different. The obvious outlier is Hole 1270B, which recovered almost exclusively gabbroic rocks, whereas the others are predominately peridotite. Holes 1270C and 1270D are very similar but are different from Hole 1270A. There are two main distinctions between these sets of holes: (1) Hole 1270A lacks the pervasive small gabbroic bodies that characterize much of the rock from Holes 1270C and 1270D and (2) Hole 1270A shows a systematic decrease in modal orthopyroxene downhole, whereas no such systematic variations are discerned in Holes 1270C and 1270D. Both points should be viewed with caution because of the very limited recovery from Hole 1270A. The harzburgite of Unit I from

F22. Lithology and stratigraphy, Hole 1270D, p. 73.

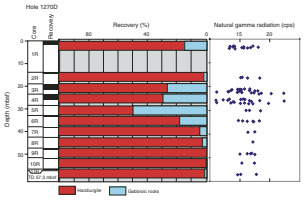

F23. Harzburgite with anastomosing gabbroic intrusion, p. 74.

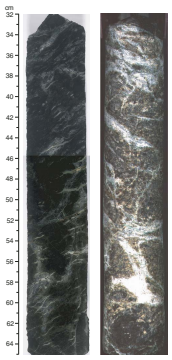

F24. Clinopyroxene crosscutting harzburgite, p. 75.

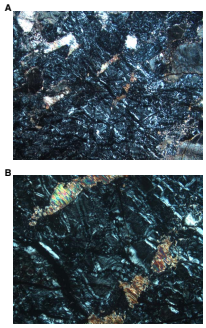

F25. Zr crystals in amphibole, p. 76.

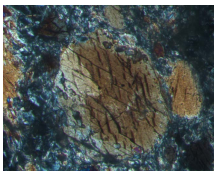

Hole 1270A is also remarkably coarse grained and rich in orthopyroxene while poor in clinopyroxene. None of the peridotite from Holes 1270C and 1270D is as coarse grained, but as these two cores have been more extensively recrystallized during deformation, the original texture and grain size have been obscured.

The peridotite from Site 1270 contrasts with the peridotite from Site 1268 in showing no continuous variation in modal orthopyroxene content from harzburgites to dunites. The habit of the orthopyroxenes also differs. Orthopyroxene from Hole 1268A is distinctly "ragged" or amoeboidal in most samples, whereas this texture is scarce or absent at Site 1270. Taken together these observations might indicate that no reaction between melt/fluid and residual harzburgite occurred or that such reaction was not a dominant process, as is proposed for Hole 1268A.

Holes 1270C and 1270D contain a network of gabbroic intrusions hosting local concentrations of accessory minerals that are unusual in abyssal peridotites. These include zircon, apatite, and epidote. Could these evolved gabbroic intrusions be related to the oxide-rich gabbronorites from Hole 1270B? The oxide gabbronorites clearly crystallized from an evolved liquid, but their low incompatible element concentrations and lack of accessory minerals such as apatite and zircon indicate that they are cumulates without a significant crystallized liquid component. It is therefore likely that an even more evolved liquid was extracted during their crystallization. This type of liquid could have given rise to the gabbroic material seen in Holes 1270C and 1270D. However, unlike the gabbroic rocks at Site 1268 that we interpreted to have crystallized from relatively H_2O-rich liquids, there is no evidence for high H_2O contents in the oxide gabbronorites from Hole 1270B.

F26. Zr crystals in amphibole, p. 77.

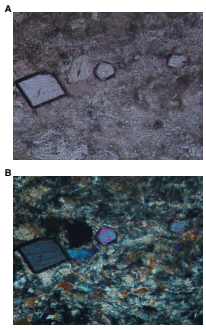

METAMORPHIC PETROLOGY

Four holes were drilled at Site 1270, reaching between 17.5 and 57.3 mbsf. The recovery ranged from 10.6% (Hole 1270C) to 37.4% (Hole 1270B). Holes 1270A and 1270B are located at a water depth of 1951 and 1910 m, respectively. Drill core from Hole 1270A is mainly composed of completely serpentinized harzburgite and dunite, whereas slightly to moderately altered gabbro was recovered from Hole 1270B. Holes 1270C (1822 meters below sea level [mbsl]) and 1270D (1817 mbsl) are <20 m apart and were drilled at a location ~250 m east of Holes 1270A and 1270B. Drill core from Hole 1270C is dominated by serpentinized harzburgite and dunite. Serpentinized harzburgite with rodingitized gabbro veins or dikes was recovered from Hole 1270D.

F27. Photograph and XRD for serpentinized harzburgite, p. 78.

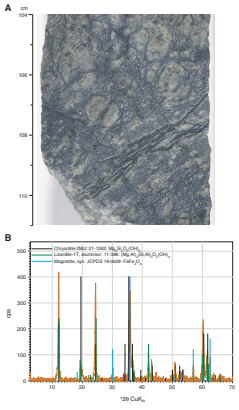

Hole 1270A

Hole 1270A reached a maximum depth of 26.9 mbsf (average recovery = 17.6%). The predominant rock type is serpentinized harzburgite with minor serpentinized dunites, completely altered gabbros, and rare breccia. The entire succession is completely altered.

Hydrothermal Alteration

Alteration of Harzburgites and Dunites

Harzburgites and dunites in Hole 1270A are dark green and are completely altered to serpentine and magnetite (Fig. F27A). This macroscopic observation was confirmed by X-ray diffraction (XRD) analyses

(Fig. F27B; Table T2). In some intervals, the core is reddish black, suggesting the presence of relict primary minerals (<2%). Serpentinite microtextures in two thin sections (Samples 209-1270A-1R-1, 35–38 cm, and 1R-1, 96–99 cm) are transitional with serrate chrysotile veins. Orthopyroxene is altered to bastite with minor talc and tremolite rims. Sample 209-1270A-1R-1, 35–38 cm, contains a serpentine mylonite with interpenetrating textures of presumed antigorite (Fig. F28A, F28B). Late chrysotile veins are deformed into the mylonite, indicating that deformation took place during or after late-stage serpentinization (Fig. F28C). The abundance of pyrite in the serpentine mylonite is unusually high. Pyrite and magnetite appear to replace spinel (Fig. F28D). Furthermore, there is minor weathering and formation of trace amounts of clay, Fe oxyhydroxide, and carbonate after olivine in Hole 1270A.

T2. XRD results, p. 175.

F28. Serpentinized harzburgite, p. 79.

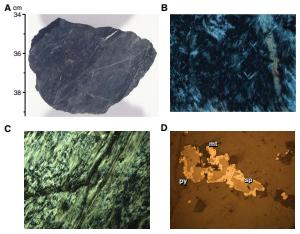

Alteration of Ultramafic Dikes

Two ultramafic dikes or veins are present in Section 209-1270A-4R-1 (intervals 4R-1, 43–46 cm, and 4R-1, 48–56 cm). Interval 209-1270A-4R-1 (Piece 12, 43–36 cm) is an amphibolized clinopyroxenite, whereas interval 4R-1, 48–56 cm, contains two pieces of harzburgite with a pyroxenite dike or vein. A thin section of Sample 209-1270A-4R-1 (Piece 16, 54–56 cm) reveals that these pyroxenite veins are ~50% altered to serpentine, chlorite, talc, amphibole, and oxides. Olivine is partly replaced by serpentine and oxides, whereas the pyroxenes are partially altered to serpentine, talc, chlorite, and amphibole.

Alteration of Gabbros

Small pieces of gabbro were recovered in intervals 209-1270A-2R-1, 81–85 cm; 2R-1, 113–117 cm; and 4R-1, 0–5 cm. The pyroxenes in these gabbros are altered to talc and serpentine, whereas the plagioclase is largely fresh.

Alteration of Breccias

A fault gouge in Section 209-1270A-3R-1 appears to consist entirely of serpentine mud. Another small piece of a fault breccia (interval 209-1270A-2R-1, 101–104 cm) is composed of angular clasts of serpentinized harzburgite embedded in a cement of green clay and abundant carbonate.

Metamorphic Veins

Metamorphic veins in Hole 1270A account for 1.2 vol% of the recovered core and consist predominantly of serpentine (Fig. F29; Table T3). Two generations of chrysotile veins can be distinguished. The first generation is paragranular and has coarse magnetite grains; the younger generation is white, magnetite-free, and transgranular. Transgranular chrysotile veins are bent into the foliation planes of mylonite zones in Section 209-1270A-1R-1. Talc-serpentine veins are crosscut by the younger generation of chrysotile veins; a crosscutting relationship to the earlier chrysotile-magnetite veins could not be established. Talc veins in Section 209-1270A-4R-1 are present in proximity to ultramafic dikes and are oriented subparallel to these dikes.

F29. Vein composition, Hole 1270A, p. 80.

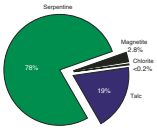

T3. Vein mineralogy, p. 176.

Hole 1270B

Hole 1270B had a core recovery of 37.4% and reached a maximum depth of 45.9 mbsf. The drill core consists of slightly to moderately al-

tered oxide-rich gabbro and microgabbro. There is no systematic variation in alteration intensity with depth (Fig. F30). Three pieces of completely talc-altered harzburgite were recovered in Cores 209-1270B-6R and 7R. These show the highest intensity of alteration among rocks from Hole 1270B.

Hydrothermal Alteration

Alteration is dominated by chlorite–green amphibole assemblages at the contacts of pyroxene and plagioclase crystals (Fig. F31). Brown amphibole of hydrothermal or magmatic origin is commonly associated with Fe-Ti oxides and replaces pyroxene at the margins and along internal cracks (Fig. F32). Brown amphibole is also present in veins/dikelets of chlorite and amphibole that locally crosscut the gabbro (Fig. F33). Two types of chlorite may be distinguished in some thin sections from Hole 1270B. Chlorite with gray to brown interference color is commonly formed at the expense of pyroxene crystals, whereas chlorite with anomalous blue interference color replaces plagioclase. Some of the plagioclase was altered to chlorite and fine-grained quartz aggregates, similar to the alteration of gabbro in Hole 1268A (cf. Fig. F34, p. 89, in the "Site 1268" chapter). Alteration of igneous calcic plagioclase to secondary sodic plagioclase took place along grain boundaries and internal cracks. Further, plagioclase experienced grain size reduction due to deformation. A relationship between deformation and intensity of hydrothermal alteration could not be established.

Sections of moderate alteration intensity (Fig. F30) show partial replacement of pyroxene by talc-chlorite-amphibole assemblages in hand specimen. Talc replacement is particularly well developed in a deformed zone of exceptional olivine-bearing gabbro in interval 209-1270B-8R-1, 23–31 cm (Fig. F34A, F34B). However, talc replacement was not complete, and thin bands (<1 mm in width) of fresh olivine were observed in a thin section of this interval (Fig. F34C). Furthermore, three pieces of completely talc-altered harzburgite were recovered (intervals 209-1270B-6R-1, 51–57 cm; 7R-1, 4–11 cm; and 7R-1, 19–24 cm) that are similar in appearance to specimens recovered from Hole 1268A (see Fig. F21, p. 76, in the "Site 1268" chapter). A microgabbro in interval 209-1270B-7R-1, 114–118 cm, contains a nodular, talc-rich patch surrounded by a 1-cm-wide light green to brown halo, which may represent a halo to an exceptionally thick talc vein (Fig. F35).

In addition to the oxide minerals, which are locally abundant in the gabbro (cf. "Igneous and Mantle Petrology," p. 3), there are noticeable amounts (<1%) of disseminated sulfides, especially in intervals 209-1270B-7R-2, 36–146 cm; 7R-3, 0–46 cm; 8R-1, 83–136 cm; and 10R-1, 80–106 cm. These sulfides are mainly pyrite with minor chalcopyrite and may represent recrystallized igneous phases. In some instances, primary Fe-Ti oxides underwent partial subsolidus exsolution/oxidation and subsequent hydrothermal alteration to aggregates of trellislike ilmenite lamellae with secondary oxides and rare titanite.

Metamorphic Veins

Veining is weakly developed in Hole 1270B, which is reflected in the comparatively low calculated value for the volume percent of veins in the core (0.5%) (Table T3). The mineralogical composition of the veins in Hole 1270B differs significantly from that in Hole 1270A, which is dominated by serpentine (Fig. F29). In Hole 1270B, talc and chlorite are

F30. Alteration intensity, Hole 1270B, p. 81.

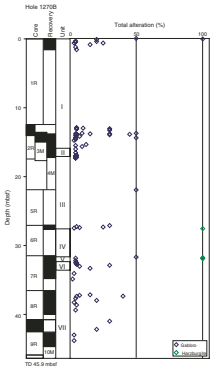

F31. Alteration of gabbro, p. 82.

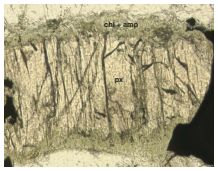

F32. Pyroxene replaced by aggregates of brown amphibole, p. 83.

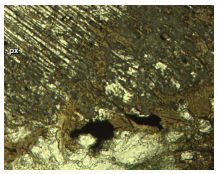

F33. Brown amphibole and chlorite crosscutting gabbro, p. 84.

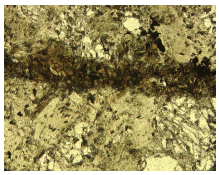

F34. Intensely deformed interval, p. 85.

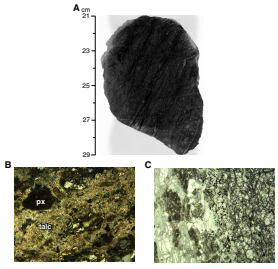

the principal phases followed by serpentine and amphibole (Fig. F36). However, sulfide-bearing veins are locally prominent.

In general, thin (<1 mm in width), irregular chlorite-amphibole veins can be distinguished from talc-chlorite veins. However, a relative age relationship could not be established. Both types of veins crosscut the foliation of the gabbro if present (e.g., interval 209-1270B-2R-1, 24–27 cm). Exceptional talc-chalcopyrite veins (~5 mm wide) were observed in interval 209-1270B-7R-1, 49–66 cm (Fig. F37). In sections of the core below this interval, noticeable amounts of disseminated sulfides were observed in the gabbro (see "Hydrothermal Alteration," p. 13, above).

Hole 1270C

Hole 1270C was drilled to a final depth of 18.6 mbsf (recovery = 10.6%). The predominant rock types are serpentinized harzburgite and dunite. Intermittently, there are intervals containing irregular, completely altered intrusions of gabbro.

Hydrothermal Alteration

The harzburgites and dunites have mostly been completely serpentinized and display ribbon texture background alteration. XRD (Table T2) and magnetic susceptibility measurement (see "Paleomagnetism," p. 41) show that completely serpentinized ultramafic rocks consist of lizardite ± chrysotile and magnetite. Orthopyroxene is commonly pseudomorphed by bastite. However, minor green amphibole rims are locally present (e.g., intervals 209-1270C-1R-1, 36–39 cm, and 3M-1, 44–48 cm).

Relict fresh olivine and orthopyroxene are preserved in a few places (Fig. F38). Here, orthopyroxene is partially replaced by talc along the margins and along internal fractures. Subsequent serpentinization replaced most of the olivine. However, some fresh olivine is preserved adjacent to the orthopyroxene. During low-temperature alteration (seafloor weathering), clay and Fe oxyhydroxides formed at the expense of relict olivine and orthopyroxene (Fig. F38). These assemblages are easily recognized at the hand specimen scale because of their rusty orange-brown color (Fig. F38A). Spotty to pervasive weathering is present in all three cores from Hole 1270C.

Gabbroic intrusions were observed intermittently throughout Hole 1270C (Fig. F39A). They are typically deformed and metamorphosed to talc-serpentine ± chlorite ± brown amphibole and host porphyroclasts of serpentinized harzburgite (Fig. F39B, F39C). Brown amphibole partially replaces and rims orthopyroxene within the deformed zones (Fig. F39E). However, amphibole is absent in the "boudins" of fresher peridotites located above and below the deformed bands, suggesting that brown amphibole pseudomorphs were formed from high-temperature fluids infiltrating along the deformed band.

Metamorphic Veins

Metamorphic veins are more abundant in Hole 1270C than in Holes 1270A and 1270B and account for 2 vol% of the core. As in Hole 1270A, serpentine is the most common mineral in veins (86%) (Fig. F40; Table T3). However, the vein mineralogy in Hole 1270C is distinctive because talc is only a minor component and iron oxides are common (12.5%). Furthermore, there are rare carbonate veins.

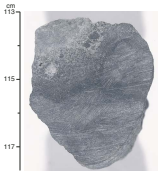

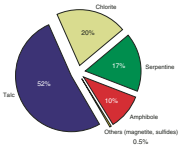

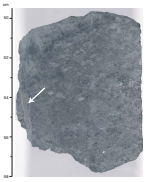

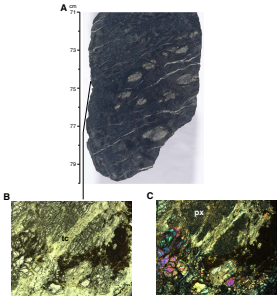

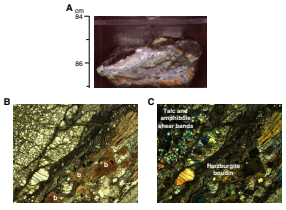

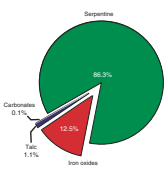

The earliest generation of veins are sigmoidal, paragranular, cross-fiber chrysotile veins, common in Core 209-1270C-2R. These are crosscut by transgranular serpentine veins that show variable orientations with respect to the foliation, varying from perpendicular to subparallel. These serpentine veins show complex interrelationships and represent several generations. Networks of iron oxide veinlets postdate the serpentine and are particularly common in Core 209-1270C-1R. A single carbonate vein in Sample 209-1270C-1R-1, 83–85 cm, cuts the massive serpentine and cross-fiber chrysotile veins, representing a late stage of vein alteration, possibly associated with seafloor weathering (Fig. F41).

F41. Carbonate vein crosscutting earlier serpentine veins, p. 93.

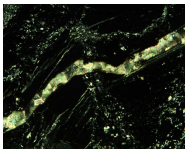

Hole 1270D

Hole 1270D reached a depth of 57.3 mbsf (average recovery = 13.4%). The core consists mainly of a complex association of deformed serpentinized harzburgite that hosts irregular, schlieren- to network-like, hydrothermally altered and partly rodingitized gabbro. Furthermore, there are minor serpentinized dunites throughout the drill core. The alteration is mainly complete; however, there are minor occurrences of less strongly altered harzburgite (Fig. F42).

F42. Alteration intensity, Hole 1270C, p. 94.

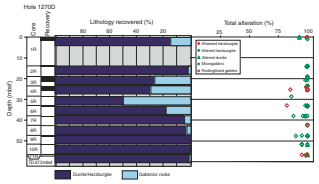

Hydrothermal Alteration

Alteration of Harzburgites and Dunites

Harzburgite and dunite in Hole 1270D were affected by three different styles of alteration: serpentinization, alteration to talc (in proximity to gabbro veins), and local weathering to orange clay and Fe oxyhydroxide. The morphology of the serpentine is dominated by ribbon texture with poorly developed core and rim structures remaining (e.g., Sample 209-1270D-3R-1, 63–65 cm). Occasional pockets of mesh texture alteration are preserved (e.g., Sample 209-1270D-5R-1, 23–28 cm) where serpentinization of olivine has not been complete. Bastite pseudomorphs after orthopyroxene are locally present but less common than at Site 1268 (e.g., Sample 209-1270D-10R-1, 4–6 cm). Fine-grained magnetite forms networks within the serpentinized matrix and was also detected by XRD analyses (Table T3). The highest visual estimates for magnetite are ~3 vol% in interval 209-1270D-4R-1, 19–22 cm. Oxide veining, which is common in Cores 209-1270D-1R, 2R, 3R, and 4R, locally grades into oxide-rich background alteration (e.g., interval 4R-1, 38–51 cm). Weathering of harzburgite to clay and Fe oxyhydroxides occurs throughout the length of the core and is particularly strongly developed in Core 209-1270D-1R (Fig. F43). Talc ± tremolite alteration locally overprints serpentinization but is largely restricted to gabbro zones and deformed zones.

F43. Clay and iron oxyhydroxide weathering of harzburgite, p. 95.

Alteration of Gabbros

The harzburgites and dunites are intruded by numerous gabbroic veins or dikes that were mylonitized, imparting a gray, foliated appearance to a large proportion of the core recovered from Hole 1270D. Locally, completely serpentinized harzburgite is present as boudins within the deformed gabbroic intrusions (Fig. F44).

F44. Serpentinized harzburgite forming boudins in gabbroic intrusion, p. 96.

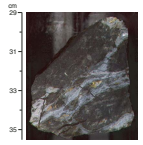

The gabbro intrusions are altered to albite, tremolite, talc, chlorite ± smectite, and, locally, to calcium silicates (e.g., hydrogrossular and prehnite in thin section of Sample 209-1270D-10R-1, 11–17 cm). Formation of calcium silicate mineral assemblages in gabbro is evidence of

calcium metasomatism. Fluids enriched in calcium are generated during serpentinization of ultramafic rocks, and calcium metasomatism of adjacent lithologies is a common phenomenon referred to as rodingitization. This indicates synchronous alteration of the ultramafic rocks and the enclosed gabbro intrusions.

In addition to these mineral assemblages, some of the gabbros show replacement of pyroxene by brown amphibole similar to Sample 209-1270C-1R-1, 84–87 cm, illustrated in Figure **F39.** Furthermore, the gabbro of Sample 209-1270D-10M-1, 142–144 cm, contains minor biotite and an amphibole replacing orthopyroxene in Sample 4R-1, 33–37 cm, contains minor biotite and rare epidote inclusions.

Metamorphic Veins

The abundance of metamorphic veins in Hole 1270D is similar to that in Hole 1270C. Veins in Hole 1270D account for 1.9 vol% of the core, and serpentine is the most common mineral in veins (83.5%) (Fig. **F45;** Table **T3**). Hematite and other iron oxides (including Fe oxyhydroxides, which are common in the weathered zones) account for 9.7 vol% of the vein minerals, followed by talc (5.4 vol%). Minor minerals include carbonate, amphibole, magnetite, and sulfides.

In general, vein alteration in Hole 1270D is dominated by serpentine and Fe oxyhydroxide. Fe oxyhydroxides can account for as much as 50% of some serpentine veins, but the modal percentage is highly variable. These variations account for the variable colors of serpentine veins in Core 209-1270D-1R.

Metamorphic Veins in Harzburgite and Dunite

Serpentine veins often show sigmoidal shapes forming semicontinuous, en echelon arrays. Locally, they cut across the deformed gabbroic intrusions (e.g., Section 209-1270D-3R-1) (Fig. **F46**). In some of the cores, sigmoidal chrysotile veins are oriented subparallel to the foliation and may represent the earliest stage of serpentine veining (e.g., Section 209-1270D-5R-1).

Overall, the serpentine veins in Hole 1270D show complex interrelationships, and three different generations can be distinguished locally based on crosscutting relationships (Fig. **F47**). However, it is often difficult to separate the different generations of serpentine veins in hand specimen because of variations in their textural relationships. For example, veins that appear as discrete generations in the upper part of Core 209-1270D-4R become indistinguishable at ~130 cm. Furthermore, there are textural variations within single veins. In Section 209-1270D-3R-2, occasional pockets of chrysotile fibers are present in the tips of otherwise massive serpentine veins. In Section 209-1270D-4R-1, these veins are accompanied by as much as 10% magnetite. Elsewhere in Section 4R-1, fine networks of chrysotile veins extend from the tips of sigmoidal serpentine veins. This differs from higher in the core, where these vein types are two separate generations.

Networks of submillimeter hematite veins commonly crosscut serpentine veins throughout Hole 1270D and are particularly abundant in the upper cores. Iron oxide veins may also follow the margins of earlier chrysotile veins or propagate along their interior. This feature is particularly prominent in interval 209-1270D-3R-2, 33–114 cm. Hematite veins crosscut all other features and are therefore one of the latest veining events. Locally, the fine hematite veining is intense. In its extreme form, the individual veins are no longer discernable and the veining

F45. Vein composition, Hole 1270D, p. 97.

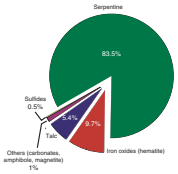

F46. Serpentine veins in serpentinized harzburgite, p. 98.

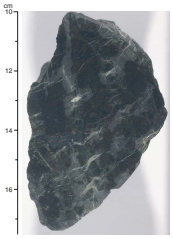

F47. Three serpentine vein generations, p. 99.

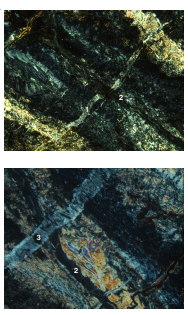

grades into the background alteration (e.g., interval 209-1270D-4R-1, 40–50 cm).

Other features of vein alteration in Hole 1270D are minor replacement of serpentine veins by talc, rare carbonate veining, and rare sulfide veining. An aragonite vein, as wide as 3 mm, is present in interval 209-1270D-6R-1, 41–50 cm (Fig. F48). Carbonate veins crosscut the surrounding serpentine veins and may be related to the late-stage weathering of the serpentinized harzburgite. A massive sulfide vein in interval 209-1270D-5R-1, 5–9 cm, consists of pyrite, chalcopyrite, and hematite (Fig. F49). It has a banded structure with a hematite core and sulfide along the margins.

Metamorphic Veins in Gabbro

Veining within the gabbro is infrequent. Minor chrysotile veins with virtually no Fe oxyhydroxides are present. A few serpentine veins occur within the gabbroic shear zones.

Discussion

Drill core recovered from Hole 1270A represents a typical example of completely serpentinized harzburgite altered under static conditions. Within the deformed zones, the mesh-textured serpentine is recrystallized to serpentine with an interpenetrating texture (antigorite?) and late chrysotile veins have been transposed into the foliation. These observations indicate that deformation occurred during late-stage serpentinization or after serpentinization was largely complete.

The alteration of the gabbro in Hole 1270B is fairly monotonous over the entire 45.9 m drilled. The chlorite-amphibole alteration on grain boundaries of pyroxene and plagioclase crystals is characteristic of greenschist facies conditions. There are fairly minor variations in the intensity of alteration and no apparent correlation with the degree of rock deformation. This is consistent with textural observations that suggest alteration was mainly static. However, in rare highly deformed shear zones there are bands with substantial talc replacement of pyroxene.

Hydrothermal veining is comparatively weak in Hole 1270B and is dominated by chlorite-amphibole and talc-chlorite veins. This mineralogy differs substantially from the serpentine veins observed in Hole 1270A. This difference is clearly related to the host rock composition, indicating that the fluids forming the veins in Hole 1270B have not interacted with ultramafic material or were saturated with serpentine and quickly evolved to chlorite-amphibole saturation by interaction with the gabbro.

Holes 1270C and 1270D were drilled within 30 m of each other and show many similarities, suggesting that they underwent the same deformation-alteration paths (see "Structural Geology," p. 21). There is an intimate association of serpentinized harzburgite and dunite with deformed, schlieren-shaped intrusions of completely altered gabbro. Within these deformed zones there is evidence for highly localized, synkinematic high-temperature alteration. The vein assemblages in Holes 1270C and 1270D show complex relationships, indicating that multiple episodes of veining took place after the deformation.

In the following sections, we will discuss the possible origin of key alteration features and their implications in terms of the relationship between alteration and deformation. A model for the relative timing of alteration-deformation events is proposed based on overprinting

F48. Aragonite veins in clay-altered serpentinized harzburgite, p. 100.

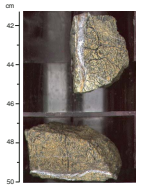

F49. Sulfide veins with pyrite chalcopyrite rims and hematite cores, p. 101.

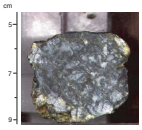

relationships of serpentinization, serpentine veins, and spatial correlation of alteration types with shear zones.

Alteration of Gabbro Protoliths

In Hole 1270B static alteration of gabbro under greenschist facies postdates the deformation. In contrast, gabbroic intrusions in Holes 1270A, 1270C, and 1270D are replaced by amphibole-chlorite-talc assemblages and are generally deformed. Locally, these assemblages are dominated by talc, especially in boudins located in shear bands. This style of alteration may be related to deformation under greenschist facies conditions. In addition, static alteration of gabbro within and outside of the shear zones occurs in Holes 1270C and 1270D, indicating that gabbro alteration was not restricted to zones of localized strain.

In the shallow part of Holes 1270C and 1270D (<20 mbsf), some of the gabbros are altered to tremolite-talc schists. These schists display penetrative schistosity defined by oriented amphibole, talc, and chlorite crystals (e.g., intervals 209-1270C-1R-1, 83–85 cm, and 1R-1, 16–18 cm). Similar talc-amphibole-chlorite schists were described in fault rocks from the Mid-Atlantic Ridge at 15°45′N and were interpreted as alteration of a peridotite protolith (Escartin et al., 2003). However, it is apparent that the schists in Holes 1270C and 1270D developed as a result of alteration of gabbro boudins in shear zones hosted by serpentinized ultramafic rocks in Holes 1270C and 1270D. This relationship indicates that deformation continued under greenschist facies conditions.

It is uncertain why the gabbroic rocks in Holes 1270B, 1270A, 1270C, and 1270D have been affected by different styles of alteration. Potential factors are the timing of gabbro emplacement (pre-, syn-, or postkinematic), the size of the gabbro intrusions, and the location of gabbro emplacement with regard to the tectonically active zones.

Multistage Serpentinization Events and Their Relationship to Deformation

Overprinting serpentinization textures are locally observed in completely serpentinized peridotites from Holes 1270A, 1270C, and 1270D. Replacement of pseudomorphic texture is locally present in Holes 1270C and 1270D where a relict mesh texture is crosscut by trains of magnetite grains to form transitional ribbon textures. Mesh textures are mainly preserved in pressure shadows of serpentine pseudomorphs after orthopyroxene. The transitional serpentinite textures may be interpreted as evidence for syntectonic serpentinization associated with the deformation of mesh textures (Wicks, 1984).

Sample 209-1270A-1R-1, 35–37 cm, contains firm evidence for synkinematic to postkinematic serpentine recrystallization, where the serpentinite mesh texture is overprinted by shear zones that recrystallized to interpenetrating serpentine (antigorite[?]) (Fig. **F28**). In this sample, chrysotile veins are transposed into the foliation, indicating that deformation occurred during late-stage serpentinization (see **"Structural Geology,"** p. 21).

Pre- to synkinematic serpentine alteration in Holes 1270C and 1270D is reflected by the prominent development of paragranular serpentine veins relative to transgranular serpentine veins (Fig. **F50**). Furthermore, some en echelon cross-fiber serpentine veins are transposed and rotated in talc shear zones. However, late generations of serpentine veins crosscut talc-rich shear zones and earlier generations of serpentine

F50. Paragranular vs. transgranular serpentine veins, p. 102.

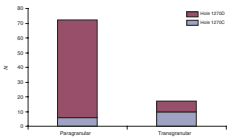

veins (Fig. F47). This observation indicates that serpentinization took place in several stages and that deformation continued after the initial high-temperature ductile deformation. Hence, in different sections of cores from Site 1270, there is evidence for serpentinization prior to, during, and after the deformation recorded by amphibole-chlorite-talc schists.

Origin of Brown Amphibole Veins

One of the prominent characteristics of shear zones in Holes 1270C and 1270D is the common presence of brown amphibole in composite microshear zones containing boudins of harzburgite and gabbro (Fig. F39). Minerals in harzburgitic and gabbroic boudins display evidence of high-temperature ductile deformation (see "Structural Geology," p. 21). Talc is common in these shear zones and postdates the development of brown amphibole. Although Holes 1270C and 1270D also contain brown amphibole as millimeter-wide layers of pyroxenites (cf. "Igneous and Mantle Petrology," p. 3), brown amphibole occurrences in shear zones are clearly distinct in terms of mineral assemblages and textures. Brown amphiboles in shear zones form discrete amphibole-rich bands oriented subparallel to the high-temperature fabric defined by porphyroclasts of orthopyroxene and plagioclase (Fig. F39).

Several textural observations suggest that the formation of brown amphibole was related to synkinematic infiltration of high-temperature fluids/melts into the shear zones. Fluid inclusions in amphibole range from three-phase inclusions to vapor-dominated inclusions, suggesting that the fluids underwent supercritical phase separation. Amphibole crystals in the shear bands are euhedral with a well-developed cleavage and lack any indication of stress-induced syntectonic deformation or recrystallization, in contrast to the minerals in harzburgitic and gabbroic boudins. In addition, amphibole replaces and overgrows plastically deformed minerals of the harzburgitic and gabbroic boudins. The style of amphibole formation appears to be controlled by the nature of the enclosing host rock. Where peridotite wallrock is present, the brown amphibole replaces orthopyroxene porphyroclasts along the margins of peridotitic boudins (Fig. F39E). Where the amphibole-rich zones are in contact with gabbroic wallrock, the brown amphibole preferentially replaces clinopyroxene while plagioclase is replaced by dark green amphibole. This observation suggests that amphibole was not in equilibrium with all the minerals in the shear zone. Furthermore, brown amphibole is exclusive to the margins and internal fractures of peridotitic or gabbroic boudins but absent in their interiors.

Synkinematic brown amphibole veins with textural characteristics similar to those of Holes 1270C and 1270D have been reported from lower crustal rocks formed at slow-spreading mid-ocean ridges (e.g., the Kane Fracture Zone [MARK] area [Leg 153; Dilek et al., 1997b] and Atlantis Bank, Southwest Indian Ridge [Hole 735B; Stakes et al., 1991]). These brown amphiboles were interpreted to be the product of crystallization from high-temperature fluids/melts circulating along shear zones. In Holes 1270C and 1270D the brown amphibole veins occur in shear bands composed of deformed gabbros and harzburgites, but there is no direct evidence to invoke a spatial association with a crystallizing pluton. However, the local presence of zircon and apatite crystals (cf. "Igneous and Mantle Petrology," p. 3) in the shear bands suggests that the brown amphibole may have been precipitated from high-temperature (800°–1200°C) fluids/melts (e.g., Ayers and Watson, 1991). The ob-

servations discussed above may be explained by a process in which fluids or melts penetrated shear zones rooted in a differentiating magmatic plumbing system.

Origin of Talc-Bearing Shear Zones

One peculiarity of Holes 1270C and 1270D is the restriction of talc alteration to microshear zones and talc veinlets along shear zones. In these shear zones, talc clearly overprints minerals formed during higher-temperature fluid circulation, such as brown amphibole. Despite being restricted to shear zones, talc-rich zones display no compelling textural evidence of syntectonic talc crystallization. The fine grain size of talc shear bands makes it difficult to prove that talc crystallization was syntectonic. However, the fact that talc alteration is mainly restricted to associations with shear zones and the apparently low crystallinity of talc veins associated with the shear zones may indicate that the formation of talc was synkinematic.

Late Veins: Carbonate and Fe Oxyhydroxide Veins

In addition to the main types of alteration described above, Holes 1270C and 1270D contain minor carbonate and oxide veins. Networks of Fe oxyhydroxide veins are generally restricted to the shallower cores of these holes and probably formed during seafloor weathering. The predominance of hematite and general lack of sulfides indicates oxidizing conditions and low aqueous H_2S activities of the fluids. Carbonate veins with red clays also formed during shallow seawater infiltration. The carbonate commonly displays a prismatic habit and is probably aragonite that is formed by interaction with cold seawater (e.g., Bonatti et al., 1980)

However, carbonate is locally present in the deeper part of Hole 1270D, where carbonate veins are spatially related to talc shear zones and cut serpentine textures. These veins do not cut across the talc-rich shear zones but appear to grade into them. Moreover, carbonate replaces orthopyroxene in Sample 209-1270D-6R-1, 29–32 cm. Potentially, this relationship may indicate that the formation of carbonate is related to the circulation of carbonate-rich fluids along the shear zones.

Tentative Timing of Alteration and Deformation Events

Figure F51 illustrates the inferred temporal relationships between background alteration, alteration veins, and deformation based on our textural observations at Site 1270. Peridotite and gabbro intrusions record ductile deformation in the granulite facies prior to deformation. Shear zones display evidence of synkinematic formation of brown amphibole by interaction with supercritical fluids in the amphibolite facies. Finally, talc and tremolite replace the previous mineral assemblages along shear zones during a greenschist facies overprint. This sequence of textural and mineralogical features suggests that shear zones were active over a large temperature range from granulite to greenschist facies conditions. It is likely that anastomosing talc-bearing shear zones are the result of increasing shear localization in previously wider shear zones. Away from these shear zones, serpentinization of peridotites and alteration of gabbro took place statically under greenschist facies conditions.

F51. Timing between alteration and deformation, p. 103.

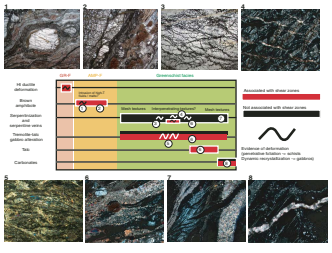

STRUCTURAL GEOLOGY

We present the results of a detailed structural analysis of core recovered from Holes 1270A, 1270B, 1270C, and 1270D. Four categories of observations were recorded in spreadsheet format including magmatic fabrics, crystal-plastic deformation, brittle deformation, and alteration veins (see the "Supplementary Material" contents list). These were supplemented by microstructural observations from 46 thin sections, although the relatively high degree of alteration in the peridotites meant that some of the features are preserved only as pseudomorphs, leading to potential ambiguity in their interpretation. Details of the structural classification scheme for each feature are given in "Structural Geology," p. 9, in the "Explanatory Notes" chapter. We conclude with a discussion of the temporal and spatial relationships of the structures and then present an initial interpretation of the evolution of each of the four holes in the context of their tectonic setting.

Hole 1270A

Crystal-Plastic Deformation

The three cores from Hole 1270A recovered largely green "popcorn" serpentinite (Fig. F52). This informal name reflects the puffed up, expanded appearance of the pyroxene pseudomorphs in hand sample. It can be seen in thin section that the pyroxene bastites (pseudomorphed orthopyroxene grains) have a halo of clear serpentine around them in a mass of green serpentine heavily veined by magnetite. Because of this type of serpentinization, these protogranular peridotites may appear to have a porphyroclastic fabric. Thus, caution should be taken when relying on visual core descriptions of these serpentinites. Instead, we rely heavily on five thin sections in our analysis. In addition to the serpentinites, a small volume of highly altered gabbro was found (3.6 vol%). The alteration commonly obscured the extent of deformation, but they generally appear to be undeformed.

F52. Green serpentinized "popcorn" harzburgite, p. 104.

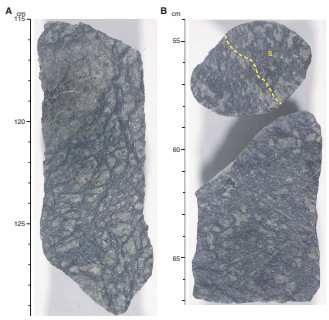

High-Temperature Crystal-Plastic Textures

Bastite pseudomorphs of orthopyroxene permit the identification of the serpentinite protoliths as harzburgite and allow characterization of the primary protogranular texture. Two examples of protogranular texture are shown in Figure F53. The rocks contain isolated orthopyroxene pseudomorphs with smooth curved grain boundaries, deep embayments, and irregular lobes locally extending into a serpentinized olivine matrix. Orthopyroxene cleavage pseudomorphs show that most grains are unstrained, although a few samples have slight kinks in them. Although some pyroxene pseudomorphs have an aspect ratio >4:1 (porphyroclastic by definition in "Fabric Intensities," p. 11, in "Structural Geology" in the "Explanatory Notes" chapter), suggesting crystal-plastic elongation, the highest crystal-plastic intensity seen in the thin sections is at most 0.5 (very weakly deformed).

F53. Serpentine bastite pseudomorphs of primary orthopyroxene, p. 105.

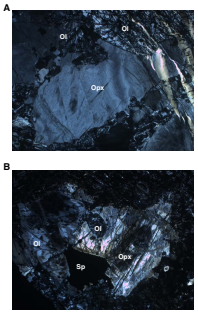

Downhole Deformation Intensity and Orientation of Crystal-Plastic Fabrics

As noted above, well-developed crystal-plastic foliations are rare in the serpentinized harzburgites. An example of a primary foliation is shown in the upper core piece in Figure F52B. Here there is a clear foliation, defined by the pyroxene shape fabric that is not the product of porphyroclastic deformation. Individual pyroxenes can be seen to have

irregular lobes and embayments characteristic of protogranular texture, but overall they are elongate in the foliation plane. Unfortunately, foliations are difficult to identify, but we estimate the average foliation dips ~45° in the cut face.

Figure F54 is a downhole plot of fabric intensity made using a running average (weighted by piece length) of the deformation intensities measured on seven contiguous core pieces. This plot suggests that the harzburgites in the upper 16 m of the hole have a weak porphyroclastic texture, whereas those deeper in the hole range from undeformed (protogranular) to very weakly porphyroclastic. As noted earlier, because of the unusual texture of these serpentinites, estimated deformation intensities during visual core description are not entirely reliable and the intensity of the porphyroclastic texture may be overestimated.

F54. Crystal-plastic deformation intensity with depth, Hole 1270A, p. 106.

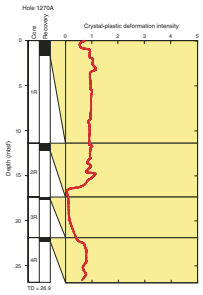

Magmatic Veins

The Hole 1270A core is generally devoid of extensive magmatic veining. Only Section 209-1270A-4R-1 contains minor volumes of veins, and none of these pieces is oriented. Two thin veins of altered pyroxenite cut harzburgite in Piece 5 of this section, and a thin altered gabbroic vein crosscuts partially serpentinized (95%) harzburgite in Pieces 14 and 15. The gabbroic veins are similar and are probably contiguous (Fig. F55). The veins cut orthopyroxene grains and consist of plagioclase pseudomorphed by prehnite and hydrogrossular and olivine replaced by serpentine. They appear undeformed and are oblique to the foliation and thus are considered postkinematic with respect to the crystal-plastic deformation. The presence of thin magmatic veins suggests that the host peridotites were near magmatic temperatures during vein formation. Two small fragments of pyroxenite without contact relationships in Section 209-1270A-4R-1 (Pieces 1 and 2) are the only other pieces that could be magmatic vein material. The amount of plutonic rock in Hole 1270A is particularly low compared to Holes 1270C and 1270D.

F55. Serpentinized harzburgite with a crosscutting altered gabbroic vein, p. 107.

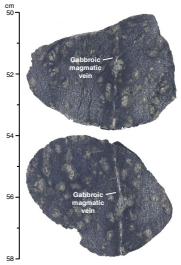

Cross-Fiber Serpentine Foliation

Some of the serpentinized peridotite recovered from Hole 1270A displays a weak to moderately strong, dominantly planar fabric defined by anastomosing arrays of serpentine veins and elongate mesh cells. Similar foliations were described in serpentinite from Ocean Drilling Program (ODP) Site 920 (Shipboard Scientific Party, 1995), and the texture was termed "ribbon texture serpentinite" by O'Hanley (1996) based on observations of serpentinite from ophiolites. Serpentine and magnetite veins that define the foliation are commonly deflected around pyroxene porphyroclasts, which causes anastomosing waves in the foliation. Serpentine fibers in veins are commonly aligned perpendicular to vein walls, suggesting growth during dilational fracture opening. This indicates that the foliation is not a result of shear deformation but is a purely dilational feature.

F56. Fault gouge/breccia, p. 108.

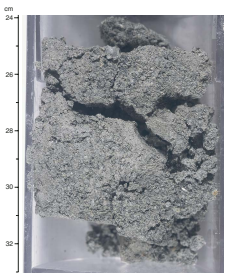

Brittle Deformation

Two intervals of fine-grained breccia interpreted as fault gouge were recovered from Section 209-1270A-3R-1 (Pieces 1 and 3). Both breccias contain subrounded to angular lithic clasts and individual crystals ranging 0.03–0.3 cm in size within a gray-green carbonate-rich serpentine matrix (Fig. F56). The primary difference between the fault gouge zones

is that Piece 1 appears to be supported by the extremely fine grained matrix and is slightly cohesive, whereas Piece 3 is clast supported and is noncohesive. The gouge reacts with hydrochloric acid, but it is unknown if this reaction is wholly with carbonate clasts or also with a carbonate fraction within the matrix. Some of the gouge characteristics described here could be a result of disturbance by drilling, and the in situ equivalent of these pieces may have different characteristics. In addition to fault gouge zones in Section 209-1270A-3R-1, there is also a small fragment of fine-grained, carbonate-matrix, cohesive cataclasite (Section 2R-1, Piece 15). This piece may have formed during an earlier phase of brittle deformation, predating formation of the gouge zones described above.

Section 209-1270A-1R-1 (Piece 7) contains a shear zone that was identified in thin section but was not apparent during visual observation of the core. The zone consists of a schistose mat of fibrous white serpentine (Fig. F57). These serpentine fibers terminate along a diffuse boundary into a very fine granular-texture serpentinite that contains clasts of pseudomorphed pyroxene and normal mesh-texture serpentine. This zone, which resembles a breccia, is several millimeters wide and lies between the schistose serpentine and normal mesh serpentinite. Its contact with the mesh serpentinite is irregular and undulatory. The foliation of the schistose serpentine is aligned at a 30° angle oblique to the contact between the breccia serpentine and the normal mesh serpentine.

F57. Serpentine shear zone, p. 109.

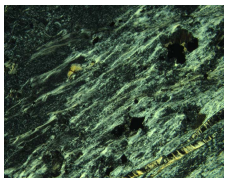

Alteration Veins

The alteration veins in the harzburgites and dunites range from planar and continuous to thin, irregular, discontinuous veinlets. They form a relatively small proportion of the core and have maximum widths of 2 mm. The veins are dominantly serpentine with subsidiary talc and oxide veins. There are at least three generations of serpentine veins: dark magnetite-rich serpentine veins, pale green serpentine veins, and late white chrysotile veins. Interval 209-1270A-2R-1, 88–93 cm (Fig. F58), shows an early generation of green serpentine and the later generation of white chrysotile veins oriented parallel to the foliation in the harzburgite. Chrysotile veins are transposed into the foliation of the sheared serpentinite (interval 209-1270A-1R-1, 34–39 cm) described in "Brittle Deformation," p. 22, above, indicating that the early phase of serpentinization occurred prior to the phase of semibrittle deformation. Interval 209-1270A-1R-1, 43–50 cm, contains normally faulted chrysotile veins, indicating that serpentinization also occurred before low-temperature brittle deformation. Two gabbroic veins are present within this core, one is cut by serpentine-filled tension cracks perpendicular to its length (interval 209-1270A-4R-1, 48–56 cm), providing evidence that the pervasive serpentinization postdates gabbroic veins. A detailed discussion of the mineralogy of the metamorphic veins can be found in "Metamorphic Petrology," p. 11.

F58. Harzburgite with serpentine veins parallel to crystal-plastic foliation, p. 110.

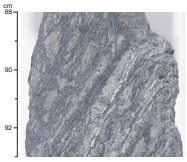

Hole 1270B

Crystal-Plastic Deformation

Crystal-plastic deformation in the oxide gabbronorites of Hole 1270B occurred over a range of conditions. High-temperature, moderate-strain fabrics (deformation intensity = 1–2.5) predominate (74.9 vol%) (Fig.

F59). Low-strain fabric deformation (intensity = <1) is also important (23.8 vol%), but higher-strain fabrics are rarely present (1.3%). Altered peridotite, largely soapstone and serpentinite, makes up 1.7% of the recovered material and displays only low strain–rate fabrics formed at high temperatures. Gabbro and peridotite deformation intensities were logged using separate, but equivalent, deformation intensity scales as explained in "Structural Geology," p. 9, in the "Explanatory Notes" chapter. The orientation of the fabrics was measured in the core reference frame.

High-Temperature, Low-Strain Fabrics

High-temperature, low-strain fabrics are found in the altered peridotites. They are completely altered but contain numerous talc and bastite pseudomorphs of orthopyroxene, allowing us to characterize the extent of deformation. The grain boundaries are generally rounded with few protrusions, and the shapes correspond to a weak to moderate porphyroclastic texture similar to those seen in the Hole 1268 altered peridotites (see earlier discussion in "Structural Geology," p. 20, in the "Site 1268" chapter).

High-Temperature, Moderate-Strain Fabrics

The majority of gabbros found in Hole 1270B have high-temperature, moderate-strain fabrics and range from weakly foliated and well-foliated porphyroclastic gneiss to protomylonite. Recrystallization of plagioclase is extensive, usually >40%, with the development of ribbon porphyroclasts (Fig. F60A) and bent and kinked clinopyroxene (Fig. F60B, F60C) and extensive development of clinopyroxene porphyroclasts with well-developed tails of neoblasts (Fig. F60D, F60E). Low-strain fabrics are also common and are characterized by undeformed clinopyroxene, bent or kinked tabular orthopyroxene grains, and only incipient recrystallization and development of tapered deformation twins in plagioclase. Nearly undeformed oxide gabbros are locally present, particularly in the lower sections of the hole (Fig. F61D).

Long sections of the core show well-developed crystal-plastic foliations (Fig. F62A). In some cases the fabric appears to be uniformly developed at a scale of tens to hundreds of centimeters, and in other cases the deformation of the rock can be heterogeneous down to the millimeter scale. Locally, more than one foliation can be seen in a single piece of core, with one crosscutting the other, as in Section 209-1270B-7R-2 (Piece 13), where a 3-cm protomylonite zone cuts weakly deformed coarse-grained oxide gabbro (Fig. F62B). The protomylonitic band contains a high concentration of iron-titanium oxide. In Section 209-1270B-1R-1 (Piece 17), a foliated microgabbro obliquely crosscuts a foliated coarse oxide gabbronorite. The foliated microgabbro is, in turn, crosscut by a nearly undeformed pyroxenite band (Fig. F63). Thus, the high-temperature deformation accompanied the magmatic construction of the gabbroic rocks.

Late Fe-Ti oxide fills cracks in broken plagioclase and orthopyroxene grains (Fig. F61A, F61B) and forms mantles and tails to clinopyroxene porphyroclasts, where oxides appear to cement neoblasts of clinopyroxene and extend out into the enclosing matrix of recrystallized plagioclase subgrains (Figs. F61C, F60D, F60E). In porphyroclastic gabbros, oxides can be seen on crosscutting microscopic shear zones, suggesting that the oxide precipitation occurred along several different planes in an anastomosing shear zone (Fig. F64C). The unusual structure of many of the lenticular oxide aggregates, parallel to the foliation plane but ex-

F59. Crystal-plastic deformation intensities, Hole 1270B, p. 111.

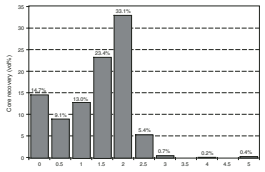

F60. Hole 1270B oxide gabbronorites, p. 112.

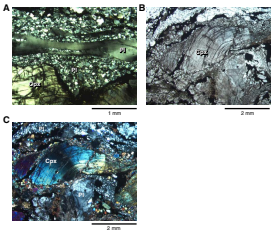

F61. Oxide gabbronorites, p. 114.

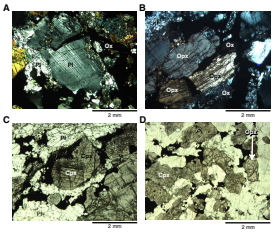

F62. Oxide gabbronorites, p. 115.

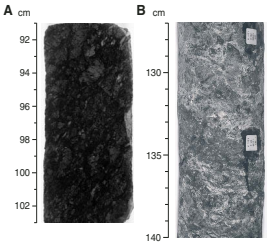

F63. Gabbronorite cut by microgabbro and pyroxenite band, p. 116.

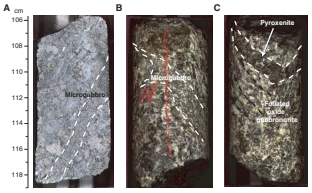

tending into the recrystallized plagioclase matrix in all directions (Fig. F64A, F64B), suggests that the oxide aggregates may have formed by late-stage migration of iron-titanium–rich liquid (for further discussion, see Fig. F24, p. 102, and associated text in the "Leg 209 Summary" chapter).

Moderate-Temperature, High-Strain Fabrics

Rocks with crystal-plastic deformation intensity >2.5 are rare (Fig. F59), with mylonitic gabbros composing only 1.3% of the recovered core. In gabbro mylonites, recrystallization of all phases including clinopyroxene is extensive (Fig. F65). These rocks were recovered in two sections near the base of the hole: Sections 209-1270D-8R-1 and 10M-1. Other than the mylonites, there is little evidence of amphibolite or greenschist facies deformation.

Orientation and Downhole Variation in Crystal-Plastic Deformation

Shown in Figure F66 is a running 10-piece average for total crystal-plastic deformation intensity (noting that the poorest recovery came in intervals with low total intensity). Peridotites with high-temperature, low strain–rate fabrics completely altered to soapstone and serpentine were recovered near the bottom of Section 209-1270B-6R-1 and from the top and middle of Section 7R-1. The lack of deformation, and character of alteration, suggest that the high-temperature downhole stratigraphy may have been emplaced a by brittle fault. Similar altered peridotites were recovered in the upper three cores in Hole 1270B, but here they may represent debris from the top of the hole.

Overall, the highest average deformation intensities are found in the upper portion of the hole above ~20 mbsf in the oxide gabbronorites/gabbronorites, where there is a nearly uniform penetrative foliation. Deformation intensity decreases from ~20 to ~23 mbsf and then spikes in Core 209-1270B-7R before rising again in strongly foliated rocks in Core 8R and the top of Core 9R. This variation in intensity is accompanied by a systematic downward decrease in the dip of the foliation. There may be a positive correlation between deformation intensity and the proportion of Fe-Ti oxides (Fig. F24, p. 102, in the "Leg 209 Summary" chapter) and a negative correlation between deformation intensity and the proportion of plagioclase in the gabbros (Fig. F66).

Shown in Figure F67 are the orientations of the crystal-plastic foliations reoriented into a common orientation using the magnetic declination data as described in "Structures in Peridotite and Gabbroic Intrusions," p. 8, in "Mantle Upwelling, Melt Transport, and Igneous Crustal Accretion" in the "Leg 209 Summary" chapter. The data in Figure F67 are plotted with the declination of the stable remanent magnetization pointing south because the paleomagnetic data suggest a reversed polarity. In this plot we have color-coded samples from the same core. Samples from individual cores cluster together, and the data as a whole define a partial girdle in the stereo plot. This probably does not correspond to a fold axis, as demonstrated by the three different foliations measured in Section 209-1270B-1R-1 (Piece 17) that share a common paleomagnetic declination and inclination. The three foliations in this piece crosscut each other but they appear to have developed penecontemporaneously, suggesting the partial girdles represent various orientations of shear planes in an anastomosing shear zone. The systematic downhole decrease in the average dip of foliation suggests that the

F64. Oxide layers in oxide gabbronorite, p. 117.

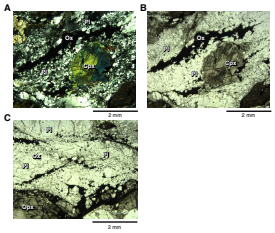

F65. Gabbroic mylonite, Hole 1270B, p. 118.

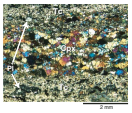

F66. Downhole crystal-plastic fabric intensity and foliation dips, p. 119.

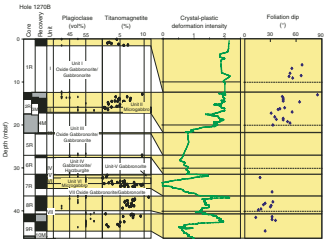

F67. Poles to crystal-plastic foliations, p. 120.

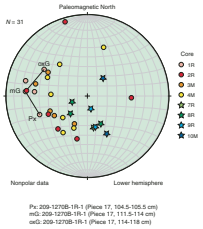

overall dip of this shear zone may decrease with depth. Caution is warranted, however, because the presence of soapstone and serpentinites in Sections 209-1270B-6R-1 and 7R-1 and the variations of deformation intensity with depth suggest that deformation might have occurred in several distinct episodes, that the section may be cut by a significant fault zone, and/or that there may be more than one gabbroic intrusion represented in the core (see "Igneous and Mantle Petrology," p. 3, and "Geochemistry," p. 34).

Strain Localization in the Oxide Gabbronorites

There is strong evidence of strain localization in the oxide gabbronorites in Hole 1270B. Textures suggest that the oxide in some of these deformed rocks may have crystallized after deformation. Similar observations have been made at the Atlantis Bank oceanic core complex (Site 735B and vicinity), where a long-lived detachment fault exposed gabbroic rock (Dick et al., 1991, 1999, 2000; Natland and Dick, 2001). Similarly, at Sites 921–924 in the MARK area of the Mid-Atlantic Ridge, a large detachment fault exposes predominantly gabbroic rock at the eastern inside-corner high of the Kane Fracture Zone (Cannat et al., 1997; Agar et al., 1997; Agar and Lloyd, 1997). In Hole 735B and at Sites 921–924, investigators have suggested that strain localization occurs within partially molten gabbros and controlled the flow and crystallization of late iron-titanium–rich liquids in these intrusions. Deformation and strain localization continued to lower temperatures in the MARK and Atlantis Bank oxide gabbros, with the formation of numerous cataclastic and mylonitic intervals. Localized cataclastic and mylonitic deformation is rare in Hole 1270B, suggesting that such later, lower-temperature strain localized elsewhere after cooling of the Hole 1270B oxide gabbronorites and gabbro.

Brittle Deformation

High-Temperature Brittle Deformation

Minor brittle deformation overprints ductile deformation in several core intervals (e.g., interval 209-1270B-8R-1, 114–116 cm). Brittle deformation is concentrated near discrete planar fracture surfaces. On a centimeter scale, brittle deformation is preferentially localized into narrow zones of fine-grained, recrystallized plagioclase neoblasts between pyroxene porphyroclasts (Fig. F68) and away from coarse plagioclase and pyroxene porphyroclasts. Brittle deformation is accomplished by fracturing of plagioclase neoblasts to produce variably sized but generally fine angular grains. Minor brittle fractures cut plagioclase porphyroclasts but in most cases do not have slip >0.1 mm. Several zones of brittle shear overprint the ductile deformation and are spatially associated with concentrations of Fe-Ti oxides (e.g., interval 209-1270B-1R-1, 90–98 cm). In some cases it appears that oxides fill voids created by dilatant brittle deformation (Fig. F69). Oxides within many of these zones contain undeformed exsolution lamellae of ilmenite within titanomagnetite. Ilmenite lamellae in similar oxide-rich gabbros collected from other locations on the Mid-Atlantic Ridge and Southwest Indian Ridge formed at temperatures >600°C (T. Schroeder, unpubl. data). If ilmenite lamellae from Hole 1270B formed under similar conditions, the brittle overprint of ductile shear zones likely occurred under amphibolite grade conditions. The lack of greenschist grade alteration of these shear zones also suggests higher-temperature brittle deformation.

F68. Brittlely deformed plagioclase neoblasts, p. 121.

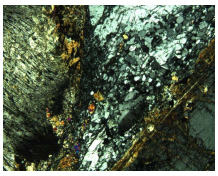

F69. Interstitial oxide along brittle shear zones, p. 122.

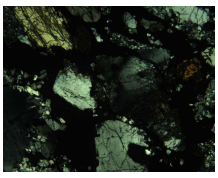

Low-Temperature Brittle Shear Zones

Very few zones of low-temperature (<500°C) deformation were recovered in Hole 1270B. These include several intervals containing slight brecciation/semibrittle deformation in which fracturing occurred concurrently with alteration and replacement of primary igneous minerals by chlorite and other greenschist facies alteration products, for example, Sections 209-1270B-5R-1 (Piece 3) (greenschist deformation of gabbro) (Fig. F70) and 7R-1 (Piece 2) (greenschist deformation of peridotite). These zones are characterized by slightly fibrous to elongate chlorite, talc, and possible amphibole with remnant clasts of pyroxene and plagioclase.

Several core intervals were encountered with moderate to high intensities of shear fracturing. These fractures generally have little or no offset, are typically filled with alteration vein material (see below), and are not thought to represent significant faults.

A plot of average deformation intensity vs. expanded depth (Fig. F71) shows that the cataclastic intensity correlates with the intensity of alteration veining in the top two cores, but the correlation is not as good in the rest of the hole. The orientations of four brittle shear zones were measured and have a wide range of dips (22°–80°). They show a trend from high dips at shallow depths to low dips deeper in the hole (Fig. F72), which corresponds with the trend observed for the dip of the crystal plastic fabric.

Alteration Veins

The alteration veins in the gabbros are planar, weakly developed, and relatively thin (1–2 mm). The veins mainly contain chlorite, with subsidiary talc, amphibole, serpentine, and sulfide and oxide veins. Crosscutting relationships in which chlorite-amphibole veins predate talc-chlorite veins are observed in the gabbros in intervals 209-1270B-2R-1, 3.5–6.5 cm; 7R-1, 133–149 cm; and 7R-2, 0–14 cm. These greenschist facies veins crosscut and therefore postdate all ductile and brittle deformation in the gabbros. The altered peridotites from the bottom of Section 209-1270B-6R-1 and the top of 7R-1 show serpentine and talc veining similar to the peridotites in the other holes at this site and are not discussed further here. A detailed discussion of the mineralogy of the alteration veins can be found in "Metamorphic Petrology," p. 11.

The intensity and orientation of veins were measured using the intensity scale outlined in "Structural Geology," p. 9, in the "Explanatory Notes" chapter. The intensity of these veins is a measure of their average frequency in a 10-cm piece of core. The vein intensity averages 0.5–0.7 over the length of the core (Fig. F71), indicating that on average there is 1 vein per 14–20 cm in the recovered core. There are regions of increased vein intensity (1 vein per 7–10 cm) in Sections 209-1270B-2R-1, 7R-1, 10R-1, and 10R-2.

The dip distribution and dip variation with depth for the alteration veins are shown in Figure F73. Only 14 dip measurements could be made from all the veins within the core and they vary from 14° to 87°. Figure F74 is a lower hemisphere plot showing the poles to both the metamorphic veins and the brittle shear zones. The data are plotted with the azimuth of the stable remanent magnetization pointing south because the negative inclination of the remanent magnetization suggests reversed polarity for this hole. The reorientation of the veins using paleomagnetic data is discussed in "Structures in Peridotite and Gabbroic Intrusions," p. 8, in "Mantle Upwelling, Melt Transport, and Ig-

F70. Synkinematic alteration to talc and chlorite, p. 123.

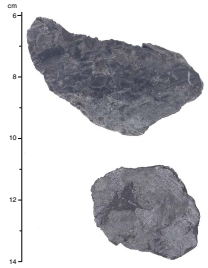

F71. Cataclastic, crystal-plastic alteration vein intensity, Hole 1270B, p. 124.

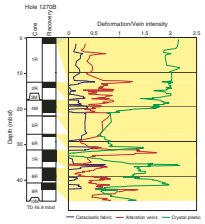

F72. Dip of brittle structures, Hole 1270B, p. 125.

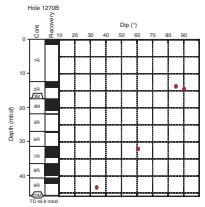

F73. Dips of alteration veins, p. 126.

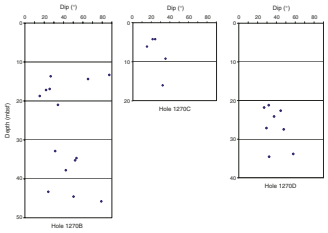

F74. Poles to alteration veins and brittle shear zones, p. 127.

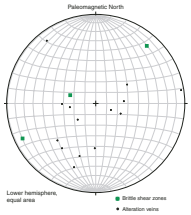

neous Crustal Accretion" in the "Leg 209 Summary" chapter. After reorientation, the data are loosely clustered.

Holes 1270C and 1270D

Crystal-Plastic Deformation

Holes 1270C and 1270D are located within meters of each other and are structurally similar, but more dunite was recovered in Hole 1270C (Fig. F75). This difference may not be significant, as recovery was sparse in both holes. Two features distinguish these holes from Hole 1270A, drilled 450 m downslope to the west. Harzburgites in Holes 1270C and 1270D, which constitute the large majority of the recovered core, are substantially more deformed than the harzburgites in Hole 1270A (see "Crystal-Plastic Deformation," p. 21, in "Hole 1270A"). Typical harzburgite from Holes 1270C and 1270D has porphyroclastic texture and average deformation intensities of 1.4 and 1.8, respectively. Observation of textures in 6 thin sections from Hole 1270C and 13 from Hole 1270D correspond well to the visual core descriptions of deformation intensities from the same samples.

There are numerous highly deformed magmatic veins in Holes 1270C and 1270D that crisscross the cores (discussed further in the next section). Strain was partitioned mainly into these gabbroic veins, as can be seen in Figure F76. The gabbroic veins have an average deformation intensity of 2.8, close to protomylonitic textures, whereas the harzburgites have an average deformation intensity of 1.4–1.8. In general, the peridotites are only affected by the deformation in the veins within a few centimeters of vein contacts. In some cases, protogranular orthopyroxene is preserved in the peridotite right at the contact. Where the peridotites form enclaves between favorably oriented veins, the peridotites may be transposed into the foliation plane and show local deformation up to protomylonite intensity (Fig. F77A). Visual inspection of the cores shows that total deformation intensity increases substantially in areas with abundant magmatic veins. This is difficult to quantify but is subtlely present in the downhole total deformation intensity plot as a series of sharp peaks in the most heavily veined regions, rising above the background level of the high-temperature porphyroclastic deformation (Fig. F75).

Peridotite High-Temperature, Low- and Moderate-Strain Fabrics

Unlike the Hole 1270A harzburgites, which were generally protogranular, the Hole 1270C and 1270D harzburgites are generally porphyroclastic. Protogranular textures are abundant in some samples with deformation grades of 1 (weakly porphyroclastic) or less, with orthopyroxene grains and pseudomorphs exhibiting the characteristic smooth curved lobate and commonly interstitial grain boundaries (Fig. F77B). However, in most samples, large grains have recrystallized into smaller subgrains and porphyroclasts (Fig. F77C, F77D). Numerous rounded porphyroclasts and strain-free, coarse subgrains are present, and porphyroclastic textures with broken, kinked, and strained orthopyroxene grains and pseudomorphs are more common (Fig. F77F). The margins of large porphyroclasts are commonly surrounded by broken fragments of pyroxene (e.g., Fig. F77E). Pyroxene neoblasts commonly lack 120° grain boundary angles at triple junctions. In some samples, favorably oriented pyroxenes have undergone stretching to form elongate grains due to sliding on the 001 crystallographic plane (Fig. F78). One ori-

F75. Crystal-plastic deformation intensity with depth, p. 128.

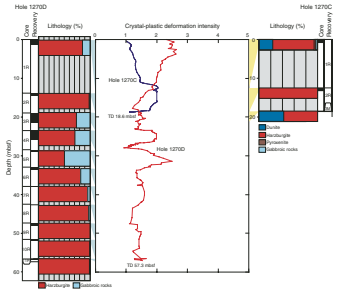

F76. Harzburgite and metagabbro crystal-plastic deformation intensities, p. 129.

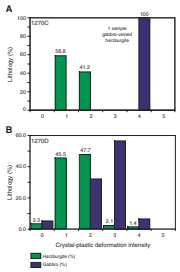

F77. Harzburgite deformation textures, p. 130.

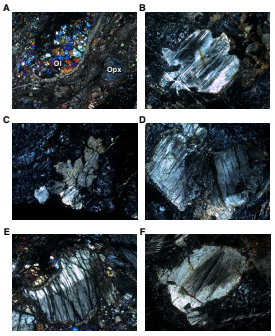

F78. Harzburgite deformation textures, p. 131.

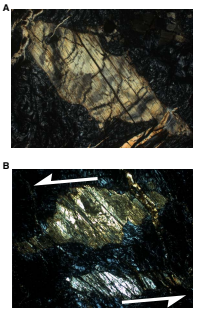

ented sample with a well-defined foliation gives a normal shear sense, though the foliation plane is nearly horizontal (~10°) (Fig. F78).

The early high-temperature, low strain–rate protogranular and porphyroclastic textures predate the intrusion of the gabbroic veins and reflect high-temperature mantle flow. This is evident from crosscutting relationships between the veins and these textures in thin section and hand sample. It was observed that where a porphyroclastic foliation has been measured in the harzburgites, its orientation is somewhat different than that of the foliations within the gabbroic veins (Fig. F79). Locally, porphyroclastic textures with granulation around orthopyroxene, strained grains, and poorly developed strained subgrains can be seen in proximity to the sheared gabbroic veins. Thus, porphyroclastic deformation of peridotites at least locally overlapped in time with deformation of the veins.

F79. Poles to magmatic and alteration veins in harzburgite, p. 132.

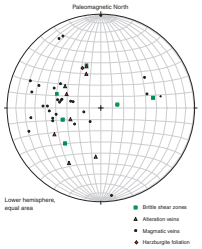

Magmatic Veins

Magmatic veins in Holes 1270C and 1270D vary in composition from pyroxenitic to gabbroic to felsic, although it is difficult to reconstitute the original composition because of alteration of their primary phases. The veins are generally <0.5 cm to 1 mm in thickness. They have typically undergone extensive dynamic and/or static metamorphism at amphibolite through greenschist facies and have been crosscut by serpentine veins. These magmatic veins are important for establishing the relative timing of deformation events. Peridotites in Holes 1270C and 1270D are cut by veins that appear to be intruded synkinematically. The veins commonly appear to localize deformation, isolating enclaves of less deformed harzburgites.

An example of strain localization in magmatic veins is present in Section 209-1270C-1R-1 (Pieces 7 and 13). These veins were deformed during high-temperature crystal-plastic deformation. A thin section from Piece 13 (Fig. F80) includes harzburgite enclaves isolated within intrusive gabbroic veins that are transformed into porphyroclastic mylonite zones. Within the mylonites, remnants of the primary mineralogy can be observed. Pyroxene and plagioclase neoblasts and smaller porphyroclasts are segregated into compositional bands. Plagioclase has undergone grain size reduction, dominantly by dynamic recrystallization but also, in part, by cataclasis. Clinopyroxene has been partially to completely replaced by brown amphibole crystals, which are now the predominant porphyroclasts in the mylonitic zones. The harzburgite at the edge of the gabbroic veins is also affected by the mylonitization, with entrainment of recrystallized orthopyroxene and olivine into the high-strain zones. Subgrains and subgrain rotation are common in olivine adjacent to the high-strain zone. Subgrain rotation appears to be the dominant mechanism of recrystallization within olivine. Away from the margins of mylonitized gabbroic zones, the harzburgites have not been dynamically recrystallized, retaining their earlier porphyroclastic deformation fabric and grain size (olivine and orthopyroxene grains >4 mm). At the edge of some mylotinized gabbroic veins, some large clinopyroxene grains have not undergone grain size reduction. These clinopyroxenes are partially replaced by brown amphibole. Their grain size is >4 mm, probably representing the original grain size of the vein material. This suggests that the harzburgite wallrock was at high temperatures during intrusion. One vein contains subhedral apatite and zircon, indicating an evolved magmatic composition, as confirmed by geochemical data (see "Geochemistry," p. 34). Amphibolitization is

F80. Mylonitic gabbroic veins, p. 133.

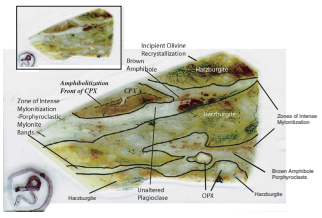

likely to have occurred by synkinematic hydration of the shear zone. Amphibole is not present in the harzburgite enclaves. Other mylonitized gabbroic veins in Hole 1270C include those found in intervals 209-1270C-2R-1 (Piece 14, 88–81 cm) and 3M-1 (Piece 3, 16–21 cm).

All of Hole 1270D except Section 209-1270D-11R-1 contains deformed magmatic veins. An example of a highly veined interval is 3R-1, 53–76 cm (Fig. F81). Crosscutting veins in Hole 1270D help establish the timing of intrusion and deformation events. Figure F82 illustrates an undeformed planar pyroxenite vein in interval 209-1270D-3R-1, 10–16 cm, that cuts the crystal-plastic fabric in the harzburgite. However, the undeformed vein is crosscut by a deformed gabbroic vein with a reverse sense of shear. The crosscutting deformed vein is roughly planar, but the texture inside the vein is porphyroclastic with vein parallel foliation. Figure F83 shows a composite gabbro-pyroxenite vein that merges with a lens of deformed gabbro and pyroxenite. The vein is mylonitized and folded where it merges with the lens. The vein is oriented subparallel to the crystal-plastic foliation defined by elongate pyroxene porphyroclasts in the harzburgite, unlike the undeformed vein in Section 209-1270D-3R-1, which is oriented at a high angle to the crystal-plastic foliation plane in the harzburgite. These relationships suggest an early pyroxenitic intrusive event prior to intrusion of the gabbroic veins.

Brittle Deformation

Several of the ductilely deformed gabbroic veins present in Holes 1270C and 1270D (see "Magmatic Veins," p. 29, above) are overprinted by semibrittle deformation characterized by fibrous bands of amphibole, chlorite, and/or talc (see "Metamorphic Petrology," p. 11). These minerals are present in nearly monomineralic bands (0.5–3 mm wide) parallel to the dominant shear foliation and, in many cases, appear to have grown synkinematically. Brown amphibole is present in shear zones as porphyroclasts with shape-preferred orientation parallel to the foliation. Colorless amphibole is present as fibrous mats or stringers between brown amphibole porphyroclasts. Talc is present as fibrous masses subparallel to foliation in shear zones or as bands of extremely fine grained aggregates with little foliation (Fig. F84). Chlorite is commonly intergrown with colorless amphibole with crystals parallel to the foliation or as random or radial masses.

Textures in greenschist facies shear zones indicate possible strain accommodation via cataclasis and diffusive mass transfer during alteration following the cessation of crystal-plastic deformation. Brown amphibole is boudinaged along cleavage planes, with colorless, fibrous amphibole between fractured grains aligned subparallel to foliation in shear zones (Fig. F85). This strain accommodation process has been referred to as incongruent pressure solution (Brodie and Rutter, 1985) and paracrystalline microboudinage (Misch, 1969, 1970). Section 209-1270D-1R-1 (Pieces 1–5) was highly deformed at greenschist-grade conditions by these processes. This interval of core is composed of amphibole-talc schist cut by phacoidal shear fractures (Fig. F86).

Serpentine surrounding semibrittle shear zones does not show evidence of significant deformation. In most occurrences, serpentine in peridotite near the boundaries of gabbroic dikes displays mesh texture, indicating static alteration (O'Hanley, 1996). There are no crosscutting relations present to determine with certainty if serpentinization of

F81. Gabbroic/pyroxenititic veins cutting peridotite, p. 134.

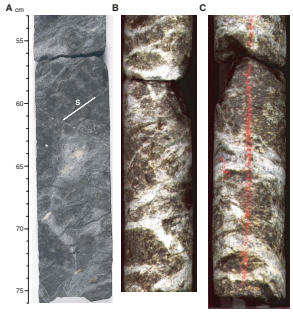

F82. Crosscutting gabbroic and pyroxenite veins, p. 135.

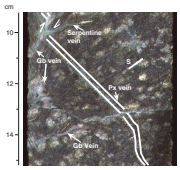

F83. Gabbroic veins in a foliated harzburgite, p. 136.

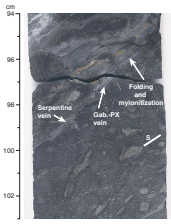

F84. Talc on the boundary of an olivine porphyroclast, p. 137.

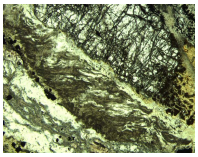

F85. Boudinaged amphibole crystal, p. 138.

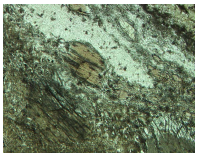

F86. Strongly deformed amphibole-talc schist, p. 139.

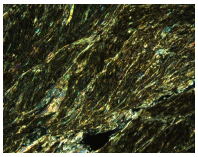

harzburgite preceded or followed semibrittle deformation of the gabbroic veins.

Intensity and Orientations of Cataclastic/Semibrittle Structures

The intensity of cataclastic/semibrittle deformation is highest at shallow levels in Hole 1270D (Fig. F87). Section 209-1270D-1R-1 (Pieces 1–5) is composed dominantly of intensely deformed semibrittle tremolite-chlorite schist. Cataclastic intensity drops rapidly with depth beneath the upper interval of Core 209-1270D-1R and is variable in the lower part of the hole. The intensity of brittle deformation is distinctly low from ~20 to 37 mbsf, where the concentration of magmatic veins is high. Orientation of brittle features, including semibrittle shear zones, minor fault zones, and cross-fiber serpentine foliation, was measured at eight locations in Hole 1270D and three locations in Hole 1270C. Unfortunately, many brittlely deformed pieces from Holes 1270C and 1270D are small fragments that are not oriented. Dips of features in Cores 209-1270D-3R, 4R, 5R, and 6R range 19°–48° (Fig. F88).

F87. Cataclastic, crystal-plastic alteration vein intensity and magmatic vein frequency, p. 140.

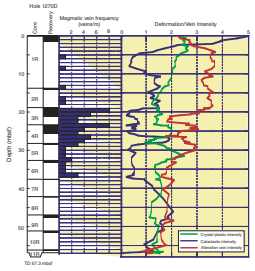

F88. Dip of brittle features, Hole 1270D, p. 141.

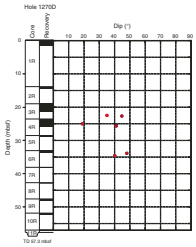

Cross-Fiber Serpentine Foliation

In serpentinite enclaves between the mylonitized gabbroic veins, cross-fiber serpentine foliation is commonly oblique to shear foliation by as much as 30°. The formation of cross-fiber serpentine foliation postdates the peak of crystal-plastic deformation in the gabbroic veins. The timing relations between greenschist-grade semibrittle overprint of gabbroic shear zones and formation of cross-fiber serpentine foliation are not known.

Alteration Veins

The alteration veins in harzburgites and dunites range in morphology from continuous veinlets to sigmoidal or en echelon, discontinuous veinlets to isolated segments. Alteration veins are more numerous than in Hole 1270A and are larger, as wide as 5 mm. The veins are dominantly serpentine with subsidiary oxide, rare talc, and late carbonate/aragonite. There are at least three generations of serpentine veins based on crosscutting relationships: dark magnetite-rich veins, pale green serpentine veins, and late white chrysotile veins. Serpentine veins appear to be localized near the gabbroic veins. Figure F89 shows examples of the last two generations of these serpentine veins. Interval 209-1270C-1R-1, 33–40 cm (Fig. F89A), shows tension cracks filled with white serpentine, crossing a thin gabbroic vein perpendicular to its length. Similar features are commonly associated with the gabbroic veining in Holes 1270C and 1270D. Good examples can be seen in intervals 209-1270C-2R-1, 35–47 cm, and 58–72 cm, 209-1270D-3R-1, 104–120 cm, and 3R-2, 1–29 cm, and throughout Core 4R. These features provide evidence that the pervasive serpentinization postdates the gabbroic vein event (Fig. F89B, F89D). Some en echelon, sigmoidal serpentine veins appear to be transposed and rotated into talc shear zones in Hole 1270D, indicating that some serpentinization occurred before or synchronously with ductile to semibrittle deformation. Figure F89C shows late serpentine veins cutting a semibrittle shear zone in interval 209-1270D-4R-1, 39–40 cm, illustrating that serpentinization also postdates some of the brittle deformation. Other intervals show brittle faulting of the serpentine veins themselves (intervals 209-1270D-10R-1, 0–9 cm, and 4R-1, 38–52 cm). All of these observations together suggest that serpentiniza-

F89. Serpentine vein geometries, p. 142.

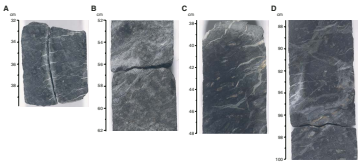

tion occurred in a number of events synchronously with, and subsequent to, the semibrittle deformation.

Oxyhydroxide veins commonly crosscut serpentine veins in cores from Hole 1270D, commonly using the preexisting serpentine veins as conduits. Oxyhydroxide veins and late carbonate veins that are concentrated in Hole 1270D in Sections 209-1270D-6R-1 and 7R-1 represent late brittle events postdating the magmatic, crystal-plastic, and semibrittle deformation. A detailed discussion of the mineralogy of the alteration veins can be found in "Metamorphic Petrology," p. 11.

The alteration vein intensity in Hole 1270D decreases with depth from 3.5 near the top of the hole to <2 at the bottom of the hole (Fig. F87). The average vein intensity in the uppermost 20 m is broadly similar to that in Hole 1270C (see the "Supplementary Material" contents list). In the uppermost part of Hole 1270D, the vein intensity is only 2.3. This value may be low because these rocks are very cataclastically deformed and fewer veins are visible. The alteration vein intensity in Hole 1270D varies in the 20- to 30-mbsf interval, corresponding to the region of most intense gabbroic veining. Overall, the metamorphic vein intensity appears to be more strongly correlated with crystal-plastic intensity than cataclastic fabric intensity, suggesting that the majority of the veining events might have occurred before brittle deformation.

The variation of the dip of the alteration veins with depth for Holes 1270C and 1270D is shown in Figure F73. Only a few orientations could be measured in each hole. Dips vary from 15° to 35° in Hole 1270C and from 27° to 58° in Hole 1270D. Figure F90 is a lower hemisphere plot showing the poles to the alteration veins and the brittle shear zones restored with the azimuth of the stable remanent magnetization reoriented to a common reference frame. The reorientation of the veins using paleomagnetic data is discussed in "Structures in Peridotite and Gabbroic Intrusions," p. 8, in "Mantle Upwelling, Melt Transport, and Igneous Crustal Accretion" in the "Leg 209 Summary" chapter. The data for Hole 1270C are clustered. However, the poles to the veins in Hole 1270D are more scattered.

F90. Poles to alteration veins and brittle shear zones, p. 143.

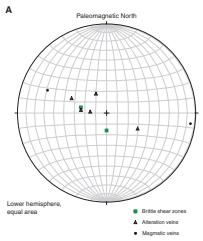

Spinel Fabrics

Following the same procedure as for Hole 1268A, 8-cm³ cube samples were cut from Site 1270 harzburgites to determine the spinel foliation. One cube each from Holes 1270A and 1270C and three from Hole 1270D were examined. The cubes from Holes 1270A and 1270C as well as two cubes from Hole 1270D show vermicular spinel in at least one of the faces of the cubes. The vermicular spinel grains are 1–3 mm in size and were intergrown with pyroxene, now pseudomorphed by serpentine. Additionally, some smaller rounded spinel grains (~0.1 mm in size) are isolated in the olivine matrix, away from pyroxene pseudomorphs. One cube from Hole 1270D (Sample 209-1270D-4R-1 [Piece 12A, 91–93 cm]) shows two compact, relatively large (4 mm) grains along with small grains. None of the cubes showed any spinel foliation. Outside of the sections of the harzburgite, including mylonitized gabbroic veins, the shape of the vermicular spinel grains (Fig. F91) indicates that they probably have not been deformed since their crystallization.

F91. Vermicular spinel in protogranular harzburgite, p. 145.

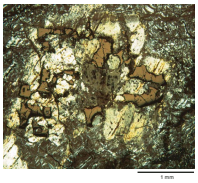

Summary

The four holes drilled at Site 1270 define a 450-m-long east–west traverse across a westerly dipping topographic slope. This slope has previously been interpreted to be an exposed west-dipping detachment fault surface on the east side of the axial valley (Fujiwara et al., 2003). Holes 1270B, 1270C, and 1270D recovered some deformed rock that is interpreted to have formed within a fault zone. The recovered rocks reveal structures that have mean dips of 40°–50°. However, their dip direction cannot be determined from the core alone. In order to determine their present-day dip directions, we oriented the core using paleomagnetic measurements of the mean magnetic azimuth and inclination. This method of orientation requires knowledge of the polarity of the Earth's magnetic field when the rocks were magnetized and assumptions about the orientation of the plausible axes about which the rocks have been rotated. We made the following assumptions:

1. The tectonic rotation axis plunge = 0° and strike = 020°, parallel to the rift valley in this area.
2. A reversed polarity inferred from negative inclinations in the rocks from Hole 1270B and a normal polarity inferred for rocks from Hole 1270D are correct (i.e., not inverted by large tectonic rotations).
3. The fabrics in the gabbros and peridotites from Holes 1270B and 1270D dip in the same direction.
4. Rotations have not substantially modified the *azimuth* of the remanent magnetic vector.

This leads to the conclusion that the present-day dip direction of the deformation fabrics is approximately east-northeast (for further discussion, see Fig. **F28,** p. 106, and accompanying text in the "Leg 209 Summary" chapter). If this result is correct, then the deformation fabrics, including the mylonitic foliation, are not parallel to the topographic slope interpreted to be a fault surface (Fig. **F92**). We note, however, that this result is nonunique, especially considering the confidence bounds on the mean inclination (±10° for the gabbros and ±13° for the peridotites) and the possibility that more complex tectonic rotations may have taken place.

Figure **F93** shows the downhole locations of all of the major fault zones recognized at this site next to recovery plots for each hole. This plot emphasizes the uncertainty in reconstructions of stratigraphic successions at this site and raises the possibility that much of the poor recovery may be due to the presence of fault zones.

Based on the preceding discussion we suggest the following structural evolution of this site:

1. High-temperature, low-strain crystal-plastic deformation of the mantle peridotites from Holes 1270B, 1270C, and 1270D, probably within the subcrustal lithosphere. The peridotites recovered from Hole 1270A do not record this early deformation.
2. Intrusion of several generations of gabbroic rocks. There may have been two or more intrusive events to form the oxide gabbro and gabbronorite intrusive bodies drilled in Hole 1270B. The mineralogy and geochemistry (see **"Geochemistry,"** p. 34) of the gabbroic veins in Holes 1270C and 1270D are consistent with the possibility that the evolved melts parental to the gab-

F92. True-scale cross-section showing structural features, p. 146.

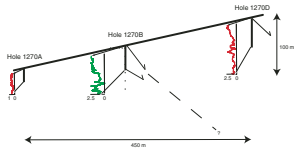

F93. Recovery plots showing location of major fault zones, p. 147.

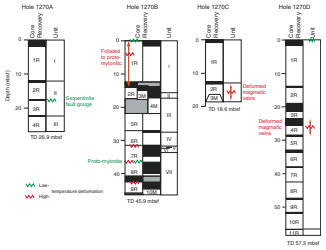

broic veins were segregations from the large gabbro bodies in Hole 1270B.

3. High temperature, moderate- to high-strain crystal plastic deformation of the intrusions, possibly while the latest intrusions were still partially molten. Hole 1270A only contains a few gabbroic veins and appears to have largely escaped intrusion and the associated moderate- to high-strain crystal-plastic deformation. The high-temperature, moderate-strain crystal-plastic deformation of the gabbros decreases downhole in Hole 1270B. It was localized in oxide gabbros during granulite grade metamorphism, possibly while they were still partially molten, and deformation continued into the upper amphibolite facies. The high-temperature, high-strain crystal-plastic deformation recorded in the gabbroic veins in Holes 1270C and 1270D may have occurred at the same time. Crosscutting magmatic relationships in Holes 1270B and 1270D attest to a complex magmatic and high-temperature deformation history.
4. The deformation recorded in Hole 1270B appears to have ceased at relatively high temperatures, and the rocks only show a relatively minor low-temperature greenschist facies cataclastic overprint. The gabbroic rocks in Holes 1270C and 1270D show evidence of a lower-temperature greenschist overprint.
5. All four holes show evidence of restricted semibrittle and lower-temperature brittle faulting, postdating the high-temperature deformation. Many of the uppermost samples from the first core of each hole are low-temperature cataclastic rocks, indicating that the rocks closest to the surface have a brittle overprint.
6. Serpentinization was both syn- and postkinematic with the semibrittle and brittle deformation events and occurred after the magmatic events and high-temperature deformation.
7. Late brittle fracturing and restricted hydrothermal circulation.

GEOCHEMISTRY

We performed chemical analyses on eight harzburgites, one dunite, and seven gabbros from Site 1270 selected by the shipboard scientific party, using inductively coupled plasma–atomic emission spectrometry (ICP-AES) for determining major and trace element concentrations and gas chromatography for H_2O and CO_2 (because of a technical problem, sulfur was not analyzed in most of the Site 1270 rocks). These 16 samples are representative of the rocks recovered from all four holes drilled at Site 1270 (see **"Igneous and Mantle Petrology,"** p. 3, and **"Metamorphic Petrology,"** p. 11, for the characterization of the lithologic units). We sampled two harzburgites from Hole 1270A, seven gabbros from Hole 1270B, one harzburgite from Hole 1270C, and five harzburgites (including one intruded by a gabbroic vein) and one dunite-harzburgite from Hole 1270D. The results for the major and trace elements, for both ultramafic and mafic rocks, are reported on a volatile-free basis in Table **T4.**

T4. Major and trace element compositions, p. 177.

Peridotites

Site 1270 peridotites are characterized by high loss on ignition (LOI) values (>8.5 wt%). Sample 209-1270D-3R-1, 63–66 cm, which is a harzburgite intruded by a gabbroic dikelet, has the lowest LOI. The

other Site 1270 peridotites have significantly higher LOI (13.0–14.4 wt%) and H_2O (14.0–15.2 wt%), similar to that of lizardite (Fig. **F94**). These high LOI values and H_2O concentrations are consistent with the visual core descriptions and XRD results (see **"Metamorphic Petrology,"** p. 11), showing that Site 1270 peridotites are predominantly altered to serpentine. The gabbroic dikelet crosscutting Sample 209-1270D-3R-1, 63–66 cm, is also altered predominantly to talc (see **"Metamorphic Petrology,"** p. 11, and **"Site 1270 Thin Sections"**). Because talc is characterized by lower water content relative to lizardite, its presence in this sample along with serpentine leads to a lower LOI (8.5 wt%) and H_2O (9.3 wt%) compared to the other peridotites.

Compared to Site 1268 peridotites, bulk rock compositions of Site 1270 peridotites show relatively restricted ranges for SiO_2 (44.5–46.5 wt%), MgO (41.4–44.6 wt%), and Fe_2O_3 (8.15–9.44 wt%) concentrations (Fig. **F94**). These ranges are similar to what has been observed in peridotites from the MARK area at Site 920 (Casey, 1997). Sample 209-1270D-3R-1, 63–66 cm, is distinguished from other Site 1270 peridotites by its slightly higher SiO_2 (49.4 wt%) and lower MgO (35 wt%) and Fe_2O_3 (7.40 wt%) concentrations (Fig. **F94**). However, its most distinctive characteristics are high Al_2O_3 (4.1 wt%) and CaO (3.48 wt%) concentrations (Fig. **F95**). The composition of this sample is displaced from the other peridotites because of the presence of an altered crosscutting gabbroic dikelet. This dikelet underwent replacement of plagioclase by talc and clinopyroxene by chlorite and amphibole (see **"Site 1270 Thin Sections"**).

With the exception of Samples 209-1270D-3R-1, 63–66 cm, and 1R-1, 70–74 cm, the Site 1270 peridotites are characterized by low Al_2O_3 (0.33–0.85 wt%) and CaO (0.33–0.85 wt%) concentrations. These elements are concentrated in pyroxenes and, more precisely, in clinopyroxene for CaO. They can be used as a proxy for the degree of fertility of peridotites. The Al_2O_3 contents of Site 1270 peridotites are similar to those of the most enriched Site 1268 peridotites but are less than the Al_2O_3 contents of Leg 153 peridotites. This suggests that prior to alteration to lizardite Site 1270 peridotites were more refractory than Leg 153 peridotites. However, Al_2O_3 and CaO are not correlated in Site 1270 peridotites, as would be expected for residues of partial melting (Fig. **F95**). Site 1270 peridotites, in fact, display low CaO/Al_2O_3 ratios compared to Bulk Silicate Earth (Jagoutz et al., 1979; Wänke, 1981), ranging between 0.76 and 0.01. Site 1268 peridotites are also depleted in CaO relative to Al_2O_3. This depletion may stem either from preferential Ca loss during serpentinization and weathering or from the increasing importance of orthopyroxene and spinel in the Al_2O_3 budget at high degrees of melting (especially in the case of the Site 1270 peridotites). The extremely low CaO content of some of these rocks is consistent with only minor amounts of clinopyroxene remaining after melting.

An additional consideration is the effect of carbonate precipitation in some of the Site 1270 peridotites (see **"Site 1270 Thin Sections"**). This precipitation is most clearly identified by Ca enrichment (CaO = 3.49 wt%) in Sample 209-1270D-1R-1, 70–74 cm. In a diagram of CaO vs. CO_2, this sample's composition is significantly displaced from that of the other peridotites analyzed from Site 1270 (Fig. **F96**). This displacement lies along a vector toward the composition of $CaCO_3$, consistent with the presence of carbonate in this sample as described in thin section. Some Site 920 peridotites also lie along this trend (also see Fig.

F94. H_2O, SiO_2, and Fe_2O_3 vs. MgO and H_2O vs. SiO_2, p. 148.

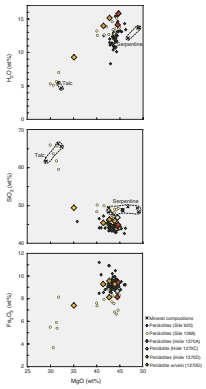

F95. CaO vs. Al_2O_3 in peridotites, p. 149.

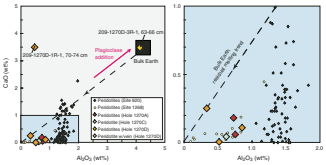

F96. CaO vs. CO_2 in peridotites, p. 150.

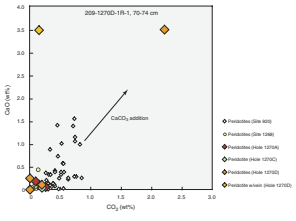

F45, p. 124, and accompanying text in the "Leg 209 Summary" chapter).

Sr concentrations in Site 1270 peridotites display a wide range of values (<5–530 ppm) (Fig. F97). Sr behaves as an incompatible element during partial melting. However, strontium is also highly mobile during alteration. Sr variations are correlated with Ca variations in Site 1270 peridotites. Probably as a result of secondary formation of carbonate during alteration, Sample 209-1270D-1R-1, 70–74 cm, is also the most Sr-enriched peridotite at Site 1270 (also see Fig. F46, p. 125, and accompanying text in the "Leg 209 Summary" chapter).

Site 1270 peridotites are depleted in TiO_2 (<0.01–0.02 wt%), Y (<2 ppm), and Zr (<2–3.6 ppm) and, to a lesser extent, in V (21–45 ppm) and Sc (5–9 ppm) compared to Leg 153 peridotites (Fig. F98). These elements behave moderately incompatibly, preferentially partitioning into the liquid during partial melting. Their concentration range suggests that Site 1270 peridotites underwent higher degrees of partial melting than Leg 153 peridotites. Cr and Ni behave as compatible elements, preferentially partitioning into the solid during partial melting. Site 1270 peridotites display high concentrations of Cr (1600–2930 ppm) and Ni (2000–2900 ppm). In both Site 1268 and 1270 peridotites, Cr is positively correlated with Al_2O_3. Because nearly all of the Cr must be concentrated in spinel in these rocks, the correlation of Cr with Al_2O_3 (Fig. F99) is evidence that spinel contributes a significant proportion to the bulk rock Al budget for the highly refractory peridotites from Sites 1268 and 1270, in addition to any pyroxene present. The relatively high Ni contents, in conjunction with low Al_2O_3 (Fig. F99), are explained by the relatively large modal proportion of olivine, in which nickel is compatible, in these peridotites prior to their alteration. Ti, Y, Zr, V, Sc, Cr, and Ni are usually considered to be relatively immobile during alteration (e.g., Hebert et al., 1990). The similarity of their concentrations for the Site 1270 and 1268 peridotites therefore suggests that prior to alteration Site 1268 and 1270 peridotites had similar compositions.

Sample 209-1270D-3R-1, 63–66 cm, which is intruded by a gabbroic dikelet, displays significantly higher incompatible element contents: TiO_2 (0.13 wt%), Y (20 ppm), Zr (96 ppm), and Sc (10 ppm). More compatible Co, Cr, and Ni have similar concentrations in Sample 209-1270D-3R-1, 63–66 cm, and other Site 1270 peridotites (the slight difference in Ni and MgO concentrations reflects the low proportion of olivine in Sample 209-1270D-3R-1, 63–66 cm). For this particular sample, compatible elements are mainly concentrated in the peridotite, whereas incompatible element variations mostly reflect the composition of the crosscutting gabbroic vein. The high incompatible element content of Sample 209-1270D-3R-1, 63–66 cm, suggests that the gabbroic vein is incompatible element enriched compared to gabbroic rocks having similar modal compositions from Sites 1268 and 1270.

Gabbroic Rocks

We analyzed seven gabbroic rocks from Hole 1270B. The recovered sequence of gabbros was divided into seven lithologic units and two major rock types (microgabbro and oxide gabbro) using visual core and thin section descriptions (see "Hole 1270B," p. 6, in "Igneous and Mantle Petrology"). We selected two oxide gabbro samples from Unit I,

F97. Sr vs. Al_2O_3 in peridotites, p. 151.

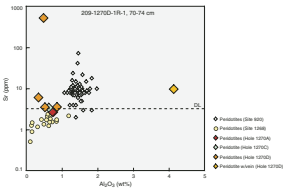

F98. TiO_2, Zr, V, and Sc vs. Al_2O_3 in peridotites, p. 152.

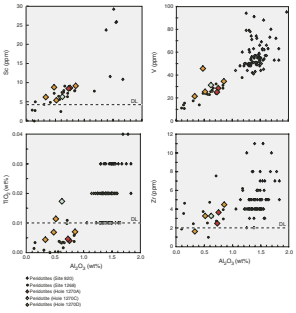

F99. Ni and Cr vs. Al_2O_3 in peridotites, p. 153.

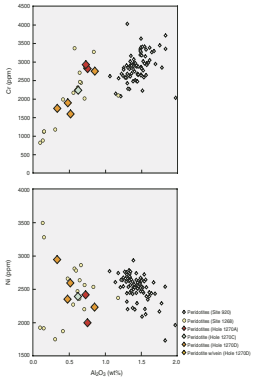

three oxide gabbro samples from Unit VII, and a microgabbro from each of Units II and VI.

The gabbros can be subdivided into two groups that correspond to the main rock types assigned using visual core and thin section descriptions on the basis of their major and trace element geochemistry. Oxide gabbros have MgO (6.0–8.4 wt%), TiO_2 (1.8–6.5 wt%), Al_2O_3 (10.7–15.8 wt%), and Fe_2O_3 (14–18.5 wt%). In contrast, the microgabbros effectively show no overlap in composition: MgO (10.7–12.5 wt%), TiO_2 (<0.8 wt%), Al_2O_3 (15.5–17.5 wt%), and Fe_2O_3 (10–13 wt%) (Fig. **F100**).

The correlation between Fe_2O_3 and TiO_2 (Fig. **F101**) shows that the variation in these two elements is related to oxide abundance in the rock, with the microgabbros having only a minor oxide content and therefore low amounts of both Fe_2O_3 and TiO_2.

Apart from one sample, all of the microgabbros and oxide gabbros have low LOI (<0.6 wt%), low H_2O (<1.2 wt%) (Fig. **F100**), and low CO_2 (0.06–0.09 wt%), attesting to their relatively low degree of alteration. A single sample of microgabbro (Sample 209-1270B-7R-1, 104–106 cm) has higher LOI (5.4 wt%), H_2O (7.7 wt%), and CO_2 (0.14 wt%) and also has distinctly lower CaO (7.34 wt%). Otherwise, there appears to be no systematic relationship between volatile species and other elements in the gabbroic rocks.

Compatible trace element geochemistry of Hole 1270B gabbros also reflects the two groupings defined by the major elements. The oxide gabbros have low concentrations of Cr (<121 ppm) and Ni (<165 ppm, the detection limit), whereas the microgabbros have significantly higher concentrations of Cr (~760 ppm) and Ni (200 and 240 ppm) (Fig. **F102**). Both of the gabbro types recovered from Hole 1270B have higher concentrations of Cr and Ni compared to those recovered from Site 1268 and overlap with the range in concentrations of Hole 735B and in the Leg 153 gabbros.

Zr and V show contrasting covariations with TiO_2 in the Site 1270 gabbros (Fig. **F103**). The microgabbros have low TiO_2 (~0.8 wt%) and V (200–240 pm) and relatively elevated Zr (22–35 ppm). In contrast, the oxide gabbros, with up to 6.5 wt% TiO_2, display an increase in Zr with increasing TiO_2, ranging up to 46 ppm Zr. Zr in the gabbroic rocks from Site 1270 is generally higher than that observed in the gabbroic rocks from Site 1268 and lies at the low end of the concentration range observed in Hole 735B and Leg 153 gabbros. The one sample of harzburgite with the altered gabbroic dikelet (Sample 209-1270D-3R-1, 63–66 cm, discussed above with the other peridotites from Site 1270) has the highest Zr (96 ppm) observed in the rocks from Site 1270. V in the oxide gabbros behaves differently from Zr (Fig. **F104**), showing a peak in V (1540 ppm) near 3 wt% TiO_2. Above this, TiO_2 and V contents decrease markedly (to 600 ppm V at 6.5 wt% TiO_2).

Sc covaries with V in the Site 1270 gabbros (Fig. **F104**), showing relatively uniform Sc values (~65 ppm) in the oxide gabbros and lower Sc (~40 ppm) in the microgabbros. The Sc content of the microgabbros overlaps with that observed in Site 1268 and Leg 153 gabbros. Y covaries with Zr in the Site 1270 gabbros (Fig. **F104**), and both elements show a slight enrichment relative to the gabbros from Site 1268 but overlap with the range seen in gabbros from Hole 735B and Leg 153.

F100. MgO, Al_2O_3, and H_2O vs. SiO_2 in gabbros, p. 154.

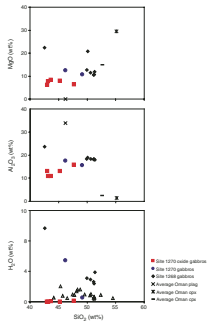

F101. Fe_2O_3 vs. TiO_2 in gabbros, p. 155.

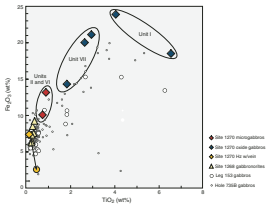

F102. TiO_2 and Cr vs. SiO_2 in gabbros, p. 156.

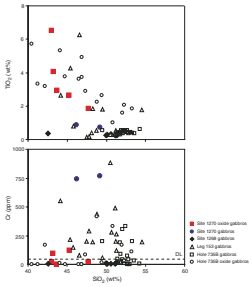

F103. V and Zr vs. TiO_2 for gabbros, p. 157.

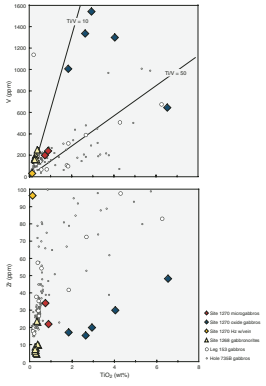

Discussion

Peridotites

Geochemical data on Site 1270 and 1268 peridotites suggest that prior to alteration Site 1268 and 1270 peridotites had similar chemical compositions. The bulk rock analyses of Site 1270 peridotites show that all these rocks have been modified by alteration, predominantly to lizardite, leading to the addition of variable amounts of volatile constituents. The addition of carbonate has affected some of the Site 1270 peridotites. The effects of this additional alteration are most clearly identified in Sample 209-1270D-1R-1, 70–74 cm, which shows an enrichment in both CaO and CO_2 compared to other peridotites analyzed from Site 1270 (Fig. **F97**). One other analyzed sample (209-1270D-3R-1, 63–66 cm) is composed of altered peridotite intruded by a plagioclase-rich gabbroic vein. This rock has markedly lower H_2O, MgO, SiO_2, and Fe_2O_3 (Fig. **F94**) and higher CaO and Al_2O_3 (Fig. **F95**). This rock is significantly enriched in trace elements such as Zr and Y, due to the presence of this vein.

Peridotites from Sites 1268 and 1270 show systematically lower Al_2O_3 compared to those from Leg 153 as well as most other abyssal peridotites (median = 1.4 wt%; Bodinier and Godard, 2003). In highly refractory peridotites such as those we have analyzed, the modal abundance of spinel, together with orthopyroxene, can exert a strong influence on the amount of Al_2O_3 present in the bulk rock. Because Cr is dominantly concentrated in spinel in these rocks, this effect produces a positive correlation between Cr and Al_2O_3. Prior to serpentinization, the peridotite protolith also underwent a relative large depletion in CaO, due to a pronounced depletion of clinopyroxene, probably during melting.

Gabbroic Rocks

Oxide abundance appears to control many of the chemical systematics in the Site 1270 gabbros, evidenced by the good correlation between Fe_2O_3 and TiO_2. The microgabbros have only a minor oxide component. For the oxide gabbros with $TiO_2 < 3$ wt%, the visual estimate of modal oxide abundances agrees reasonably well with the estimates of the amount of magnetite present determined from bulk magnetic susceptibility (see **"Discussion,"** p. 10, in "Igneous and Mantle Petrology"). However, at higher TiO_2 concentrations, the estimates of magnetite abundance from magnetic susceptibility measurements underestimates the amount of oxide observed in these rocks, which is consistent with an increased proportion of ilmenite in the oxide assemblage.

The Ti/V elemental ratio in oxide gabbros at Site 1270 shows a large range (10–60). In comparison, the microgabbros Ti/V (20) is similar to the value found in mid-ocean-ridge basalt (MORB) (Shervais, 1982). The igneous behavior of V is unique because its variable oxidation state (+3, +4, or +5) affects its partitioning behavior during magma evolution. At relatively low oxygen fugacity, such as is typically found in MORB systems, V is present in the +3 state and behaves as a relatively incompatible element, similar to Ti. Early stages of crystallization of olivine + plagioclase will produce a fractionation trend of relatively constant Ti/V ratios because these phases have low partition coefficients for both Ti and V. The crystal/liquid distribution coefficient (bulk D) for V in ocean ridge basaltic systems is usually greater than the bulk D for Ti, so extensive silicate fractionation can drive magma to higher Ti/V ratios (Sher-

F104. Sc vs. V and Zr vs. Y for gabbros, p. 158.

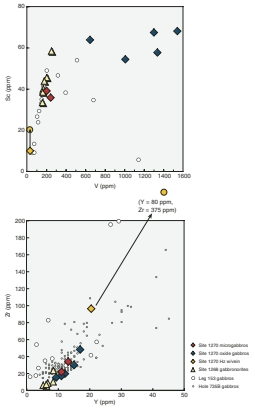

vais, 1982). Once magnetite becomes a crystallizing phase, Ti and V concentrations will decrease and there may be a dramatic increase in Ti/V ratio because V is highly compatible in magnetite (partition coefficient [K_D] for magnetite in MORB = ~5–70, depending on oxygen fugacity) (Shervais, 1982). The variation of V with Ti in the oxide gabbros of Site 1270 (Fig. **F103**) is consistent with the presence of a significant quantity of oxide in these rocks (5–15 vol%) (see **"Site 1270 Thin Sections"**). The two oxide gabbros at Site 1270 that have high Ti/V ratios (20–50) also have high TiO_2 (4–6.5 wt%), consistent with a higher proportion of ilmenite in these rocks.

The Sc budget in gabbroic rocks is largely controlled by the amount of clinopyroxene present. The Sc–V relationship shown in Figure **F104** is consistent with the relatively uniform amount of clinopyroxene in the oxide gabbros (35–45 vol%) based on the igneous petrology thin section descriptions. However, Sc may also be compatible in magnetite, along with V. Notably, the Leg 153 gabbros show a sharp decrease in Sc content when V is above ~500 ppm.

An intriguing question is whether there is a genetic linkage between the gabbroic vein observed in the harzburgite analyzed from Hole 1270D and the gabbroic rocks from Hole 1270B. Despite the fact that no attempt was made to separate the vein and harzburgite lithologies prior to the analysis of Sample 209-1270D-3R-1, 63–66 cm, this sample has Zi and Y contents that are higher than those in the most enriched oxide gabbros from Hole 1270B. The approximate proportions observed in this sample were 3:1 to 4:1 (harzburgite:gabbro). For illustrative purposes, we have made an estimate of the composition of the gabbroic liquid by subtracting the mean composition of the other peridotites at Site 1270 from the analysis of this sample, renormalized to 100%. The composition of this reconstituted gabbro is, of course, sensitive to the proportion of harzburgite estimated in the bulk analysis, and this is uncertain. Nevertheless, the illustration demonstrates that any such gabbro composition has SiO_2 near 60 wt%. To obtain reasonable MgO contents by this calculation (2–10 wt%) for the gabbro vein requires the proportion of harzburgite to be 75%–80%. This produces ranges of Zr (375–470 ppm), Y (80–100 ppm), V (43–47 ppm), Sc (20–23 ppm), TiO_2 (0.5–0.6 wt%), and Fe_2O_3 (1.0–2.6 wt%) for the reconstituted vein. These values are shown in Figures **F101** and **F104** for comparison to the other gabbro results.

The above calculation reveals that trace element–enriched liquids may be present in the crust beneath Site 1270. Similar enrichments in Zr and Y have been observed previously in some of the Leg 153 gabbros, where Zr and Y range to values >1400 and 150 ppm, respectively. The concentrations estimated for Zr (375 ppm) and Y (80 ppm) for the gabbroic vein are also consistent with simple mass balance estimates of equilibrium liquid compositions for the gabbros analyzed from Site 1270. For example, taking bulk rock Zr and Y contents of 20 and 12 ppm, respectively (as observed in the microgabbros), assuming all the Zr and Y in the rock resides in clinopyroxene with a modal abundance of 40%, and assuming appropriate K_D values for Zr (0.12) and Y (0.47) for clinopyroxene (Hart and Dunn, 1993), the equilibrium liquid will have values of Y (65 ppm) and Zr (400 ppm) quite similar to the values calculated independently for the reconstituted vein.

PHYSICAL PROPERTIES

The physical properties of the peridotites and gabbros cored in Holes 1270A, 1270B, 1270C, and 1270D were characterized through a series of measurements on whole-core sections, split-core pieces, and discrete samples as described in "Physical Properties," p. 18, in the "Explanatory Notes" chapter. We measured NGR activity and magnetic susceptibility on the multisensor track (MST) system and thermal conductivity, compressional wave velocity, density, and porosity. The rock names reported in data tables correspond to the primary lithologies determined by the igneous core description group.

Natural Gamma Radiation

All cores recovered during Leg 209 were measured using the NGR logger on the MST at intervals of 10 cm with a time period of 30 s. Results are output in counts per second. The cores in Holes 1270A, 1270B, 1270C, and 1270D display natural radioactivity in the same range as the background radiation in the core laboratory onboard the *JOIDES Resolution*. No significant peak was recorded in the NGR data in these cores.

Magnetic Susceptibility

Magnetic susceptibility values were acquired on the MST at 2.5-cm intervals for all recovered cores. All cores from Site 1270 have high magnetic susceptibility (Fig. F105), which is related to the presence of magnetite in the oxide-rich gabbros and serpentinized peridotites. The magnetic susceptibilities of the rocks from Site 1270 are comparable to the susceptibilities of ultramafic rocks and gabbros from Hess Deep (Gillis, Mével, Allan, et al., 1993) or the MARK area (Cannat, Karson, Miller, et al., 1995) (see Fig. F88, p. 145, in the "Site 1268" chapter), whereas the magnetic susceptibilities of the highly altered gabbros and peridotites recovered at Site 1268 are two orders of magnitude lower than the values for cores recovered during Legs 147 and 153.

F105. MST magnetic susceptibility, p. 159.

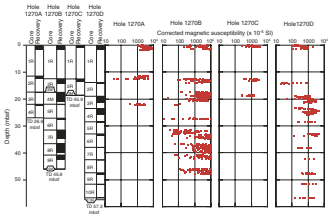

Thermal Conductivity

Thermal conductivity measurements were made at irregularly spaced intervals along cores from Holes 1270A, 1270B, 1270C, and 1270D (Fig. F106). The data are summarized in Table T5. The thermal conductivities of the ultramafic samples range 2.4–3.1 W/(m·K) (mean = 2.64 W/[m·K]). Thermal conductivity in the gabbros ranges 2.0–2.4 W/(m·K) (mean = 2.24 W/[m·K]). These values are comparable to the thermal conductivities of gabbros and ultramafic rocks from ODP sites at Atlantis Bank (Robinson, Von Herzen, et al., 1989; Dick, Natland, Miller, et al., 1999), Hess Deep (Gillis, Mével, Allan, et al., 1993), and MARK (Cannat, Karson, Miller, et al., 1995).

As described in "Thermal Conductivity," p. 19, in "Physical Properties" in the "Explanatory Notes" chapter, measurements were taken in three directions on the cut face of the archive sample half, whenever possible. The purpose of these measurements was to determine the degree of anisotropy. The apparent conductivity anisotropy of peridotites and gabbros measured in samples from Site 1270 ranges 1.1%–10.9%. Apparent thermal conductivity anisotropies measured in samples from

F106. Thermal conductivity, p. 160.

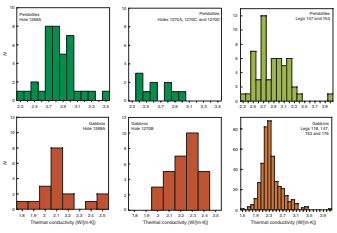

T5. Thermal conductivity measurements, p. 179.

Sites 1268 and 1270 are compiled in Figure F107. Anisotropy ranges 0.2%–12.6% (mean = 4.95%) in both gabbros and peridotites.

Thermal conductivity measurements were also made at 10° intervals on a foliated oxide gabbro (interval 209-1270B-1R-1, 120–128 cm). These measurements are shown in Table T6 and Figure F108. There is a clear conductivity minimum in the direction perpendicular to the foliation of this rock (i.e., the needle probe aligned with the foliation). The two measurements at –40° and 40° from the core axis may be biased by the position of the probe, too oblique with respect to the core axis, with the needle tips very close to the curved outer surface of the core and may therefore be underestimated. The apparent maximum at –20° may thus be an artifact.

Porosity, Density, and Seismic Velocity

Bulk density, grain density, and porosity were measured on minicores and chips from Holes 1270A, 1270B, 1270C, and 1270D. *P*-wave velocity was measured in only three minicores (Table T7). *P*-wave velocity and wet bulk density were measured in a larger suite of cube samples, as described in "*P*-Wave Velocity," p. 20, and "Porosity and Density," p. 20, both in "Physical Properties" in the "Explanatory Notes" chapter. These data are summarized in Table T8.

The density and velocity data are compared with data from Legs 147 and 153, as well as Site 1268, in Figure F109. Velocities and densities in the peridotite and gabbro samples from Site 1268 are notably lower than the velocities and densities of samples from Legs 147 (Gillis, Mével, Allan, et al., 1993) and 153 (Cannat, Karson, Miller, et al., 1995). The velocities and bulk densities of the peridotite samples from Site 1270 are comparable to the velocities and densities of samples from Site 1268, whereas the velocities and densities of gabbro samples are higher. The velocities in gabbro samples from Site 1270 are comparable to the velocities in similar samples from Hole 923A (Cannat, Karson, Miller, et al., 1995), but the densities are significantly higher, probably because of the higher oxide content of the gabbros sampled at Site 1270.

PALEOMAGNETISM

Paleomagnetic measurements were limited by poor recovery (<15% in Holes 1270A, 1270C, and 1270D) and the small lengths of most pieces. For example, only a single oriented piece could be measured in Hole 1270A. The higher recovery (37.4%) in Hole 1270B allowed sufficient archive-half measurements and discrete sampling to provide a more robust statistical characterization of the remanence. Therefore, much of the discussion will focus on results from the oxide gabbros cored in Hole 1270B (10 discrete samples and 73 core pieces measured) (Tables T9, T10). Holes 1270C and 1270D were drilled some 200 m east of Hole 1270B. These two holes are located within ~30 m of each other, and similar peridotite samples were recovered at both locations. The combined magnetic results from these two holes (10 discrete samples and 34 core pieces measured) provide a useful comparison to the data from Hole 1270B.

F107. Apparent thermal conductivity anisotropy, p. 161.

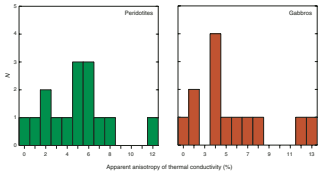

T6. Apparent thermal conductivity anisotropy, p. 180.

F108. Apparent thermal conductivity anisotropy in one sample, p. 162.

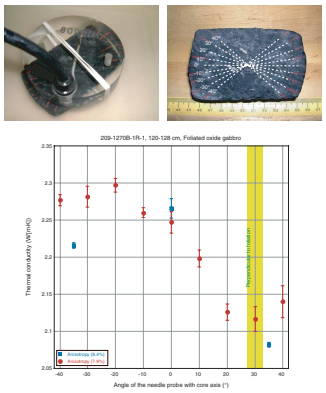

T7. Paleomagnetic minicore and chip measurements, p. 181.

T8. Saturated "cube" sample measurements, p. 182.

F109. *P*-wave velocity vs. wet bulk density, p. 163.

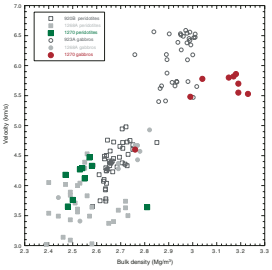

T9. Discrete sample data, p. 183.

T10. Archive-half piece orientations, p. 184.

Continuous Measurements

Susceptibility data were acquired with the MST for all suitable core samples. The serpentinized peridotites from Holes 1270C and 1270D have susceptibility values as high as 4×10^{-2} SI. However, the discontinuous nature of these data makes it difficult to recognize any downhole trends. For the oxide-rich gabbro samples from Hole 1270B, the whole-core susceptibility data were frequently >0.1 SI, resulting in clipping of the data from the Bartington susceptibility meter. In order to identify and correct these intervals of clipped data, individual archive-half pieces were remeasured (see "Igneous and Mantle Petrology," p. 3). The smaller volume of these half-core pieces allowed most of the overrange values to be identified, and the corrected susceptibility values yielded a semiquantitative estimate of the magnetite content.

As might be expected from their high magnetite content (up to 12 vol%), the natural remanent magnetization (NRM) of Hole 1270 B archive halves was commonly too high to reliably measure even at the slowest possible track speeds (1 cm/s) in the LongCore program. Stepwise alternating-field (AF) demagnetization reveals that the initial remanence of the oxide gabbros is dominated by a steep, downward-directed, low-stability magnetization component that was likely acquired during drilling (Fig. F110). As a result of this significant low-stability overprint, stepwise demagnetization often yields vectors that lie along a great circle path between a steep (drilling induced) component and near-horizontal inclinations. Despite the substantial low-stability overprint, the remanence directions after the highest demagnetization steps (>40 mT) generally cluster at shallow negative inclinations (e.g., Fig. F110A). The remanent intensity of these high-field steps typically represents only a few percent of the NRM intensity (Table T10), and so the archive-half data alone do not provide a compelling case that a geologically significant magnetization direction has been measured. However, based on the demagnetization behavior of discrete samples, we suggest that these shallow remanence directions do, in fact, approximate the characteristic remanent magnetization (ChRM) direction.

A low-stability drilling remanence is also identifiable in archive-half data from Holes 1270C and 1270D. However, this steep component represents a much smaller fraction of the NRM (Table T10). For the peridotite samples from these two holes, stable remanence directions are commonly isolated at AF treatments above 25–30 mT. As discussed below, the remanent declinations derived from selected archive-half pieces are likely to provide a close approximation of the ChRM declination even though the inclination derived from the continuous measurements may be biased.

F110. Demagnetization of archive halves, Hole 1270B, p. 164.

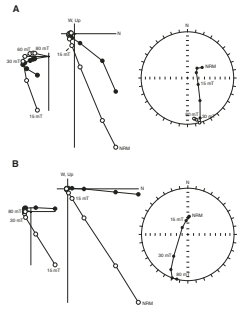

Discrete Sample Data

Hole 1270B

A total of 10 discrete samples from Hole 1270B were subjected to stepwise AF demagnetization. The NRM intensity of these samples ranges from 2.9 to nearly 50 A/m (Table T9). As observed for the archive halves, a substantial portion of this initial magnetization may be attributed to the drilling process. All discrete samples exhibit a low-stability magnetization component with steep positive inclinations (Fig. F111). This low-stability component is removed by AF treatment levels of ~15–

F111. Demagnetization of discrete samples, Hole 1270B, p. 165.

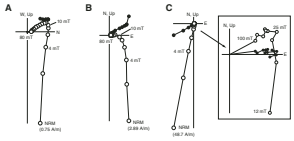

25 mT, allowing isolation of a stable remanence direction with shallow (typically negative) inclinations in some cases (Fig. F111A). The high-stability magnetization component represents as much as 17% to as little as 0.8% of the NRM, resulting in a continuum of demagnetization behavior, from clear isolation of the ChRM to samples that apparently only record a steep, drilling-induced magnetization (Fig. F111). For the latter samples, however, a small negative inclination component may also be isolated at treatments >25 mT (Fig. F111). Indeed, the high-coercivity part of the remanence (>15–25 mT) is relatively consistent both in magnitude (0.1–1 A/m) and direction, despite the more than one order of magnitude variation in the NRM intensity.

These observations are most easily explained by the presence of two populations of remanence-carrying grains with different coercivities. Although we presently have no compositional information on the iron-titanium oxides in the Hole 1270B oxide gabbros, relatively low-Ti titanomagnetites (mean ulvöspinel content = 0.15) have been documented in similar rocks recovered from Hole 735B (Natland et al., 1991). Relatively fine grained (titano)magnetite would carry the higher-coercivity ChRM, whereas a population of coarser, lower-coercivity (titano)magnetite grains would preferentially acquire a remanence during the drilling process. The presence of two relatively discrete grain size populations is supported by the coercivity spectra obtained during demagnetization (Fig. F112). Data for all samples show curved trends, which could be interpreted as a combination of two linear trends with distinctly different slopes on a logarithmic plot of remanence decay during AF demagnetization, suggesting the presence of two discrete grain size populations. The volumetric importance of coarse-grained (titano)magnetite is also supported by the low median destructive field (MDF; the alternating field required to reduce the vector difference sum to 50% of its initial value). MDF values of ~2–5 mT (Table T9) are consistent with the presence of coarse-grained multidomain magnetite. Abundant coarse-grained magnetite is found in Hole 1270B gabbros (see **"Igneous and Mantle Petrology,"** p. 3). In the absence of an isothermal remanence from drilling, these coarse grains would not contribute significantly to the NRM (e.g., Dunlop and Ödzemir, 1997).

F112. Normalized magnetization decay curves of discrete samples, p. 166.

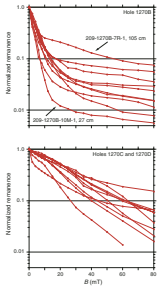

Holes 1270C and 1270D

The NRM intensity of peridotite samples from Holes 1270C and 1270D ranges from 0.6 to 4.3 A/m (Table T9). In contrast to the oxide-rich gabbros from Hole 1270B, peridotites recovered from Holes 1270C and 1270D have a much smaller drilling-related overprint. This steep, low-stability component is removed by demagnetization at ~6–12 mT (Fig. F113). The characteristic remanence generally accounts for >50% of the total NRM and decays linearly to the origin at fields of 50–80 mT. In contrast to Hole 1270B, the uniform slopes of the remanence decay in the log scale upon AF demagnetization (Fig. F113) suggest a unimodal (normal) distribution of magnetite grain sizes, where the contribution of unstable coarse-grained magnetite is negligible. As a result, observed MDF values (10–20 mT) are systematically higher than in the oxide-rich gabbros of Hole 1270B.

F113. Demagnetization of discrete samples, Holes 1270C and 1270D, p. 167.

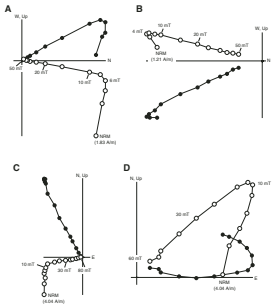

Remanence Directions

Despite the small number of samples, most of the paleomagnetic directions from Hole 1270B have negative inclinations. Results from dis-

crete samples range from –35° to +5°, whereas long-core continuous measurements show a wider variance, typically from –20° to +15° (Fig. F114). The discrepancy between discrete and long-core inclinations is more obvious in Holes 1270C and 1270D, where the characteristic component represents a larger proportion of the NRM (Fig. F113; Table T9) and calculation of paleomagnetic directions has less error. For example, the demagnetization data from the archive halves often show nearly unidirectional demagnetization trends at the same depth interval where off-line treatment of discrete samples yields a distinct two-component magnetization (Fig. F114). This discrepancy may reflect heterogeneities in the archive-half magnetization (note that there is a factor of 3 difference in the NRM intensity). Alternatively, the drilling overprint may be more pronounced in the outer portion of the core, leading to a relatively larger contribution in the archive halves than in the discrete samples (taken closer to the center of the core). Given the different demagnetization behavior in the archive-half and discrete sample data, two points should be mentioned. First, because the drilling-related low-field overprint is nearly vertical, declinations are not excessively affected by a partial overlap of the drilling component. Stepwise demagnetization yields great circles aligned about nearly vertical planes (see Fig. F110). Thus, the half-core declinations generally show good agreement with discrete sample results (Fig. F115). For samples from Holes 1270C and 1270D, the two types of data are always within 20° of each other. Somewhat larger discrepancies between archive-half and discrete sample declinations are evident for Hole 1270B gabbroic samples, which have a substantial drilling-induced overprint. Where both types of data are available the paleomagnetic directions obtained from discrete samples should be regarded as more accurate (see "Paleomagnetism," p. 41, in the "Site 1268" chapter).

The drilling-induced remanence precludes the use of a north-directed recent viscous component for core reorientation. In the absence of azimuthal constraints, the polarity interpretation of the directional data relies exclusively on the inclination of the remanence. In the case of Hole 1270B, inclinations are shallow and predominantly negative. Moreover, the mean inclination for 10 discrete samples is –14° (+10°/–10°; κ = 25) using the inclination-only technique of McFadden and Reid (1982). These data are most easily interpreted as representing a reversed polarity magnetization acquired during the Matuyama chron (older than 0.78 Ma) (Cande and Kent, 1995). On the other hand, the combined data set from Holes 1270C and 1270D yields a mean inclination of –3° (+13°/–13°; κ = 15; N = 10) for discrete samples and a distribution (including both discrete and archive-half data) that is slightly skewed toward positive inclinations. The polarity interpretation is therefore ambiguous. Perhaps the simplest scenario would be that all holes from Site 1270 have the same reversed polarity. Alternatively, the different lithologies recovered from Hole 1270B (oxide gabbros) and Holes 1270C and 1270D (harzburgites) and the spacing between these holes suggest another possible interpretation; namely, low-temperature (~300°C) serpentinization and remanence acquisition in the peridotites might represent a normal polarity magnetization acquired at a somewhat later time than the magnetization in the gabbros.

The mean paleomagnetic inclinations of the gabbros and the harzburgites are not significantly different. However, their values are significantly lower than the expected inclination for the time-averaged dipole field at the site (±28°). As suggested for Site 1268, rotation about a ridge-parallel, near-horizontal axis may have affected Site 1270. Be-

F114. Paleomagnetic inclinations, p. 168.

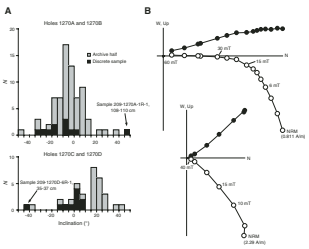

F115. Remanent declination from discrete samples and archive halves, p. 169.

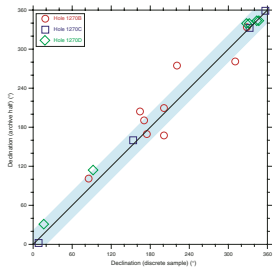

cause the remanence of Hole 1270B is interpreted as reversed polarity, an alternative explanation for the shallow remanent inclination would be that the drilling overprint has overlapped the characteristic magnetization. In contrast, the drilling remanence and characteristic component are well separated in discrete samples from Holes 1270C and 1270D (Fig. F113). Thus, the shallow inclinations for these holes apparently require some rotation. The uncertainty of the magnetic polarity of samples from Holes 1270C and 1270D does not affect this conclusion, but it does affect the reorientation of any structural data.

Declinations determined from both archive halves and discrete samples from Hole 1270B and Holes 1270C and 1270D are not randomly distributed in the core reference frame (Fig. F116). Although the cores are not azimuthally oriented, the dominant foliation was used to determine the splitting line for the cores. The clustering of declination data therefore indicates the general success of this procedure and the existence of a relatively uniform foliation plane. The declinations for Hole 1270B are near 200°, while the declinations from Holes 1270C and 1270D cluster near 350°. This difference indicates that either the foliations do not have a common attitude or the polarity in the two locations is different (see "Structural Geology," p. 21, for a complete discussion).

F116. Rose diagram of paleomagnetic declinations, p. 170.

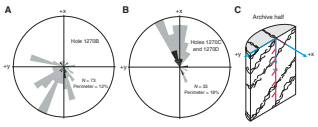

Anisotropy of Magnetic Susceptibility

Anisotropy of magnetic susceptibility (AMS) was routinely measured on all discrete samples (Table T11). The degree of anisotropy (P = maximum/minimum eigenvalues) ranges from 1.03 to 1.19. The majority of samples have an oblate magnetic fabric. The bulk susceptibility values for all samples are sufficiently high (>10^{-3} SI) that the contribution from paramagnetic silicate grains can be neglected (Rochette et al., 1992). The AMS signal reflects either the shape anisotropy of grains (or grain clusters) or the anisotropic distribution of magnetite. Although the precise relationship of the magnetic anisotropy to the silicate fabric in the Site 1270 samples is presently not known, the poles to magnetic foliation (i.e., the minimum eigenvector of the susceptibility tensor) are broadly consistent with the mesoscopic foliations (Fig. F117).

T11. Anisotropy of magnetic susceptibility, p. 186.

F117. Projections of minimum eigenvector of the susceptibility tensor, p. 171.

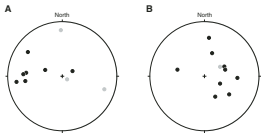

MICROBIOLOGY

Solid Sample 209-1270D-4R-1 (Piece 14, 112–131 cm)

At Site 1270 one rock interval, Sample 209-1270D-4R-1 (Piece 14, 112–131 cm), was collected to characterize the microbial community inhabiting this environment. The rock sample is a completely serpentinized harzburgite.

The outer surface was quickly flamed with a propane torch. The speed of this sterilization technique helped minimize the time (~20 min) the rock sample was exposed to oxygen. Our cruise sampling strategy was to characterize the microbiological community in serpentinized peridotite over the range of depths of penetration we achieved. At this site we hoped to collect a sample from ~30 mbsf. However, owing to poor recovery from previous holes at this site, we collected a sample from a shallower core with sufficient recovery to address all the cruise objectives. The sample was placed in the anaerobic chamber in a sterile container on ice for 2 hr, until the next core arrived on deck. Core 209-

1270D-5R (encompassing our target depth interval) was only a few rounded pieces of gabbro and peridotite, so we elected to process the provisional sample taken from Core 4R. After being kept cool, samples were prepared for enrichment cultures, deoxyribonucleic acid (DNA) analysis, total organic carbon analysis, and scanning electron microscope studies as described in "Microbiology," p. 24, in the "Explanatory Notes" chapter.

Seawater and Water Samples and Atmospheric Data

Aliquots of surface water were collected and prepared for DNA analysis and direct counts as described in "Seawater and Water Samples," p. 26, in "Microbiology" in the "Explanatory Notes" chapter. One method was used to examine the type and extent of contamination caused by drill fluids that penetrated the interior of the rock sample used for microbial studies, perfluorocarbon tracer (PFT), as described in "Contamination Tests," p. 26, in "Microbiology" in the "Explanatory Notes" chapter. The results of the PFT analyses confirm delivery of the tracer to the core. We could also detect PFT in samples from the interior of the core, but at a level lower than that measured in a blank (Table T12; Fig. F118).

Table T13 is a summary of atmospheric and surface water data for the period of 29 May to 4 June 2003. For surface water direct count data, 1 mL of water was stained as described in "Microbiology," p. 24, in the "Explanatory Notes" chapter. One milliliter of funnel rinse water was used as a control. Salinity, temperature, and pH values for all surface waters varied; salinity ranged 36.0–37.0 psu, temperature 25.3°–25.8°C, and pH for all samples was 7.96. Surface water samples were collected between 1221 and 1440 hr. Air samples were collected for culture-based studies between 0630 and 0746 hr. Air sample volumes were 112–443.7 L per sample (two samples taken). Microbial growth (colony forming units) was for the total volume at 48 and 96 hr of incubation (Table T13). Air temperatures, humidity, wind speed, and wind direction ranged 24.9°–26.1°C, 68.2%–77.5%, 2.2–7.8 m/s, and 58°–110°, respectively. Samples for shore-based analysis of bacterial community DNA and bacteria and viral direct counts were collected daily and stored according to protocol.

T12. PFT in standards and core pieces, p. 187.

F118. PFT in standards and core pieces, p. 172.

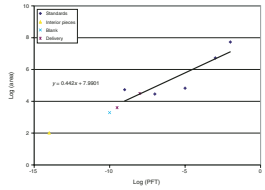

T13. Surface water and atmospheric microbiology data, p. 188.

REFERENCES

Agar, S.M., Casey, J.F., and Kempton, P.D., 1997. Textural, geochemical, and isotopic variations in gabbroic shear zones from the MARK area. *In* Karson, J.A., Cannat, M., Miller, D.J., and Elthon, D. (Eds.), *Proc. ODP, Sci. Results,* 153: College Station, TX (Ocean Drilling Program), 99–121.

Agar, S.M., and Lloyd, G.E., 1997. Deformation of Fe-Ti oxides in gabbroic shear zones from the MARK area. *In* Karson, J.A., Cannat, M., Miller, D.J., and Elthon, D. (Eds.), *Proc. ODP, Sci. Results,* 153: College Station, TX (Ocean Drilling Program), 123–141.

Ayers, J.C., and Watson, E.B., 1991. Solubility of apatite, monazite, zircon, and rutile in supercritical aqueous fluids with implications for subduction zone geochemistry. *Philos. Trans. R. Soc. London, Ser. A,* 335:365–375.

Bodinier, J.-L., and Godard, M., 2003. Orogenic, ophiolitic, and abyssal peridotites. In Carlson, R.W., (Ed.), *Treatise on Geochemistry* (vol. 2)*: Geochemistry of the Mantle and Core,* New York (Elsevier), 103–170.

Bonatti, E., Lawrence, J.R., Hamlyn, P.R., and Breger, D., 1980. Aragonite from deep sea ultramafic rocks. *Geochim. Cosmochim. Acta,* 44:1207–1214.

Brodie, K.H., and Rutter, E.H., 1985. On the relationship between deformation and metamorphism, with special reference to the behavior of basic rocks. *In* Thompson, A.B., and Rubie, D.C. (Eds.), *Metamorphic Reactions: Kinetics, Textures, and Deformation:* New York (Springer-Verlag), 138–179.

Cande, S.C., and Kent, D.V., 1995. Revised calibration of the geomagnetic polarity timescale for the Late Cretaceous and Cenozoic. *J. Geophys. Res.,* 100:6093–6095.

Cannat, M., Ceuleneer, G., and Fletcher, H., 1997. Localization of ductile strain and the magmatic evolution of gabbroic rocks drilled at the Mid-Atlantic Ridge (23°N). *In* Karson, J.A., Cannat, M., Miller, D.J., and Elthon, D. (Eds.), *Proc. ODP, Sci. Results,* 153: College Station, TX (Ocean Drilling Program), 77–98.

Cannat, M., Karson, J.A., Miller, D.J., et al., 1995. *Proc. ODP, Init. Repts.,* 153: College Station, TX (Ocean Drilling Program).

Casey, J.F., 1997. Comparison of major- and trace-element geochemistry of abyssal peridotites and mafic plutonic rocks with basalts from the MARK region of the Mid-Atlantic Ridge. *In* Karson, J.A., Cannat, M., Miller, D.J., and Elthon, D. (Eds.), *Proc. ODP, Sci. Results,* 153: College Station, TX (Ocean Drilling Program), 181–241.

Deer, W.A., Howie, R.A., and Zussman, J., 1992. *An Introduction to the Rock-Forming Minerals* (2nd ed.): London (Longman).

Dick, H.J.B., Meyer, P.S., Bloomer, S., Kirby, S., Stakes, D., and Mawer, C., 1991. Lithostratigraphic evolution of an in-situ section of oceanic Layer 3. *In* Von Herzen, R.P., Robinson, P.T., et al., *Proc. ODP, Sci. Results,* 118: College Station, TX (Ocean Drilling Program), 439–538.

Dick, H.J.B., Natland, J.H., Alt, J.C., Bach, W., Bideau, D., Gee, J.S., Haggas, S., Hertogen, J.G.H., Hirth, G., Holm, P.M., Ildefonse, B., Iturrino, G.J., John, B.E., Kelley, D.S., Kikawa, E., Kingdon, A., LeRoux, P.J., Maeda, J., Meyer, P.S., Miller, D.J., Naslund, H.R., Niu, Y.-L., Robinson, P.T., Snow, J., Stephen, R.A., Trimby, P.W., Worm, H.-U., and Yoshinobu, A., 2000. A long in situ section of the lower ocean crust: results of ODP Leg 176 drilling at the Southwest Indian Ridge. *Earth Planet. Sci. Lett.,* 179:31–51.

Dick, H.J.B., Natland, J.H., Miller, D.J., et al., 1999. *Proc. ODP, Init. Repts.,*176 [CD-ROM]. Available from: Ocean Drilling Program, Texas A&M University, College Station, TX 77845-9547, U.S.A.

Dick, H.J.B., Schouten, H., John, B., Kinoshita, H., Natland, J.H., MacLeod, C.J., and Hirth, J.G., 1999. Evidence for a "melt lens" equivalent in the lower crust at an ultraslow spreading ridge. *Eos, Trans. Am. Geophys. Union,* 80:F956.

Dilek, Y., Coulton, A., and Hurst, S.D., 1997a. Serpentinization and hydrothermal veining in peridotites at Site 920 in the MARK area. *In* Karson, J.A., Cannat, M.,

Miller, D.J., and Elthon, D. (Eds.), *Proc. ODP, Sci. Results,* 153: College Station, TX (Ocean Drilling Program), 35–59.

Dilek, Y., Kempton, P.D., Thy, P., Hurst, S.D., Whitney, D., and Kelley, D.S., 1997b. Structure and petrology of hydrothermal veins in gabbroic rocks from Sites 921 to 924, MARK area (Leg 153): alteration history of slow-spread lower oceanic crust. *In* Karson, J.A., Cannat, M., Miller, D.J., and Elthon, D. (Eds.), *Proc. ODP, Sci. Results,* 153: College Station, TX (Ocean Drilling Program), 155–178.

Dunlop, D.J., and Özdemir, Ö., 1997. *Rock Magnetism: Fundamentals and Frontiers:* Cambridge (Cambridge Univ. Press).

Escartin, J., Mével, C., MacLeod, C.J., and McCraig, A., 2003. Constraints on deformation conditions and the origin of oceanic detachments, the Mid-Atlantic Ridge core complex at 15°45′N. *Geochem., Geophys., Geosyst.,* 4:10.1029/2002GC000472.

Fujiwara, T., Lin, J., Matsumoto, T., Kelemen, P.B., Tucholke, B.E., and Casey, J., 2003. Crustal evolution of the Mid-Atlantic Ridge near the Fifteen-Twenty Fracture Zone in the last 5 Ma. *Geochem., Geophys., Geosyst.,* 4:10.1029/2002GC000364.

Gillis, K., Mével, C., Allan, J., et al., 1993. *Proc. ODP, Init. Repts.,* 147: College Station, TX (Ocean Drilling Program).

Hart, S.R., and Dunn, T., 1993. Experimental CPX/melt partitioning of 24 trace elements. *Contrib. Mineral. Petrol.,* 113:1–8.

Hebert, R., Adamson, A.C., and Komor, S.C., 1990. Metamorphic petrology of ODP Leg 109, Hole 670A serpentinized peridotites: serpentinization processes at slow spreading ridge environment. *In* Detrick, R., Honnorez, J., Bryan, W.B., and Juteau, T., et al., *Proc. ODP, Sci. Results,* 106/109: College Station, TX (Ocean Drilling Program), 103–115.

Jagoutz, E., Palme, H., Baddenhausen, H., Blum, K., Cendales, M., Dreibus, G., Spettel, B., Lorenz, V., and Waenke, H., 1979. The abundances of major, minor and trace elements in the Earth's mantle as derived from primitive ultramafic nodules. *Proc. 10th Lunar Planet. Sci. Conf.,* 2031–2050.

Lachize, M., 1993. La chambre magmatique fossile d'Haymiliyah (massif de Haylayn, ophiolite de Semail: un cas de précipitation de sulfures magmatiques dans la couche 3 de la lithosphère océanique [Thèse de Doctorat]. Université de Bretagne Occidentale.

McFadden, P.L., and Reid, A.B., 1982. Analysis of paleomagnetic inclination data. *Geophys. J. R. Astron. Soc.,* 69:307–319.

Misch, P., 1969. Paracrystalline microboudinage of zoned grains and other criteria for synkinematic growth of metamorphic minerals. *Am. J. Sci.,* 267:43–63.

————, 1970. Paracrystalline microboudinage in a metamorphic reaction sequence. *Geol. Soc. Am. Bull.,* 81:2483–2485.

Natland, J.H., and Dick, H.J.B., 2001. Formation of the lower ocean crust and the crystallization of gabbroic cumulates at a very slowly spreading ridge. *J. Volcanol. Geotherm. Res.*, 110:191–233.

Natland, J.H., Meyer, P.S., Dick, H.J.B., and Bloomer, S.H., 1991. Magmatic oxides and sulfides in gabbroic rocks from Hole 735B and the later development of the liquid line of descent. *In* Von Herzen, R.P., Robinson, P.T., et al., *Proc. ODP, Sci. Results,* 118: College Station, TX (Ocean Drilling Program), 75–111.

O'Hanley, D.S., 1996. Serpentinites: records of tectonic and petrological history. *Oxford Monogr. Geol. Geophys.,* 34.

Robinson, P.T., Von Herzen, R., et al., 1989. *Proc. ODP, Init. Repts.,* 118: College Station, TX (Ocean Drilling Program).

Rochette, P., Jackson, M., and Aubourg, C., 1992. Rock magnetism and the interpretation of anisotropy of magnetic susceptibility. *Rev. Geophys.,* 30:209–226.

Shervais, J.W., 1982. Ti-V plots and the petrogenesis of modern and ophiolitic lavas. *Earth Planet. Sci. Lett.,* 59:101–118.

Shipboard Scientific Party, 1995. Site 920. *In* Cannat, M., Karson, J.A., Miller, D.J., et al., *Proc. ODP, Init. Repts.,* 153: College Station, TX (Ocean Drilling Program), 45–119.

Stakes, D., Mével, C., Cannat, M., and Chaput, T., 1991. Metamorphic stratigraphy of Hole 735B. *In* Von Herzen, R.P., Robinson, P.T., et al., *Proc. ODP, Sci. Results,* 118: College Station, TX (Ocean Drilling Program), 153–180.

Wänke, H., 1981. Constitution of terrestrial planets. *Philos. Trans. R. Soc. London, Ser. A,* 303:287–302.

Wicks, F.J., 1984. Deformation histories as recorded by serpentinites. II. Deformation during and after serpentinization. *Can. Mineral.,* 22:775–788.

Figure F1. Bathymetric map indicating subsea camera survey tracks and hole locations. Bathymetric data courtesy of T. Fujiwara and T. Matsumoto of JAMSTEC (Fujiwara et al., 2003).

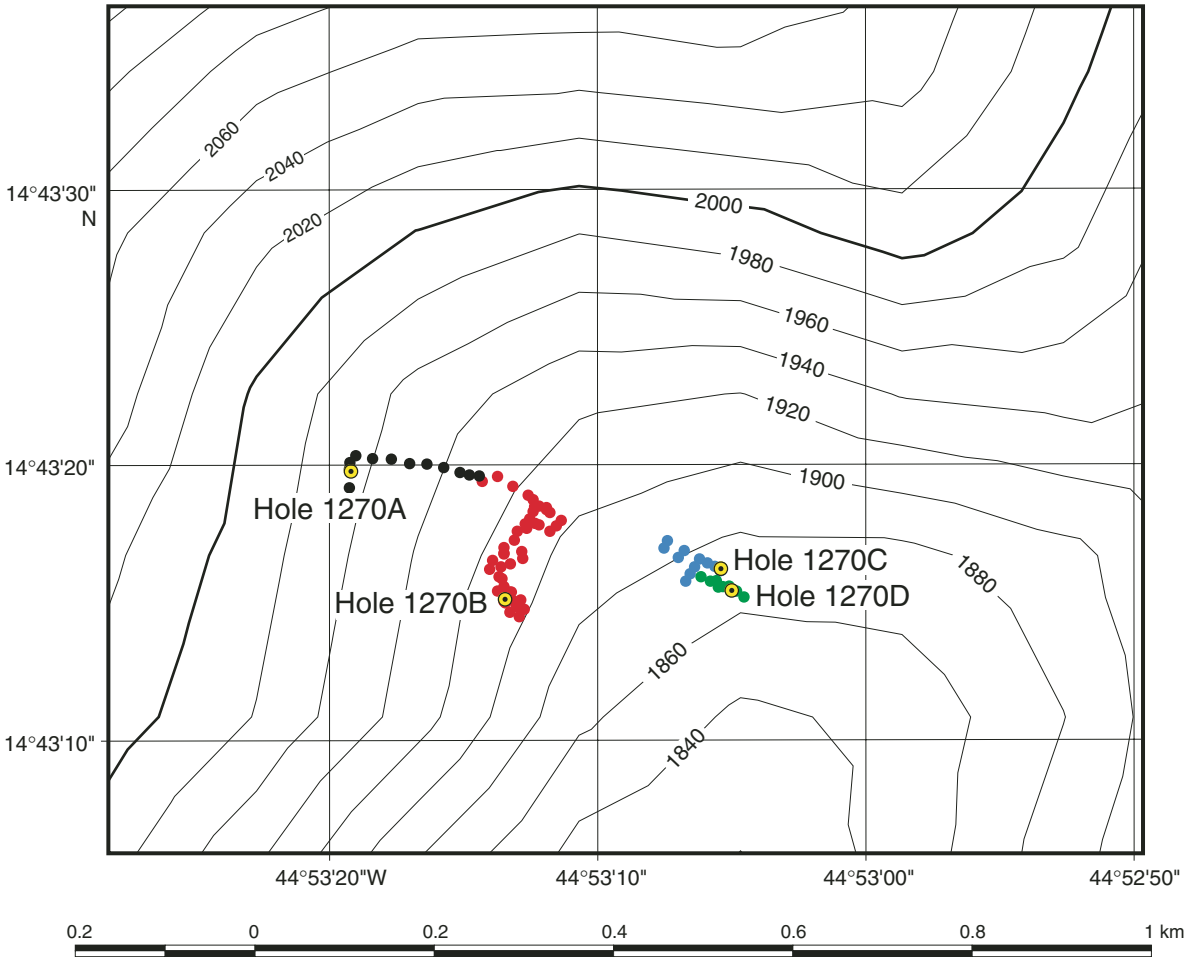

Figure F2. A. Location map with track of *Shinkai* 6500 Dive 425 (red dotted line), locations and lithologies of samples from that dive, and the approximate positions of Holes 1270A, 1270B, 1270C, and 1270D. (Continued on next page.)

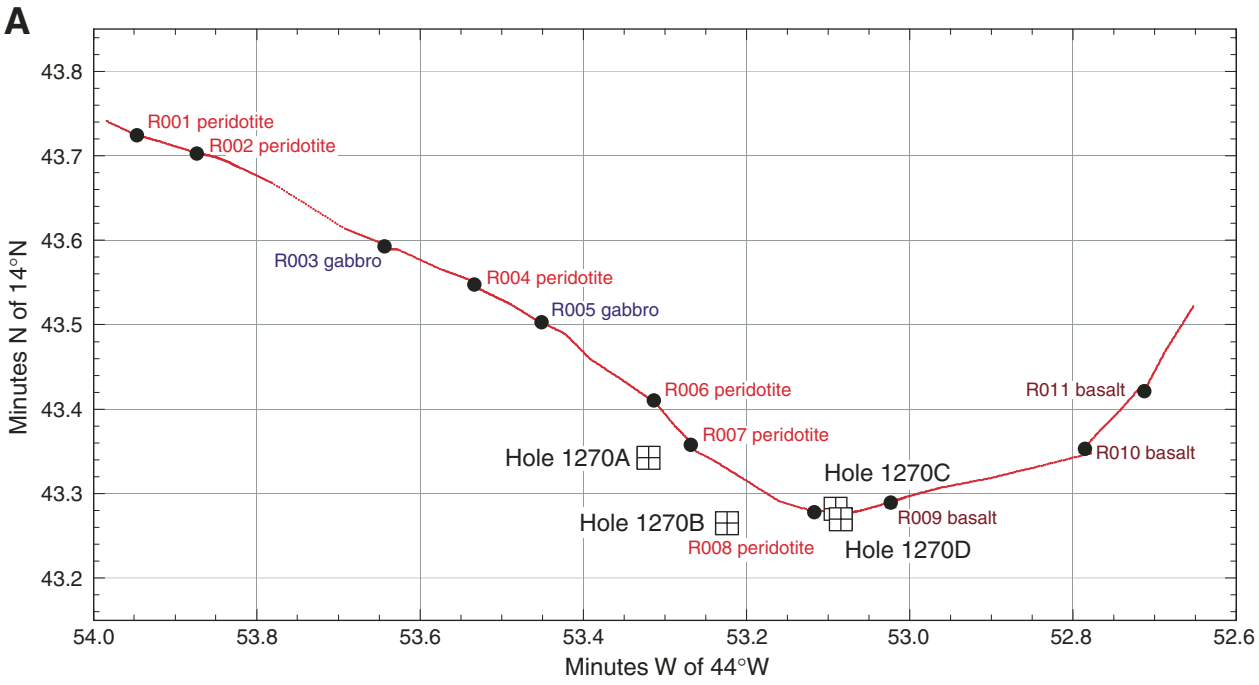

Figure F2 (continued). B. Bathymetric section based *Shinkai* 6500 Dive 425, projected along 100° with no vertical exaggeration. Locations and lithologies of samples collected during the dive, as well as the approximate positions of Holes 1270A, 1270B, 1270C, and 1270D are indicated.

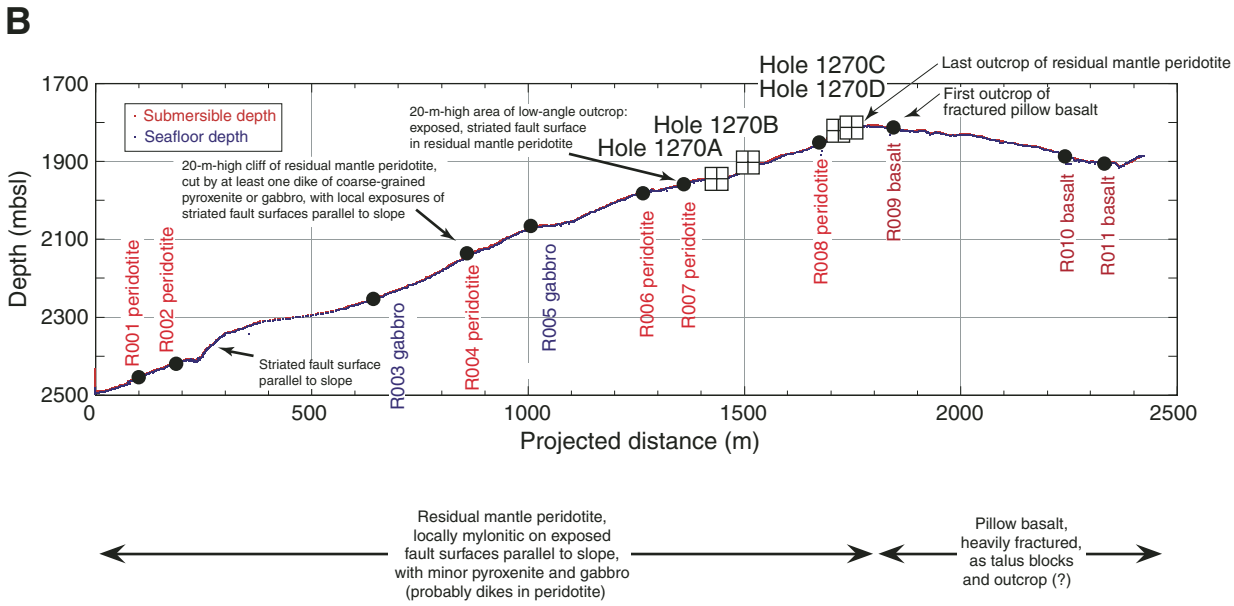

Figure F3. Lithostratigraphic summary for Hole 1270A. TD = total depth.

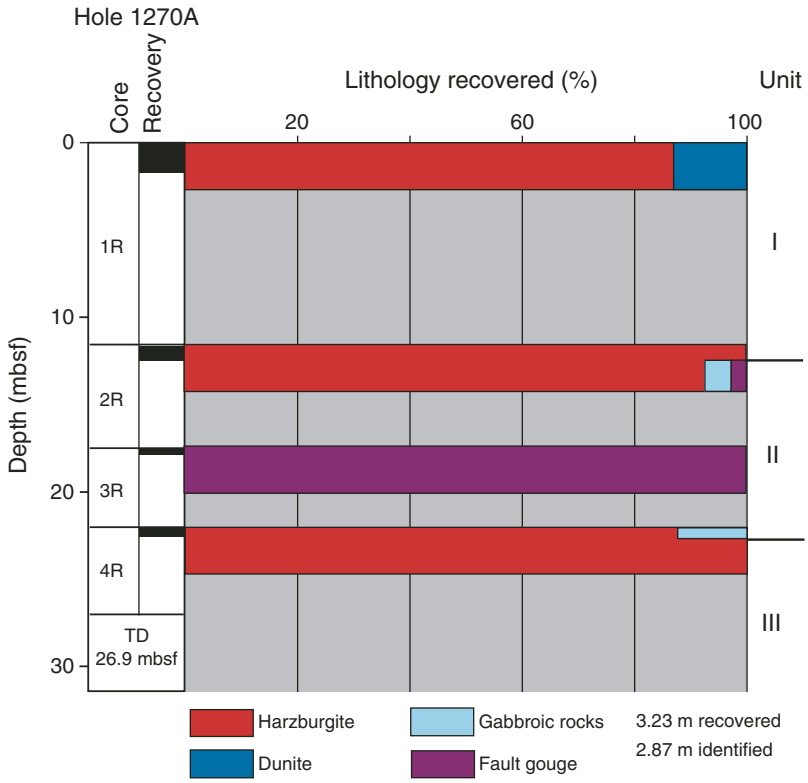

Figure F4. Photograph of a very coarse grained orthopyroxene-rich harzburgite from Unit I (interval 209-1270A-1R-2 [Piece 6, 33–40 cm]).

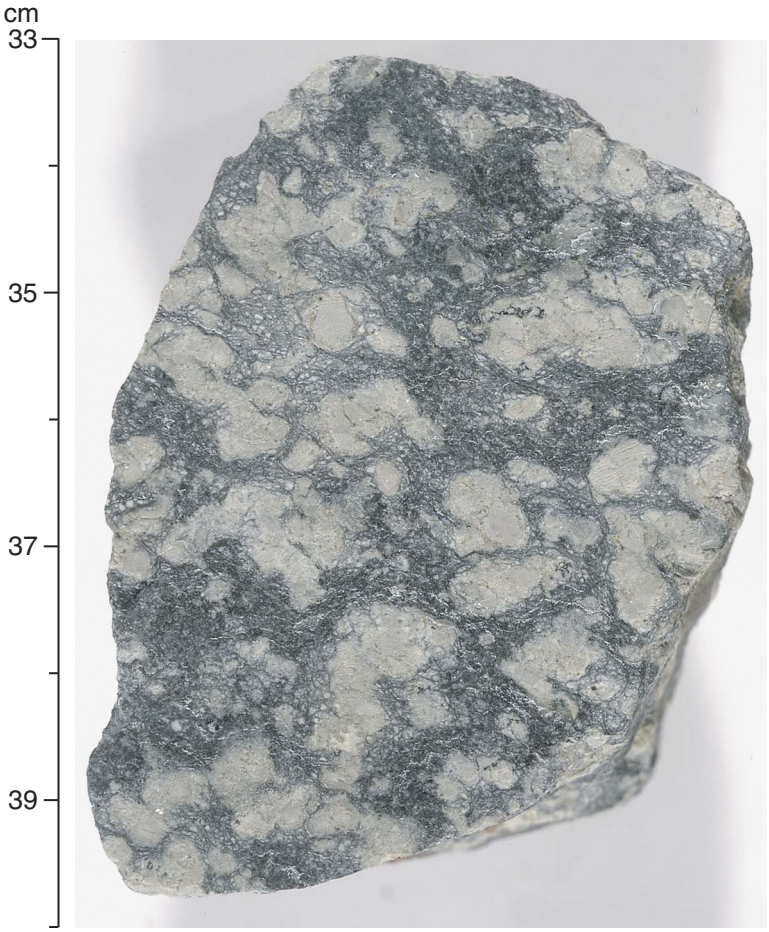

Figure F5. Photomicrograph showing amphibole-bearing ultramafic vein or dike crosscutting Unit III harzburgite (Sample **209-1270A-4R-1, 54–56 cm**) (cross-polarized light: blue filter; field of view = 5.5 mm; image 1270A_003).

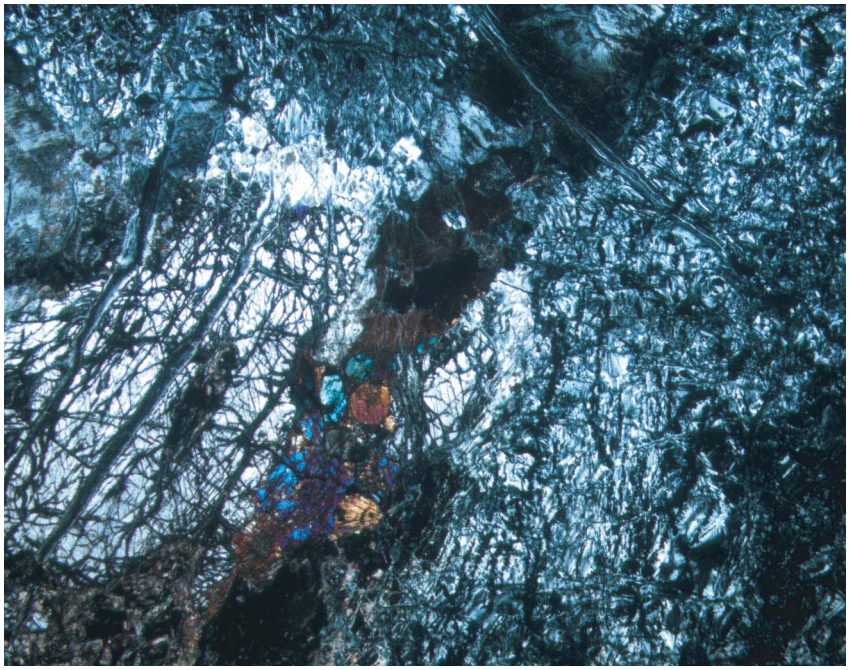

Figure F6. Photomicrograph showing orthopyroxene porphyroclast altered to bastite in Unit I harzburgite (Sample **209-1270A-1R-1, 96–99 cm**) (cross-polarized light: blue filter; field of view = 2.75 mm; image 1270A_009).

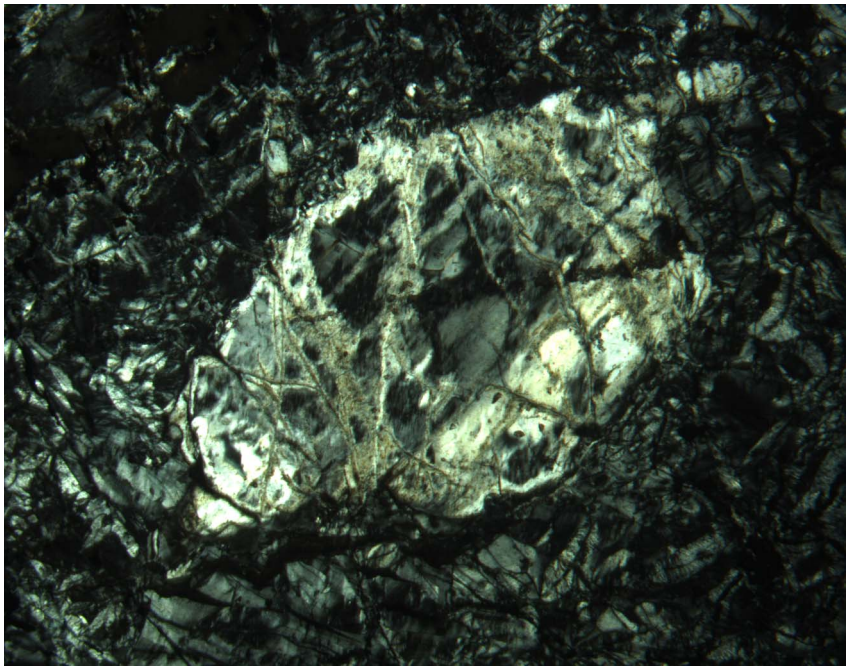

Figure F7. Photomicrograph showing orthopyroxene porphyroclast recrystallized into subgrains and altered to bastite in Unit I harzburgite (Sample **209-1270A-1R-1, 96–99 cm**) (cross-polarized light: blue filter; field of view = 2.75 mm; image 1270A_008).

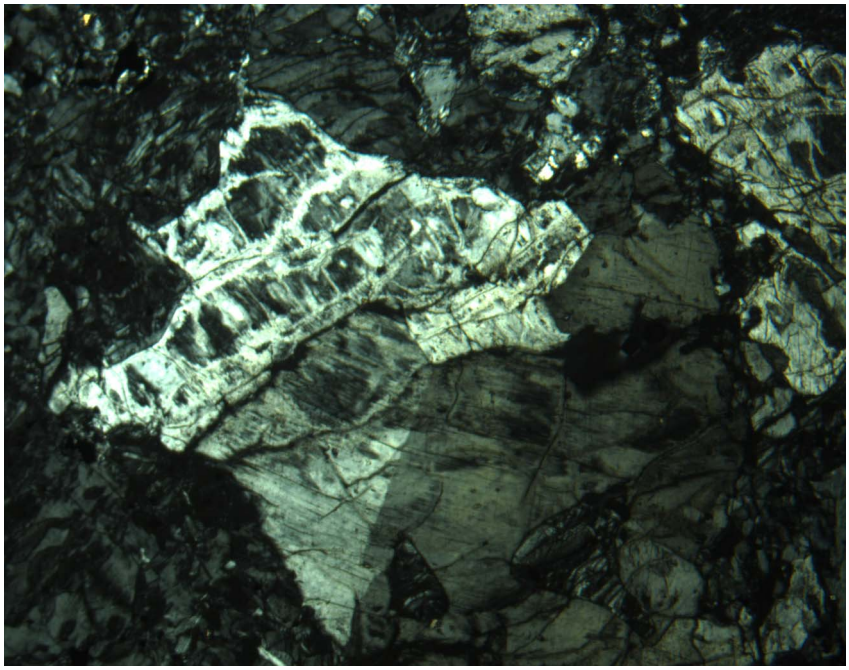

Figure F8. Photomicrographs showing very coarse orthopyroxene from an orthopyroxene-rich band in Unit I harzburgite, recrystallized into subgrains with interstitial olivine and clinopyroxene and intergrown with coarse spinel (Sample **209-1270A-1R-1, 96–99 cm**) (cross-polarized light: blue filter). **A.** Field of view = 2.75 mm; image 1270A_006. **B.** Interstitial clinopyroxene (in blue) and olivine (serpentinized) grains in orthopyroxene subgrain mosaic (field of view = 0.7 mm; image 1270A_007).

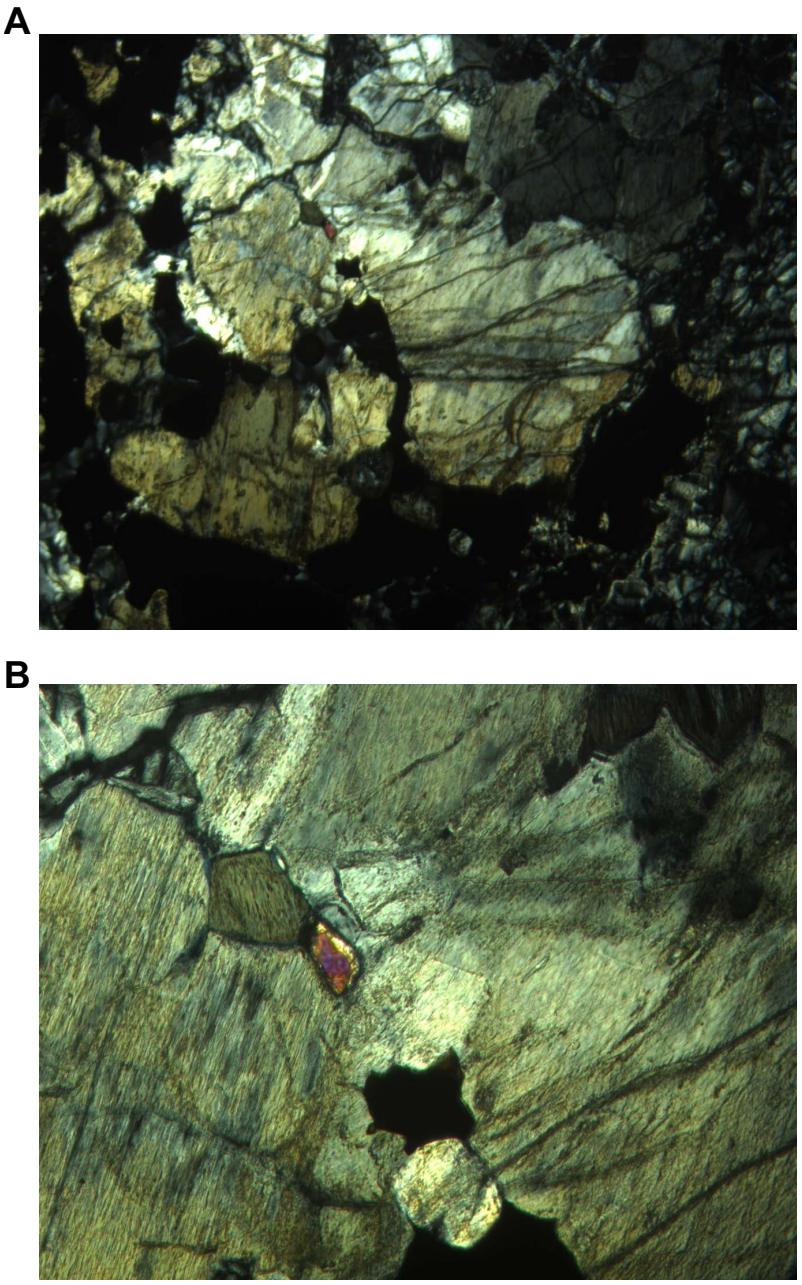

Figure F9. Photomicrograph showing brown amphibole and iron oxides interstitial to small olivine grains in a 2- to 3-mm-wide pyroxenite dike or vein (Sample **209-1270A-4R-1, 54–56 cm**) (plane-polarized light: blue filter; field of view = 0.35 mm; image 1270A_002).

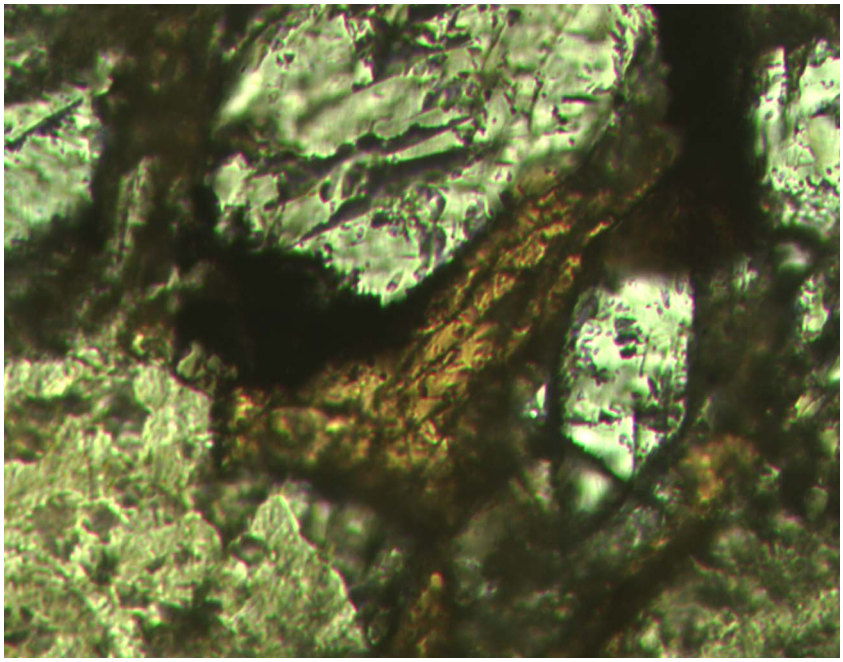

Figure F10. Downhole variations in modal plagioclase, estimated magnetite content from susceptibility, and position and recovery for the 10 drilled intervals in Hole 1270B. TD = total depth.

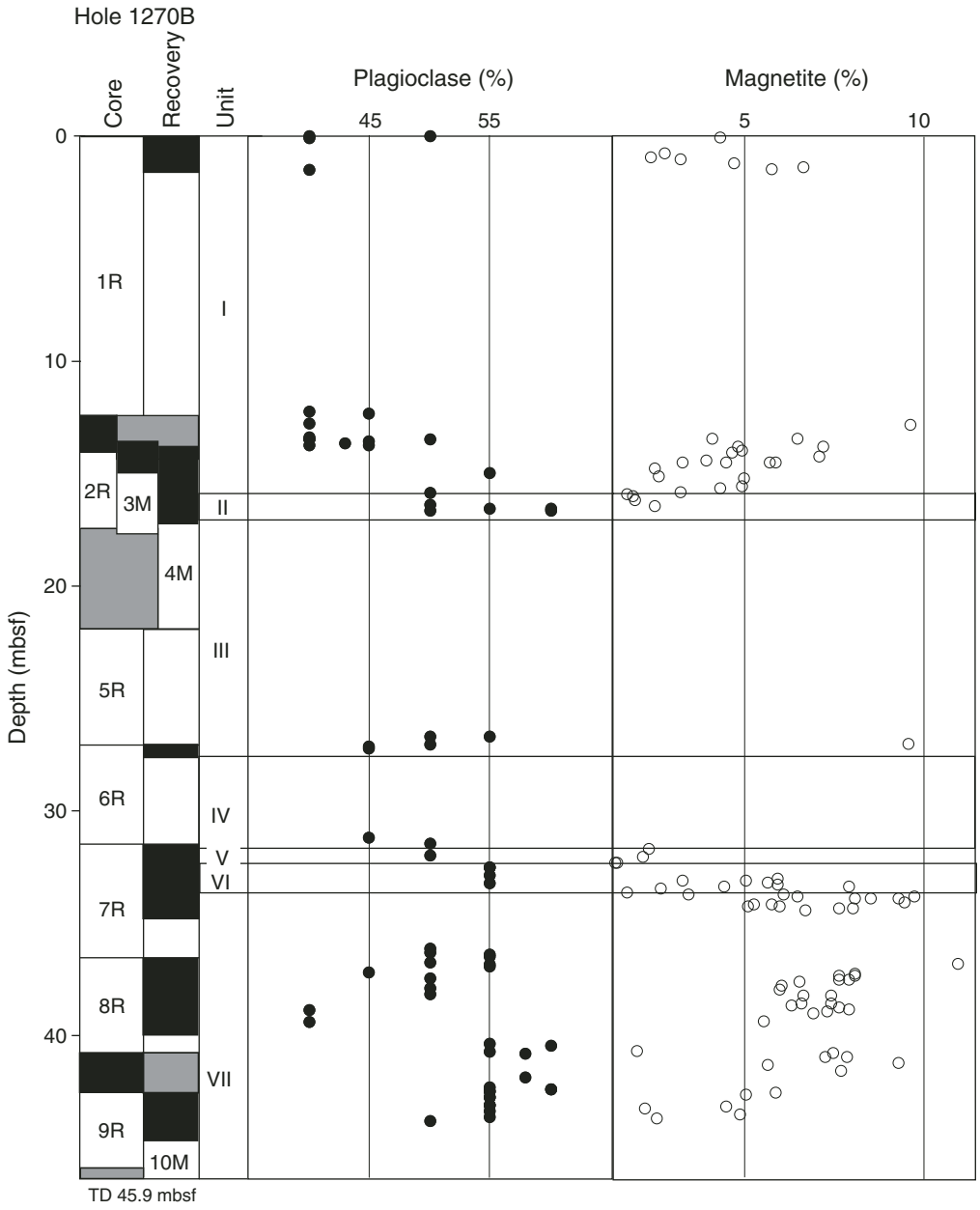

Figure F11. Cartoon showing how the bulk magnetic susceptibility of the core half-round samples were used to estimate the amount of magnetite. The front view shows the fractional area that the half core occupies in the susceptibility loop compared to the expected cross-sectional area the loop is designed to measure. The side view schematically depicts the response function of the loop and shows that a ~7 cm length is required to capture 95% of the measured response. Also included is the equation used to calculate the percent magnetite (Mt).

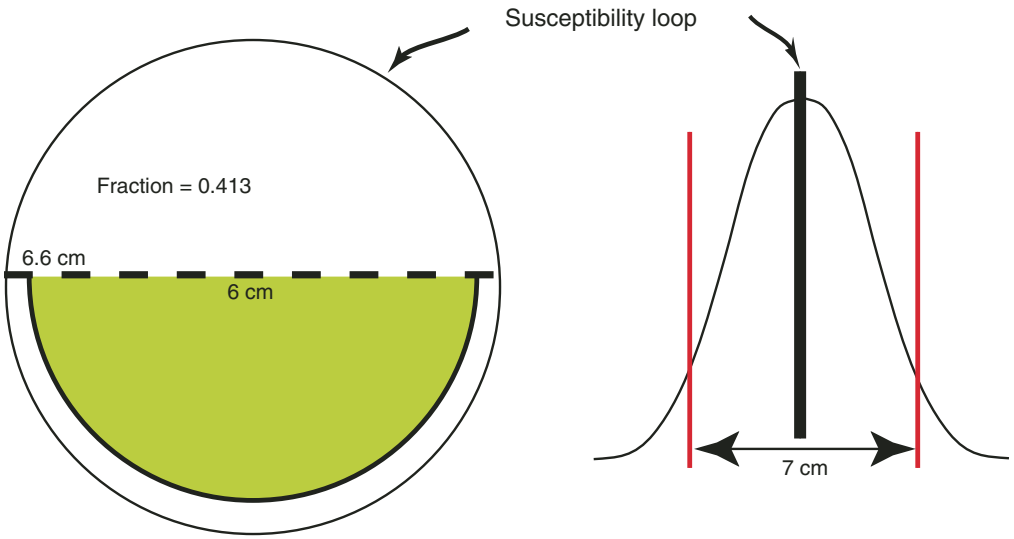

Mt (%) = [(Susceptibility)/(Volume%) X (1/0.413)] X (3.3/10,000)

Figure F12. Photomicrographs depicting the variations in deformation of the oxide gabbronorites ranging from relatively undeformed to strongly deformed. **A–C.** This oxide-gabbronorite has an undeformed igneous texture with lath-shaped euhedral plagioclase, subhedral to euhedral clinopyroxenes, subhedral orthopyroxene, and interstitial oxides (Sample **209-1270B-10M-1, 117–120 cm**). (A) The red box indicates the position of the magnified image in B (plane-polarized light: blue + dark gray filter; field of view [FOV] = 11 mm; image 1270B_033). (B) Close-up showing that although the texture is magmatic the rock has experienced some deformation as indicated by kinked plagioclase and release of strain associated with the polysynthetic twinning (cross-polarized light [XPL]: blue + dark gray filter; FOV = 2.75 mm; image 1270B_034). (C) Preservation of an optically zoned core (outlined in red) in a slightly deformed plagioclase (XPL: blue filter; FOV = 1.4 mm; image 1270B_013). **D.** Ribbon-textured plagioclase surrounded by plagioclase neoblasts in a strongly deformed oxide gabbronorite (Sample **209-1270B-1R-1, 90–93 cm**) (XPL: blue filter; FOV = 2.75 mm; image 1270B_036). (Continued on next page.)

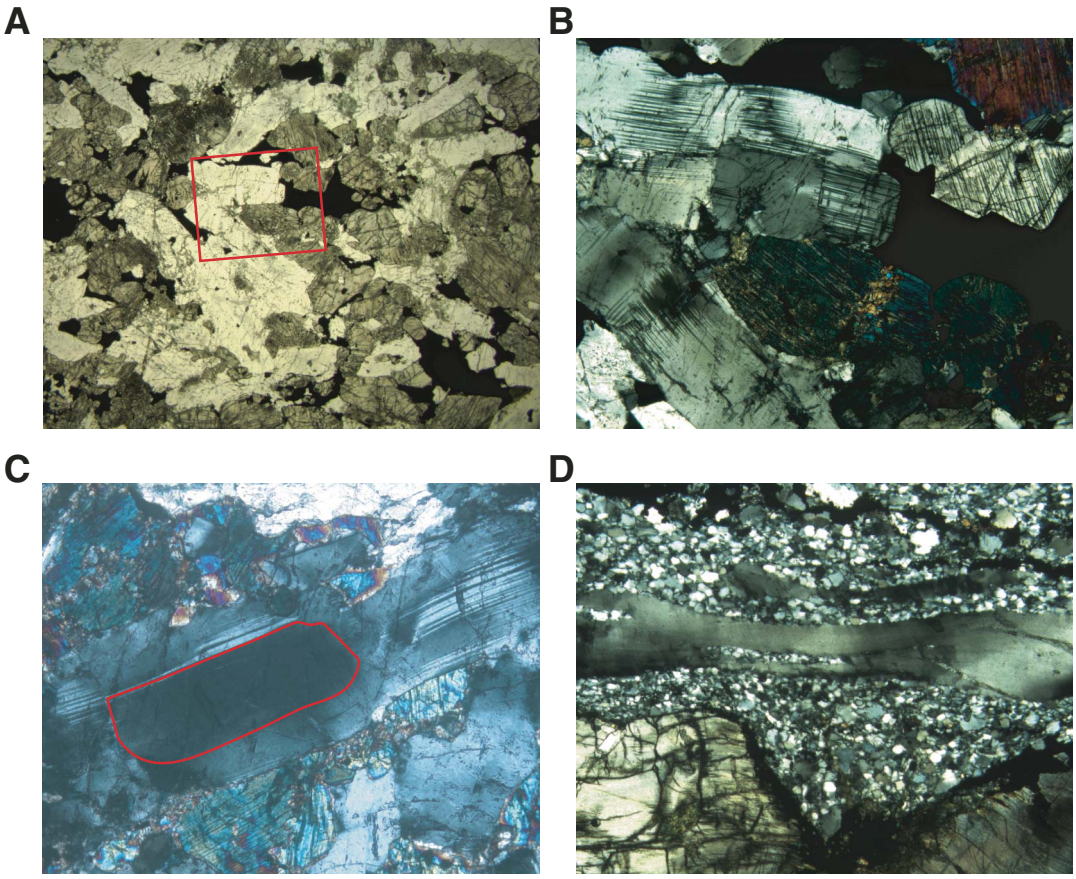

Figure F12 (continued). E, F. Sample 209-1270B-4M-1, 108–111 cm. (E) A stretched orthopyroxene grain is outlined in red. It sits in a matrix of plagioclase neoblasts and has a neoblast of orthopyroxene in the middle of the grain where it has failed. The yellow box shows the location of a detailed view of the central boudinaged part of this grain (XPL: blue filter; FOV = 11 mm; image 1270B_037). (F) Detail of a boudinaged orthopyroxene crystal with neoblasts of orthopyroxene and plagioclase (XPL: blue filter; FOV = 2.75 mm; image 1270B_038).

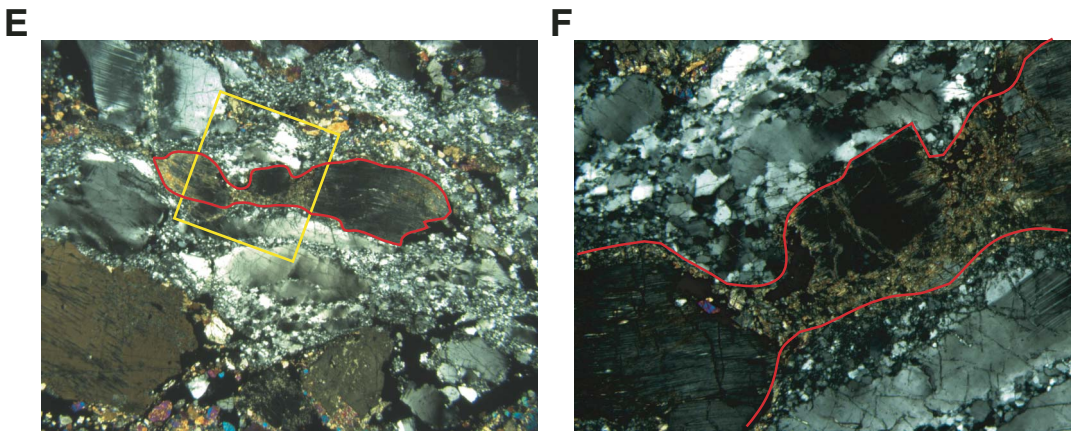

Figure F13. Photomicrograph showing a large crystal of clinopyroxene with inclusions of euhedral oxide crystals. Below this crystal, deformed clinopyroxene and abundant neoblasts of plagioclase, clinopyroxene, and oxides(?) are visible (Sample **209-1270B-4M-1, 108–111 cm**) (cross-polarized light: blue filter; field of view = 11 mm; image 1270B_039).

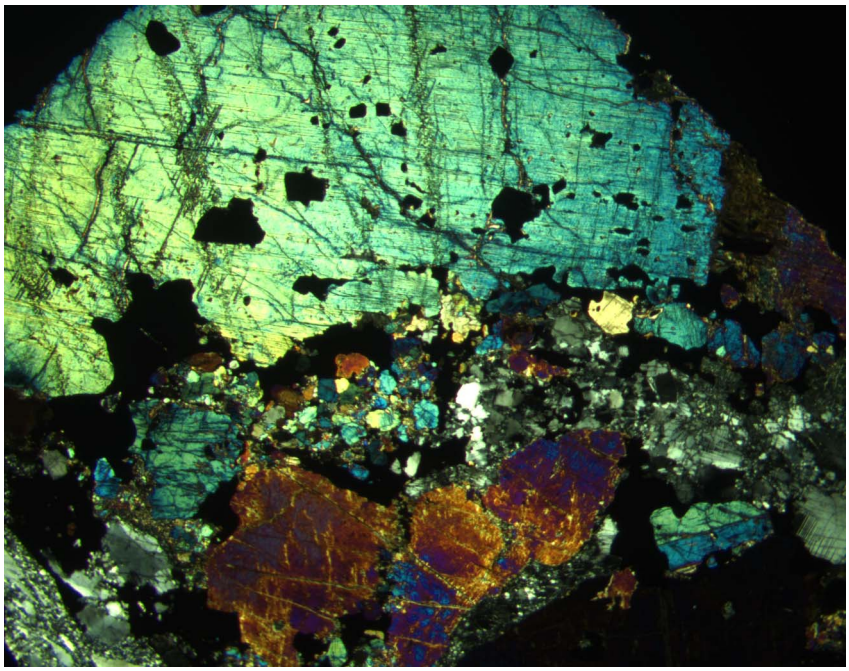

Figure F14. Photomicrograph showing a single subhedral, unstrained plagioclase crystal preserved in an oxide-rich part of an otherwise strongly deformed oxide gabbronorite (Sample **209-1270B-1R-1, 90–93 cm**) (cross-polarized light: blue filter; field of view = 5.5 mm; image 1270B_010).

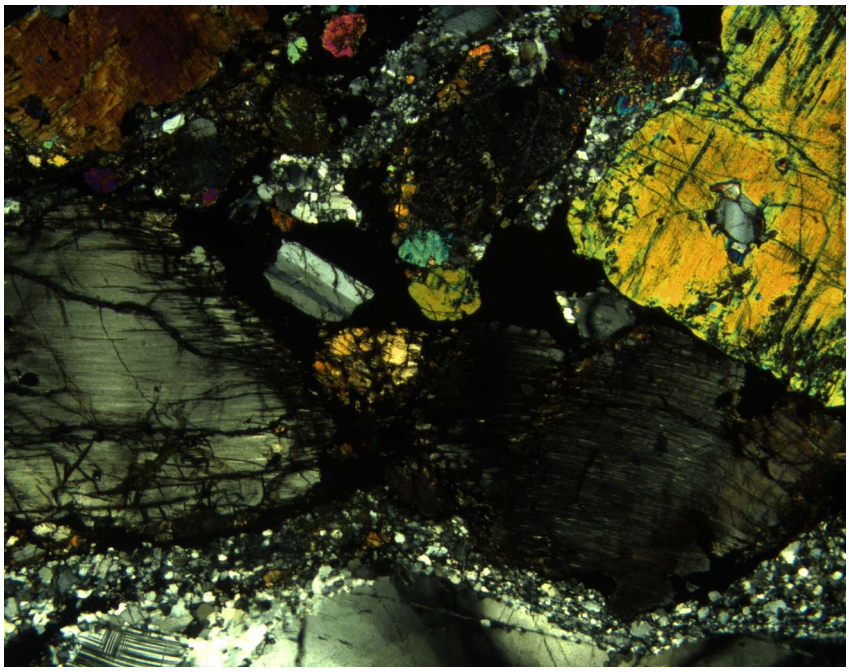

Figure F15. Photomicrograph showing that the ophitic nature of this clinopyroxene crystal (blue) is still clear despite the strain the sample has experienced. Note that the plagioclase included in the clinopyroxene is also only slightly strained in a sample that is otherwise similar to Figure **F12D,** p. 62, and **F12E** and **F12F,** p. 63 (Sample **209-1270B-9R-1, 60–62 cm**) (cross-polarized light: blue filter; field of view = 5.5 mm; image 1270B_011).

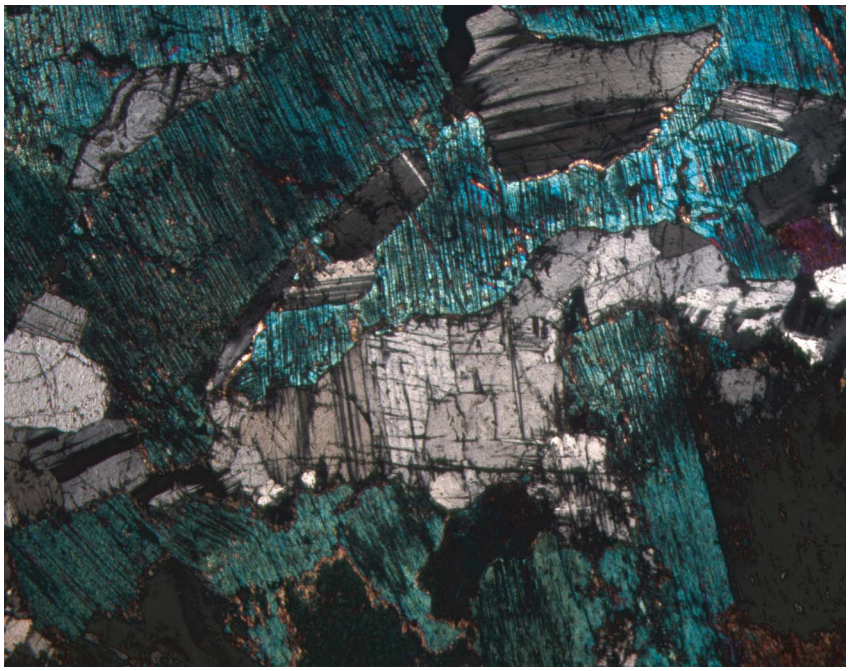

Figure F16. Lithostratigraphic summary for Hole 1270C. TD = total depth.

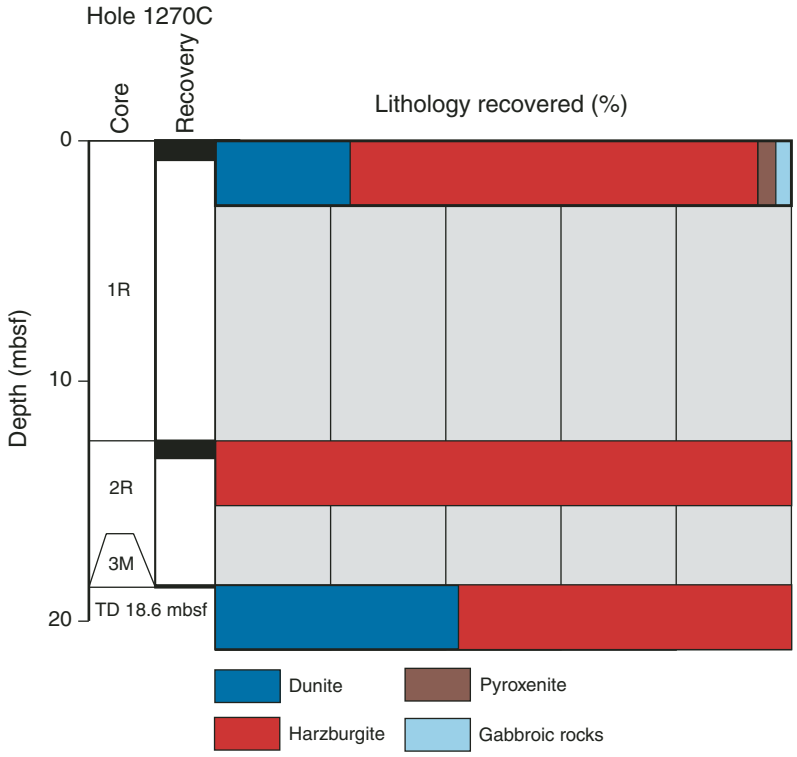

Figure F17. Photomicrograph showing altered anhedral orthopyroxenes with gently curved grain boundaries in an altered olivine matrix. A small black grain in the upper middle of the image is spinel (Sample **209-1270C-1R-1, 36–39 cm**) (cross-polarized light: blue filter; field of view = 5.5 mm; image 1270C_001).

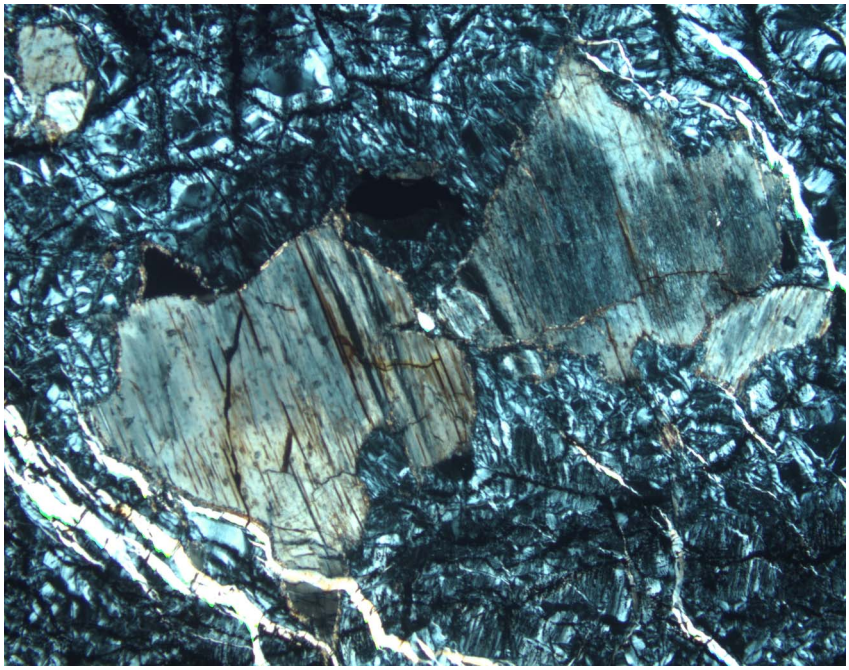

Figure F18. Close-up view of variation of altered orthopyroxene porphyroclasts (in light gray) in an altered harzburgite. Note that modal orthopyroxene is highest between 73 and 76 cm (interval 209-1270C-1R-1 [Piece 11, 69–81 cm]). Figure F17, p. 68, shows an image from a thin section at 72–75 cm.

Figure F19. Photomicrograph showing vermicular spinel enclosed in altered orthopyroxene crystals (pale brown) (Sample **209-1270C-1R-1, 72–75 cm**) (cross-polarized light: blue filter; field of view = 1.4 mm; image 1270C_016).

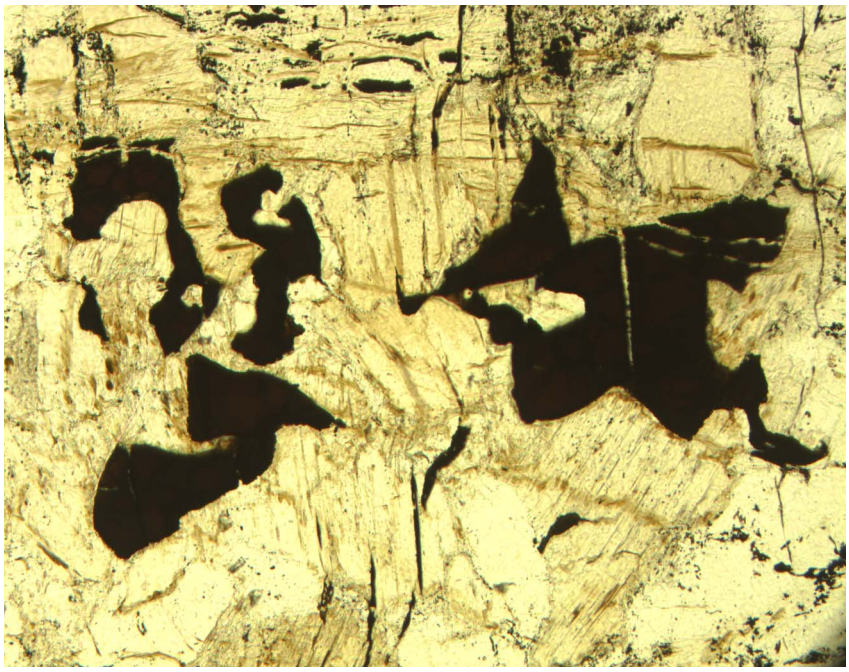

Figure F20. Photomicrograph showing gabbroic intrusion with mylonitic texture. Whitish and brownish bands lying near the center contain plagioclase and brown amphibole, respectively (Sample **209-1270C-1R-1, 83–85 cm**) (plane-polarized light: blue filter; field of view = 5.5 mm; image 1270C_021).

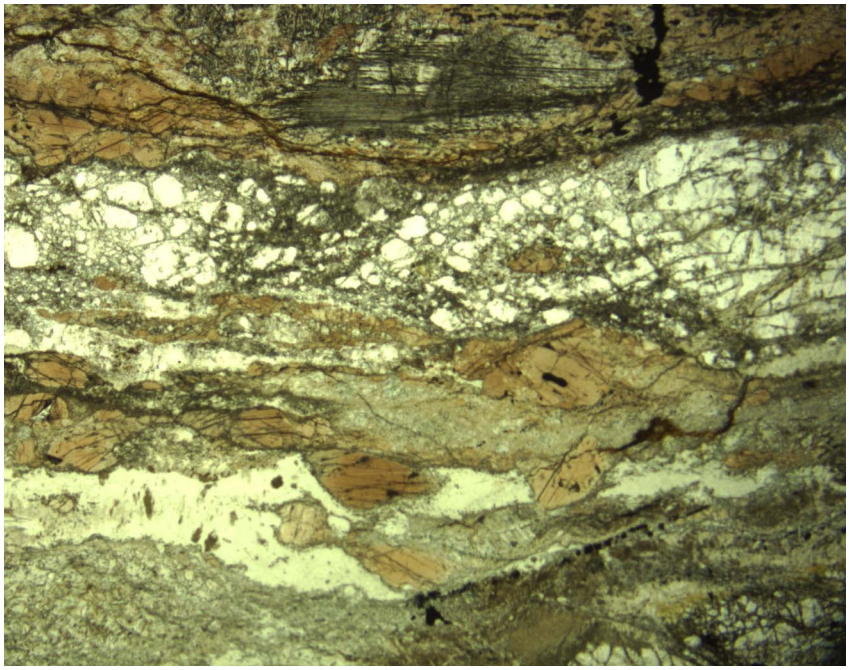

Figure F21. Photomicrograph showing elongated dunite lens with mylonitic texture preserving fresh olivine and orthopyroxene (Sample 209-1270C-1R-1, 83–85 cm) (cross-polarized light: blue filter; field of view = 5.5 mm; image 1270C_017).

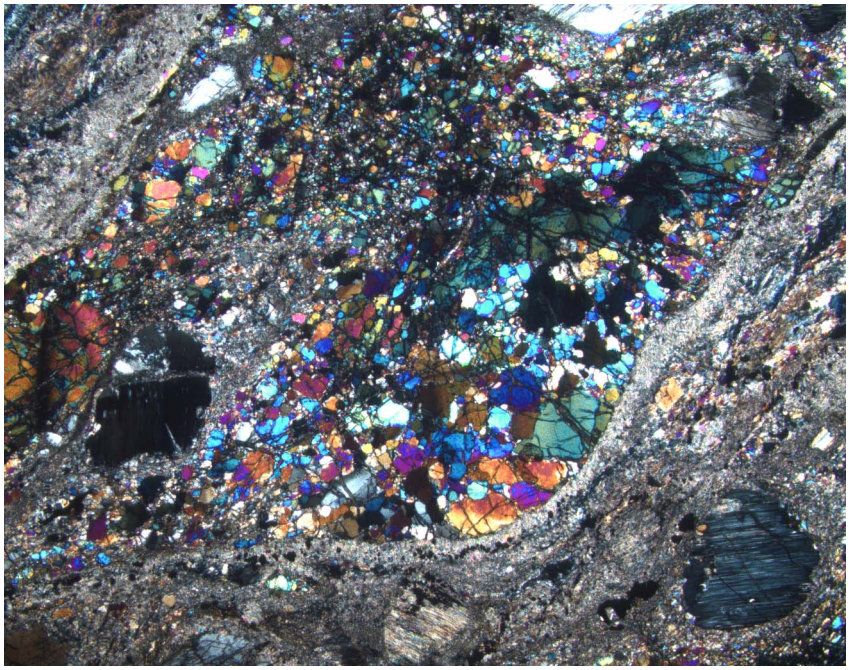

Figure F22. Lithostratigraphic summary for Hole 1270D. Natural gamma radiation measurements are shown in the right column. TD = total depth.

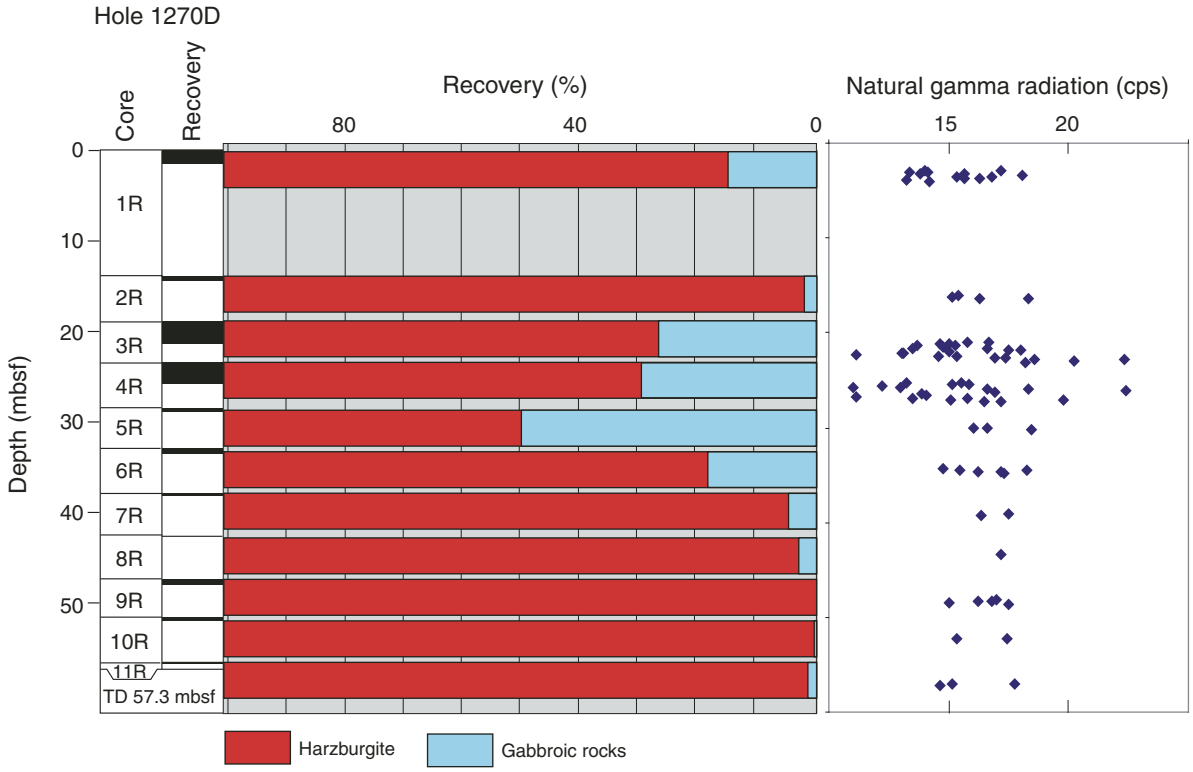

Figure F23. Close-up photograph of harzburgite with a net of anastomosing gabbroic intrusion (archive-half cut face and back) (interval 209-1270D-3R-2, 32–65 cm).

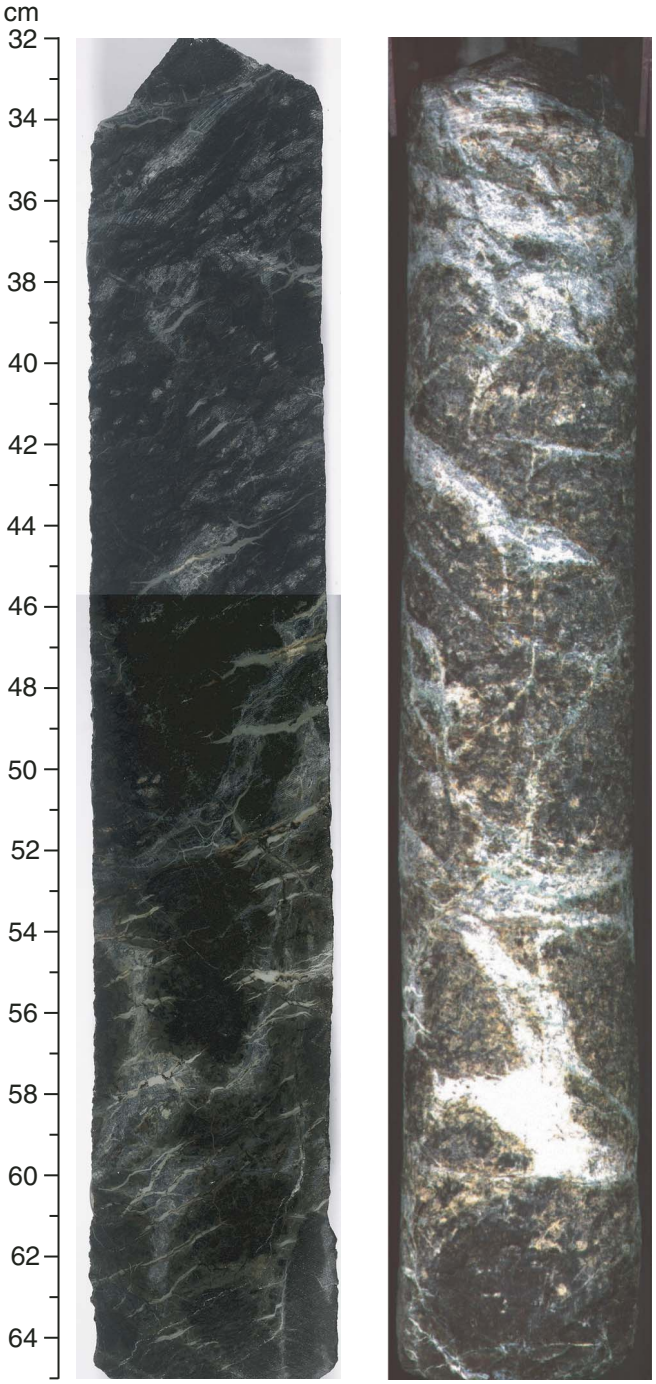

Figure F24. Photomicrographs showing discontinuous, aligned clinopyroxene crystals (altered) crosscutting the harzburgite matrix (Sample 209-1270D-3R-1 [Piece 11, 94–97 cm]) (cross-polarized light: blue filter). **A.** Field of view = 1.4 mm; image 1270D_007. **B.** General outline of the clinopyroxene crystals (field of view = 1.4 mm; image 1270D_008).

A

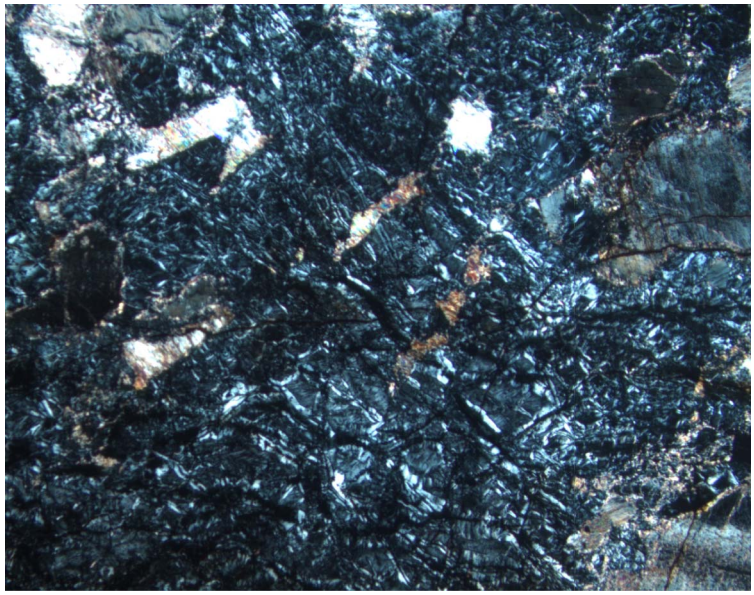

B

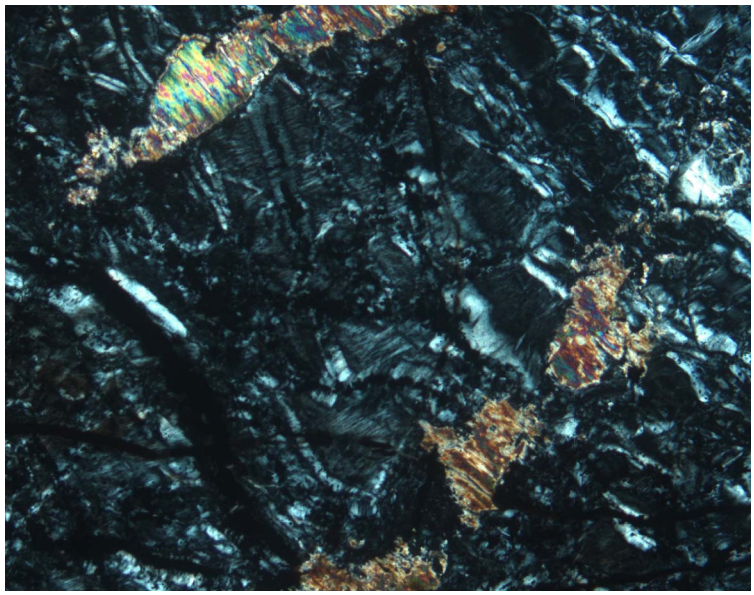

Figure F25. Photomicrograph showing zircon and other accessory minerals (epidote? apatite?) enclosed in the outer margin of a magmatic amphibole crystal (Sample **209-1270D-4R-1 [Piece 7, 33–37 cm]**) (cross-polarized light: blue filter; field of view = 0.7 mm; image 1270D_006).

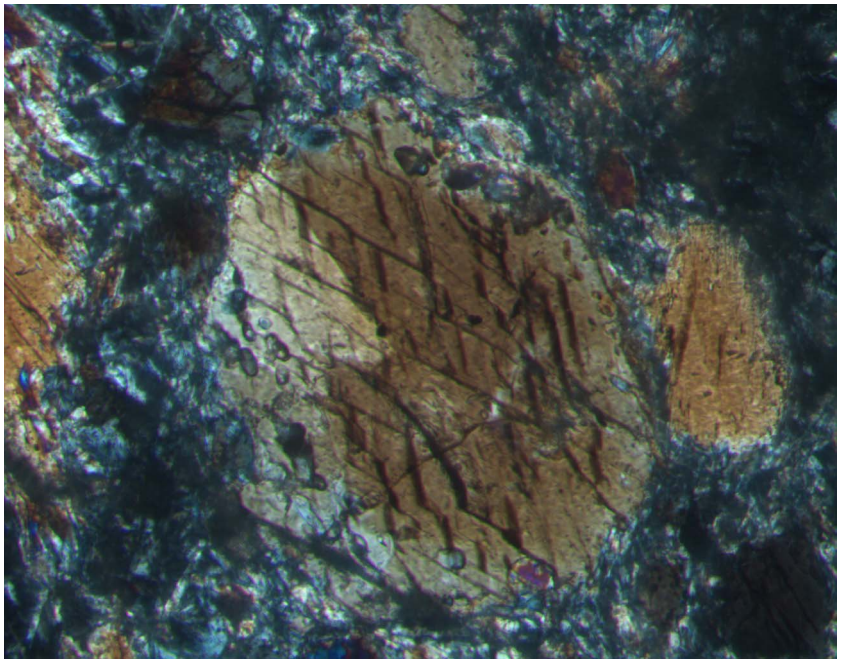

Figure F26. Photomicrographs showing zircon crystals in amphibole layer (Sample 209-1270D-4R-1 [Piece 7, 33–37 cm]) (field of view = 0.7 mm). **A.** Plane-polarized light: blue filter; image 1270D_002. **B.** Cross-polarized light: blue filter; image 1270D_003.

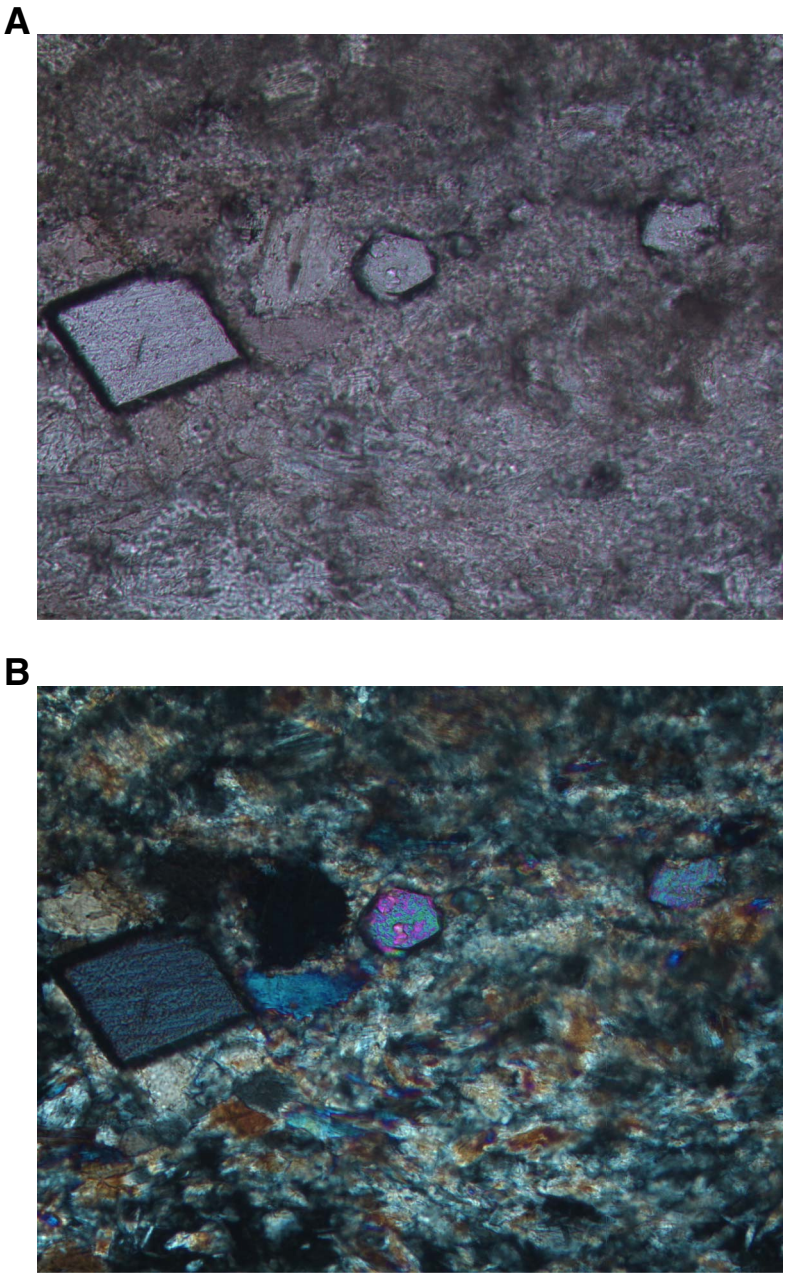

Figure F27. A. Photograph of hand specimen of a typical example of completely serpentinized harzburgite (interval 209-1270A-1R-1, 104–111 cm). **B.** XRD spectrum of the sample shown in A indicates that this rock consists almost entirely of serpentine and magnetite.

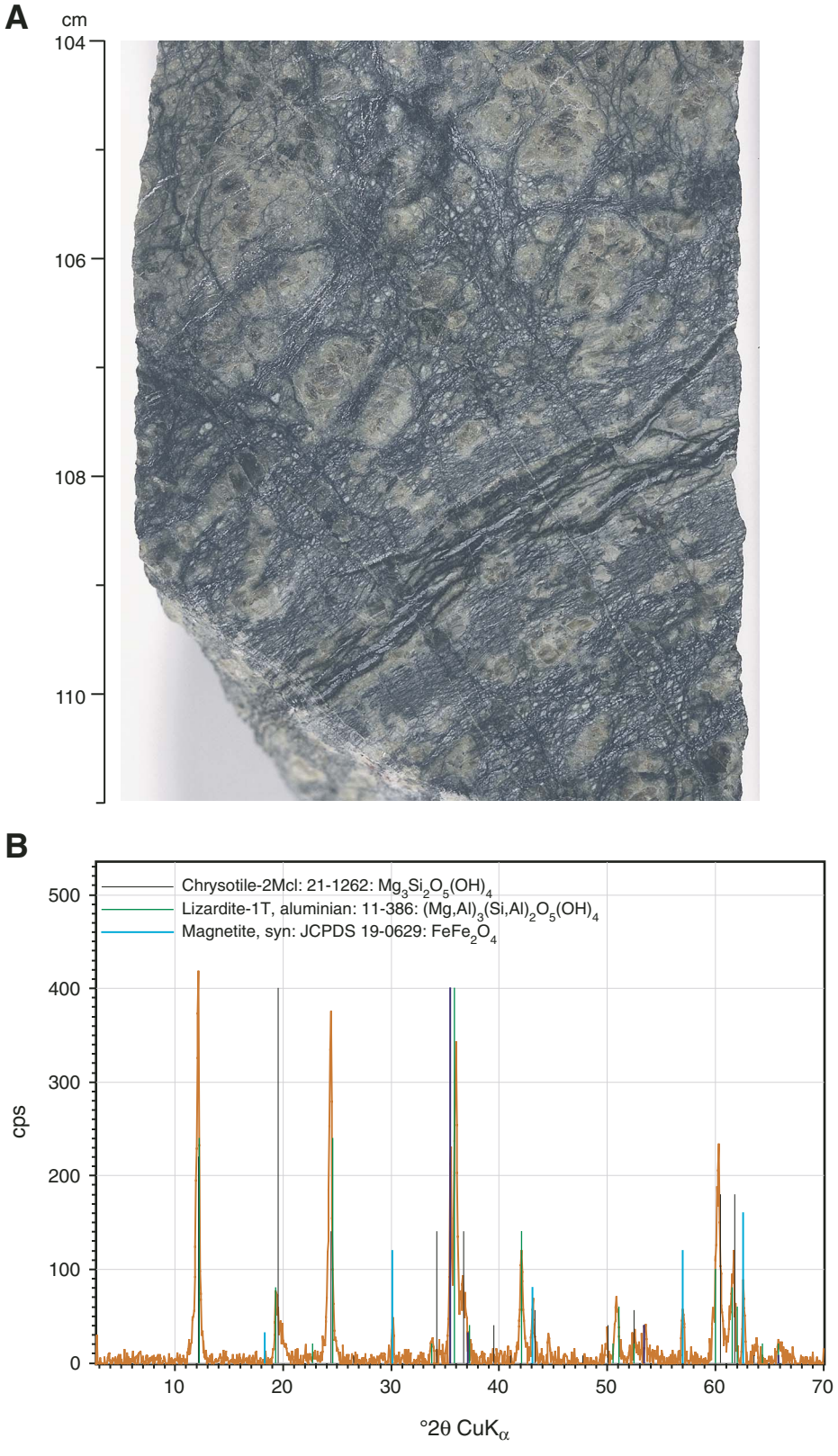

Figure F28. The serpentinized harzburgite in Hole 1270A locally contains deformed mylonitic zones. **A.** In this photograph of a hand specimen, the light gray domain on the right shows a strong foliation (interval 209-1270A-1R-1, 34–39 cm). **B–D.** Photomicrographs showing features from the same interval as that shown in A (Sample **209-1270A-1R-1, 35–38 cm**). (B) The deformed domain locally contains serpentine with an interpenetrating texture that may be antigorite (plane-polarized light: blue filter; field of view [FOV] = 0.7 mm; image 1270A_004). (C) A late chrysotile vein is deformed and transposed (arrow) into the foliation of the deformed domain of this serpentinite (cross-polarized light: blue + light gray filters; FOV = 1.4 mm; image 1270A_010). (D) Pyrite is a common phase in the serpentine mylonite and appears to replace spinel along with magnetite (mt = magnetite, py = pyrite, sp = spinel) (reflected light, FOV = 1.4 mm; image 1270A_005).

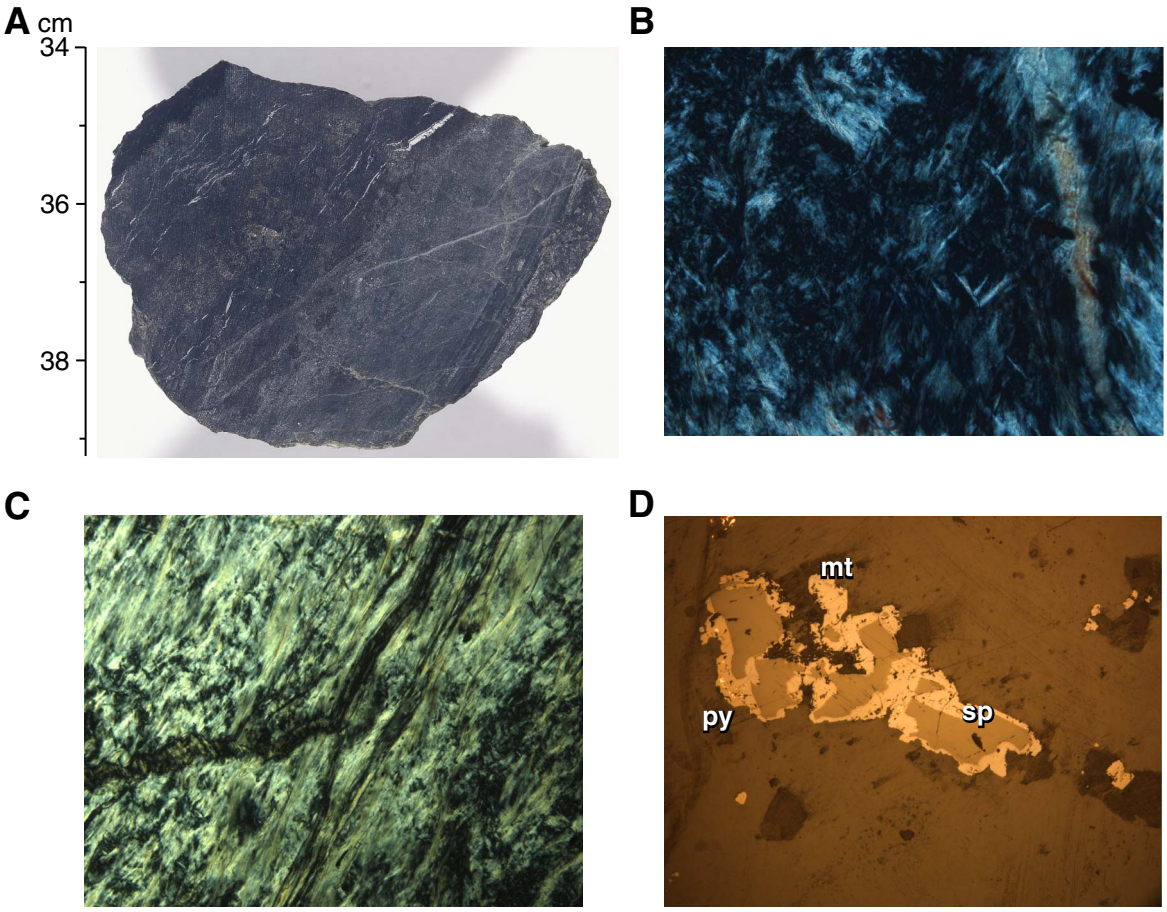

Figure F29. Veins in Hole 1270A consist predominantly of serpentine (78%) followed by talc (19%) and magnetite (2.8%). Chlorite is rare in veins from Hole 1270A. Details of the vein statistics are presented in Table T3, p. 176. This pie chart has been generated using volume normalized data.

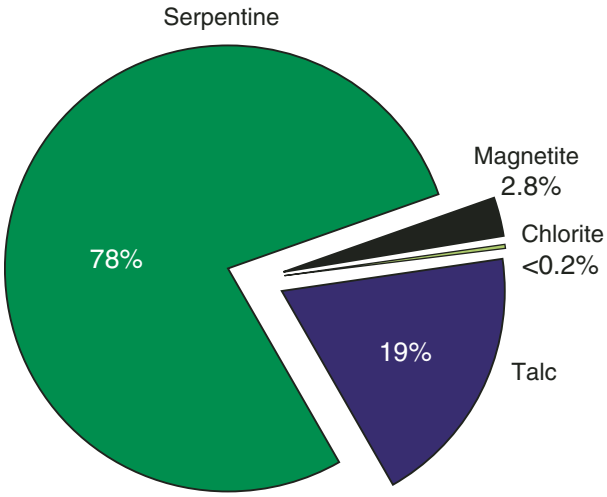

Figure F30. Downhole variability of alteration intensity based on macroscopic observations in Hole 1270B, which consists predominantly of slightly altered gabbro. TD = total depth.

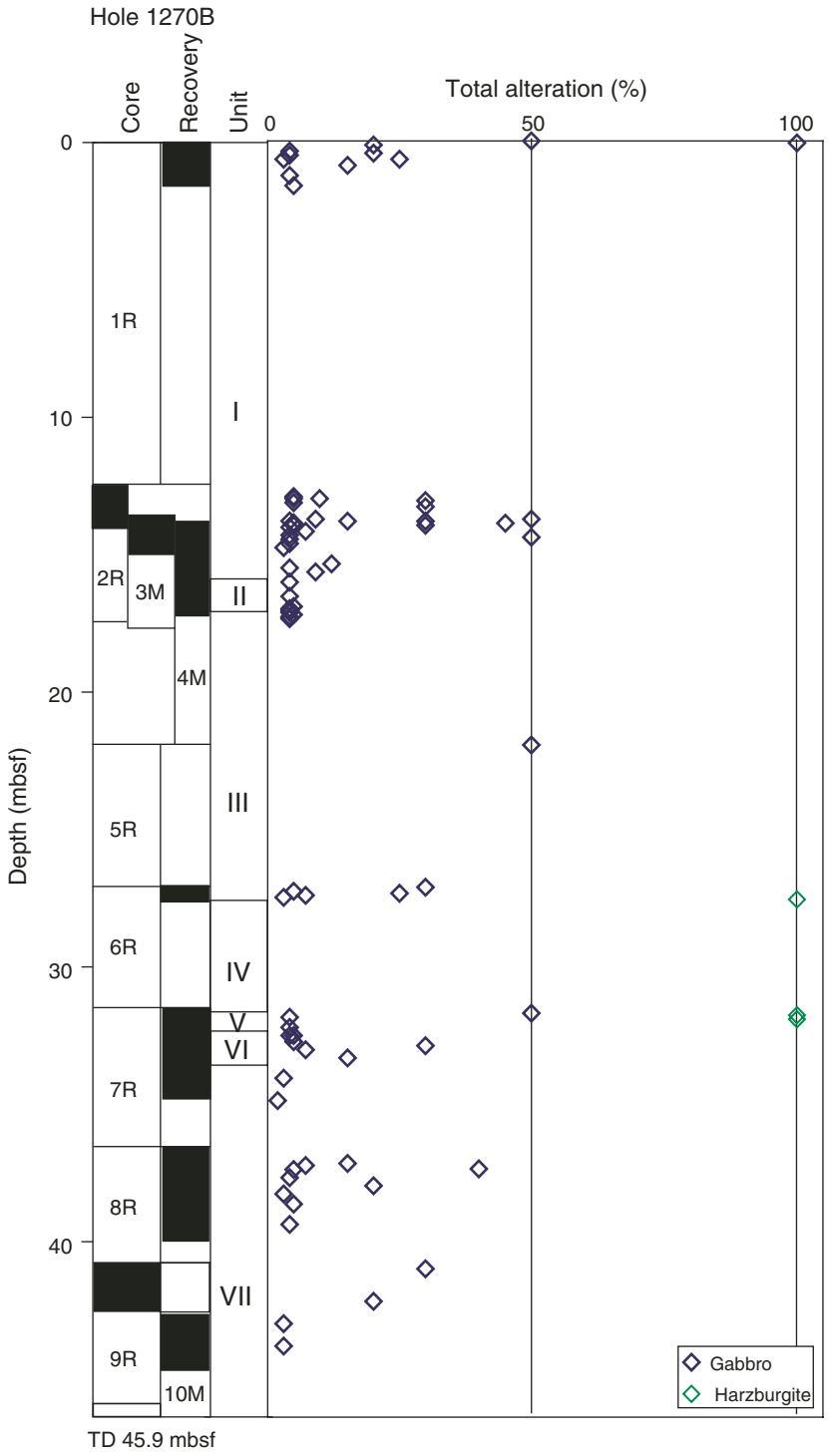

Figure F31. Photomicrograph showing alteration of the gabbro drilled in Hole 1270B is dominated by chlorite (chl)–amphibole (amp) assemblages that form at the contacts of pyroxene (px) and plagioclase crystals (Sample **209-1270B-7R-1, 47–49 cm**) (plane-polarized light: blue filter; field of view = 0.7 mm; image 1270B_004).

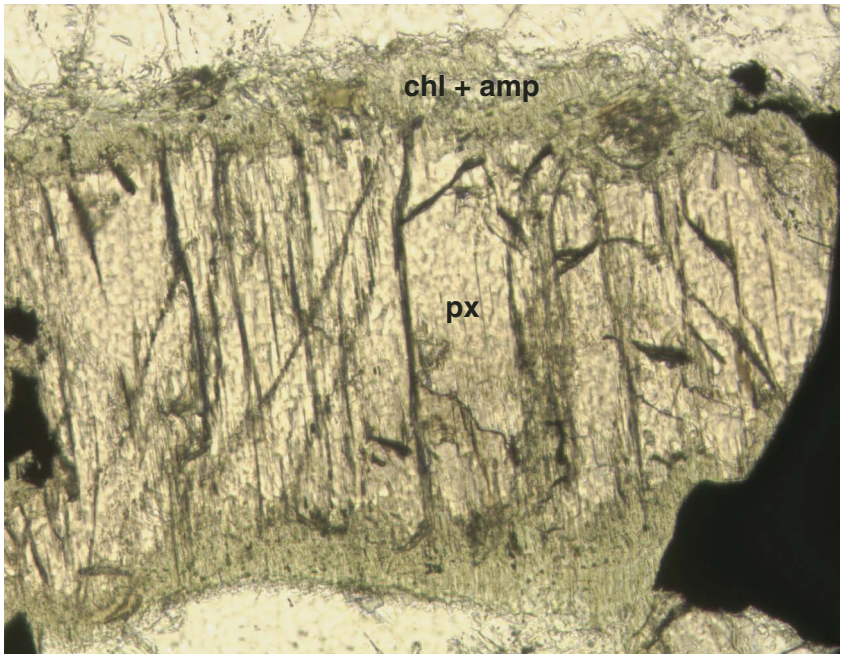

Figure F32. Photomicrograph showing that locally, pyroxene (px) is replaced by aggregates of brown amphibole. Here, brown amphibole formed on the margins and along the cleavage of a pyroxene crystal (arrow) (Sample **209-1270B-10M-1, 21–23 cm**) (plane-polarized light: blue + light gray filters; field of view = 0.7 mm; image 1270B_028).

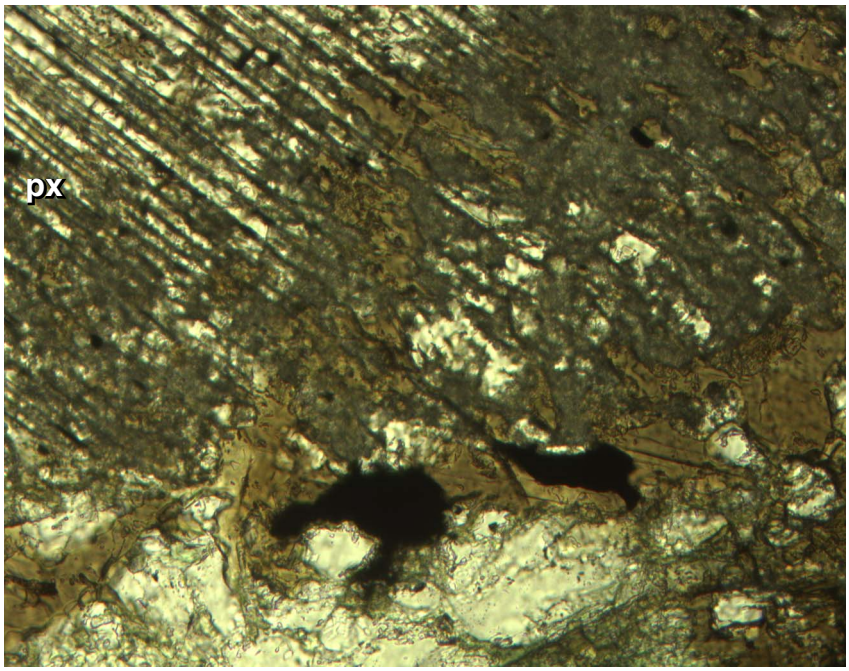

Figure F33. Photomicrograph showing a band of brown amphibole and chlorite crosscutting this gabbro and may represent a magmatic dikelet or a metamorphic vein (Sample **209-1270B-7R-1, 110–112 cm**) (plane-polarized light: blue filter; field of view = 1.4 mm; image 1270B_002).

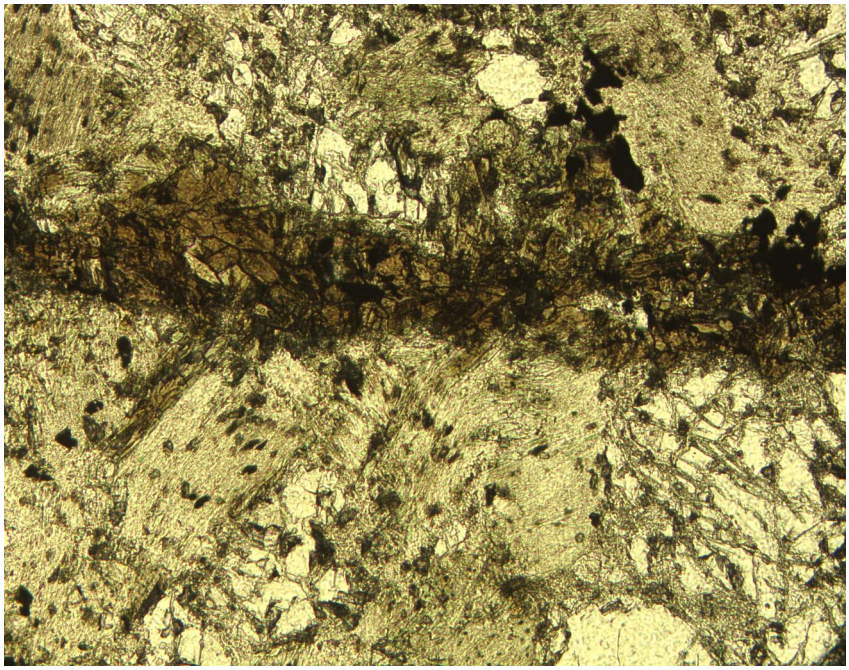

Figure F34. A. Photograph of hand specimen of a rare example of an intensely deformed interval in Hole 1270A (interval 209-1270B-8R-1, 21–29 cm). **B, C.** Photomicrographs showing features from the same interval as that in A (Sample **209-1270B-8R-1, 26–29 cm**). (B) Bands with intense talc replacement are common (px = pyroxene) (cross-polarized light: blue + light gray filter; field of view = 1.4 mm; image 1270B_27). (C) In the same thin section there are bands of fresh olivine (right side of image) juxtaposed with bands consisting of talc, chlorite, and amphibole with relict pyroxene and plagioclase (left side of image) (plane-polarized light: blue + dark gray filters; field of view = 2.75 mm; image 1260B_031).

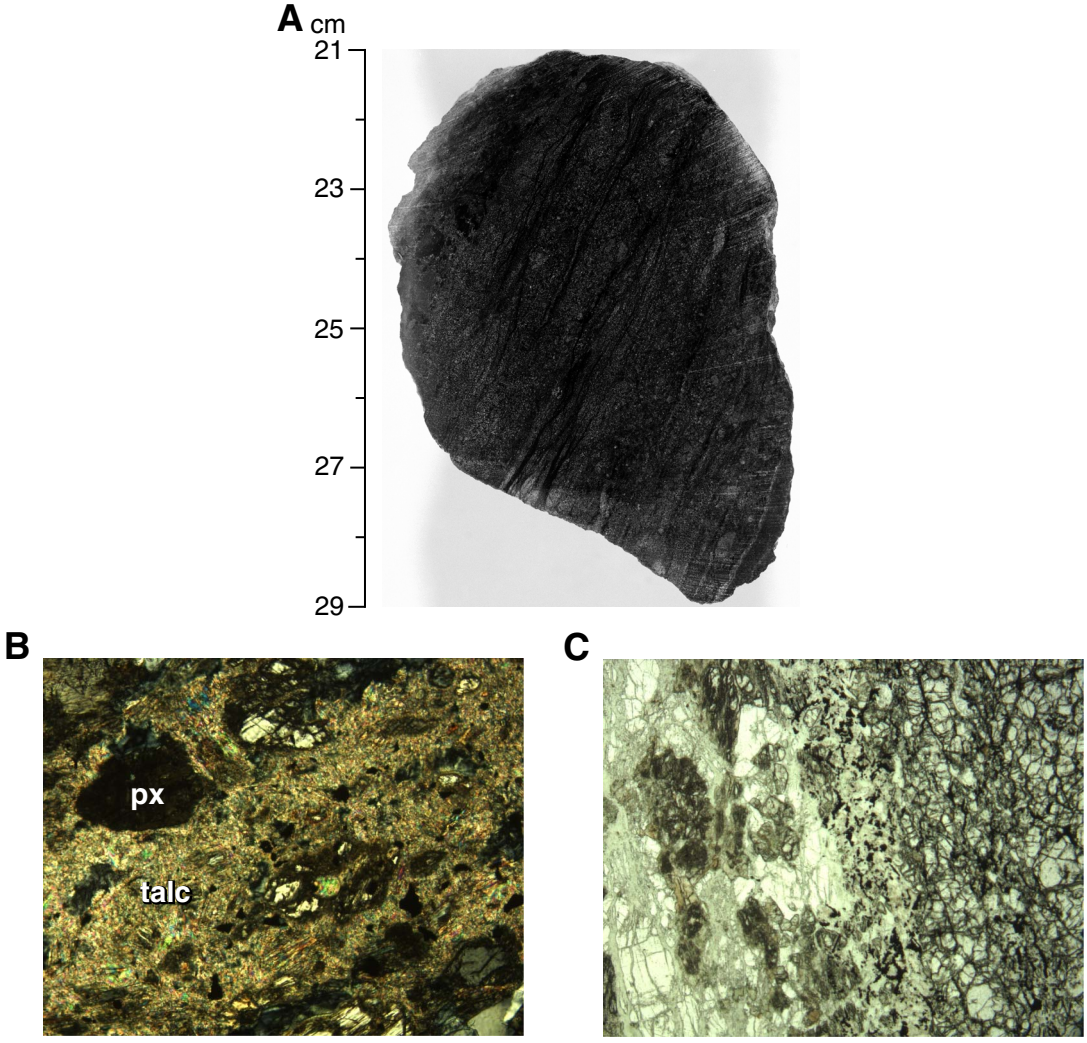

Figure F35. Photograph of hand specimen of microgabbro that contains a talc-rich domain on its right margin. This talc-rich patch has a ~1-cm-wide halo that may represent an alteration front (interval 209-1270B-7R-1, 113–118 cm).

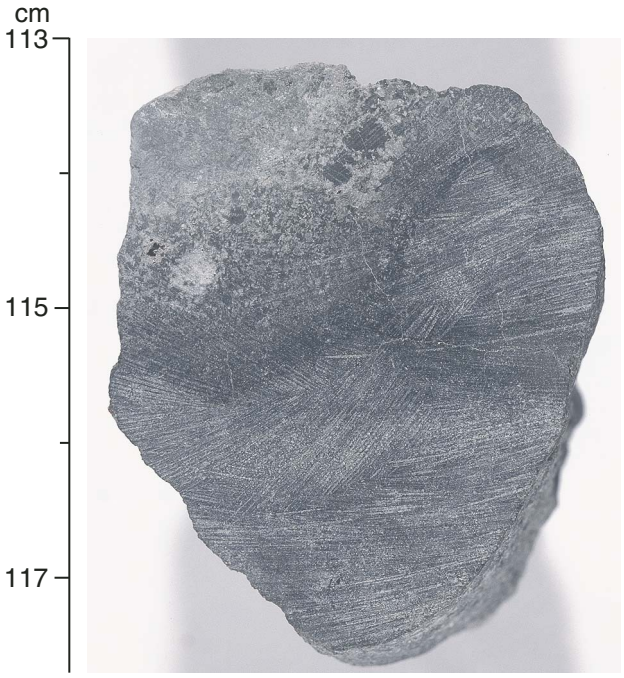

Figure F36. Veins in Hole 1270B consist of talc (52%), chlorite (20%), serpentine (17%), amphibole (10%), and rare oxides and sulfides. Details of the vein statistics are presented in Table **T3,** p. 176. This pie chart has been generated using volume normalized data.

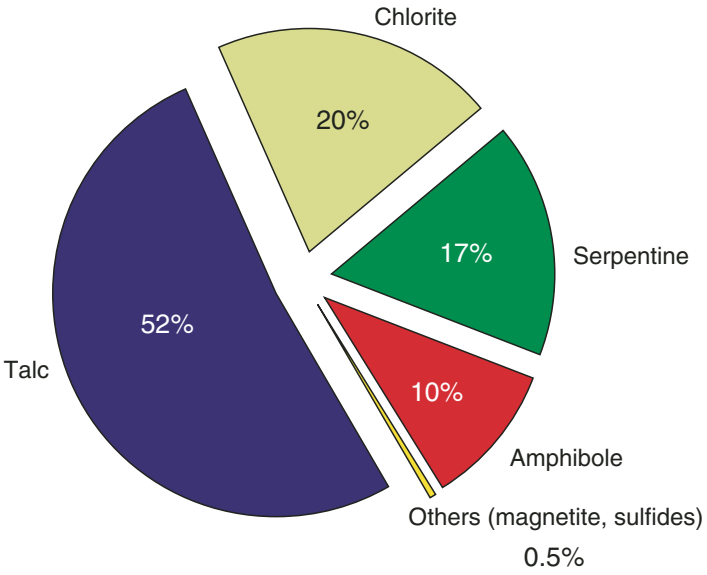

Figure F37. Photograph of a chalcopyrite-rich talc vein (arrow) (interval 209-1270B-7R-1, 50–58 cm).

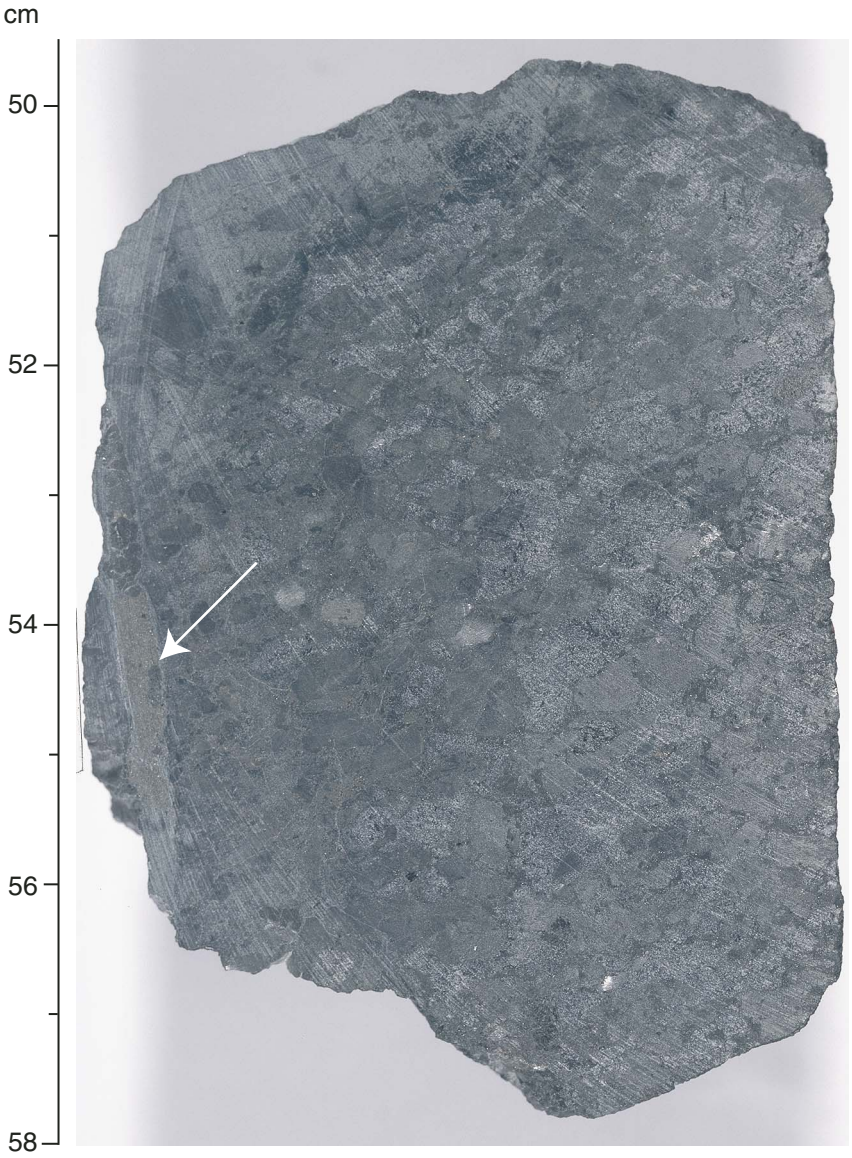

Figure F38. Locally, fresh pyroxene and olivine are preserved in serpentinized harzburgite recovered from Hole 1270C. **A.** Photograph of hand specimen of serpentinized harzburgite. Some of the orthopyroxene crystals have an orange-brown halo indicative of alteration under low-temperature conditions (seafloor weathering). Adjacent to some of these orthopyroxenes there are minor relics of fresh olivine (interval 209-1270C-1R-1, 71–80 cm). **B, C.** Photomicrographs showing features from the interval in A (Sample 209-1270C-1R-1, 72–75 cm). (B) Orthopyroxene has been partially replaced by talc (tc) prior to serpentinization. Some of the olivine adjacent to the pyroxene is preserved, indicating that serpentinization did not go to completion. Dark brown clays + Fe oxyhyroxides (arrow) partially replaced olivine during seafloor weathering (plane-polarized light: blue + dark gray filters; field of view = 1.4 mm; image 1270C_22). (C) Serpentine (arrow) formed at the expense of olivine. The partially talc-altered pyroxene (px) has not been affected by serpentinization (cross-polarized light: blue filter; field of view = 1.4 mm; image 1270C_23).

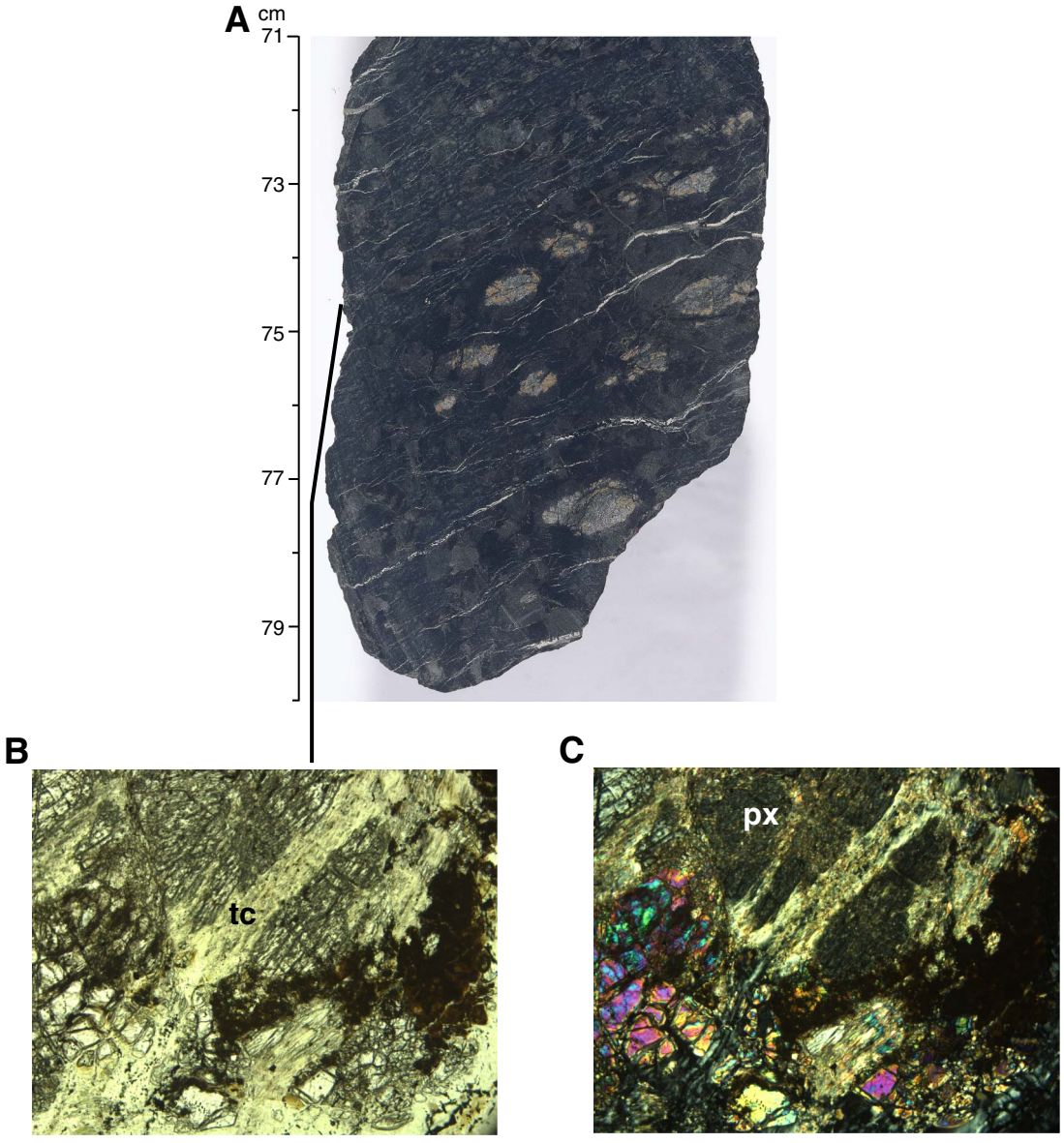

Figure F39. Macroscopic and microscopic textures of deformed serpentinized harzburgite hosting gabbroic schlieren (interval 209-1270C-1R-1, 84–87 cm). **A.** Close-up photograph of serpentinized harzburgite with deformed gabbroic veins or dikes. The veins contain clasts of fresh harzburgite (arrow) that have been incorporated into the deformed zone. **B–E.** Photomicrographs showing features from the same interval as that in A (Sample **209-1270C-1R-1, 83–85 cm**). (B) In thin section, the gabbroic veins are anastomosing talc-rich shear bands that probably formed during high-temperature deformation. Brown amphibole (b) replaces pyroxene neoblasts and porphyroclasts in the shear band. Folded veins of chrysotile (c) also occur in the shear band (dark vein, lower right) (plane-polarized light: blue + light gray filters; field of view = 5.5 mm; image 1270C_008). (C) Boudins of fresh harzburgite are cut by smaller shear bands containing talc and brown amphibole (cross-polarized light: blue + light gray filters; field of view = 5.5 mm; image 1270C_007). (Continued on next page).

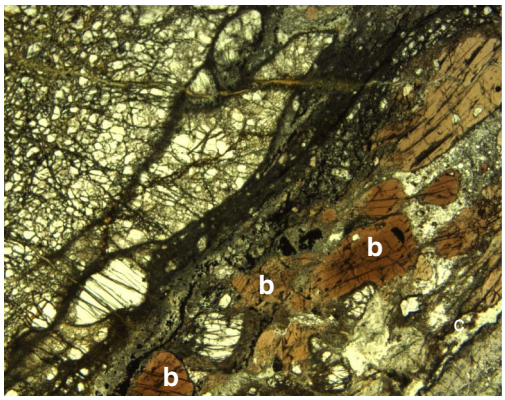

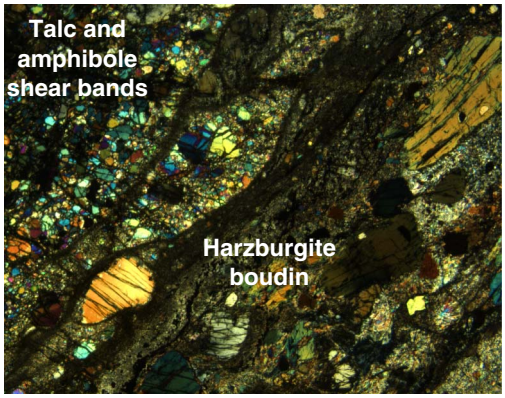

Figure F39 (continued). (D) A large clinopyroxene crystal in a boudin within sheared peridotite is replaced by pseudomorphic brown amphibole close to a sheared gabbroic band. Relics of clinopyroxene are preserved within amphibole and have continuous extinction (plane-polarized light: blue + dark gray filters; field of view = 2.75 mm; image 1270C_004). (E) An orthopyroxene porphyroclast in a gabbroic shear band is partly replaced by brown amphibole. Brown amphibole also replaces smaller pyroxene neoblasts along the shear band. Note that amphibole is absent within the boudins of fresher peridotite located above and below the shear band (plane-polarized light: blue + dark gray filters; field of view = 2.75 mm; image 1270C_003).

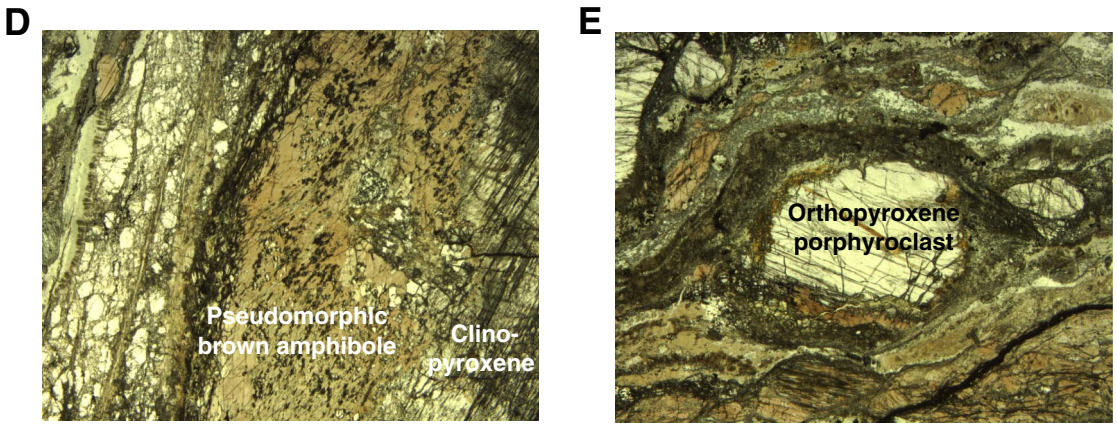

Figure F40. Veins in Hole 1270C consist dominantly of serpentine (86.3%), iron oxide (12.5%), and minor talc (1.1%). Rare carbonate veins are also present. Details of the vein statistics are presented in Table T3, p. 176. This pie chart has been generated using volume normalized data.

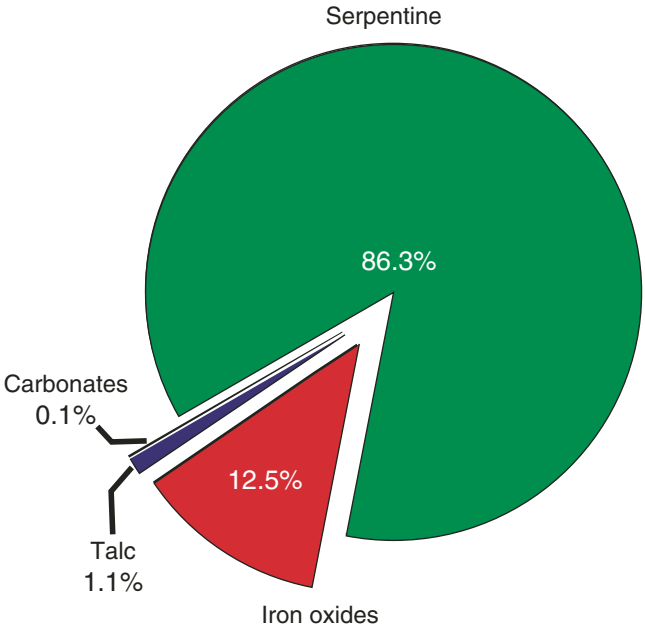

Figure F41. Photomicrograph showing a rare carbonate vein crosscuts the earlier serpentine veins (Sample 209-1270C-1R-1, 83–85 cm) (cross-polarized light: blue + light gray filters; field of view = 1.4 mm; image 1270C_006).

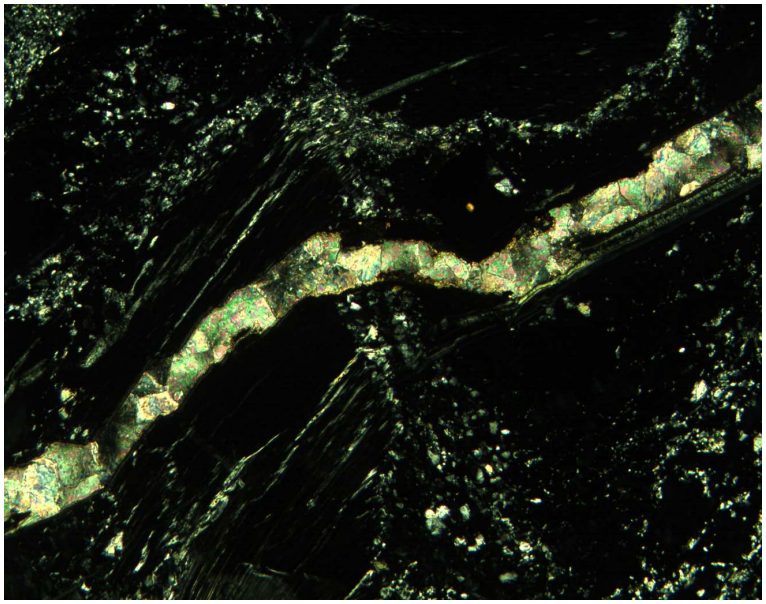

Figure F42. Downhole variability of alteration intensity in Hole 1270C. TD = total depth.

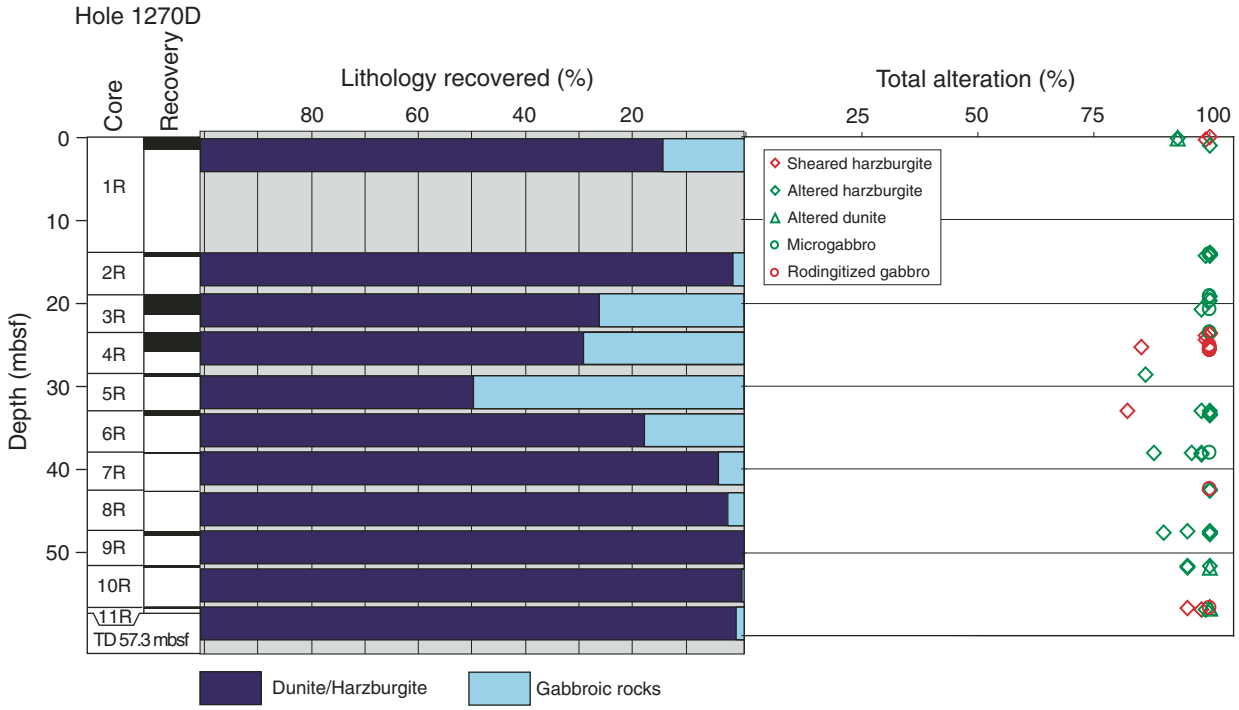

Figure F43. Close-up photograph of clay and iron oxyhydroxide weathering of harzburgite generates a typical orange-brown coloration. This style of alteration is present in most cores recovered from Hole 1270D but is most prominently developed in Cores 209-1270D-1R to 4R. The light gray schlieren in this hand specimen are deformed gabbroic intrusions (interval 209-1270D-1R-1, 108–114 cm).

Figure F44. Close-up photograph of completely serpentinized harzburgite (dark gray) forming boudins within the deformed gabbroic intrusion (light gray) (interval 209-1270D-2R-1, 30–36 cm).

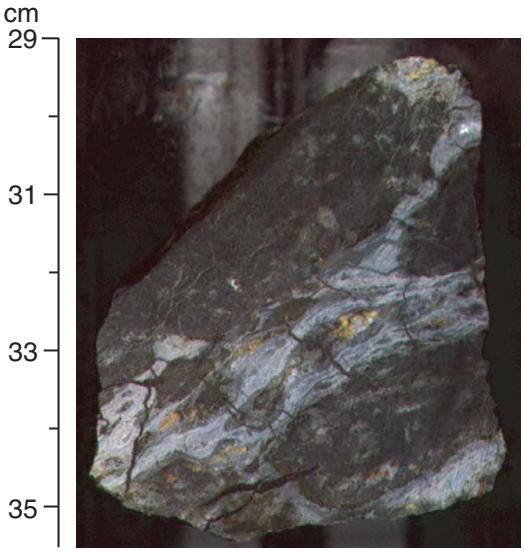

Figure F45. Veins in Hole 1270D consist dominantly of serpentine (83.5%), iron oxide (9.7%), and minor talc (5.4%). Rare carbonate veins are also present. Details of the vein statistics are presented in Table T3, p. 176. This pie chart has been generated using volume normalized data.

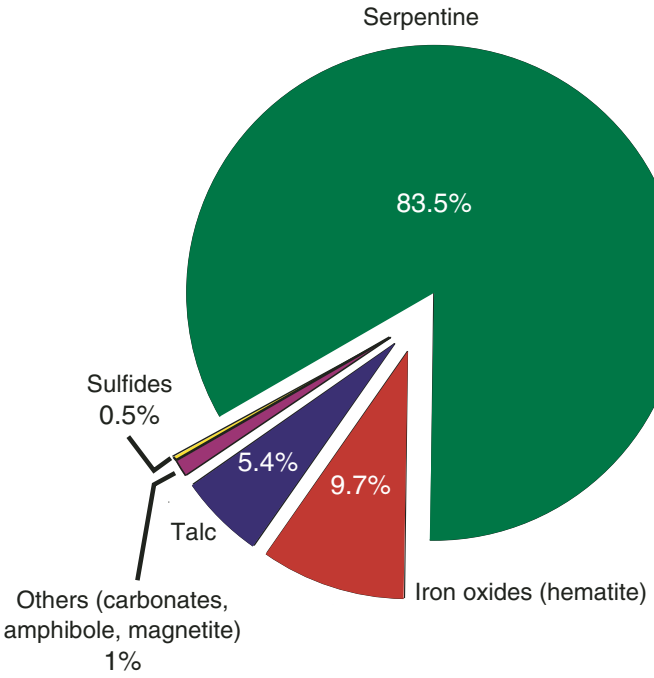

Figure F46. Close-up photograph of sigmoidal, semicontinuous, en echelon arrays of serpentine veins in serpentinized harzburgite crosscut gabbroic veins or dikes (interval 209-1270D-3R-1, 10–17 cm).

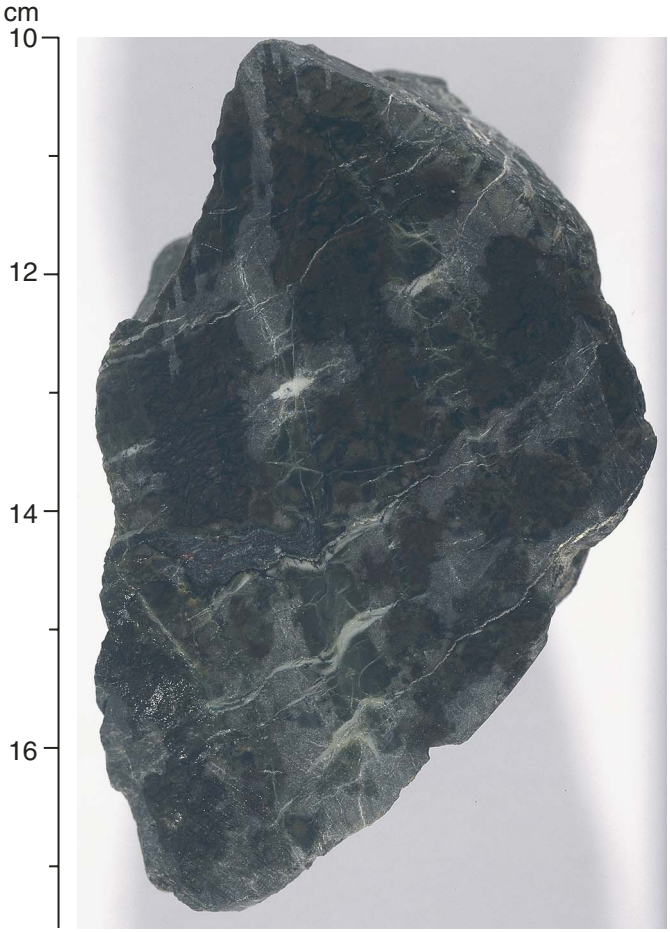

Figure F47. Photomicrographs showing three discrete serpentine vein generations (Sample 209-1270D-6R-1, 18–21 cm). **A.** Chrysotile vein (1), which crosscuts an altered and deformed gabbroic intrusion, is subsequently cut by a second generation of chrysotile veins propagating along the shear zone (2). An iron oxide vein in the top left corner is also crosscutting the gabbroic intrusion (cross-polarized light: blue filter; field of view 2.75 mm; image 1270D_016). **B.** This image shows an adjacent part of the same thin section as the one shown in A. Here, a late chrysotile vein (3) crosscuts a second generation serpentine vein (2) in the gabbroic shear zone. The iron oxide vein in the bottom right corner is the same as in A (cross-polarized light: blue + light gray filters; field of view = 1.4 mm; image 1270D_017).

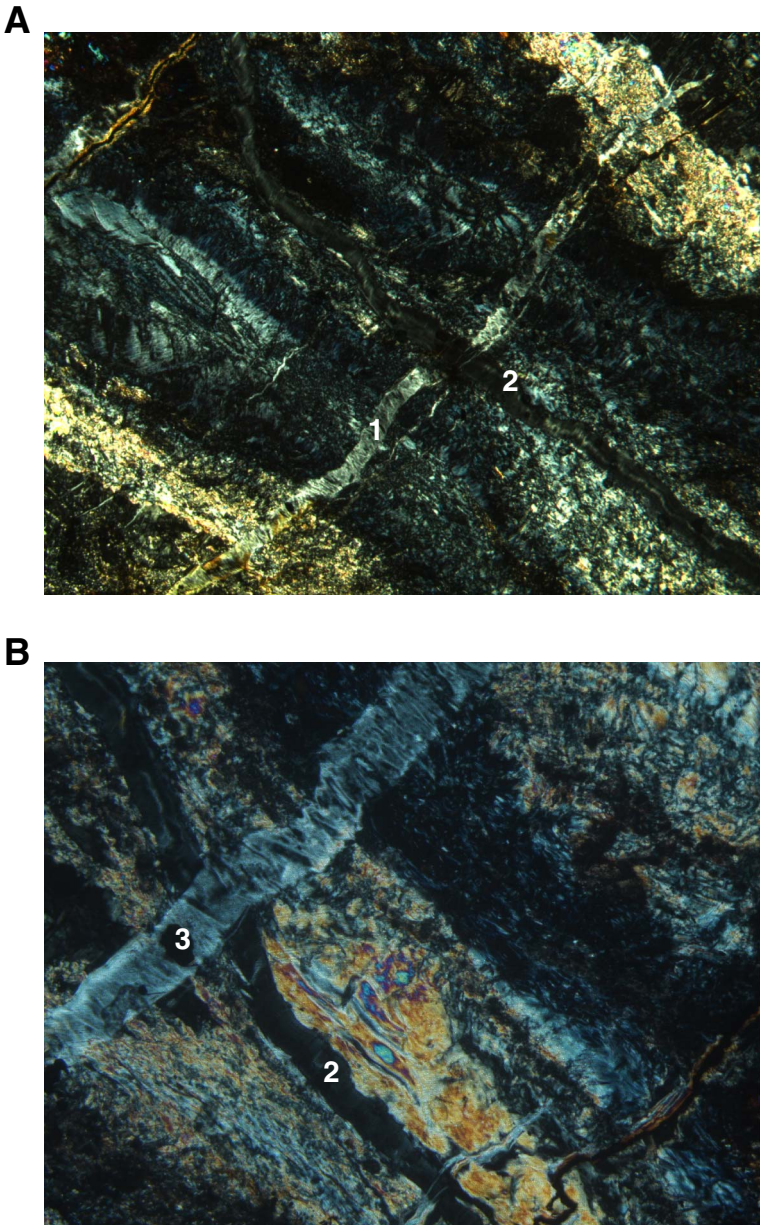

Figure F48. Photograph of aragonite veins in highly clay-altered serpentinized harzburgite. These veins crosscut earlier generations of serpentine veins (interval 209-1270D-6R-1, 41–50 cm).

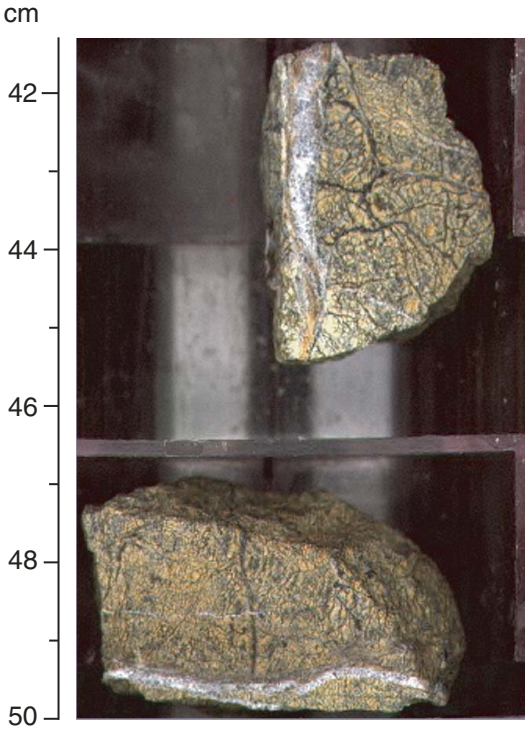

Figure F49. Photograph of serpentinized harzburgite with a blocky network of sulfide veins that have pyrite chalcopyrite rims and hematite cores (interval 209-1270D-5R-1, 5–9 cm).

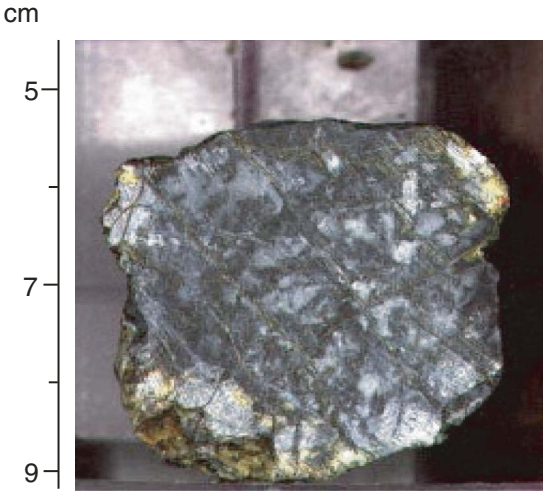

Figure F50. Paragranular serpentine veins are more abundant than transgranular serpentine veins in Holes 1270C and 1270D.

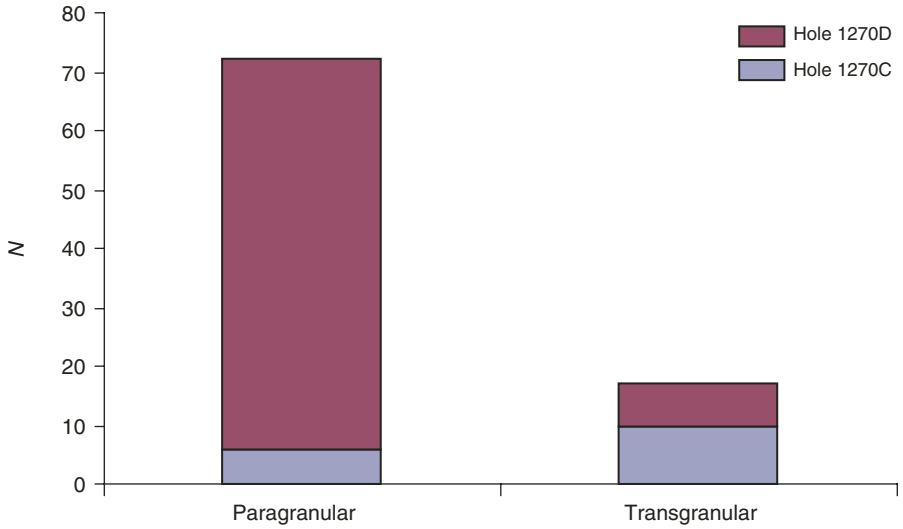

Figure F51. Timing relationships between alteration and deformation. Ht = high temperature, GR-F = granulite facies, AMP-F = amphibolite facies.

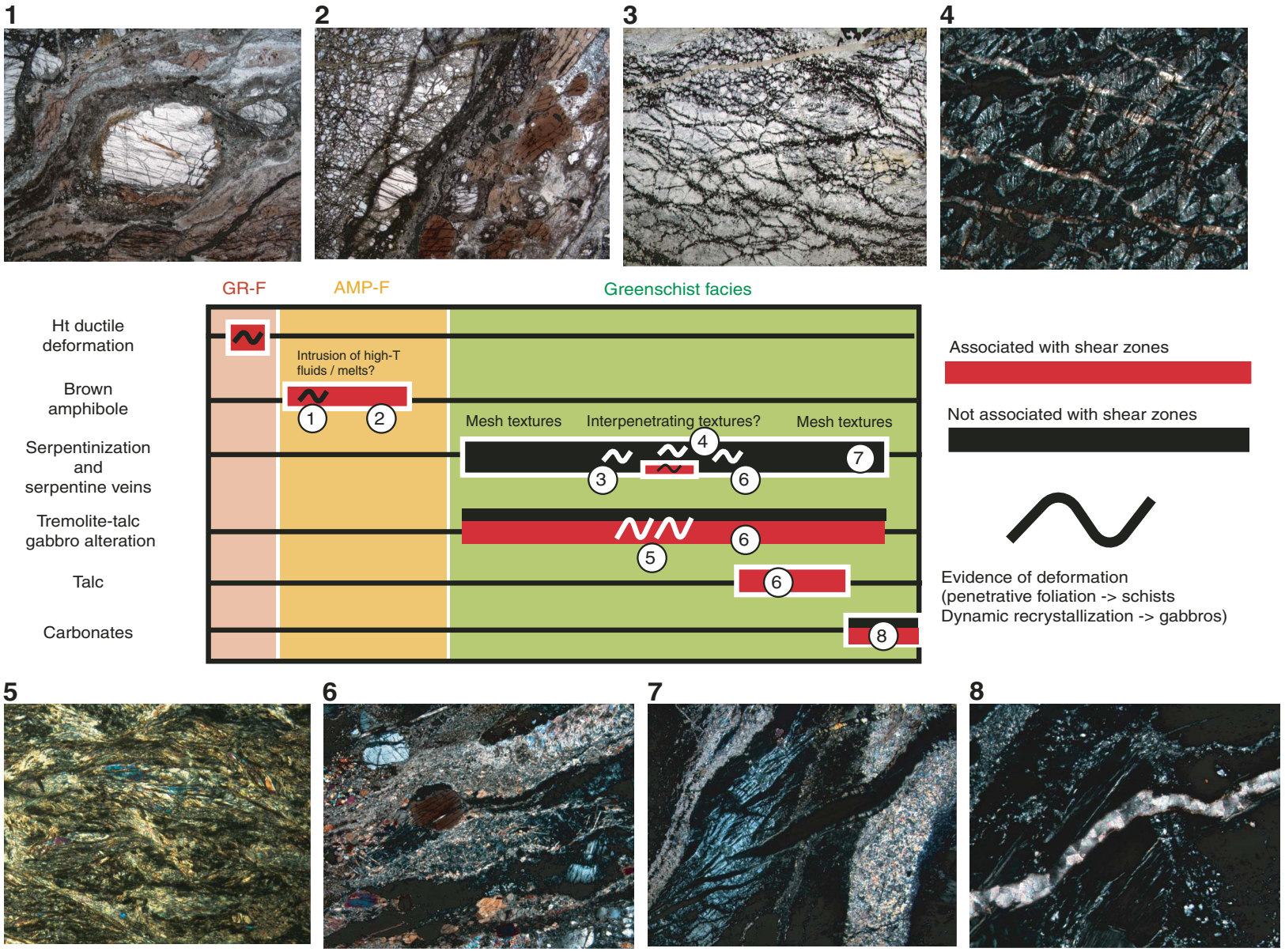

Figure F52. Close-up photographs of green serpentinized "popcorn" harzburgite from Hole 1270A, showing modified protogranular texture as a result of serpentinization. **A.** Interval 209-1270A-1R-1 (Piece 20, 115–130 cm). **B.** Interval 209-1270A-1R-1 (Pieces 11 and 12, 54–67 cm). Note that Pieces 11 and 12 have a weak foliation defined by a shape fabric in the pyroxene bastites.

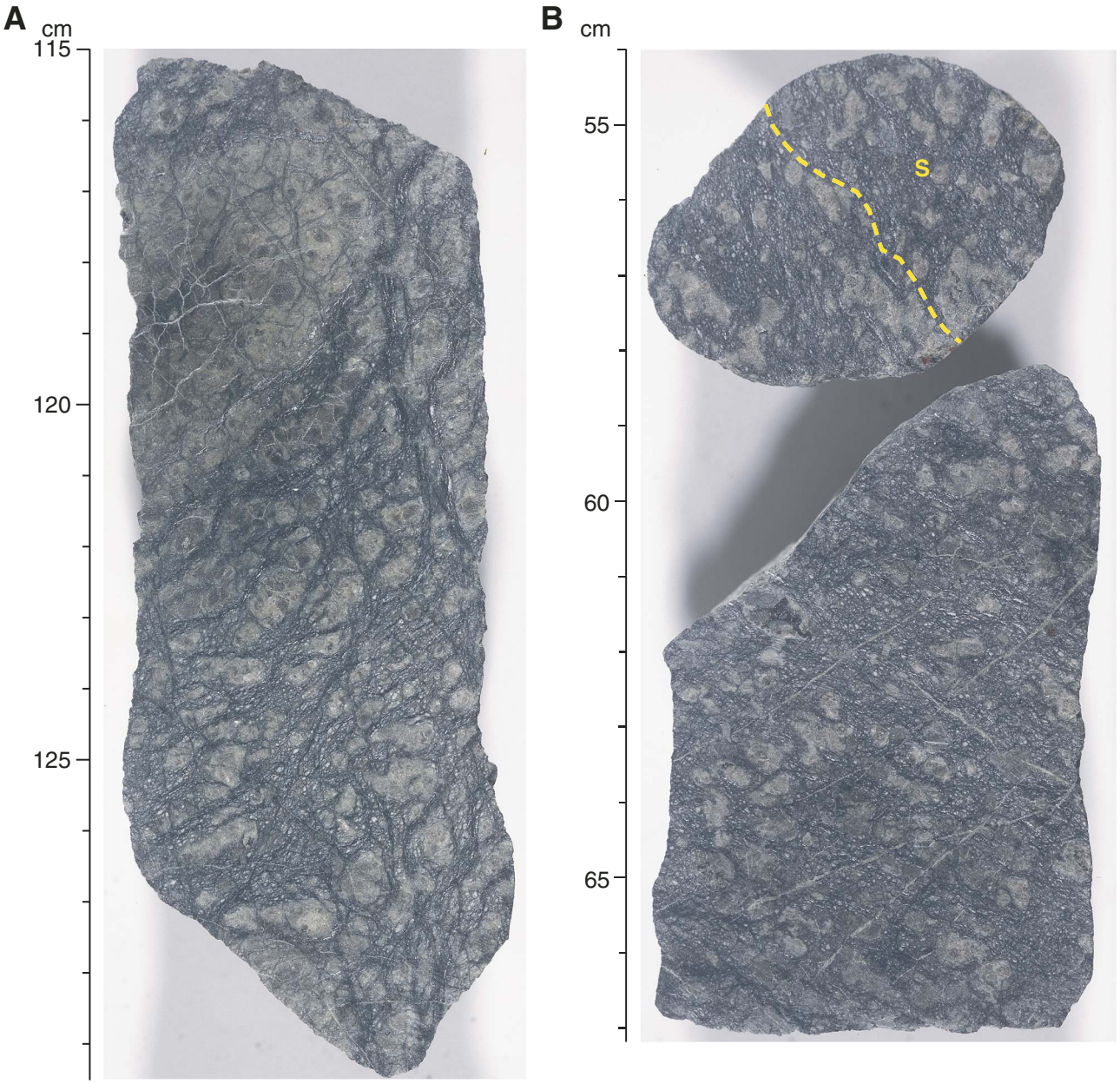

Figure F53. Photomicrographs of serpentine bastite pseudomorphs of primary orthopyroxene grains in Hole 1270A harzburgites exhibiting undeformed protogranular texture (plane-polarized light: blue filter; field of view = 5.5 mm). The primary mineral pseudomorphed is indicated on the photomicrographs: ol = olivine, opx = orthopyroxene, sp = spinel. **A.** Orthopyroxene pseudomorph (Sample **209-1270A-1R-1, 35–38 cm**) (image 1270A_015). **B.** An enclosed olivine pseudomorph and a large euhedral spinel grain (Sample **209-1270A-1R-1, 139–141 cm**) (image 1270A_017).

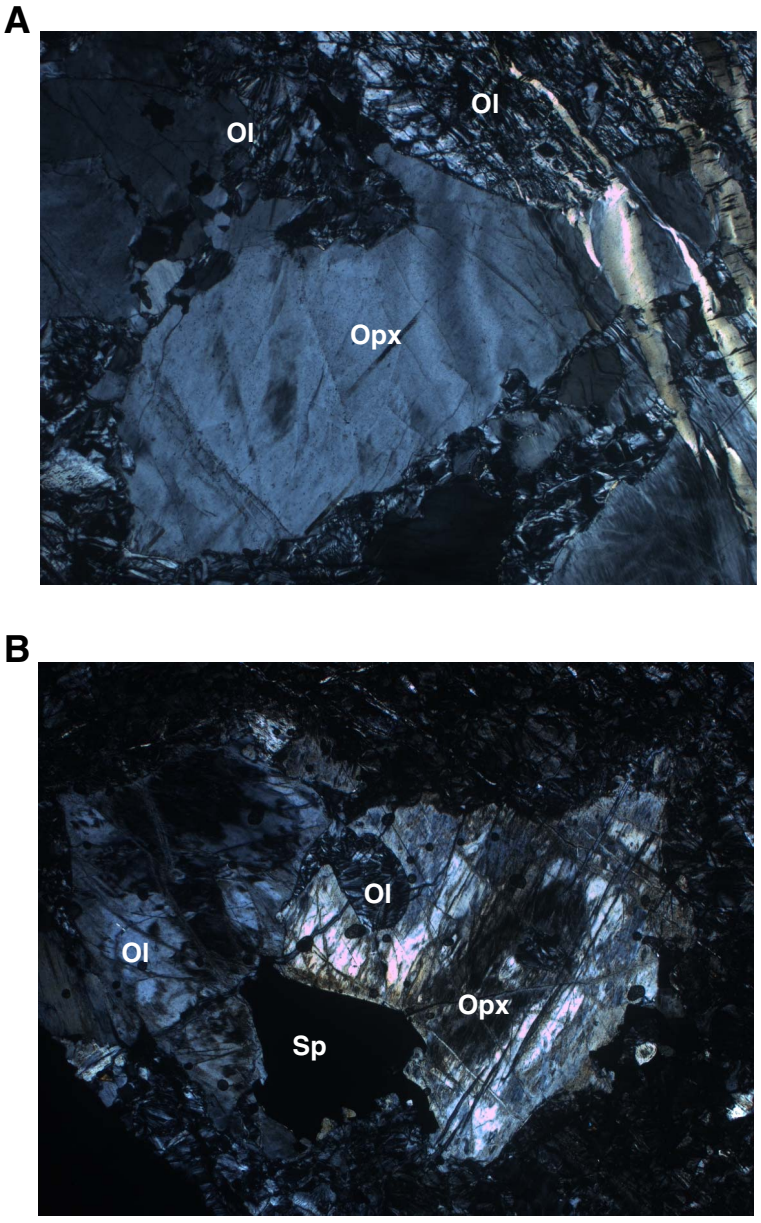

Figure F54. Downhole plot of crystal-plastic deformation intensity in Hole 1270A. Intensities are plotted as a running downhole average of seven pieces weighted by piece length at each depth (76 pieces total). TD = total depth.

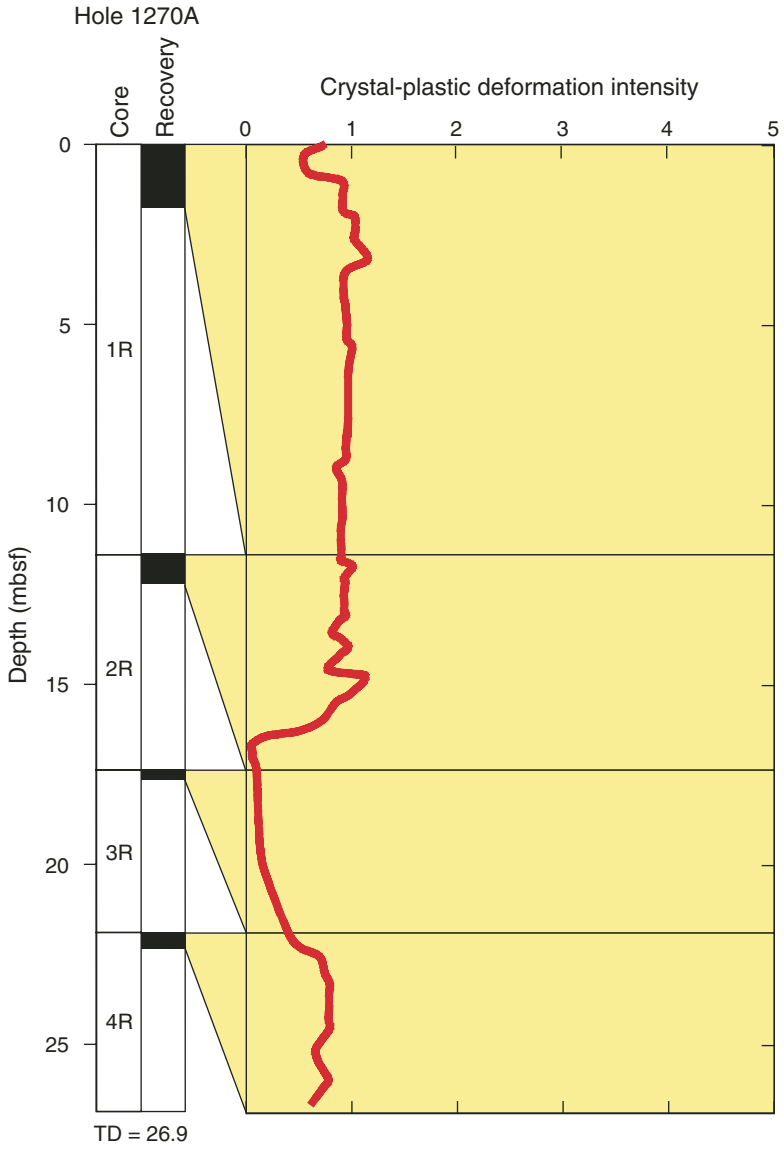

Figure F55. Close-up photograph of a serpentinized harzburgite with a crosscutting altered gabbroic vein (interval 209-1270A-4R-1 [Pieces 14 and 15, 50–58 cm]).

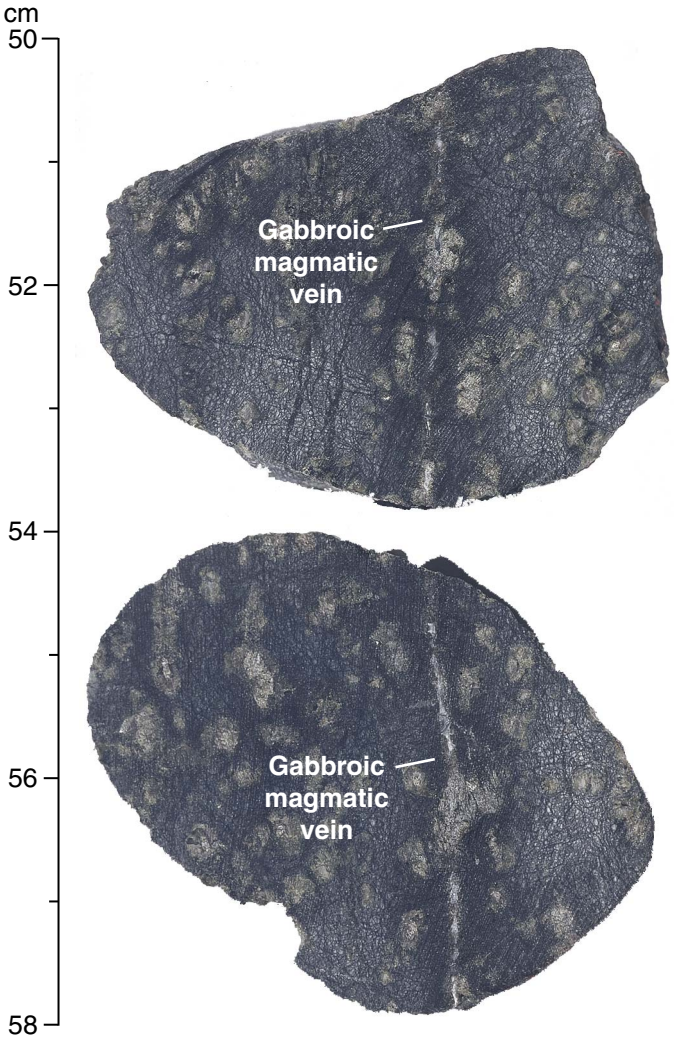

Figure F56. Close-up photograph of noncohesive, fine-grained fault gouge/breccia. Breccia contains sand-sized lithic clasts in a carbonate-rich serpentine matrix (interval 209-1270A-3R-1, 24–33 cm).

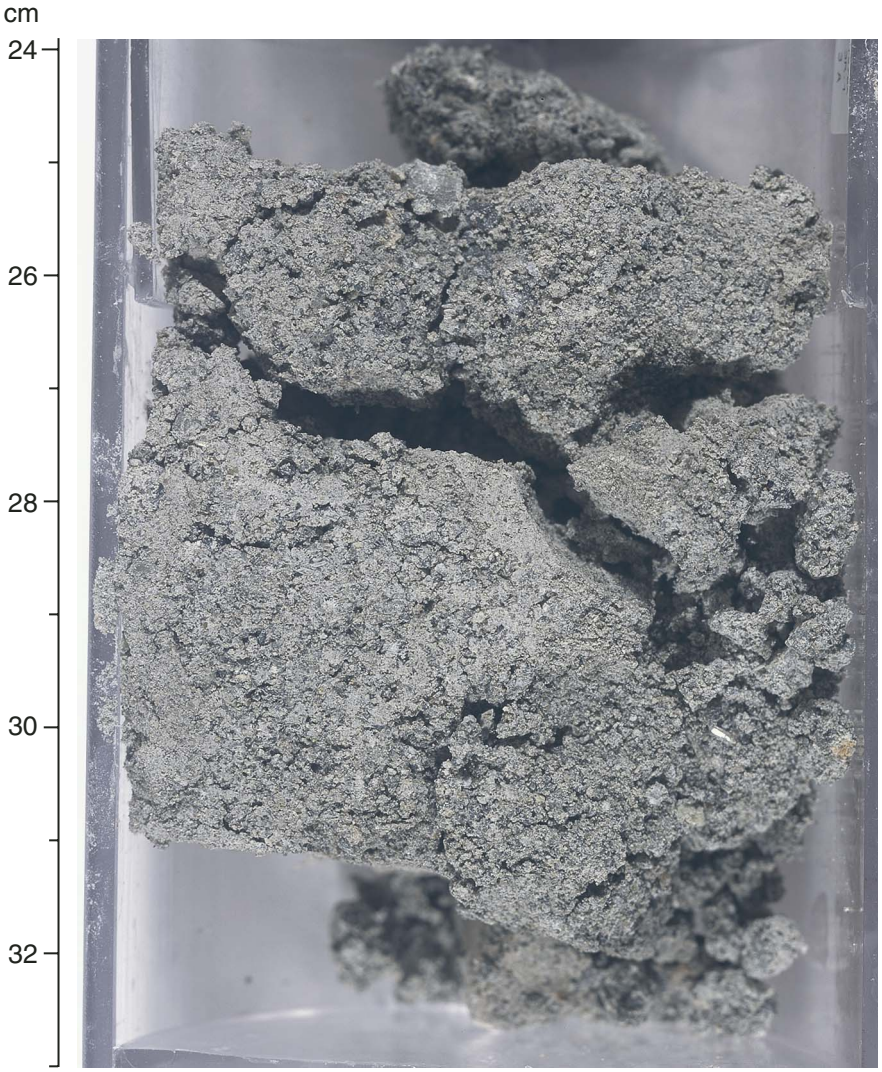

Figure F57. Photomicrograph of serpentine shear zone. Fibers of schistose serpentine terminate in a zone of fine, granular serpentine that contains clasts of pyroxene and mesh-texture serpentinite (Sample **209-1270A-1R-1, 35–38 cm**) (cross-polarized light: blue + light gray filters; field of view = 5.5 mm; image 1270A_011).

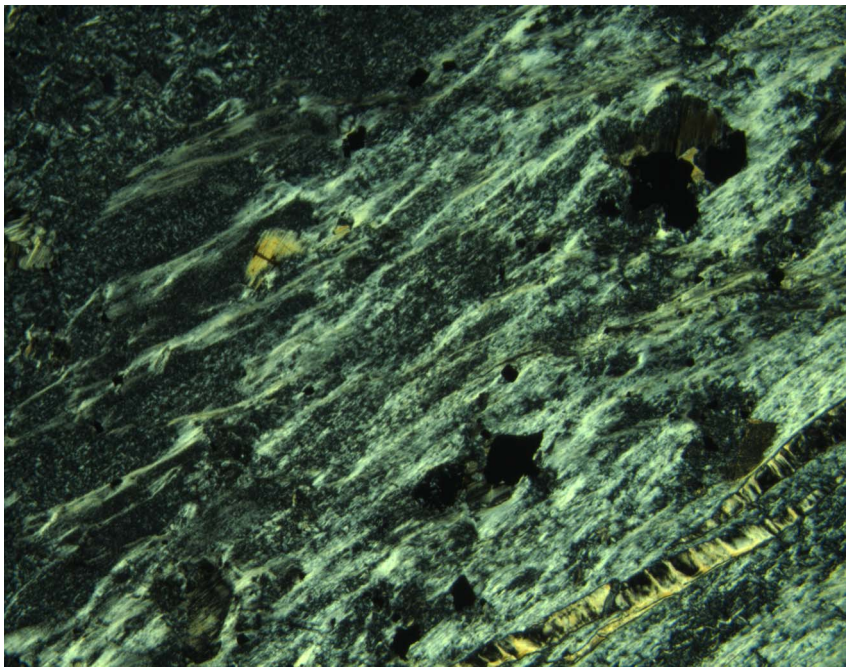

Figure F58. Close-up photograph of harzburgite with two generations of serpentine veins running parallel to the crystal-plastic foliation (interval 209-1270A-2R-1, 88–93 cm).

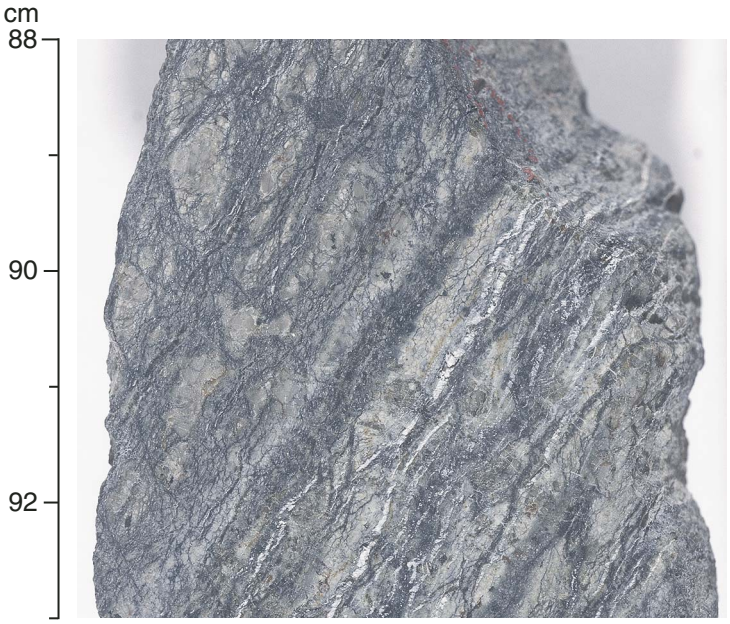

Figure F59. Crystal-plastic deformation intensity in 269 individual core pieces from Hole 1270B estimated during visual core description. Grade 0 = undeformed, 1 = weakly deformed, 2 = well foliated, 3 = protomylonite, 4 = mylonite, and 5 = ultramylonite.

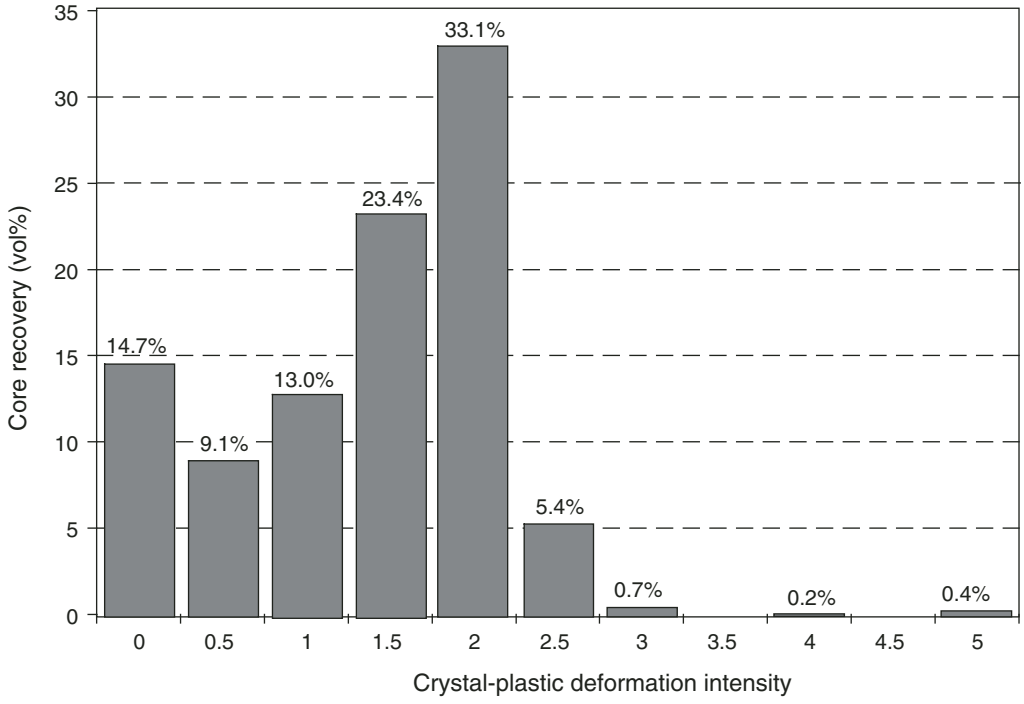

Figure F60. Photomicrographs of Hole 1270B oxide gabbronorites. Opx = orthopyroxene, Cpx = clinopyroxene, Pl = plagioclase. **A–C.** Sample **209-1270B-1R-1, 90–93 cm.** (A) Plagioclase ribbon porphyroclasts and recrystallized feldspar matrix adjacent to undeformed orthopyroxene (cross-polarized light [XPL]: blue filter; field of view [FOV] = 2.75 mm; image 1270B-036). (B) Spectacularly bent clinopyroxene enclosed in recrystallized plagioclase and late magmatic oxide (plane-polarized light: blue filter; FOV = 5.5 mm; image 1270B_018). (C) Same view as B (XPL: blue filter; FOV = 5.5 mm; image 1270B_016). (Continued on next page).

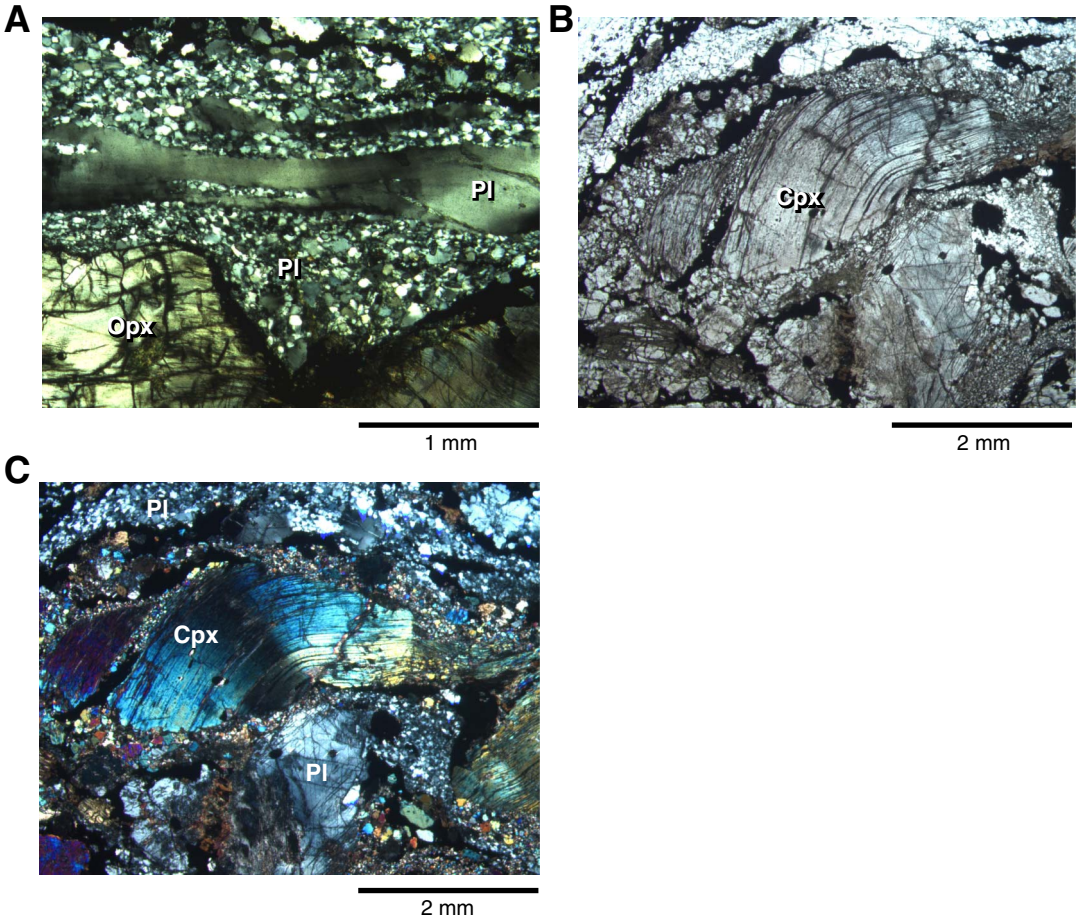

Figure F60 (continued). D. Magmatic oxide enclosing a rolled pyroxene augen, with a fragment of the pyroxene enclosed in the mantling oxide and oxide cementing isolated pyroxene neoblasts in the tail, all enclosed in recrystallized plagioclase (Sample **209-1270B-3M-1, 129–131 cm**) (PPL: blue + dark gray filters; FOV = 5.5 mm; image 1270B_050). **E.** Mat of magmatic oxide enclosing isolated plagioclase and clinopyroxene neoblasts in the tail of a clinopyroxene porphyroclast. Oxide also extends into the enclosing matrix of plagioclase neoblasts (Sample **209-1270B-1R-1, 83–85 cm**) (PPL: blue + dark gray + light gray filters; FOV = 2.75 mm; image 1270B_040).

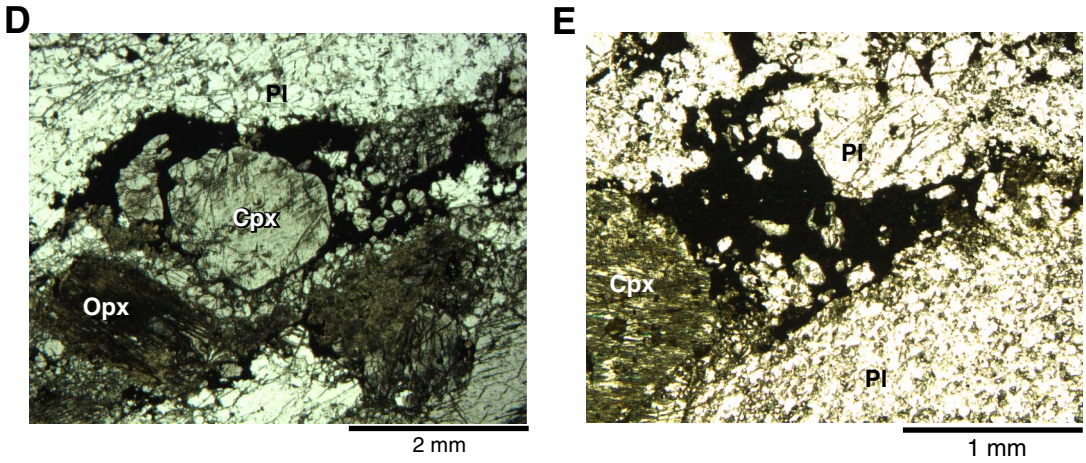

Figure F61. Photomicrographs of oxide gabbronorites from 1270B. Ox = oxides, Pl = plagioclase, Opx = orthopyroxene, Cpx = clinopyroxene. **A.** Oxide-filled, wedge-shaped crack in idiomorphic plagioclase (Sample **209-1270B-10M-2, 53–59 cm**) (cross-polarized light [XPL]: blue filter; field of view [FOV] = 5.5 mm; image 1270B_047). **B.** Wedge of oxide filling a crack in a broken, tabular orthopyroxene grain (Sample **209-1270B-1R-1, 90–93 cm**) (XPL: blue filter; FOV = 5.5 mm; image 1270B_014). **C.** Magmatic oxide enclosing and forming tails on a rolled pyroxene porphyroclast in a matrix of recrystallized plagioclase (Sample **209-1270B-10M-2, 53–56 cm**) (plane-polarized light [PPL]: blue + dark gray filters; FOV = 5.5 mm; image 1270B_048). **D.** Distributed oxide in undeformed oxide gabbronorite (Sample **209-1270B-10M-1, 21–23 cm**) (plane-polarized light: blue + dark gray filters; FOV = 5.5 mm; image 1270B_045).

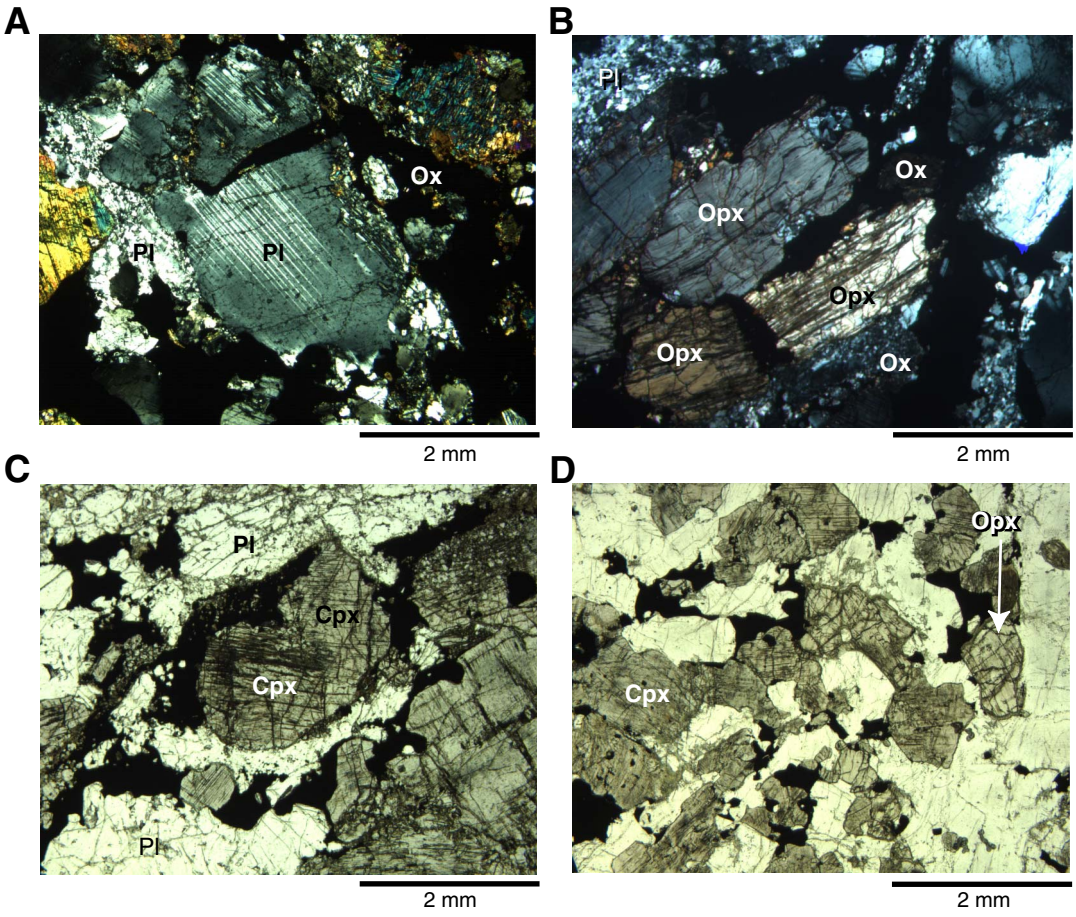

Figure F62. Close-up images of oxide gabbronorites from Hole 1270B. **A.** Well-developed foliation in gabbronorite, with oxide concentrated in thin lamellae along the foliation plane (interval 209-1270B-1R-1, 91–103 cm). **B.** Shear zone through gabbronorite with massive oxide concentration (interval 209-1270B-7R-2, 127–140 cm).

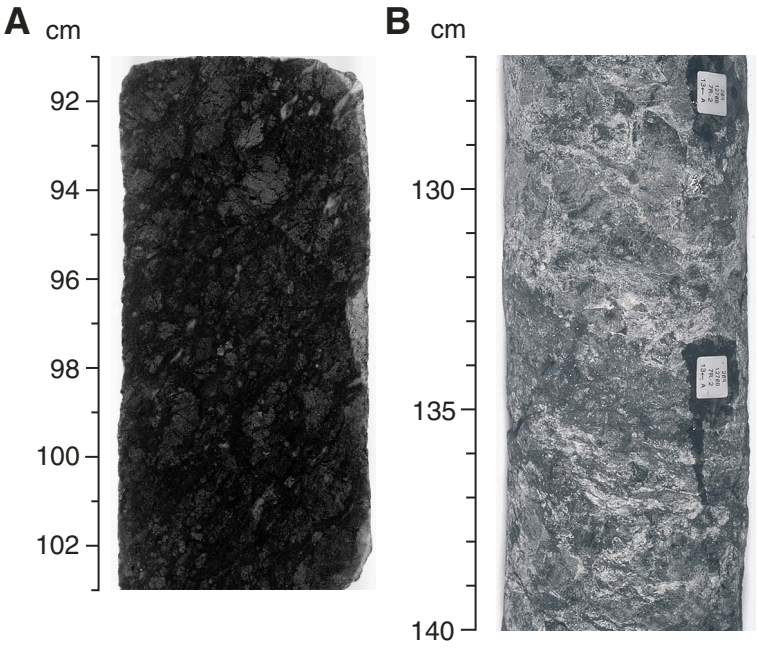

Figure F63. Photographs of foliated, coarse oxide gabbronorite intruded by a foliated microgabbro that crosscuts the foliation plane of the coarse oxide gabbronorite host and then pinches out (interval 209-1270B-1R-1, 106–119 cm). **A.** Cut face. **B.** Whole-round core. **C.** Whole-round core rotated with respect to B. A pyroxenite band in the same piece appears nearly undeformed, cutting the foliation in the coarse gabbronorite at a different angle compared to the microgabbro.

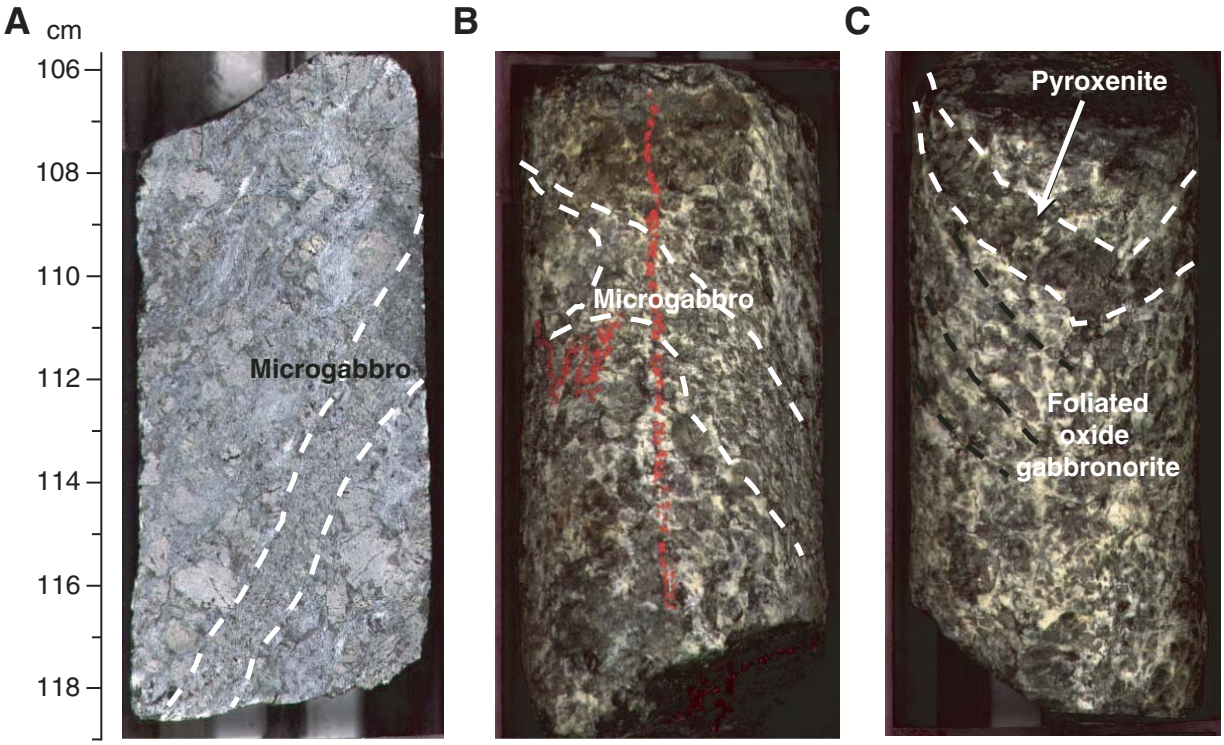

Figure F64. Photomicrographs showing oxide layers in Hole 1270B oxide gabbronorite (Sample 209-1270B-1R-1, 90–93 cm); Ox = oxide, Pl = plagioclase, Cpx = clinopyroxene, Opx = orthopyroxene. **A.** Oxide lens in recrystallized plagioclase, adjacent to a rolled clinopyroxene augen with tails consisting of agate neoblasts partially cemented by magmatic oxides (cross-polarized light: blue + dark gray filters; field of view [FOV] = 5.5 mm; image 1270B_052). **B.** Same view as A (plane-polarized light: blue + dark gray filters; FOV = 5.5 mm; image 1270B_051). **C.** Anastomosing oxide foliation in recrystallized plagioclase, suggesting multiple generations of deformation and oxide crystallization (plane-polarized light: blue + dark gray filters; FOV = 5.5 mm; image 1270B_053).

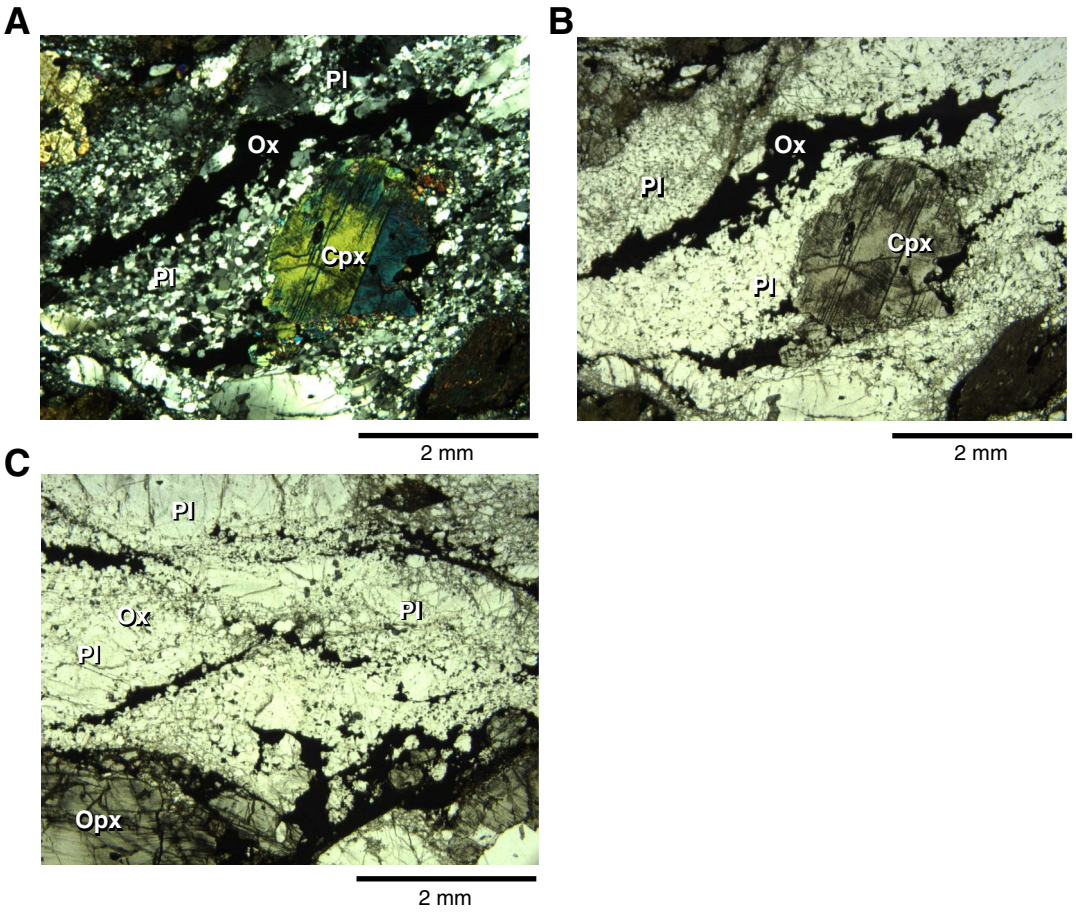

Figure F65. Photomicrograph of recrystallized clinopyroxene band in mylonite with recrystallized plagioclase and orthopyroxene pseudomorphs composed of talc (Sample **209-1270B-8R-1, 26–29 cm**) (cross-polarized light: blue + dark gray filters; FOV = 5.5 mm; image 1270B_043). Cpx = clinopyroxene, Pl = plagioclase, Tc = talc.

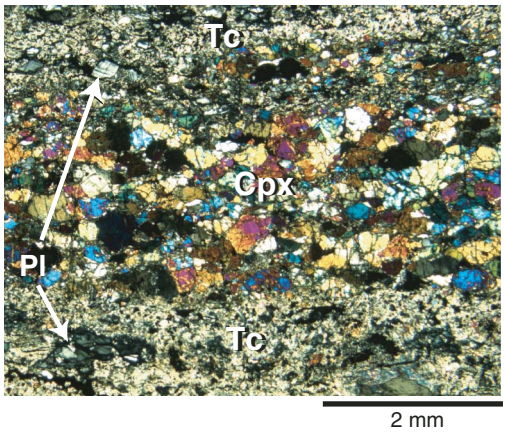

Figure F66. Downhole plot of plagioclase, titanomagnetite, crystal-plastic fabric intensity, and crystal-plastic foliation dips for Hole 1270B (see **"Igneous and Mantle Petrology,"** p. 3). Intensities are plotted as a running average of 10 pieces weighted by piece length at each depth.

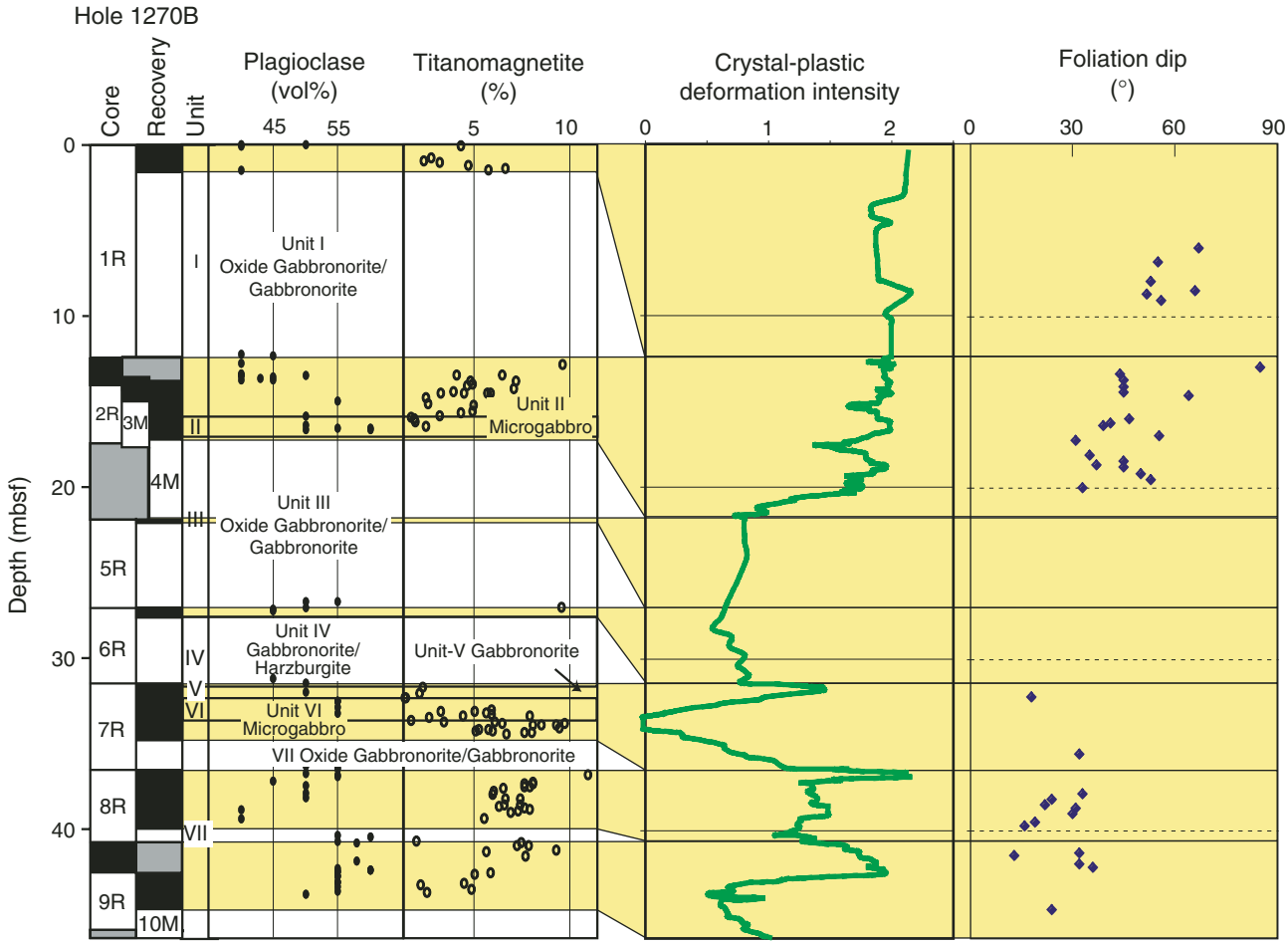

Figure F67. Lower hemisphere stereographic projection of poles to crystal-plastic foliations, measured in the core reference frame and rotated into a common reference frame using the measured paleomagnetic declination as described in **"Structures in Peridotite and Gabbroic Intrusions,"** p. 8, in "Mantle Upwelling, Melt Transport, and Igneous Crustal Accretion" in the "Leg 209 Summary" chapter. All samples have measured negative inclinations, assumed to be indicative of a reversed polarity at the time of magnetization. The solid line connects measurements in Section 209-1270B-1R-1 (Piece 17) of a pyroxene band (Px) and a foliated oxide-microgabbro (mG) that crosscut a foliated coarse oxide gabbro (oxG).

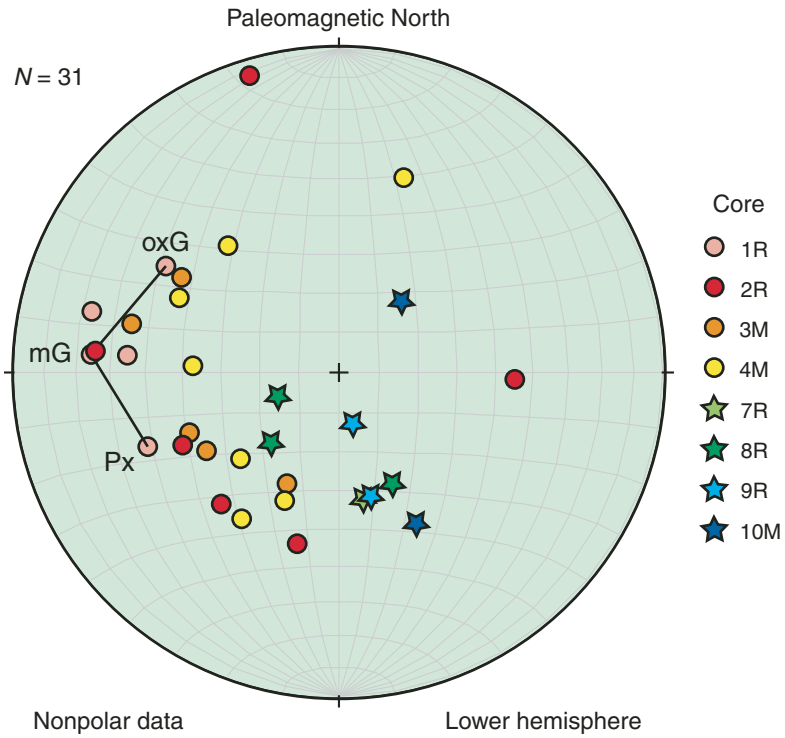

Px: 209-1270B-1R-1 (Piece 17, 104.5-105.5 cm)
mG: 209-1270B-1R-1 (Piece 17, 111.5-114 cm)
oxG: 209-1270B-1R-1 (Piece 17, 114-118 cm)

Figure F68. Photomicrograph of a zone of brittlely deformed plagioclase neoblasts between a clinopyroxene porphyroclast and a plagioclase porphyroclast (Sample 209-1270B-8R-2, 114–116 cm) (cross-polarized light: blue filter; field of view = 2.75 mm; image 1270B_060).

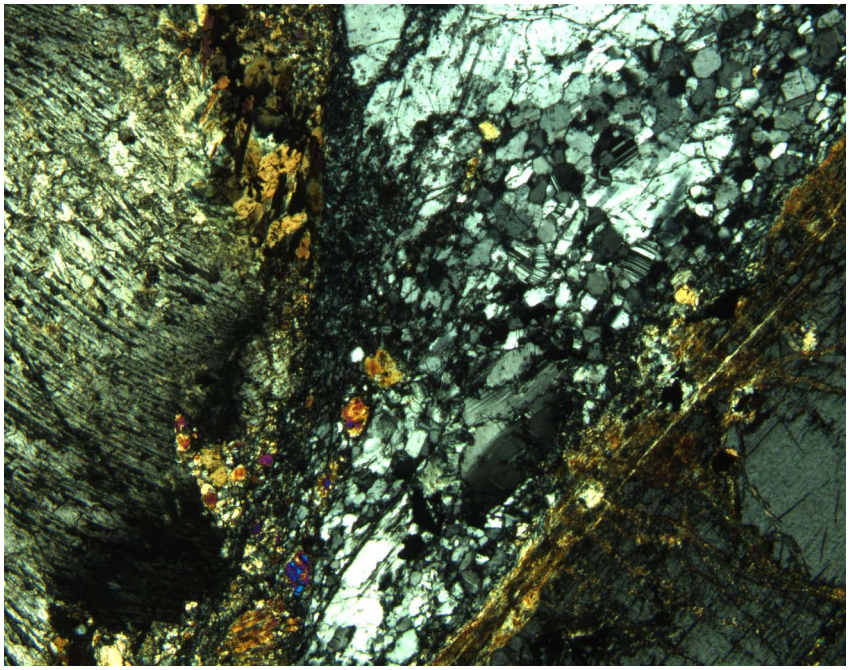

Figure F69. Photomicrograph of a zone of interstitial oxide along brittle shear zones in gabbro. Aggregates of plagioclase neoblasts with plagioclase and clinopyroxene porphyroclasts are separated by fractures filled with oxide. Textures suggest ductile deformation of gabbro, followed by brecciation and infilling by Fe-Ti oxides, perhaps from an Fe-Ti–rich magma (Sample **209-1270B-1R-1, 90–93 cm**) (cross-polarized light: blue + light gray filters; field of view = 5.5 mm; image 1270B_059).

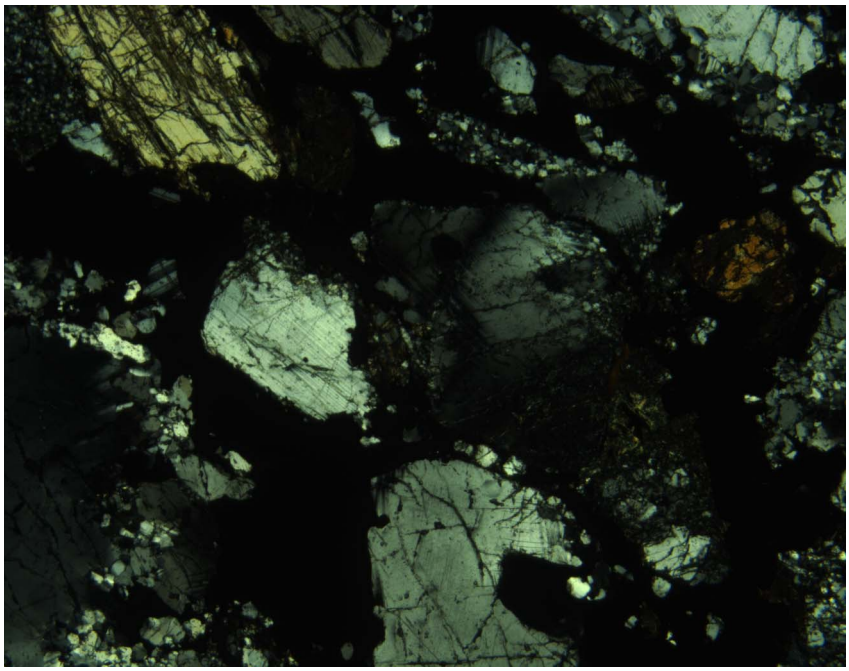

Figure F70. Close-up image of gabbro deformed during synkinematic alteration to talc and chlorite (interval 209-1270B-8R-1, 6–14 cm).

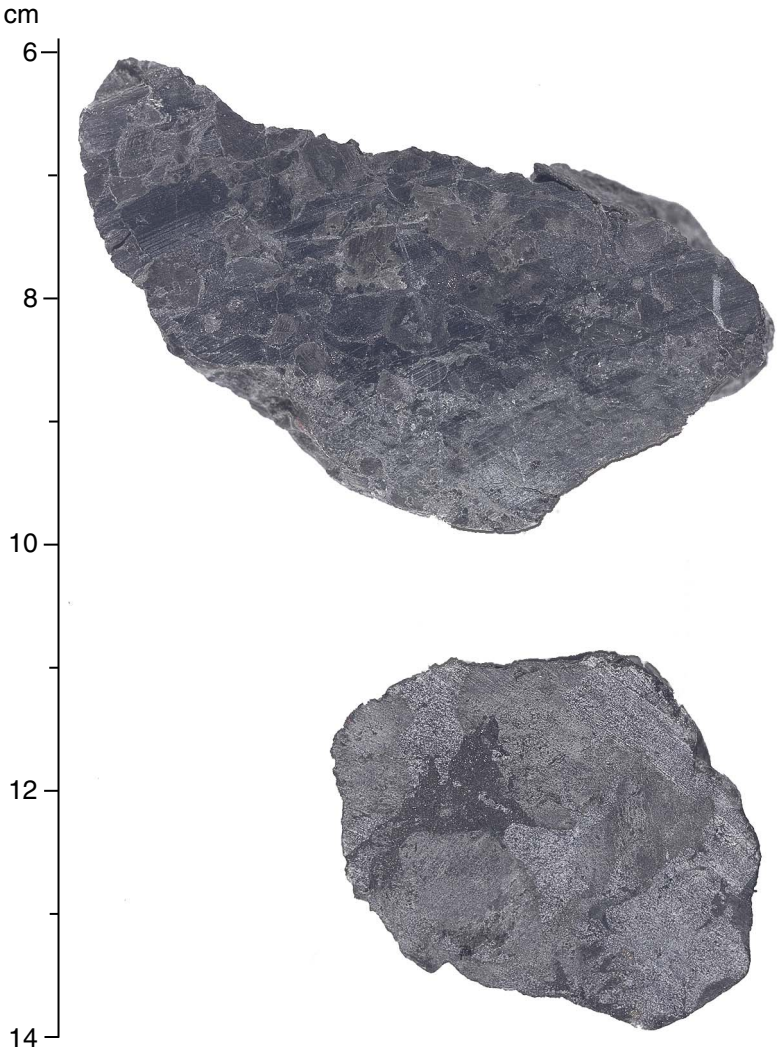

Figure F71. Variation of total cataclastic, crystal-plastic alteration vein intensity in Hole 1270B (running average over ~50 cm) with depth. TD = total depth.

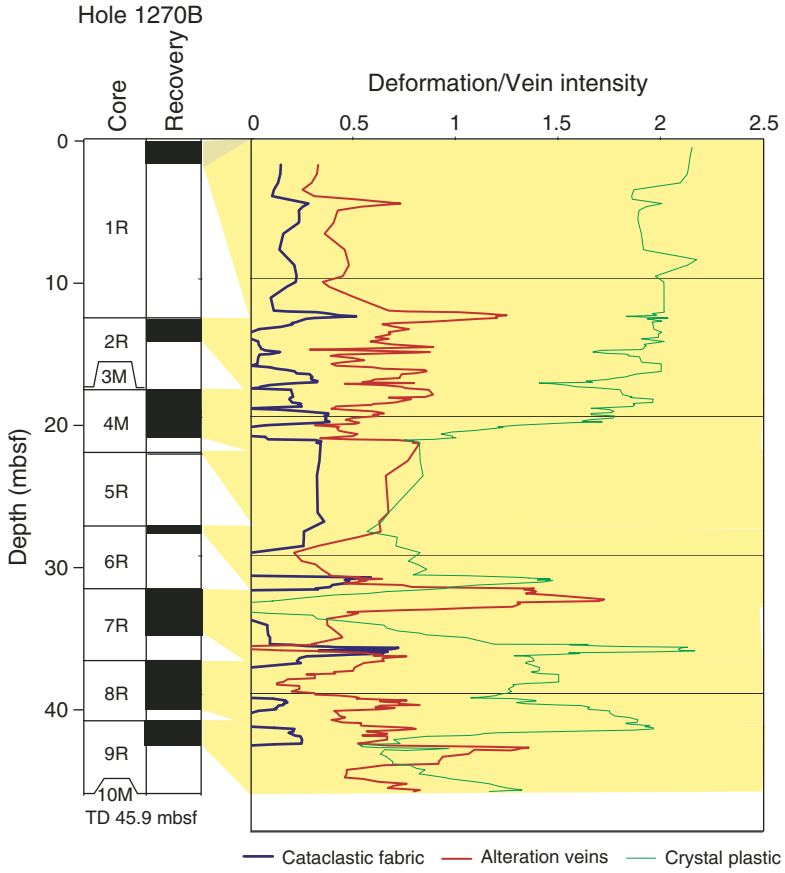

Figure F72. Plot of the dip of brittle structures vs. expanded depth in Hole 1270B. TD = total depth.

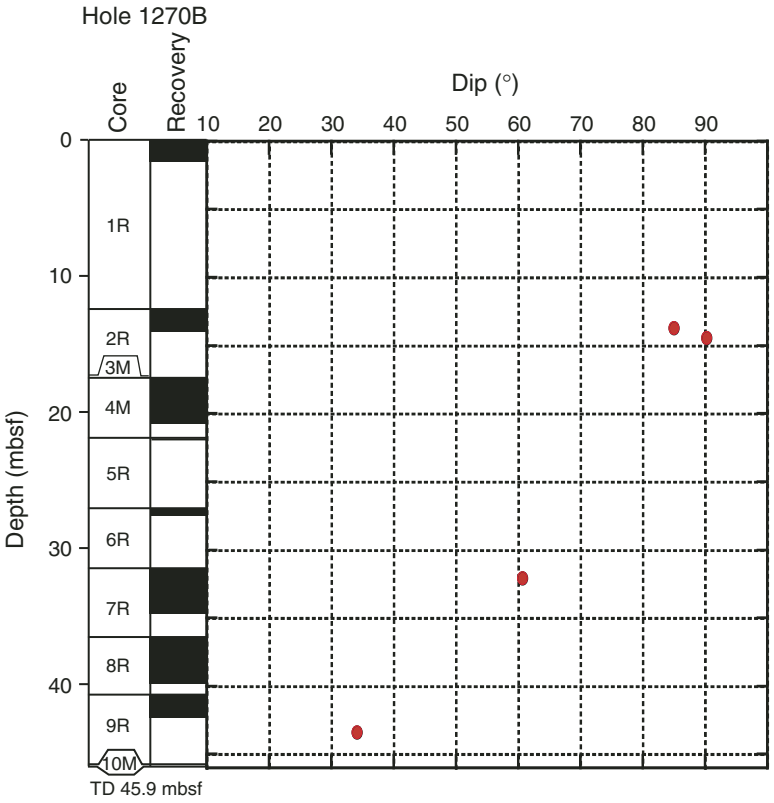

Figure F73. Plots of the dips of alteration veins with depth for Holes 1270B, 1270C, and 1270D.

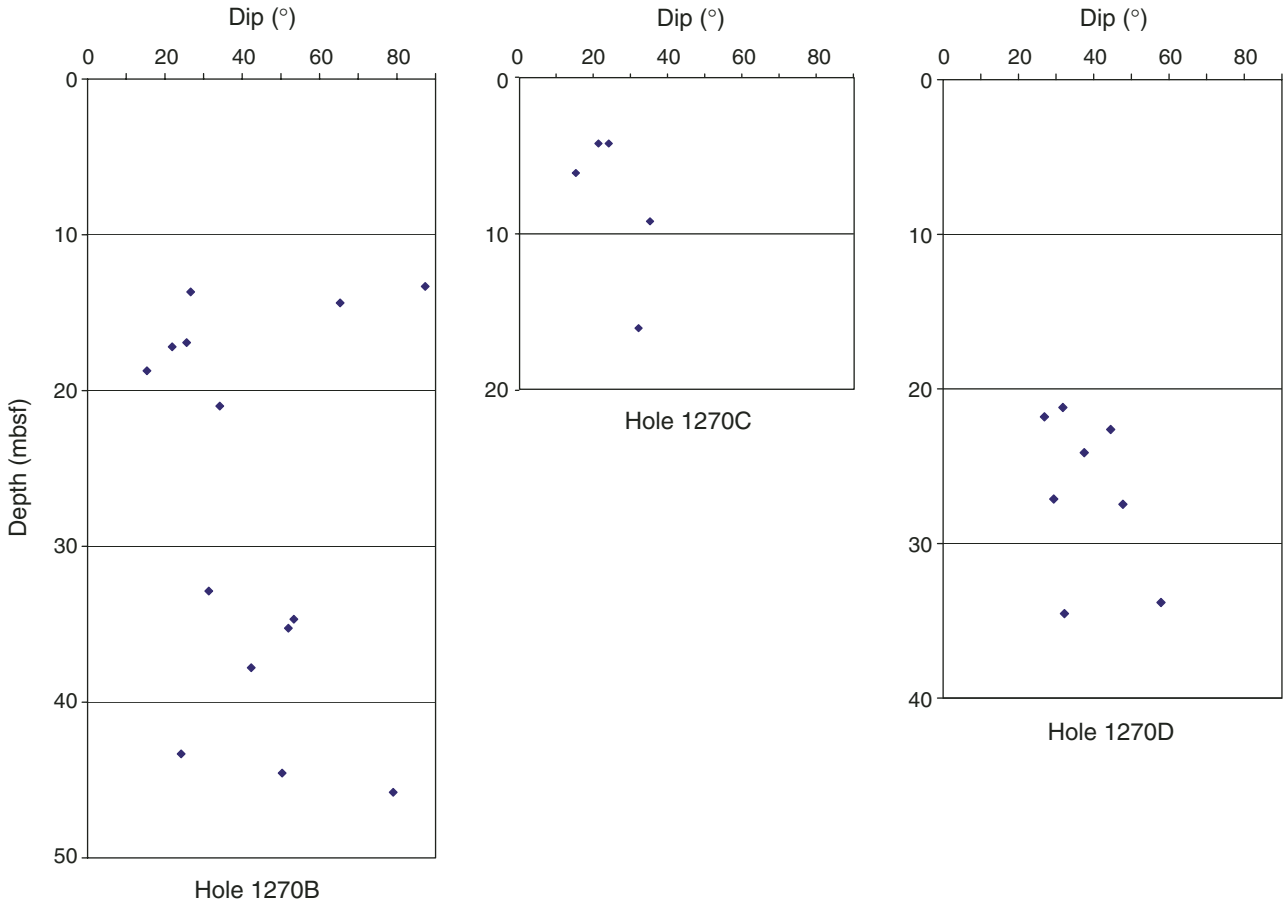

Figure F74. Lower hemisphere equal-area stereographic projection of poles to alteration veins and brittle shear zones in Hole 1270B, measured in the core reference frame and rotated using the measured paleomagnetic declination back to a common orientation as described in **"Structures in Peridotite and Gabbroic Intrusions,"** p. 8, in "Mantle Upwelling, Melt Transport, and Igneous Crustal Accretion" in the "Leg 209 Summary" chapter. All samples have measured negative inclinations, assumed to be indicative of a reversed polarity at the time of magnetization.

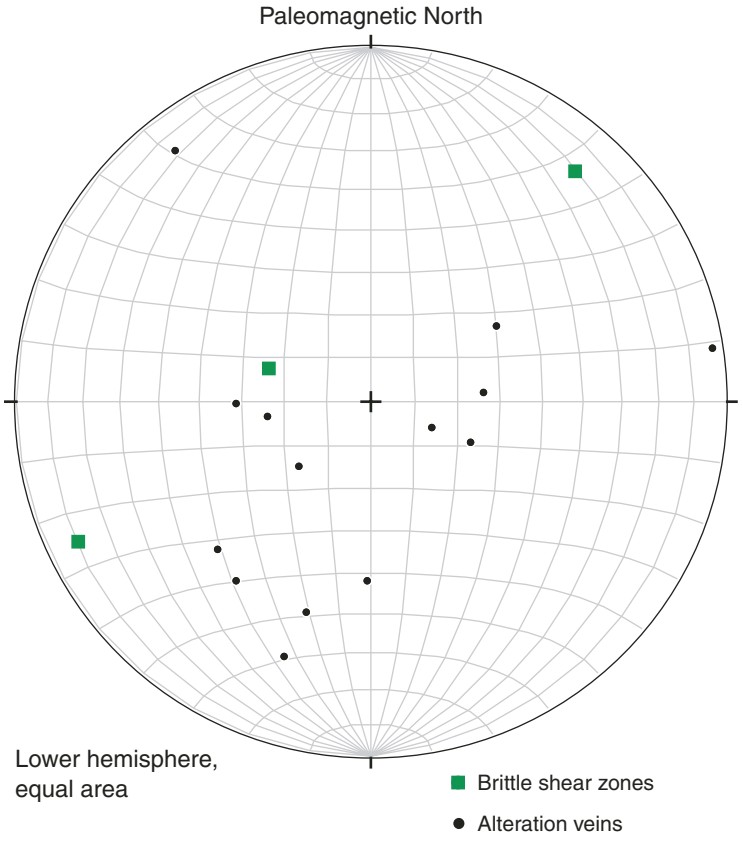

Figure F75. Downhole plot of crystal-plastic deformation intensity in Holes 1270C and 1270D. Intensities are plotted as a running average of five pieces for Hole 1270C and seven pieces for Hole 1270D (155 pieces total) weighted by piece length at each depth. TD = total depth.

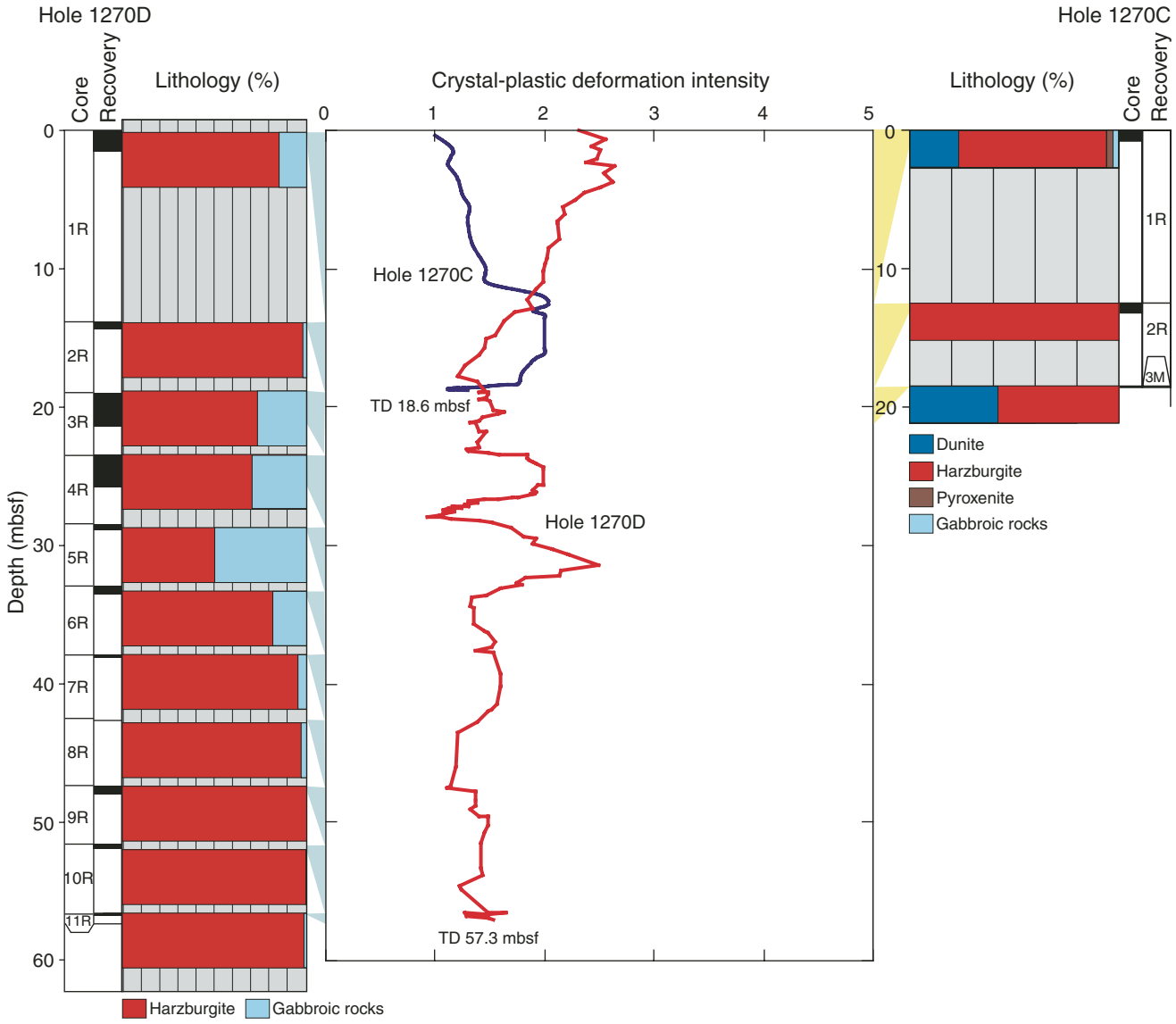

Figure F76. Crystal-plastic deformation intensities measured in (**A**) Hole 1270C and (**B**) Hole 1270D harzburgites and metagabbro veins.

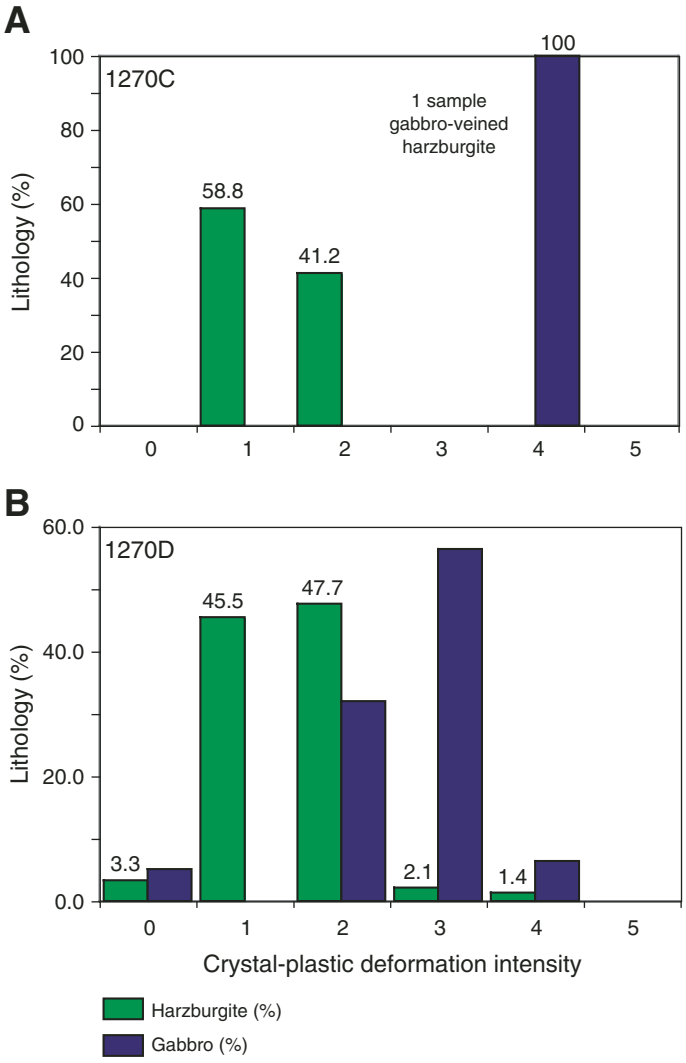

Figure F77. Photomicrographs of Hole 1270C and 1270D harzburgites showing deformation textures (cross-polarized light; field of view = 5.5 mm). Ol = olivine, Opx = orthopyroxene. **A.** Protomylonitic harzburgite enclave adjacent to gabbro mylonite veins (Sample **209-1270C-1R-1, 83–85 cm**) (image 1270C_028). **B.** Protogranular orthopyroxene bastite pseudomorph (Sample **209-1270D-3R-1, 94–97 cm**) (image 1270D_030). **C.** Protogranular orthopyroxene bastite showing incipient breakup of grain during porphyroclastic deformation (Sample **209-1270D-6R-1, 29–32 cm**) (image 1270D_034). **D.** Protogranular orthopyroxene bastite broken into two new porphyroclasts (Sample **209-1270D-3R-2, 68–71 cm**) (image 1270D_033). **E.** Orthopyroxene porphyroclast with granulated and crushed pyroxene grains along its mantle (Sample **209-1270C-3M-1, 44–46 cm**) (image 1270C_029). **F.** Orthopyroxene bastite pseudomorph showing internal strain and incipient fracture (Sample **209-1270C-1R-1, 72–75 cm**) (image 1270C_027).

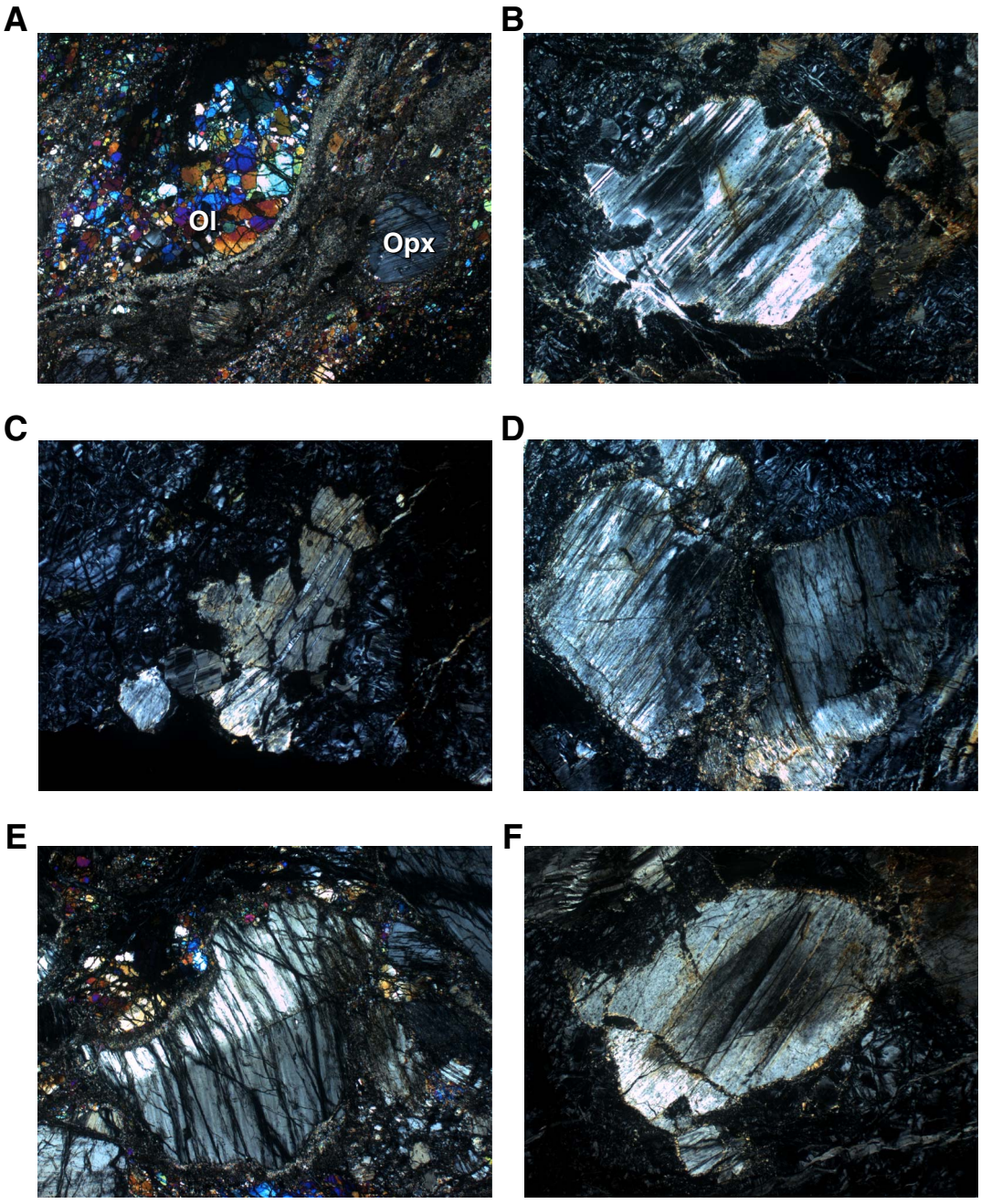

Figure F78. Photomicrographs of Hole 1270C and 1270D harzburgites showing deformation textures (cross-polarized light; field of view = 5.5 mm). **A.** Single orthopyroxene pseudomorph crosscut by serpentine veins with little internal deformation (Sample **209-1270C-1R-1, 40–42 cm**) (image 1270C_026). **B.** Elongate, parallel, partially serpentinized orthopyroxene grains defining a low-angle (~10°) foliation with a normal shear sense (Sample **209-1270D-10R-1, 4–6 cm**) (image 1270D_037).

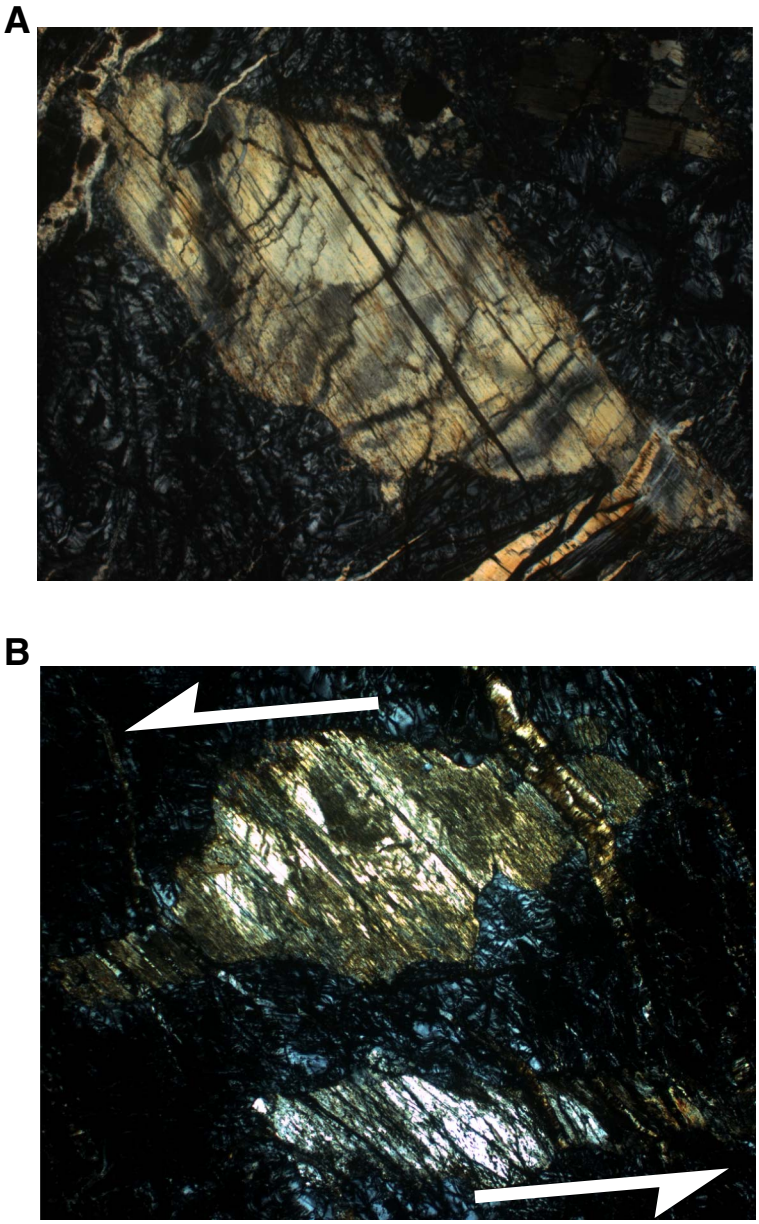

Figure F79. Lower hemisphere stereoplot showing poles to magmatic veins, alteration veins, and one crystal-plastic harzburgite foliation in Holes 1270C and 1270D. The individual pieces of the core are rotated to a common direction with paleomagnetic declination data as described in **"Structures in Peridotite and Gabbroic Intrusions,"** p. 8, in "Mantle Upwelling, Melt Transport, and Igneous Crustal Accretion" in the "Leg 209 Summary" chapter. The scatter in the orientation of the veins gives some indication of the anastomosing nature of the gabbroic vein network. The measured porphyroclastic foliation in harzburgite is from interval 209-1270D-6R-1 (Piece 4, 24–40 cm).

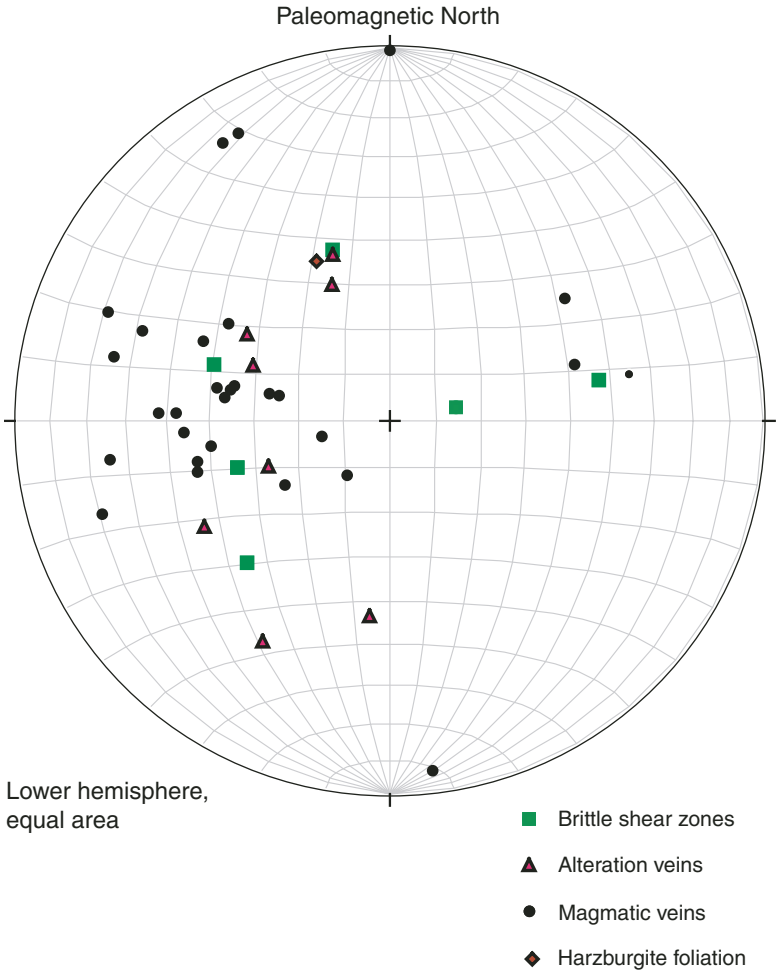

Figure F80. Scanned image of thin section showing mylonitic gabbroic/pyroxenitic veins. The mylonitization of the vein material had little effect on adjacent harzburgite enclaves, except along contacts between the enclaves and mylonite zones. Brown patches associated with the mylonitized veins are brown amphiboles, which replace clinopyroxene in the vein and at the edge of the mylonitized zones (upper left). Orthopyroxene and olivine from harzburgite along the edge of the vein are commonly entrained within the mylonite as porphyroclasts (see orthopyroxene [opx] example in lower right) (Sample 209-1270C-1R-1 [Piece 13, 83–85 cm]).

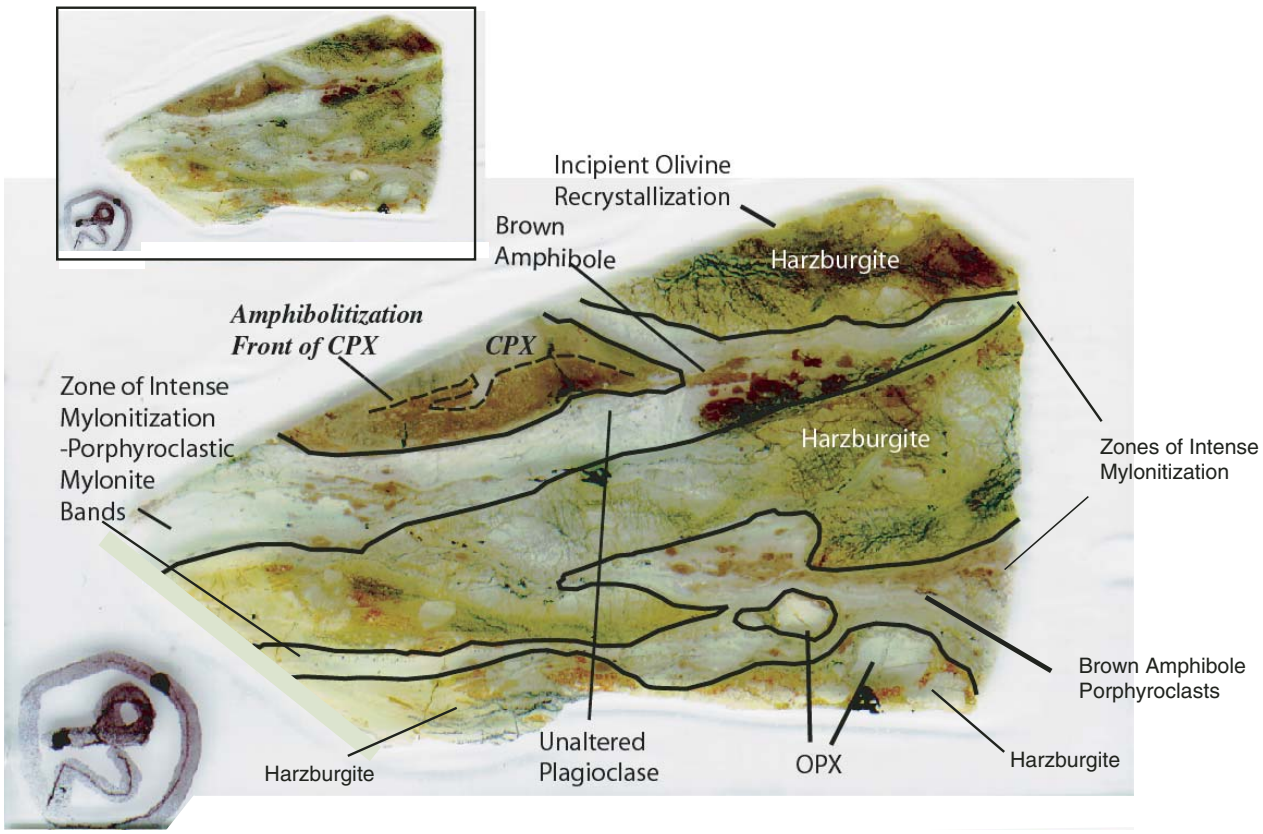

Figure F81. Close-up photographs illustrating the complex nature of gabbroic and pyroxenititic veins that cut peridotite in Hole 1270D. Some gabbroic veins, at the top and bottom of the piece, are near parallel to the foliation in harzburgite, but there are also crosscutting veins at a high angle to the foliation in the center of the piece. The veins that are near parallel to the harzburgite foliation appear to have localized deformation within the piece (interval 209-1270D-3R-1 [Piece 8, 53–76 cm]). **A.** Cut face. **B, C.** Two outer edges of the precut core.

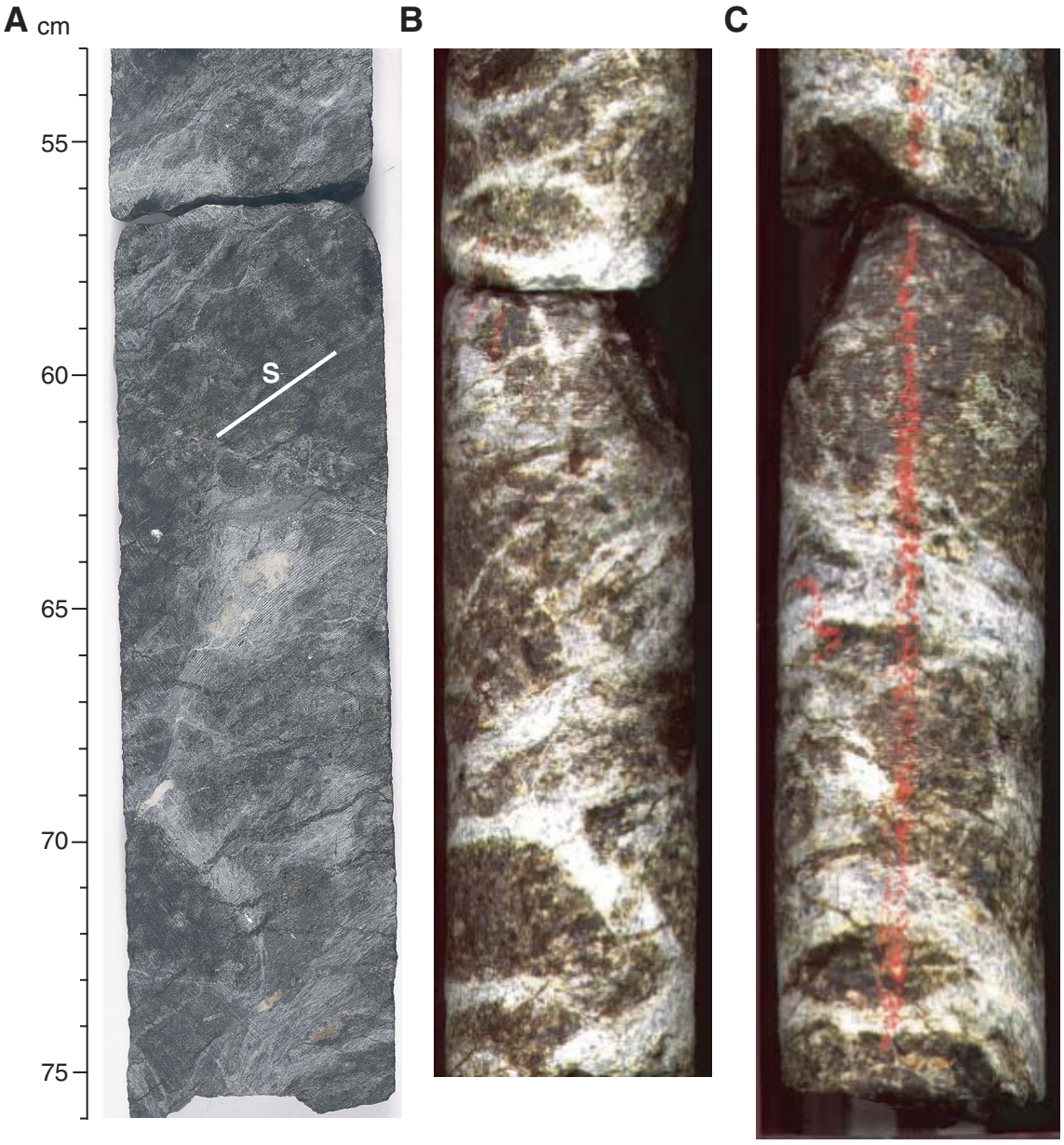

Figure F82. Close-up photograph of a diagonal, planar, pyroxenite vein (Px) cutting harzburgite. The pyroxenite is undeformed and is cut by a subhorizontal gabbroic vein (Gb) (also undeformed) and a second vein that is internally deformed and offsets the pyroxenite vein with a reverse sense of shear (upper left corner of photo). S = the harzburgite crystal-plastic foliation plane (interval 209-1270D-3R-2, 10–16 cm).

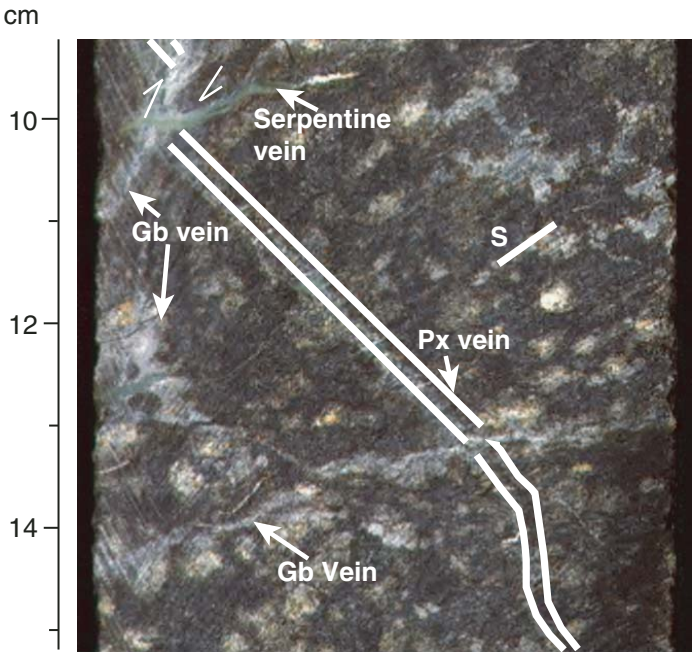

Figure F83. Close-up photograph of a diagonal, pyroxene (PX)-rich gabbroic (Gab.) vein cutting across a harzburgite showing a crystal-plastic foliation. The foliation is defined by elongate orthopyroxene porphyroclasts in the lower right of the photo (S). Note that the vein merges with a lens of pyroxenitic and gabbroic veins that is elongate subparallel to the foliation plane. The vein includes a banded mylonite zone that is parallel to the vein contacts. Where the vein merges with the gabbroic to pyroxenitic compositions lens, the vein is folded. Also note undeformed serpentine vein crosscutting the gabbroic vein (interval 209-1270D-4R-1, 94–103 cm).

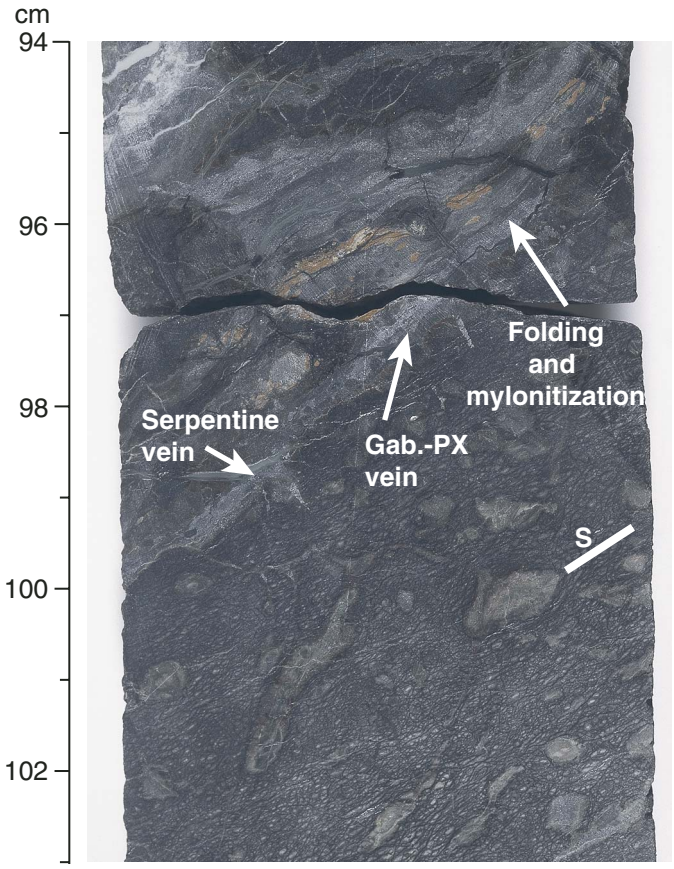

Figure F84. Photomicrograph of fibrous talc and fine granular talc on the boundary of an olivine porphyroclast. Fibrous talc forms a wispy foliation oblique to the dominant foliation. Fine-grained, granular talc forms a thin band between the fibrous talc and the olivine (Sample **209-1270D-4R-1, 33–37 cm**) (plane-polarized light; field of view = 2.75 mm; image 1270D_057).

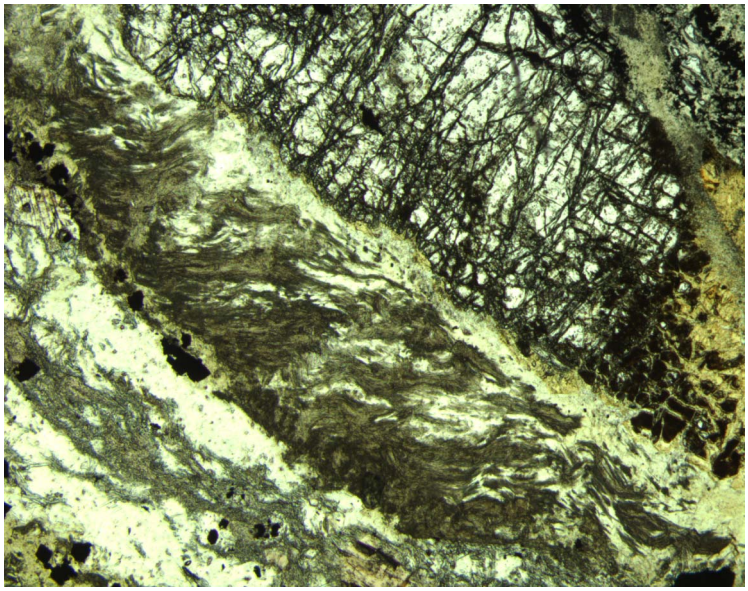

Figure F85. Photomicrograph of a boudinaged amphibole crystal. The amphibole is extended along an axis subparallel to the foliation, and colorless amphibole fibers have grown in the tensile zone between the grains (Sample **209-1270D-4R-1, 33–37 cm**) (plane-polarized light; field of view = 1.40 mm; image 1270D_054).

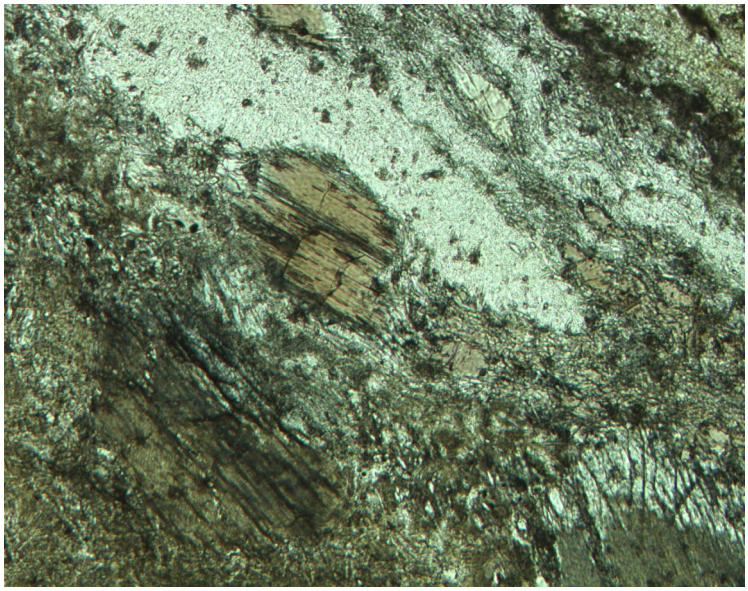

Figure F86. Photomicrograph of strongly deformed amphibole-talc schist from the upper portion of Hole 1270D. This texture represents extreme deformation at greenschist facies metamorphic conditions (Sample 209-1270D-1R-1, 16–18 cm) (cross-polarized light; field of view = 2.75 mm; image 1270D_058).

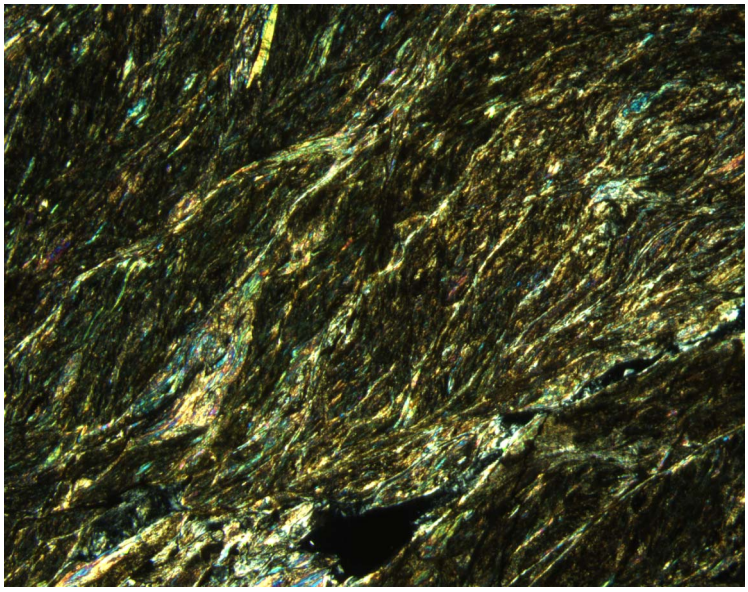

Figure F87. Downhole plot showing variation of total cataclastic, crystal-plastic alteration vein intensity (running average over ~50 cm) and magmatic vein frequency with depth in Hole 1270D. TD = total depth.

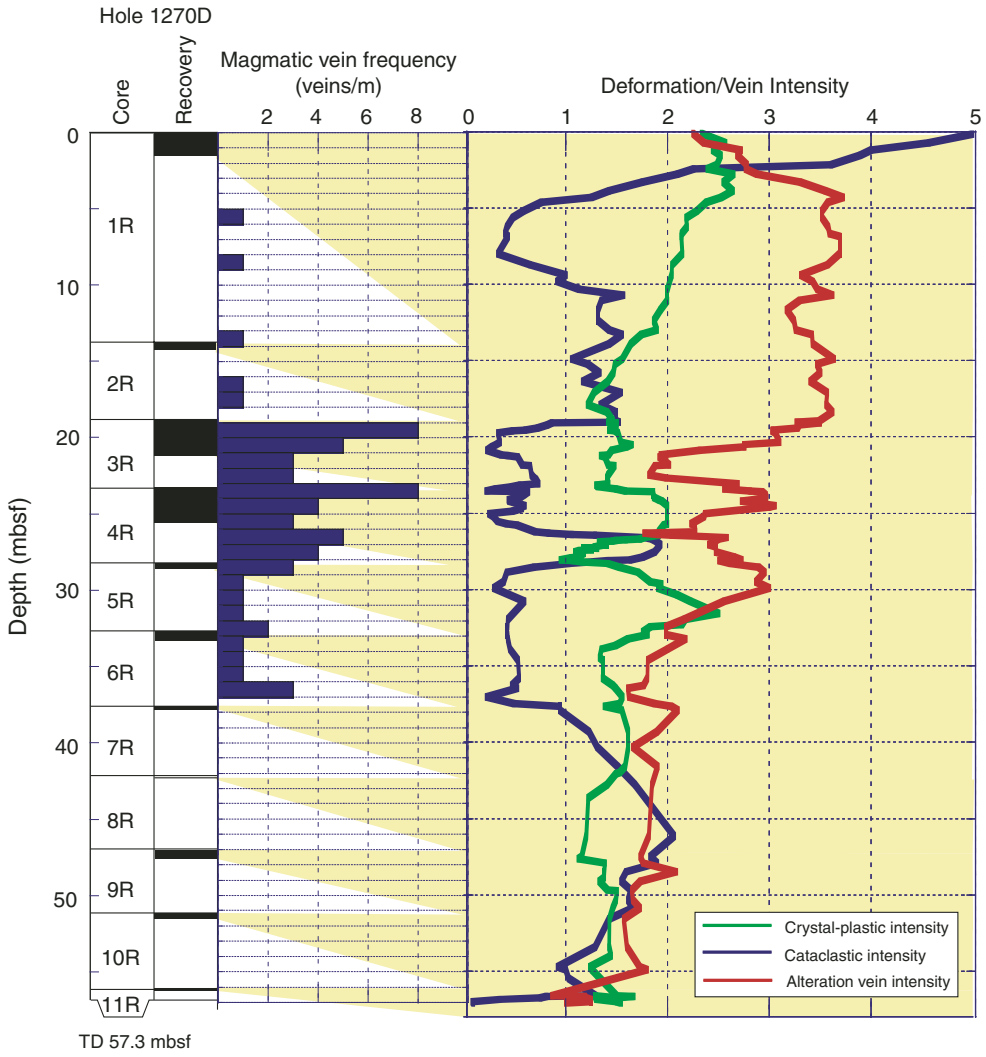

Figure F88. Plot of expanded depth vs. measured dip of brittle features in Hole 1270D. TD = total depth.

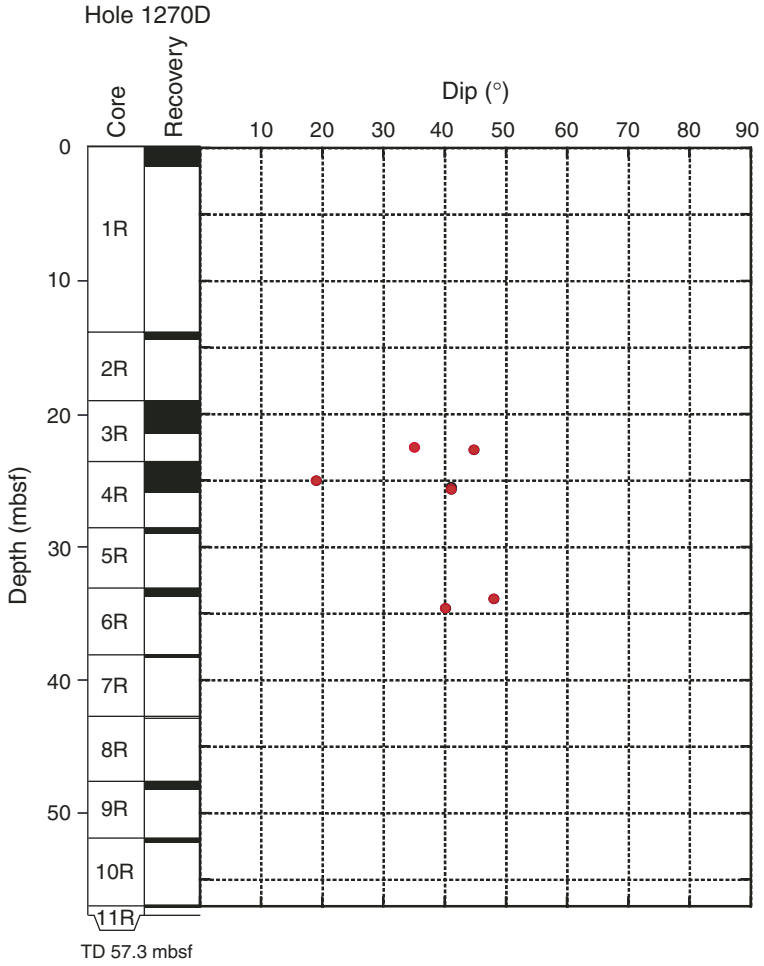

Figure F89. Close-up images of serpentine vein geometries from Hole 1270C and 1270D. **A, B.** Serpentine veins orthogonally cutting gabbroic veins in the serpentinized harzburgite. (A) Interval 209-1270C-1R-1, 33–40 cm. (B) Interval 209-1270D-3R-1, 52–62 cm. **C.** Serpentine veins cutting a subhorizontal brittle shear zone at 39–40 cm (interval 209-1270D-4R-1, 39–48 cm). **D.** Two generations of serpentine veins cutting gabbroic veins (interval 209-1270D-4R-1, 89–100 cm).

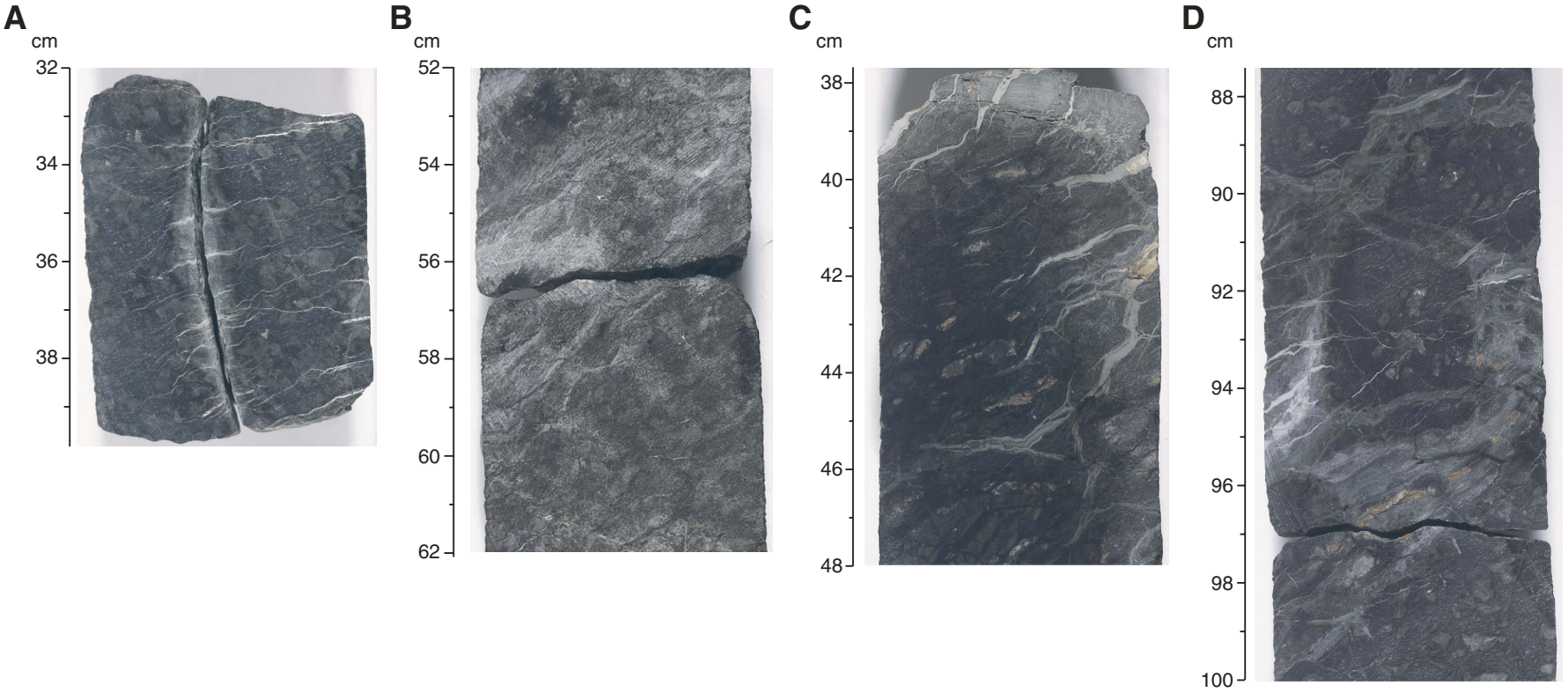

Figure F90. Lower hemisphere stereographic projection of poles to alteration veins and brittle shear zones measured in the core reference frame and rotated using the measured paleomagnetic declination back to a common orientation as described in **"Structures in Peridotite and Gabbroic Intrusions,"** p. 8, in "Mantle Upwelling, Melt Transport, and Igneous Crustal Accretion" in the "Leg 209 Summary" chapter. It was assumed that samples from these holes record normal polarity magnetization. **A.** Hole 1270C. (Continued on next page.)

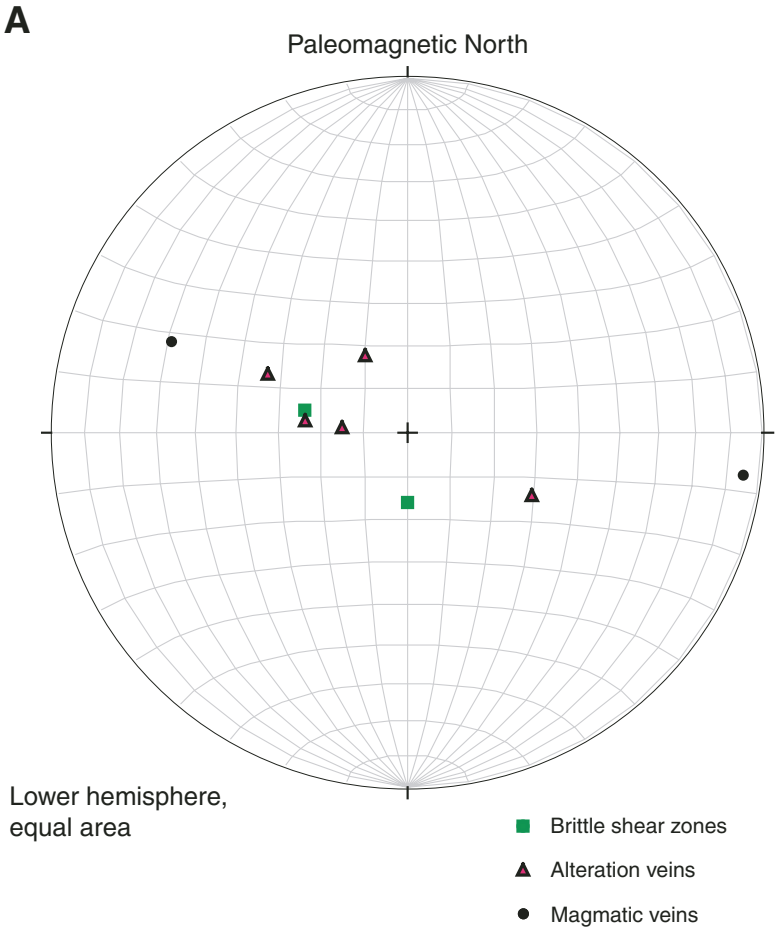

Figure F90 (continued). B. Hole 1270D.

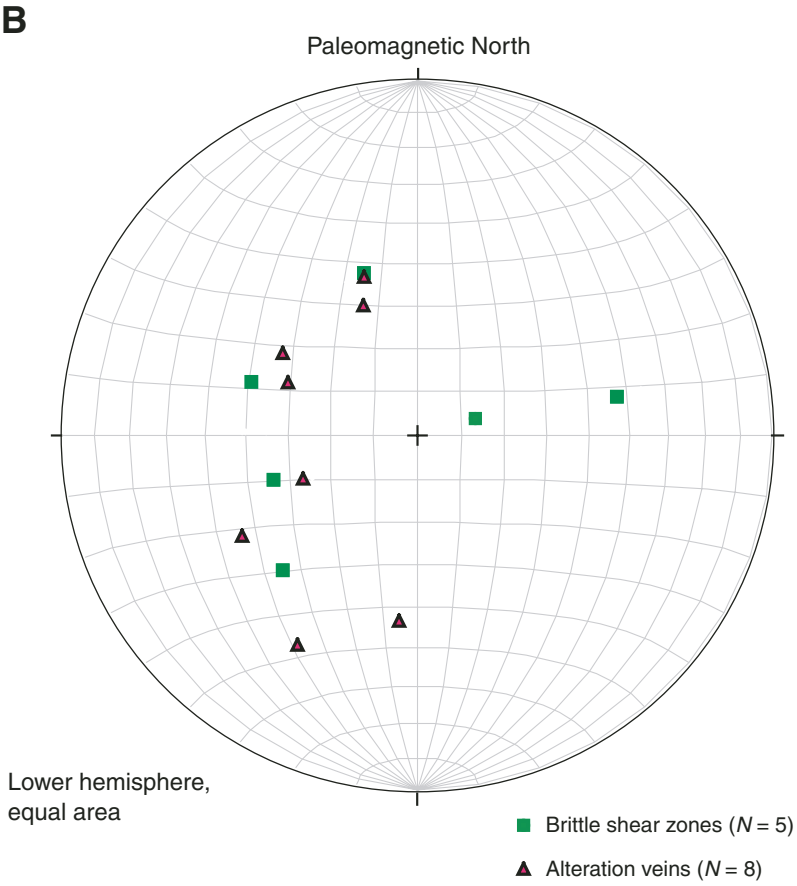

Figure F91. Photomicrograph showing vermicular spinel in harzburgite with protogranular texture (Sample **209-1270D-3R-1, 94–97 cm**) (cross-polarized and reflected light: blue + dark gray filters; field of view = 2.75 mm; image 1270D_029). A similar texture is present in Sample 209-1270C-1R-1, 72–75 cm. This texture is characteristic of harzburgite that was not affected by intrusion and deformation of magmatic veins in Holes 1270C and 1270D. This texture suggests that the harzburgite has not experienced significant ductile deformation since formation of the protogranular orthopyroxene and vermicular spinel.

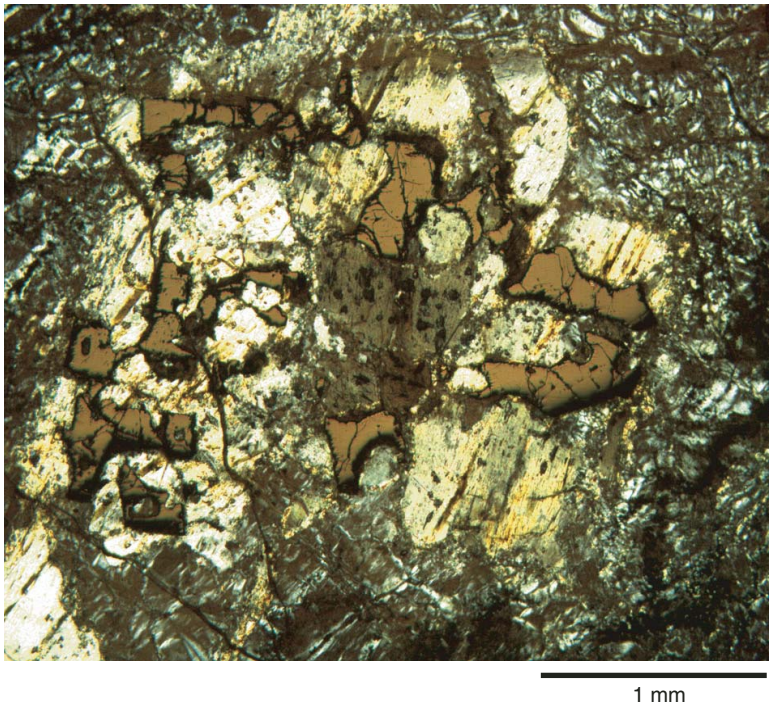

Figure F92. Schematic, true-scale cross section showing the relative locations of Holes 1270A, 1270B, and 1270D, their crystal-plastic intensity with depth, and the paleomagnetically reoriented dips of the fabrics in the holes. Rocks from Hole 1270B are assumed to record a reversed polarity, whereas rocks from Holes 1270C and 1270D are assumed to record normal polarity magnetization.

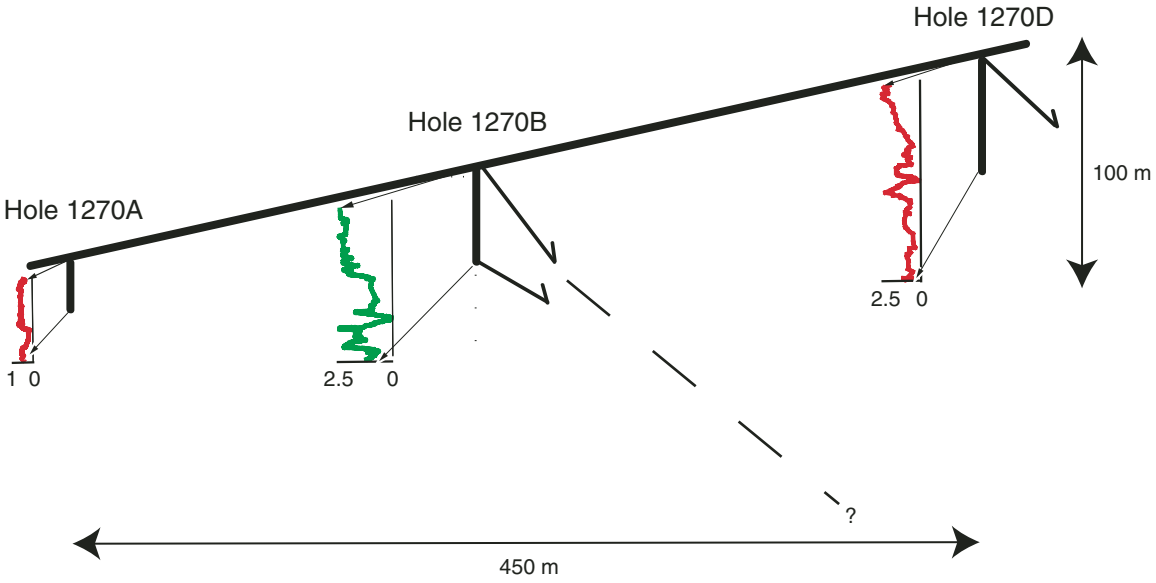

Figure F93. Recovery plots and unit boundaries for all four holes showing the location of the major crystal-plastic and brittle fault zones. Red and green arrows denote the downhole thickness of the fault or shear zones. TD = total depth.

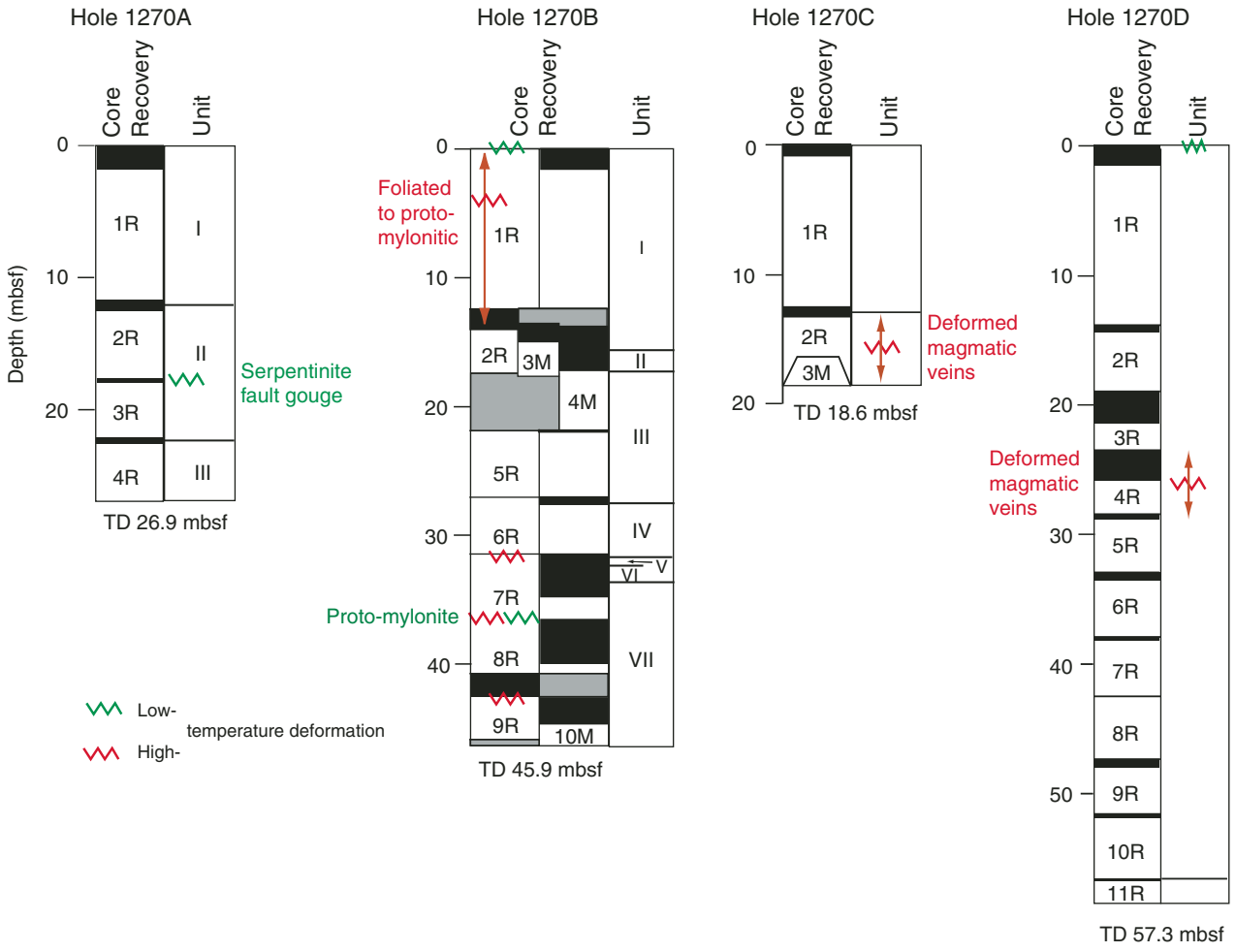

Figure F94. H_2O, SiO_2, and Fe_2O_3 vs. MgO and H_2O vs. SiO_2 for peridotites from Site 1270. Also shown for comparison are end-member compositions for lizardite and talc (Deer et al., 1992), and analyses of Site 920 serpentinites (Dilek et al., 1997a).

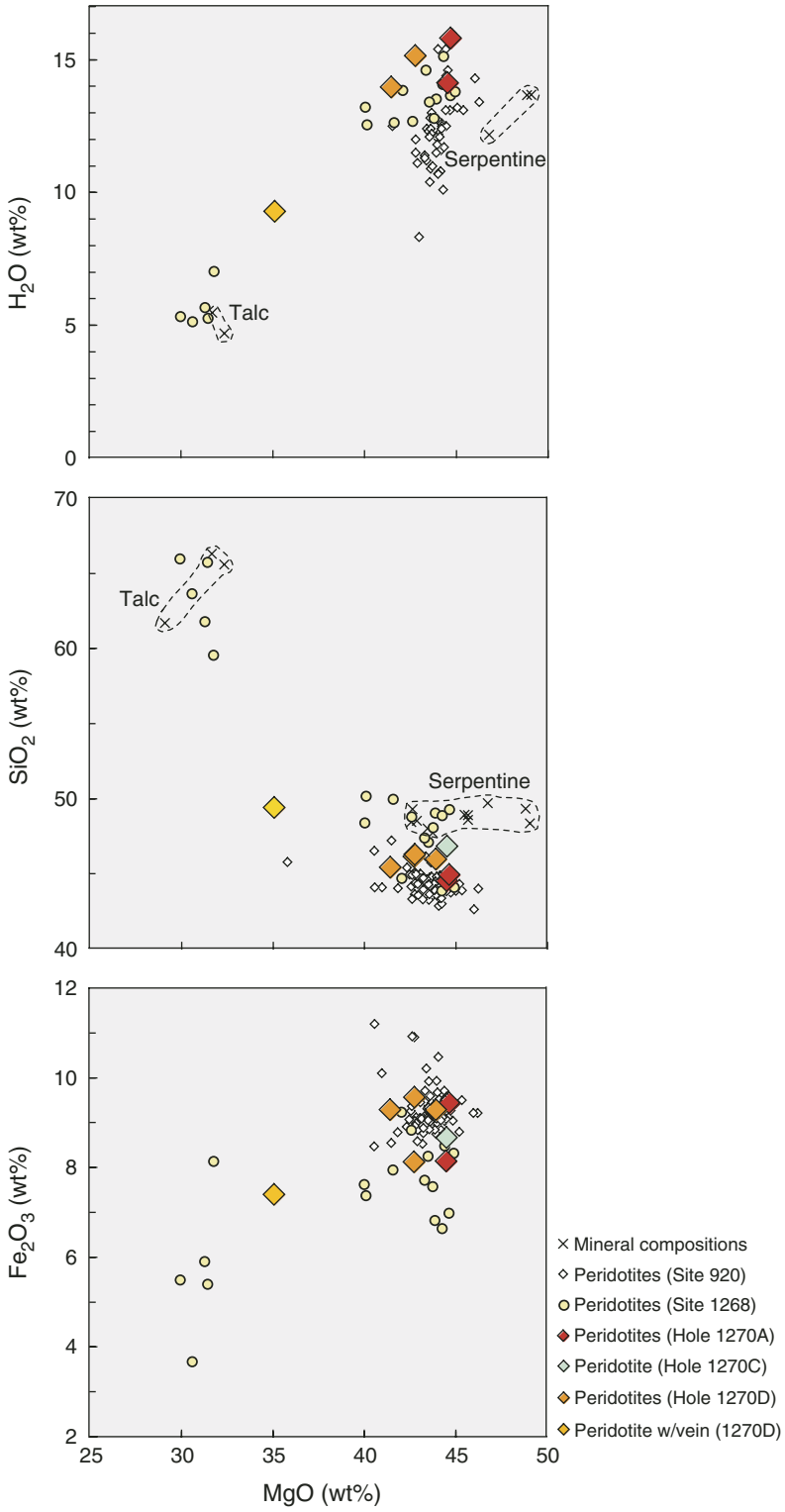

Figure F95. CaO vs. Al_2O_3 for peridotites from Site 1270. Sample 209-1270D-3R-1, 63–66 cm, is displaced from the other peridotites because of the presence of a gabbroic dike in the analyzed sample. The dashed line shows the trajectory expected for a melting residue of peridotite that initially had a Bulk Earth composition. Sample 209-1270D-1R-1, 70–74 cm, is enriched in CaO due to secondary carbonate precipitation.

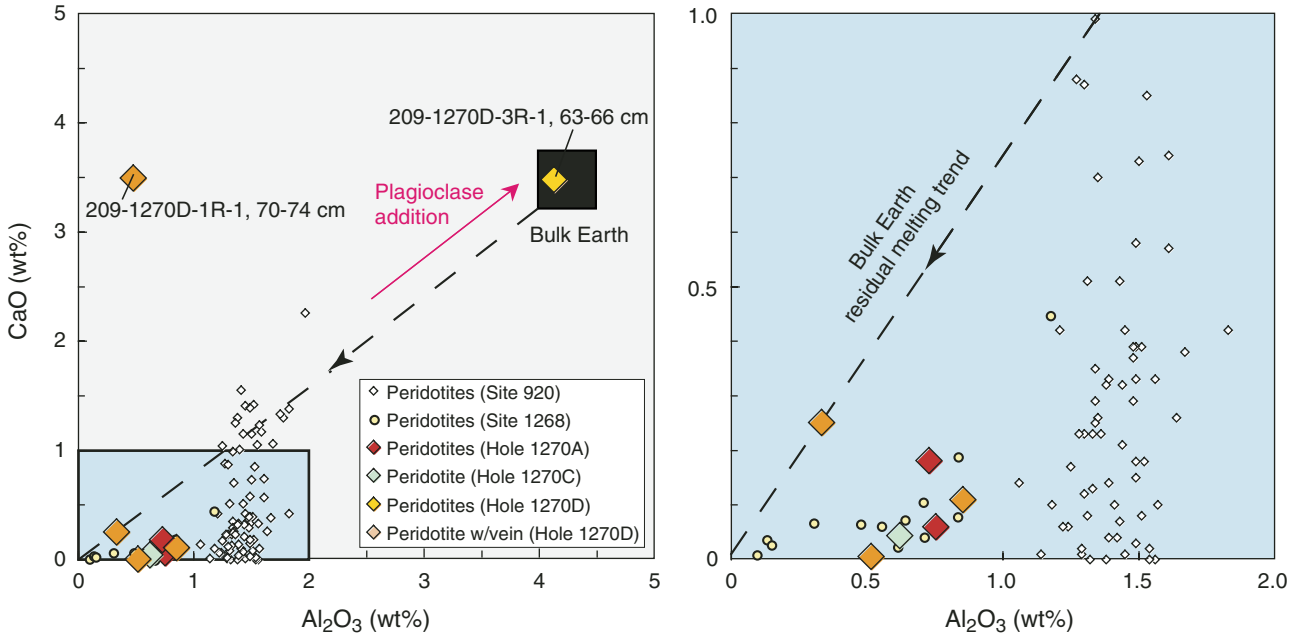

Figure F96. CaO vs. CO_2 for peridotites from Site 1270. Sample 209-1270D-1R-1, 70–74 cm, lies along a vector indicating the addition of carbonate during late-stage alteration, as do many serpentinized peridotites from Site 920.

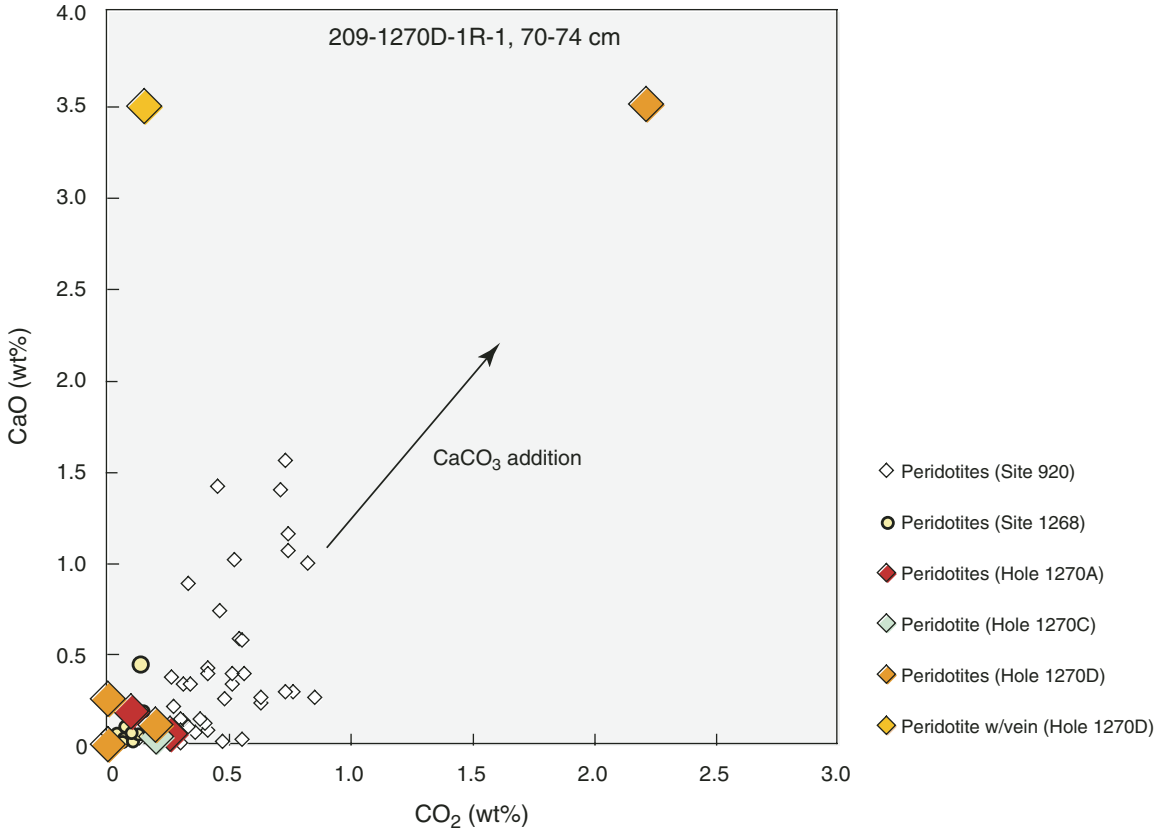

Figure F97. Sr vs. Al_2O_3 in peridotites from Site 1270. Published data on Leg 153 Site 920 peridotites (Casey, 1997) are shown for comparison. Dashed line = detection limit (DL) for Sr (5 ppm).

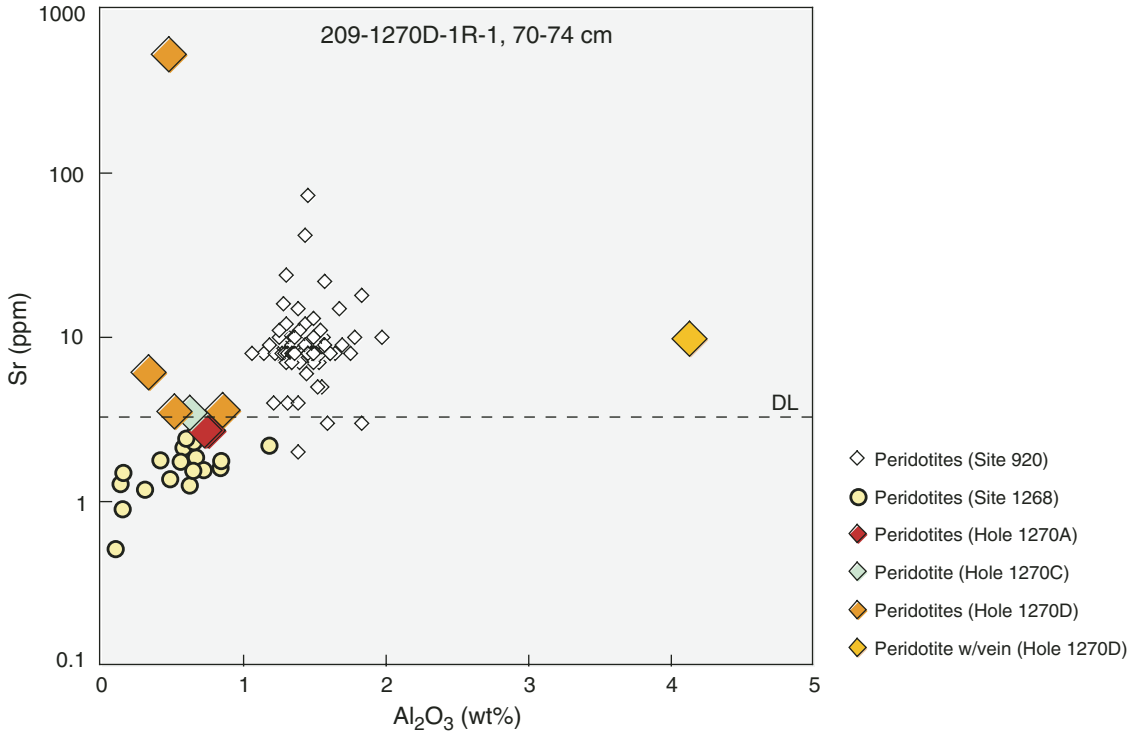

Figure F98. TiO_2, Zr, V, and Sc vs. Al_2O_3 in peridotites from Site 1270. Published data on Leg 153 Site 920 peridotites (Casey, 1997) are shown for comparison. Dashed lines = detection limits (DL) for Sc, TiO_2, and Zr.

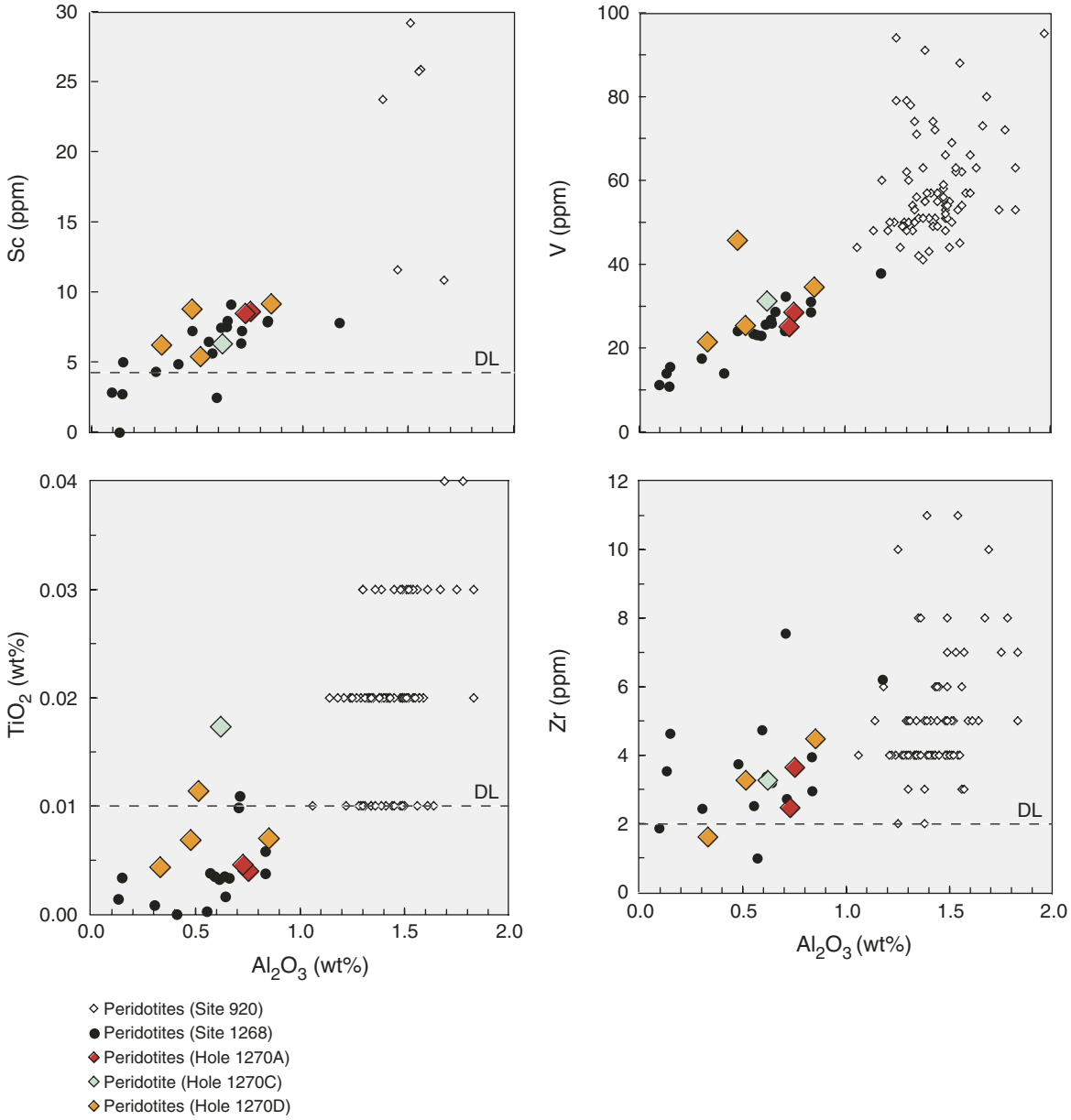

Figure F99. Ni and Cr vs. Al_2O_3 in peridotites from Site 1270. Published data on Leg 153 Site 920 peridotites (Casey, 1997) are shown for comparison.

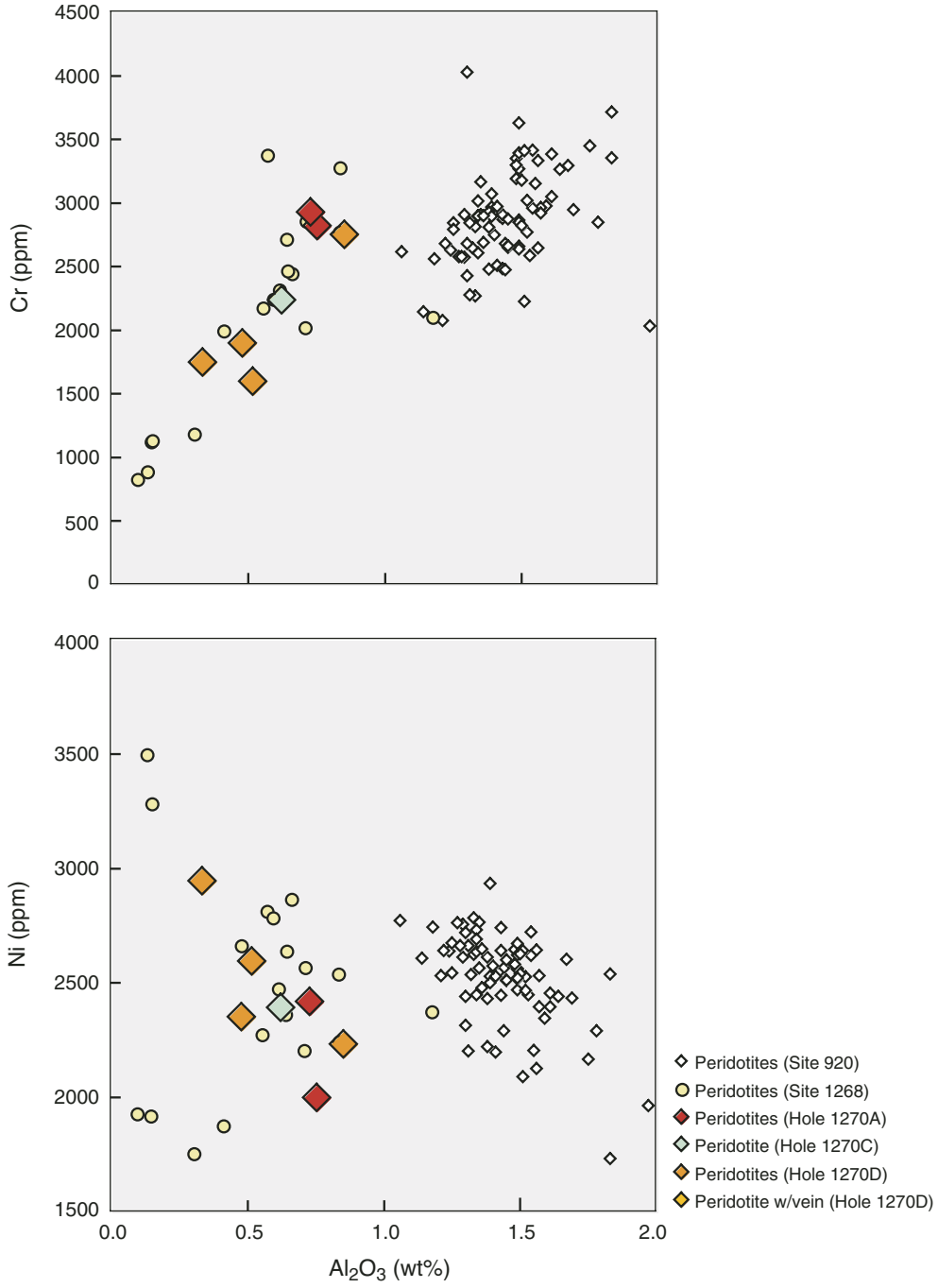

Figure F100. MgO, Al_2O_3, and H_2O vs. SiO_2 in gabbros from Hole 1270B. Site 1268 gabbros and average mineral compositions from Oman are shown for comparison (Lachize, 1993). The Hole 1270B gabbros are somewhat depleted in SiO_2 when compared to average mineral compositions from Oman and to the Site 1268 gabbros, probably because Hole 1270B gabbros are richer in Fe-Ti oxides than Oman and Site 1268 gabbros. Plag = plagioclase, opx = orthopyroxene.

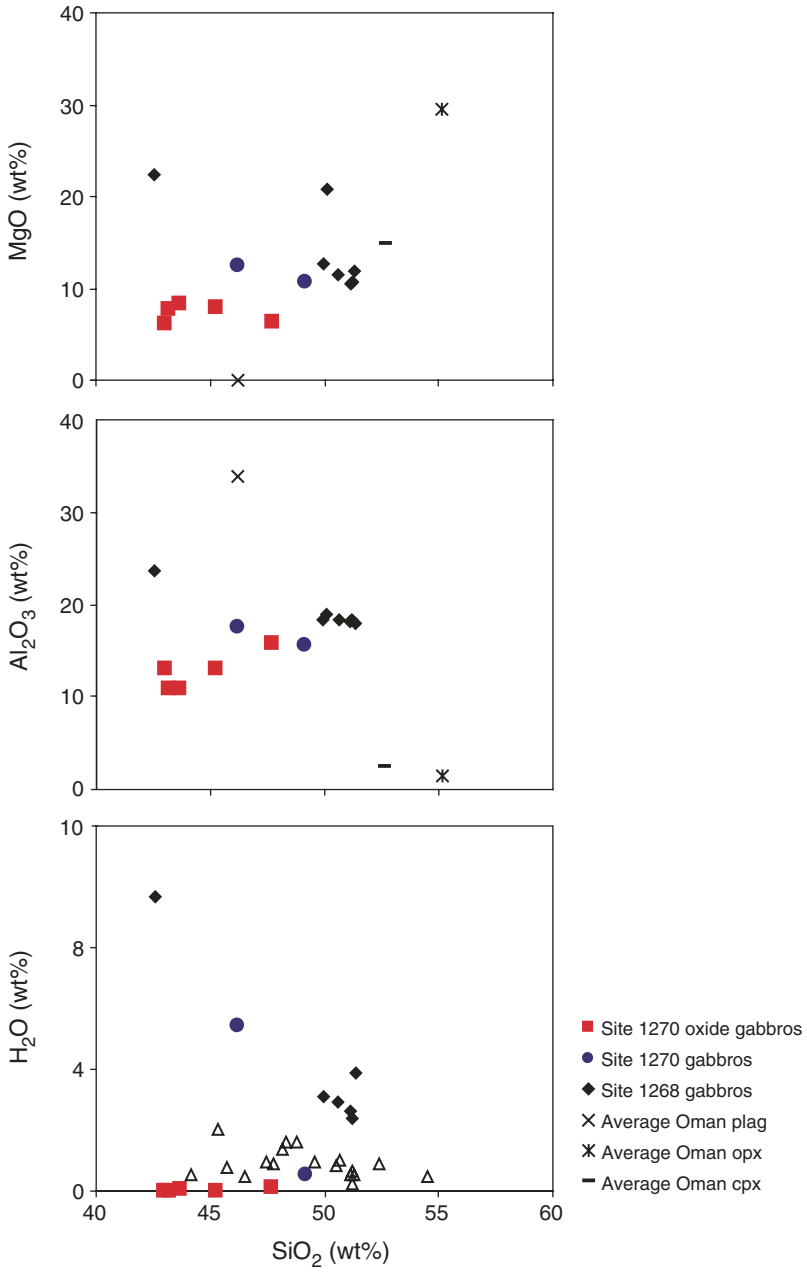

Figure F101. Fe_2O_3 vs. TiO_2 in gabbros from Hole 1270B. Also shown are data from Leg 153 gabbros (Agar et al., 1997) and from Hole 735B (Dick, Natland, Miller, et al., 1999). Igneous units at Site 1270 are from the igneous petrology group. The gold circle represents a computed, reconstituted composition for the gabbro vein contained within Sample 209-1270D-3R-1, 63–66 cm (see text for discussion). Hz = harzburgite.

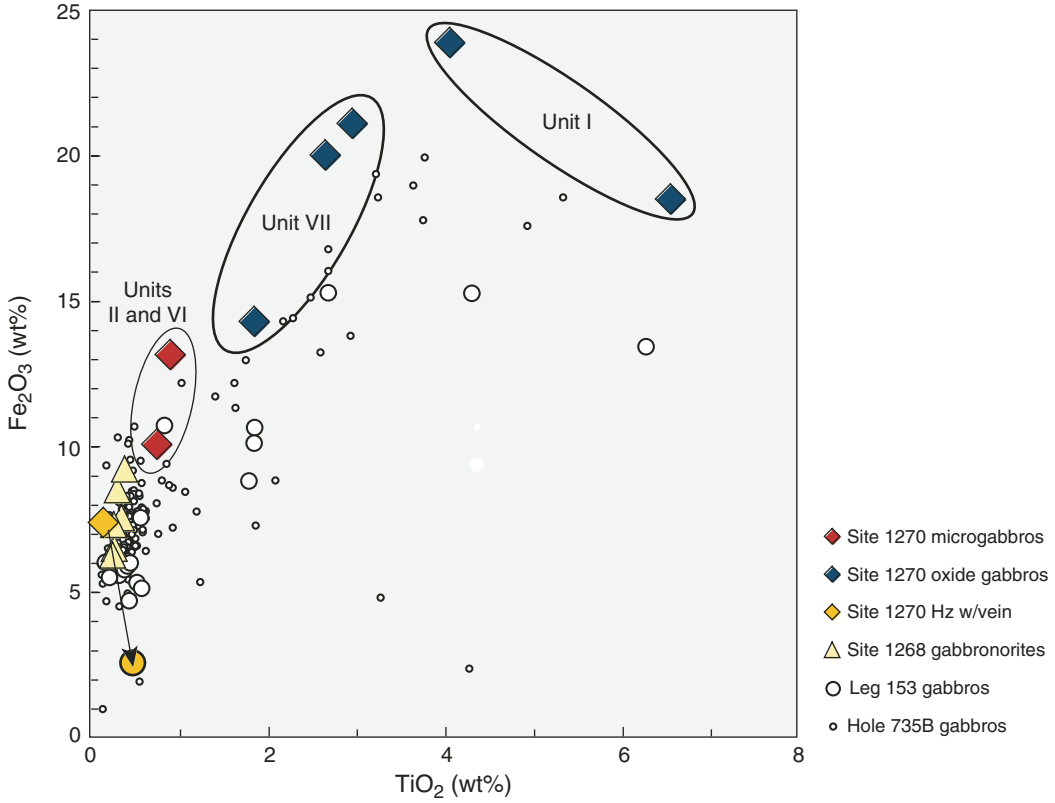

Figure F102. TiO_2 and Cr vs. SiO_2 in gabbros from Hole 1270B. Published data for Leg 153 gabbros (Agar et al. 1997) and Hole 735B (Dick, Natland, and Miller, et al., 1999) are shown for comparison. Dashed line = detection limit (DL) for Cr.

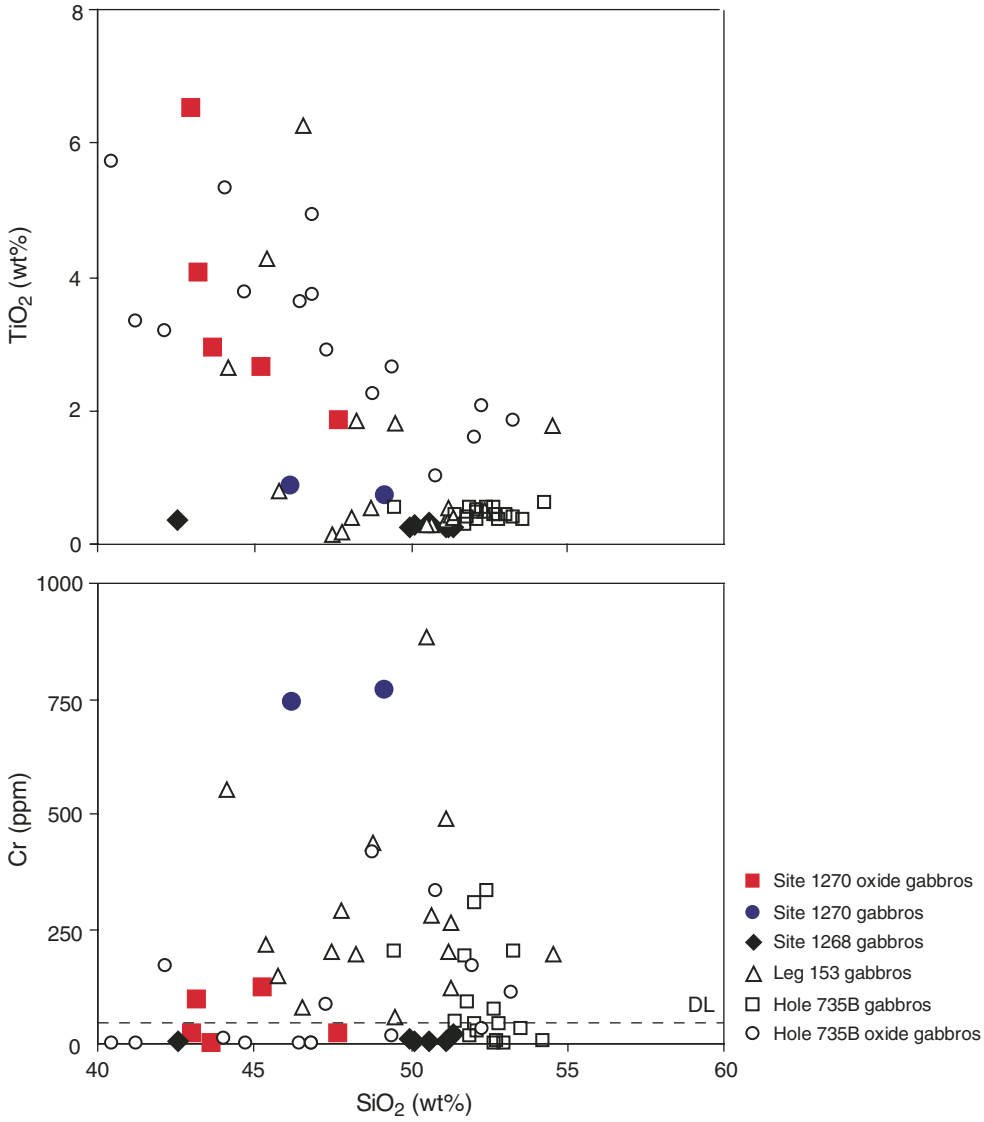

Figure F103. V and Zr vs. TiO_2 for gabbros from Hole 1270B. Also shown are data from Leg 153 gabbros (Agar et al., 1997) and from Hole 735B (Dick, Natland, and Miller, et al., 1999). Lines indicate Ti/V elemental weight ratios (ppm/ppm) of 10 and 50. Hz = harzburgite.

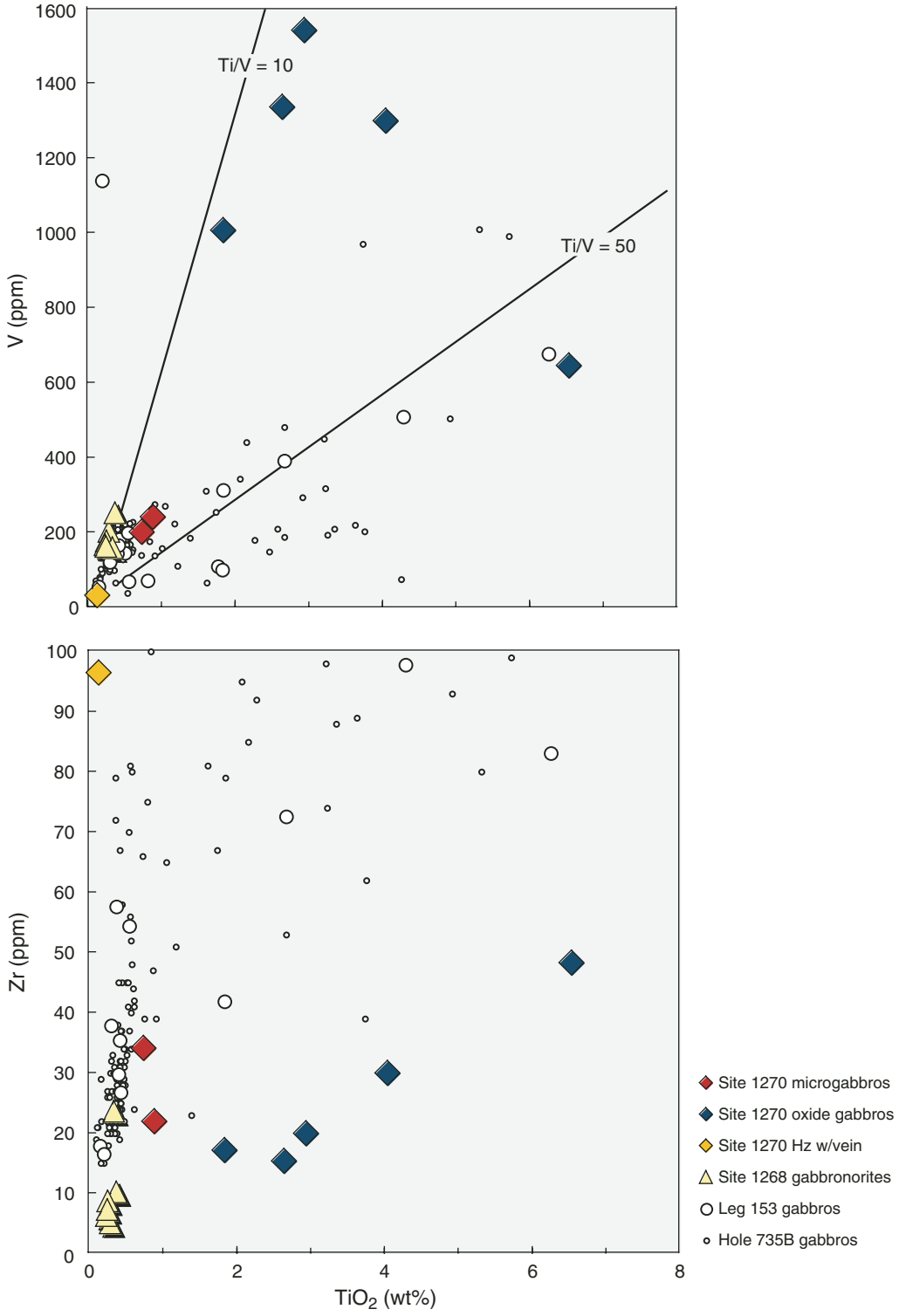

Figure F104. Sc vs. V and Zr vs. Y for gabbros from Hole 1270B. Also shown are data from Leg 153 gabbros (Agar et al., 1997) and from Hole 735B (Dick, Natland, and Miller, et al., 1999). The gold circle represents a computed, reconstituted composition for the gabbroic vein in Sample 209-1270D-3R-1, 63–66 cm (see text for discussion). Hz = harzburgite.

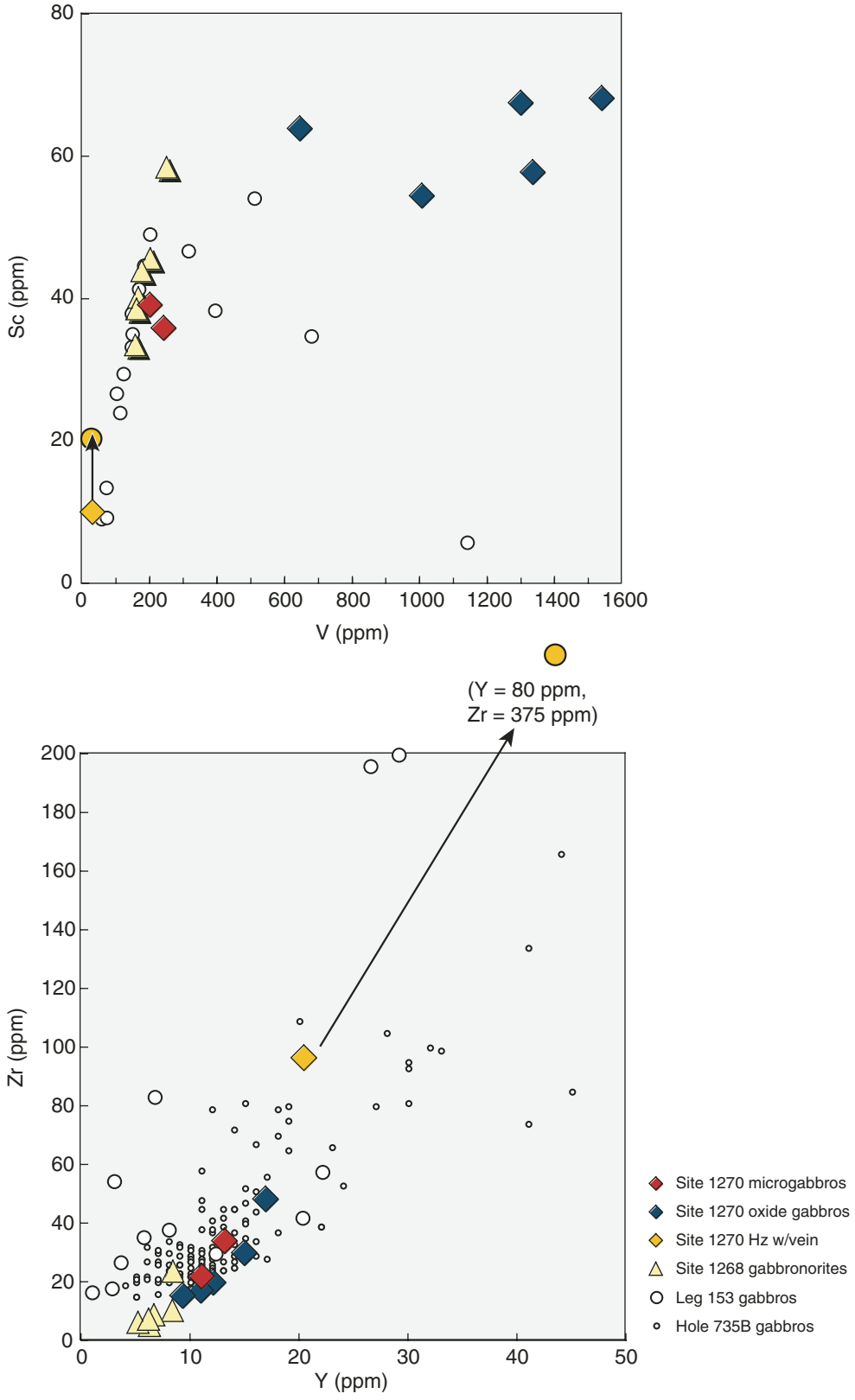

Figure F105. Magnetic susceptibility of cores from Holes 1270A through 12790D, measured on the MST. TD = total depth.

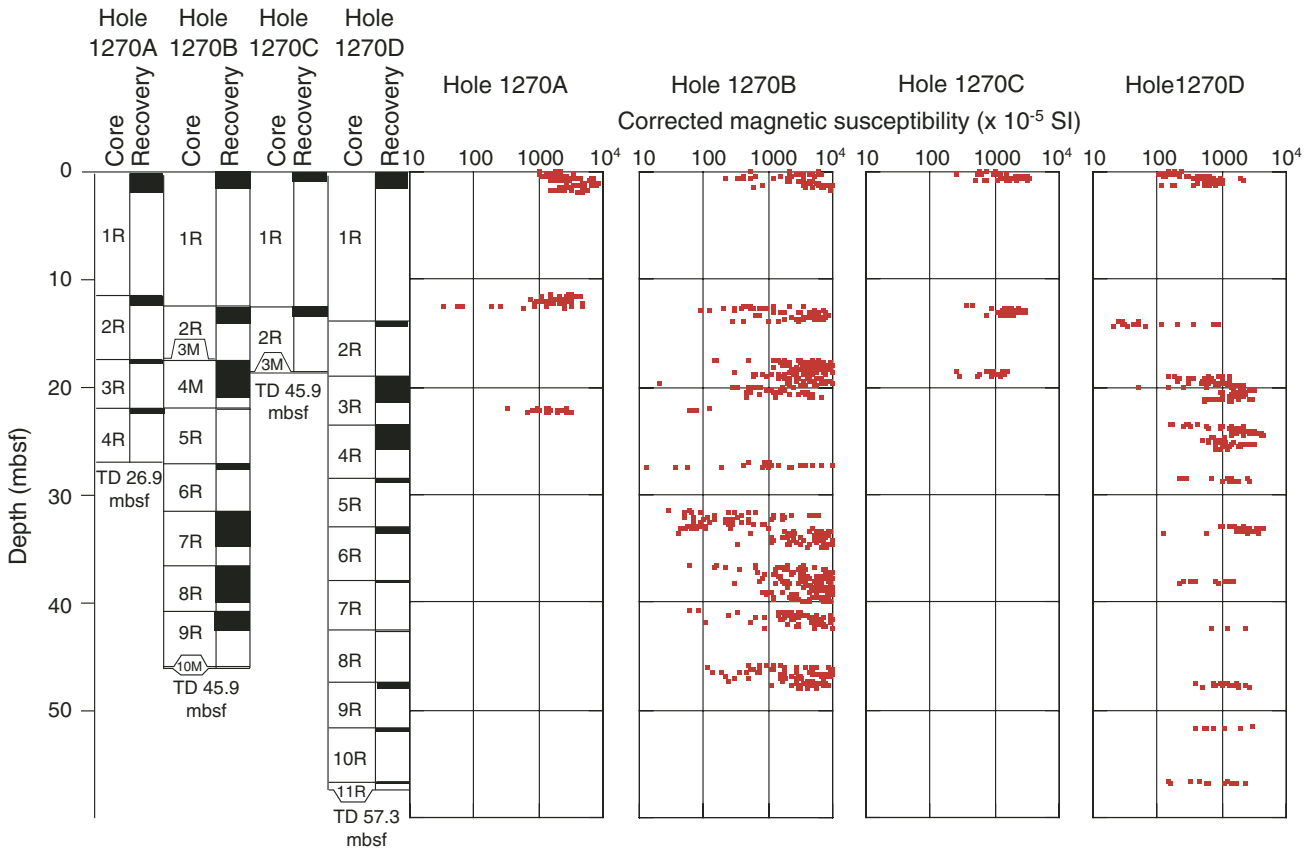

Figure F106. Thermal conductivity of peridotite and gabbro samples from Sites 1268 and 1270, compared with values from Legs 147 (Gillis, Mével, Allan, et al., 1993) and 153 (Cannat, Karson, Miller, et al., 1995).

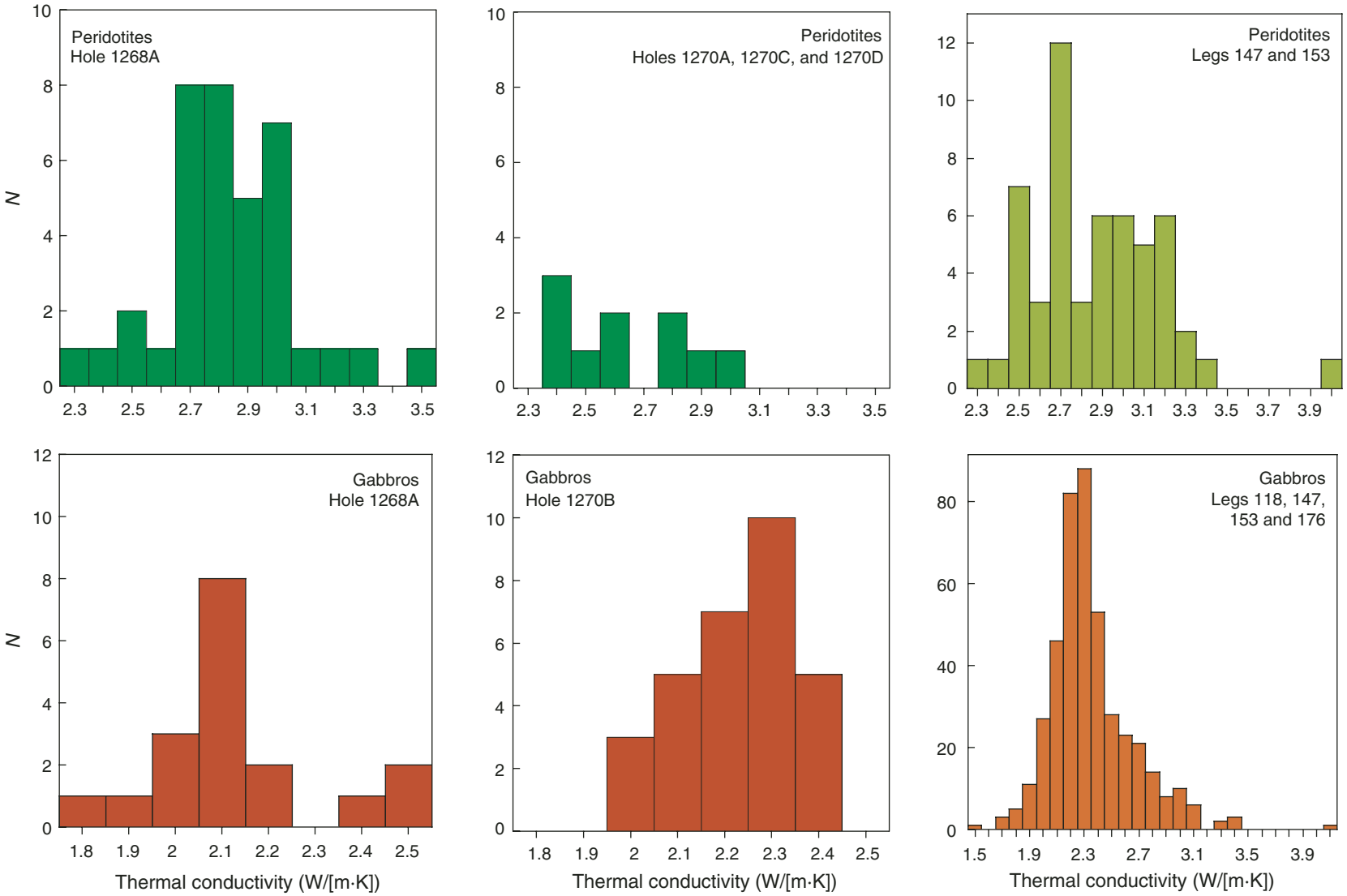

Figure F107. Apparent thermal conductivity anisotropy in peridotite and gabbro samples from Sites 1268 and 1270.

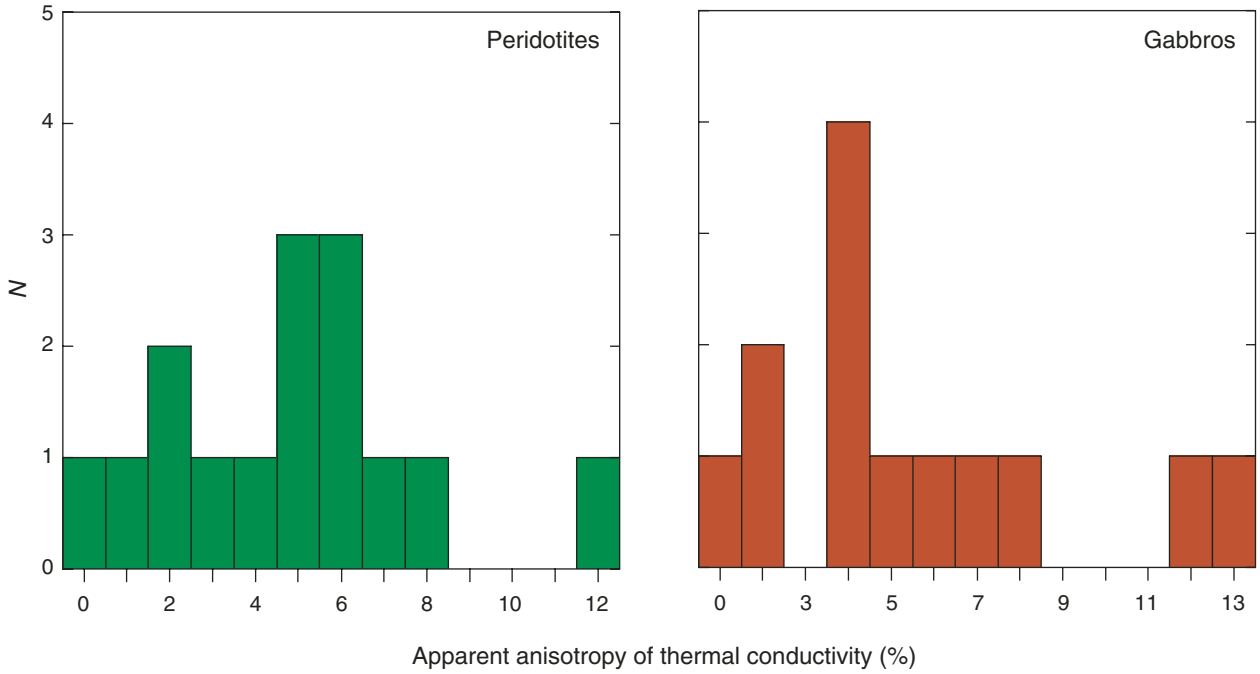

Figure F108. Apparent thermal conductivity anisotropy in Sample 209-1270B-1R-1, 120–128 cm. The error bars show the standard errors in our measurements (Table T6, p. 180). Blue squares are the regular series of three measurements made earlier a few days before the series of 10° interval measurements (red circles).

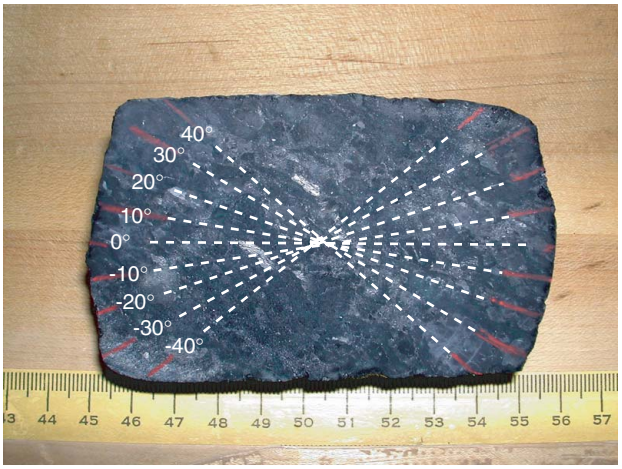

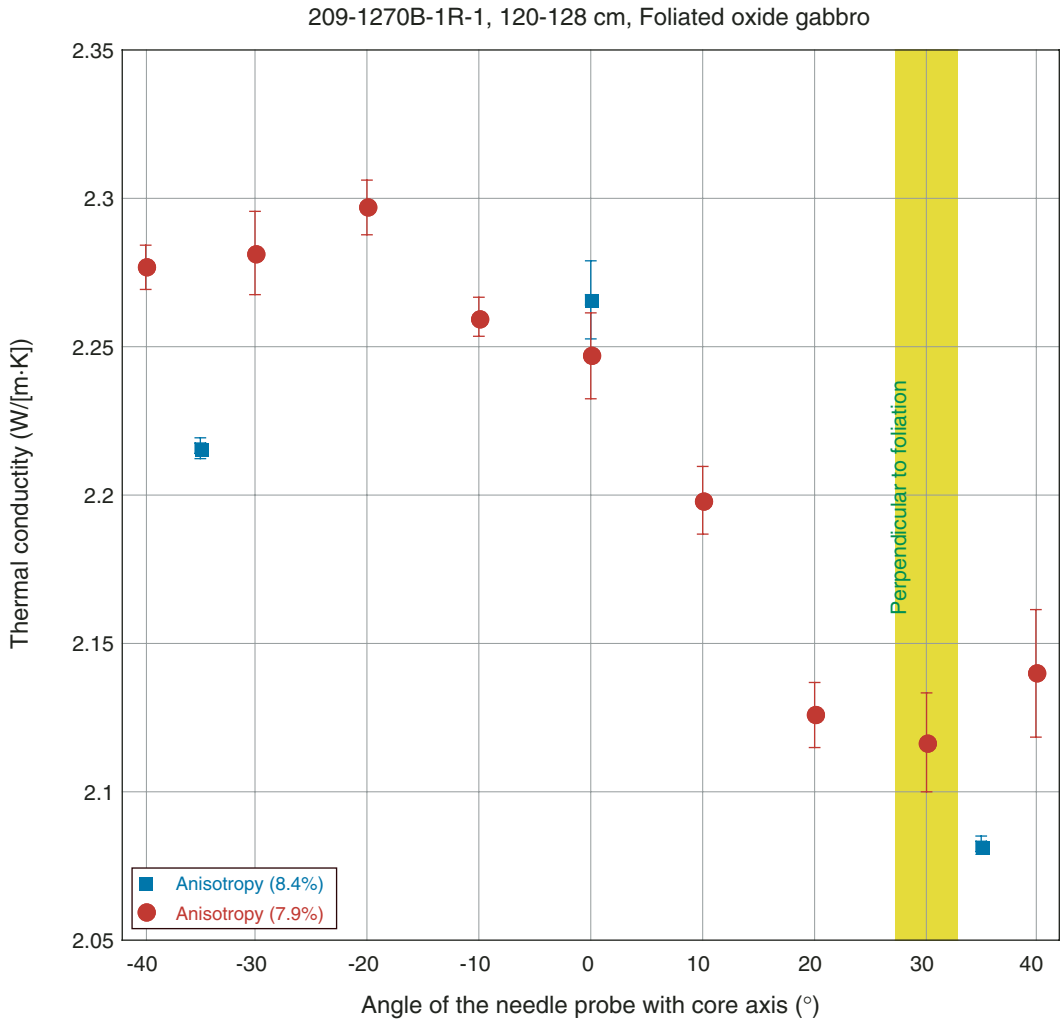

Figure F109. *P*-wave velocity vs. wet bulk density in peridotite and gabbro samples from Site 1270, compared with data from Legs 147 (Gillis, Mével, Allan, et al., 1993) and 153, as well as Site 1268.

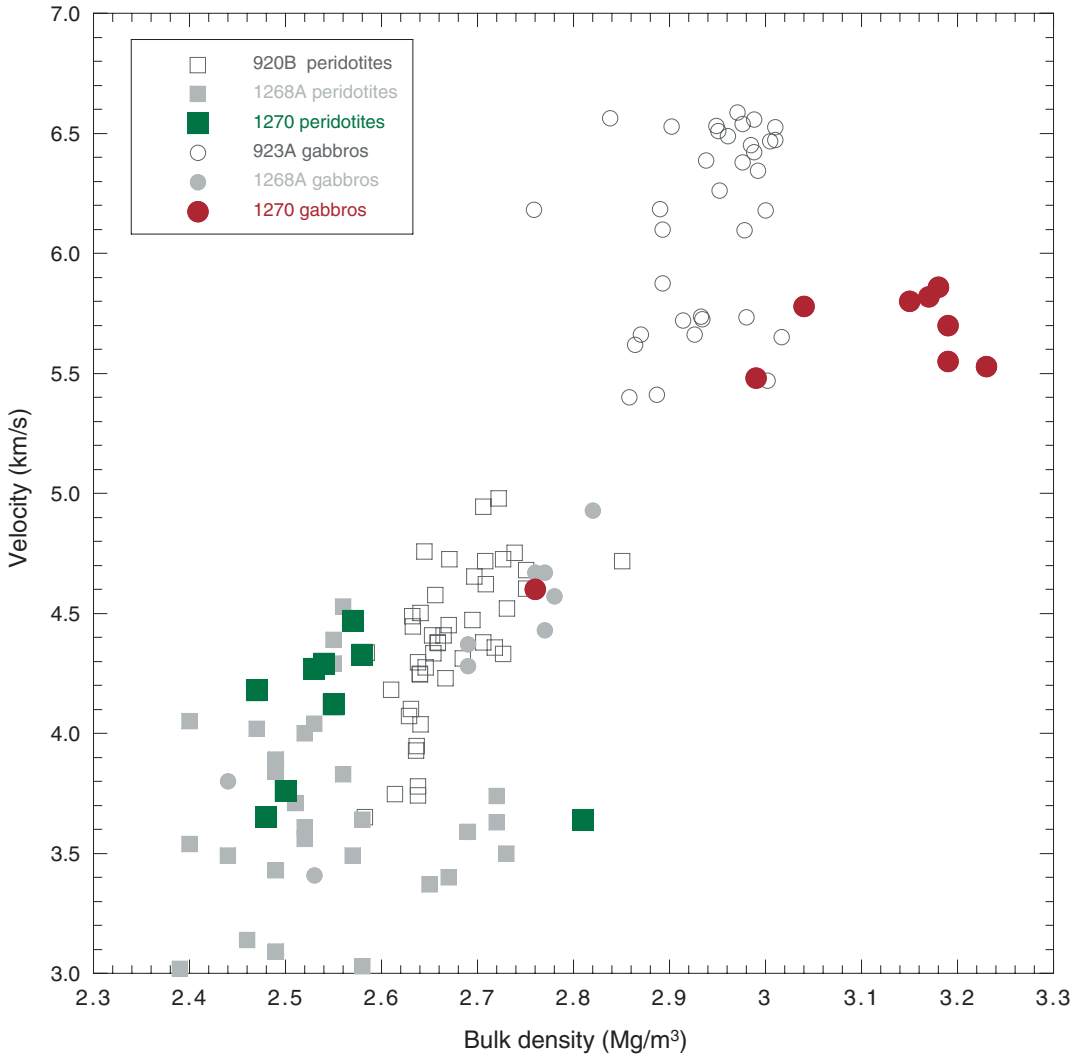

Figure F110. Representative vector endpoint demagnetization diagrams of long-core measurements from Hole 1270B. The low-coercivity drilling component accounts for >90% of the remanence. Although the remanence remaining after AF treatment to 20 mT is insignificant, the projection of the data on the stereonet shows great circle trends from nearly vertical directions to (**A**) very shallow negative inclinations (Section 209-1270B-1R-1, 96 cm) or (**B**) horizontal directions (Section 209-1270B-3M-1, 114 cm). A detailed view of the orthogonal plot at high demagnetization levels shows that directions pass the origin and a higher-coercivity component is present in most of the samples. NRM = natural remanent magnetization. Solid circles = projections onto the horizontal plane and open circles = projections onto the vertical plane.

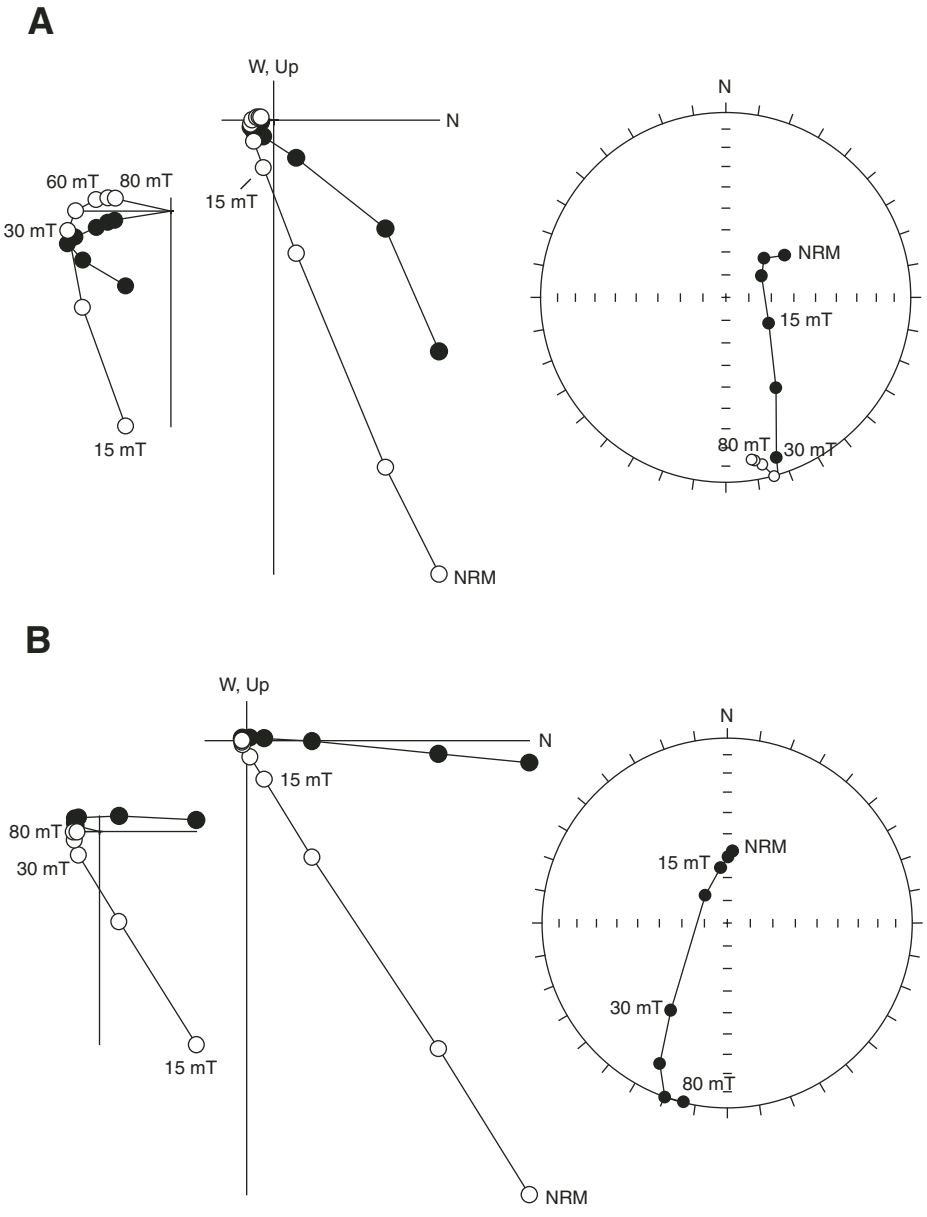

Figure F111. Vector endpoint demagnetization diagrams for discrete samples from Hole 1270B illustrating the range of steep, presumably drilling-induced overprints. **A.** Sample 209-1270B-7R-1, 105–107 cm. **B.** Sample 209-1270B-4M-2, 125–127 cm. **C.** Sample 209-1270B-10M-1, 27–27 cm. NRM = natural remanent magnetization. Solid circles = projections onto the horizontal plane and open circles = projections onto the vertical plane.

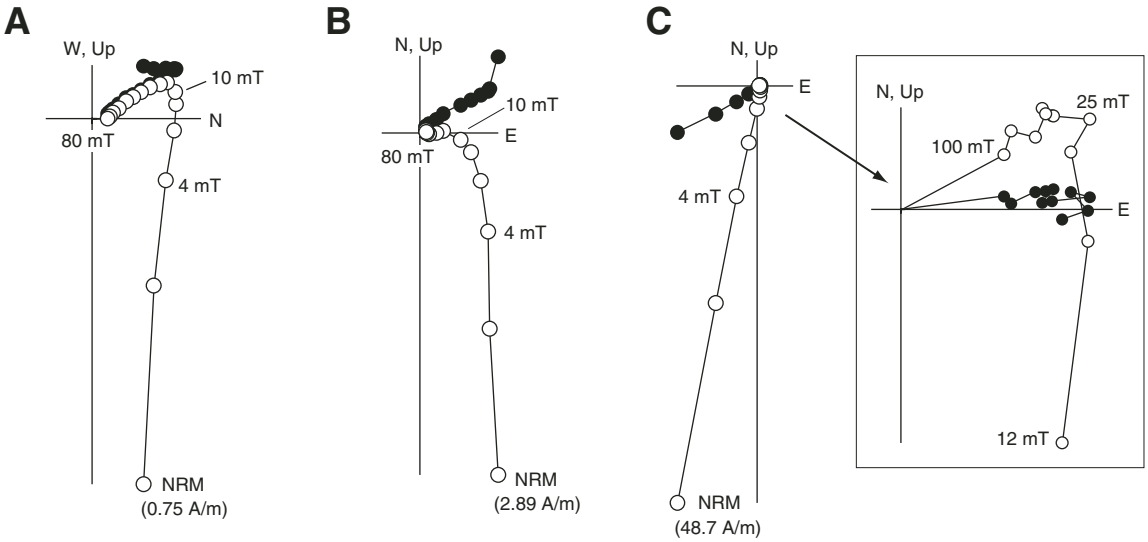

Figure F112. Normalized magnetization decay curves of discrete samples from Holes 1270B (below) and 1270C and 1270D (above). Decay is plotted as a function of the vector difference sum, the cumulative sum of vector differences between demagnetization steps. The two slopes evident in samples from Hole 1270B are correlated with the presence of two distinct remanences, a partial low-field IRM induced during drilling, and a characteristic remanence that is stable over a higher range of coercivities. Steep slopes below 10 mT correspond to the presence of coarse-grained magnetite. In contrast, samples from Holes 1270C and 1270D yield uniform slopes over the whole coercivity range, indicating a more homogenous grain size distribution and less significant contribution from very low coercivity grains. *B* = the peak induction during demagnetization.

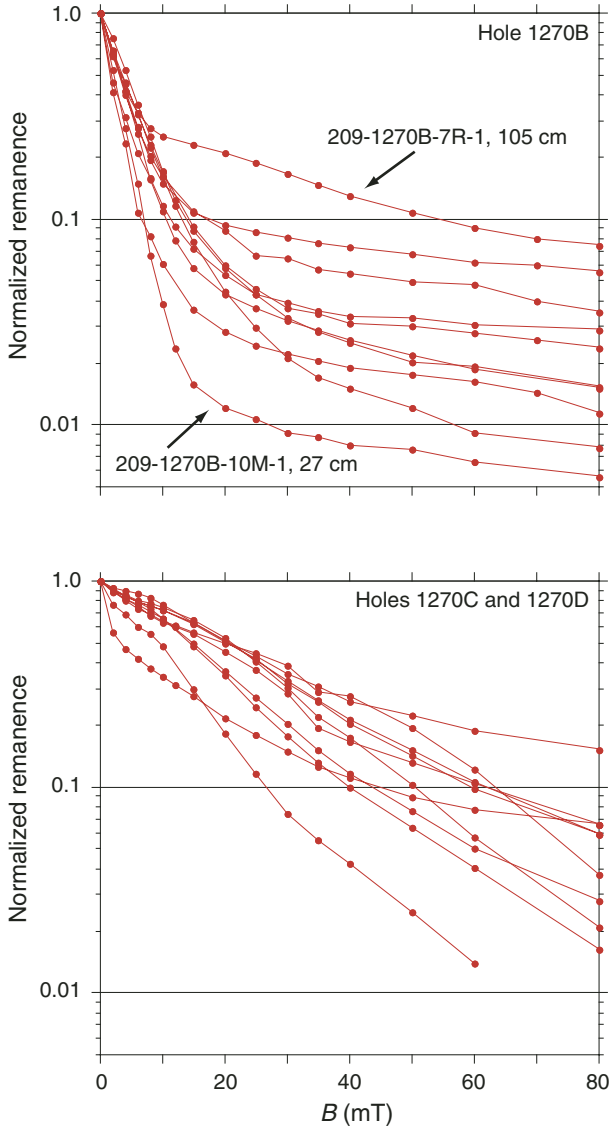

Figure F113. Vector endpoint demagnetization diagrams of discrete samples from Holes 1270C and 1270D. The drilling-induced overprint is successfully removed at 6–10 mT. The stable characteristic remanence represents >50% of the natural remanent magnetization (NRM) and yields both positive and negative inclinations. **A.** Sample 209-1270C-1R-1, 50–52 cm. **B.** Sample 209-1270C-2R-1, 67–69 cm. **C.** Sample 209-1270D-4R-1, 91–93 cm. **D.** Sample 209-1270D-6R-1, 33–35 cm. Solid circles = projections onto the horizontal plane and open circles = projections onto the vertical plane.

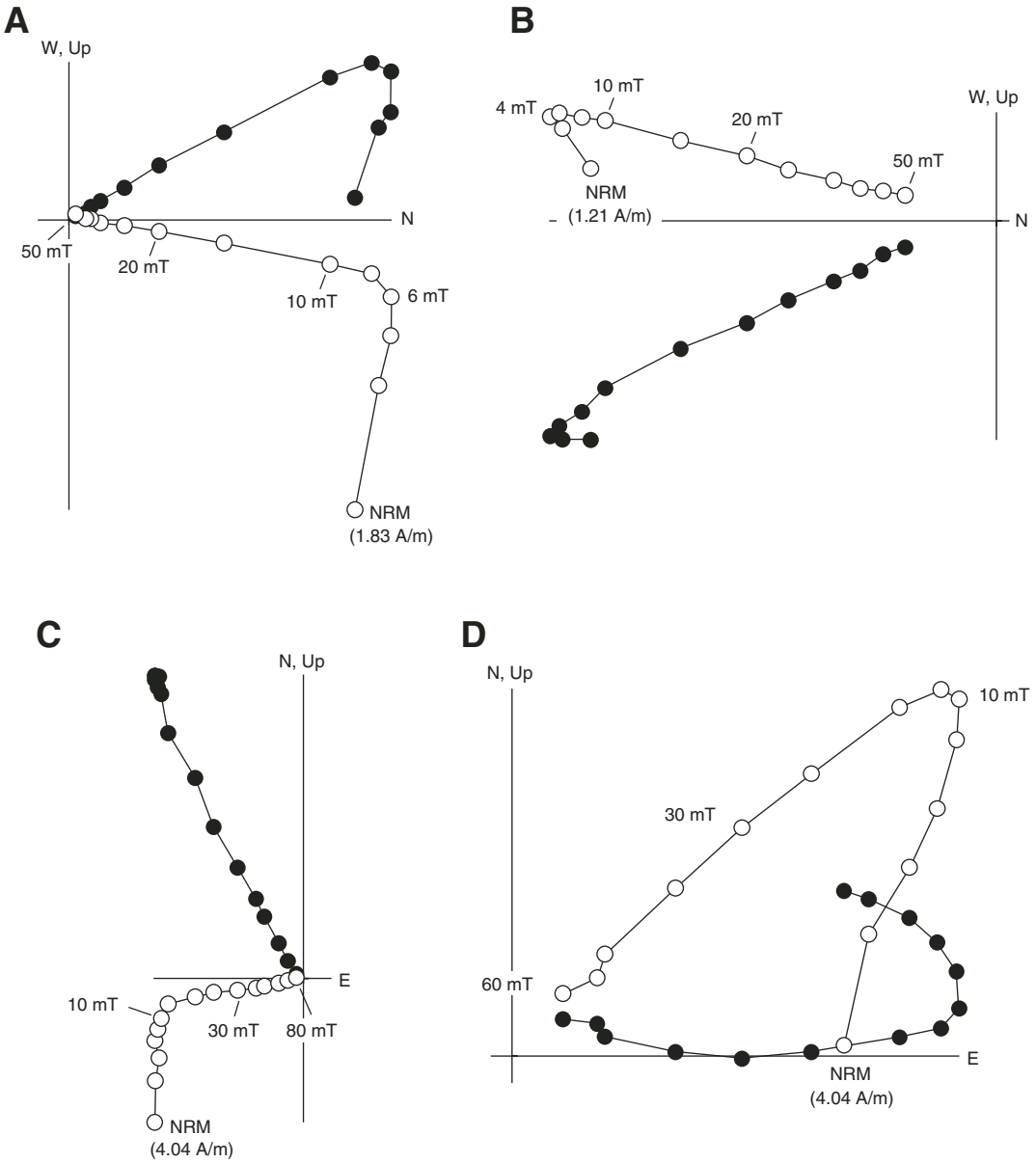

Figure F114. A. Histograms of paleomagnetic inclinations from Holes 1270A and 1270B (top) and 1270C and 1270D (bottom). Note the difference between inclinations determined from discrete samples (black) and archive halves (gray). **B.** Vector endpoint diagrams for the same depth interval determined from a discrete sample (top) (Sample 209-1270D-3R-2, 49–51 cm) and an archive half (bottom) (Section 209-1270D-3R-2, 50 cm). NRM = natural remanent magnetization. Solid circles = projections onto the horizontal plane and open circles = projections onto the vertical plane.

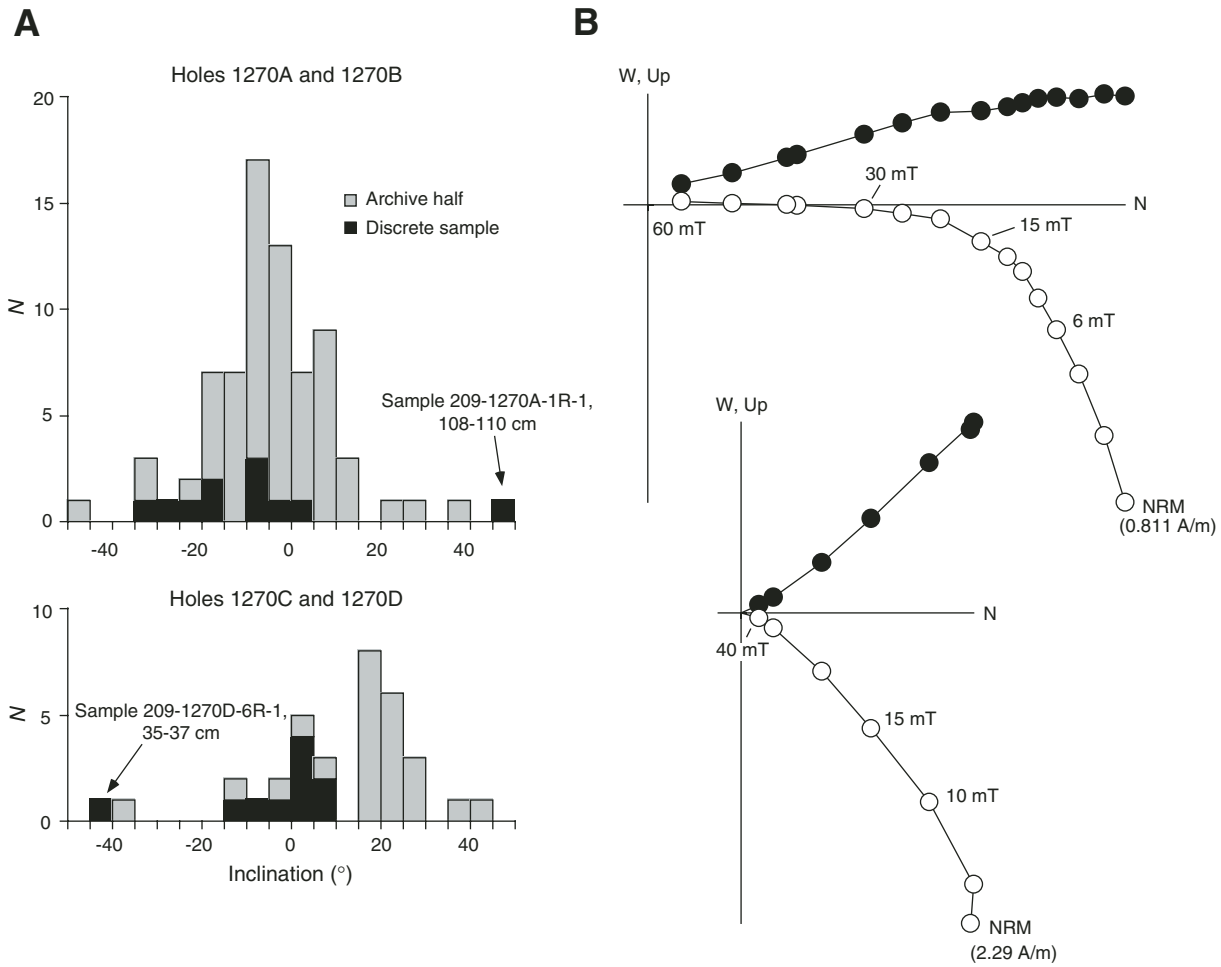

Figure F115. Comparison of remanent declination values from discrete samples and archive halves. All pairs of discrete sample and archive-half data from Holes 1270C and 1270D agree within 20° (shaded region). Larger differences are evident for Hole 1270B, where the characteristic remanence represents a smaller portion of the NRM.

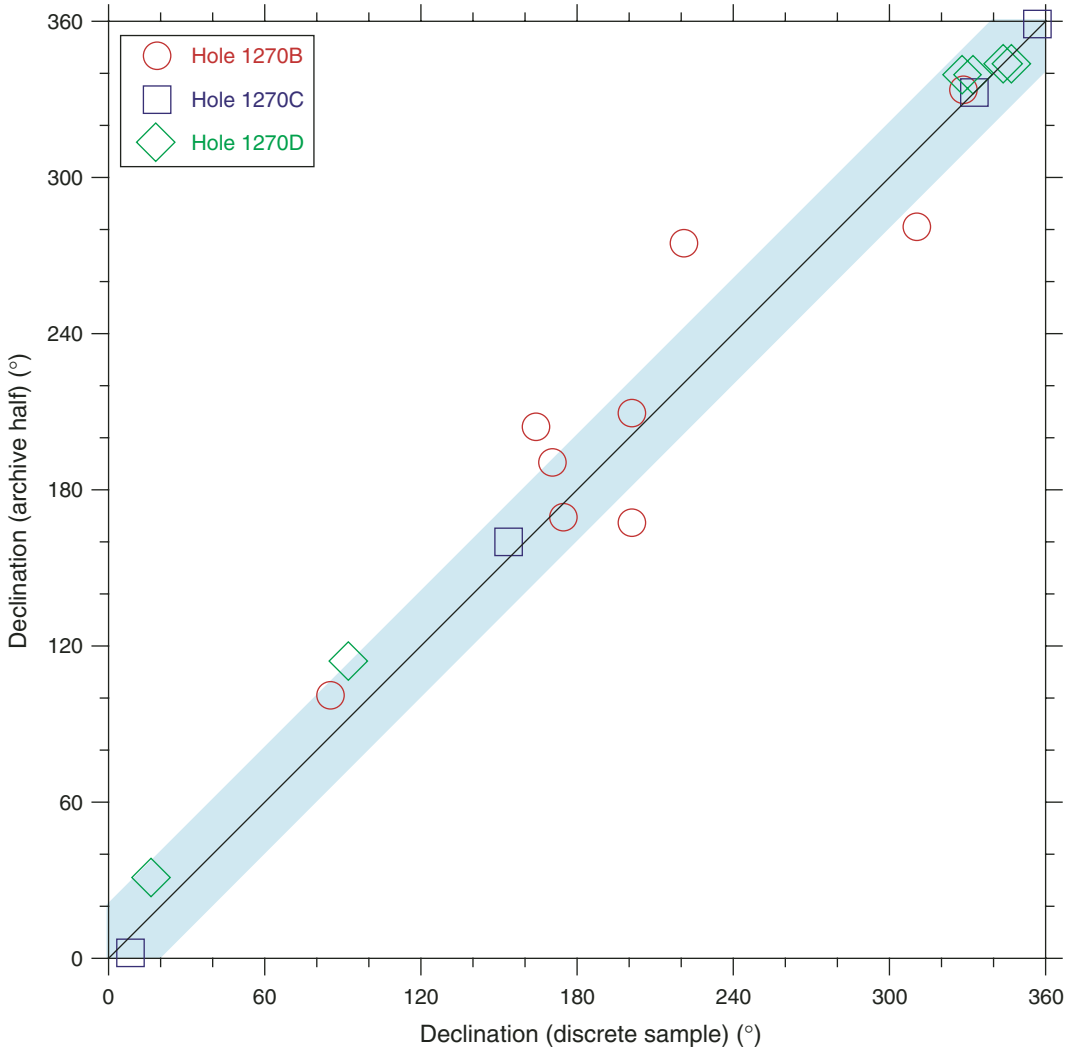

Figure F116. Rose diagram of paleomagnetic declinations from discrete samples (black) and long-core measurements (gray) from (**A**) Hole 1270B and (**B**) Holes 1270C and 1270D. Directions are projected into archive-half coordinates, which have structural meaning since the core splitting face is routinely traced orthogonal to the strike of the foliation (**C**). As a result, archive-half +x and +y axes tend to parallel the strike and dip directions, respectively (right-hand rule nomenclature). The nonrandom distribution of declinations demonstrates the existence of a preferred orientation of the main planar structures in both the gabbros from Hole 1270B and the peridotites from Holes 1270C and 1270D.

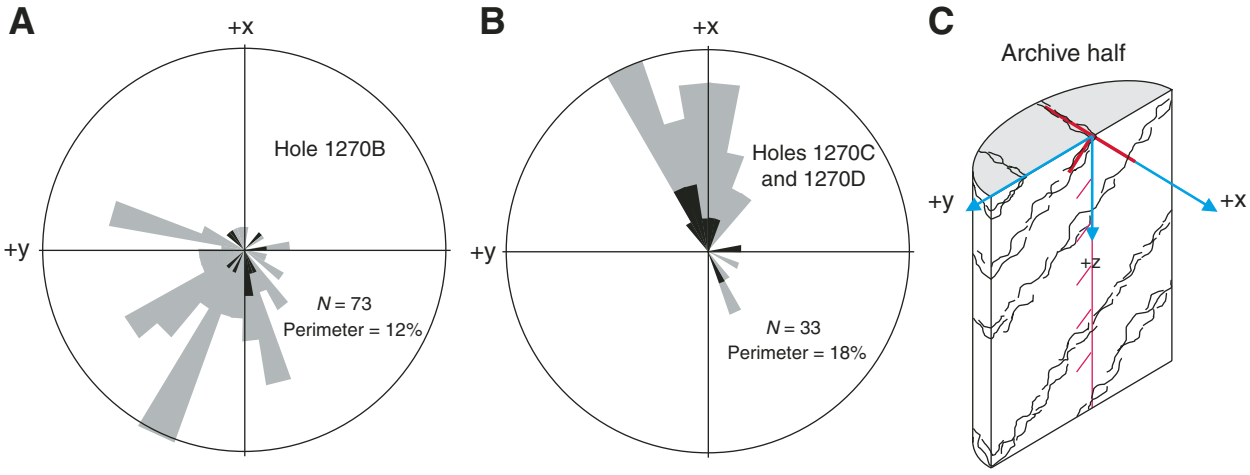

Figure F117. Lower hemisphere equal-area projections of minimum eigenvector of the susceptibility tensor for (**A**) Hole 1270B and (**B**) Holes 1270C and 1270D. Black symbols = samples with foliation larger than lineation, gray symbols = samples with foliation smaller than lineation.

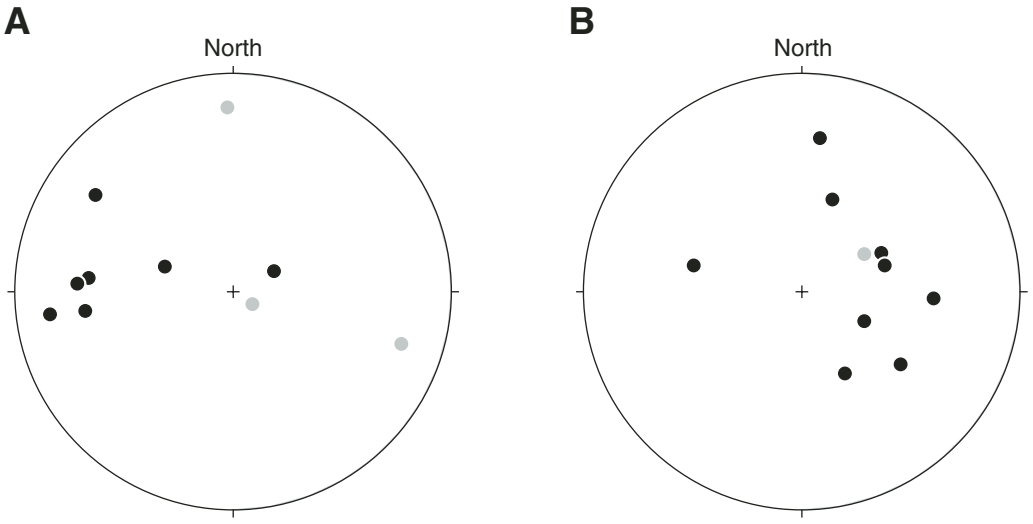

Figure F118. Graphical display of the gas chromatography area counts of the perfluorocarbon tracer in standards and sample pieces.

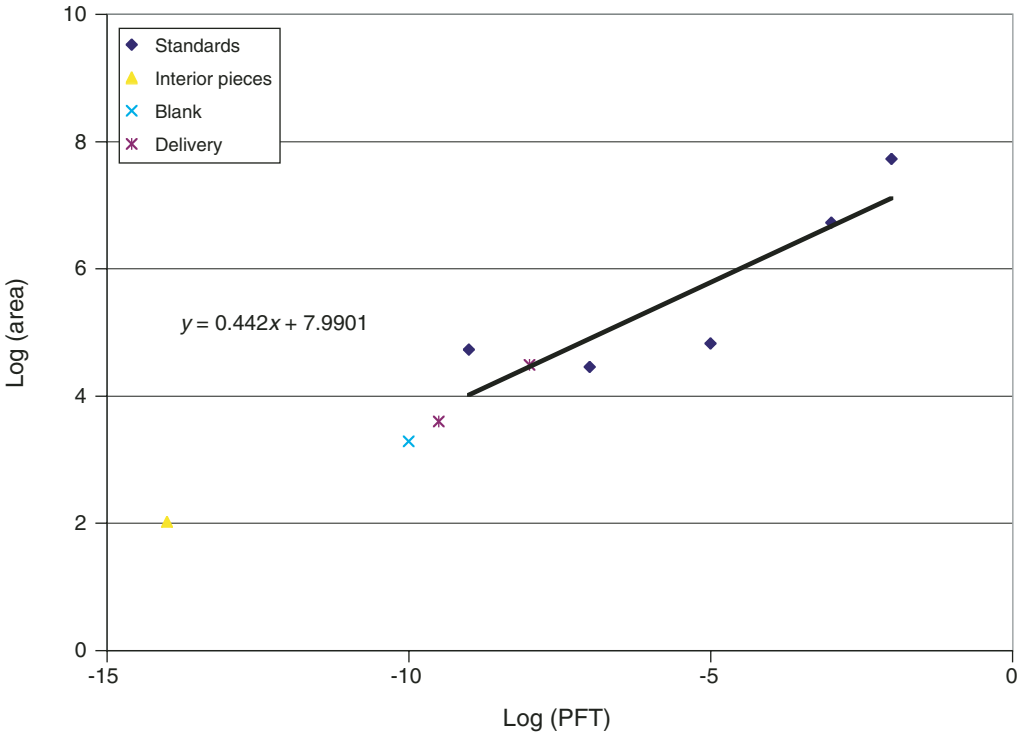

Table T1. Coring summary, Site 1270. (Continued on next page.)

Hole 1270A
Latitude: 14°43.3424′N
Longitude: 44°53.3206′W
Time on site: 112.75 (2200 hr, 28 May–1445 hr, 2 June 2003)
Time on hole: 18.00 (2200 hr, 28 May–1600 hr, 29 May 2003)
Seafloor (drill pipe measurement from rig floor, mbrf): 1962.0
Distance between rig floor and sea level (m): 11.0
Water depth (drill pipe measurement from sea level, m): 1951.0
Total depth (drill pipe measurement from rig floor, mbrf): 1988.9
Total penetration (mbsf): 26.9
Total length of cored section (m): 26.9
Total core recovered (m): 3.28
Core recovery (%): 12.2
Total number of cores: 4

Hole 1270B
Latitude: 14°43.2650′N
Longitude: 44°53.2249′W
Time on hole: 44.00 (1600 hr, 29 May–1200 hr, 31 May 2003)
Seafloor (drill pipe measurement from rig floor, mbrf): 1921.0
Distance between rig floor and sea level (m): 11.1
Water depth (drill pipe measurement from sea level, m): 1909.9
Total depth (drill pipe measurement from rig floor, mbrf): 1966.9
Total penetration (mbsf): 45.9
Total length of cored section (m): 45.9
Total core recovered (m): 17.17
Core recovery (%): 37.4
Total number of cores: 10

Hole 1270C
Latitude: 14°43.2835′N
Longitude: 44°53.0906′W
Time on hole: 15.00 (1200 hr, 31 May–0300 hr, 1 June 2003)
Seafloor (drill pipe measurement from rig floor, mbrf): 1833.0
Distance between rig floor and sea level (m): 11.1
Water depth (drill pipe measurement from sea level, m): 1821.9
Total depth (drill pipe measurement from rig floor, mbrf): 1851.6
Total penetration (mbsf): 18.6
Total length of cored section (m): 18.6
Total core recovered (m): 1.98
Core recovery (%): 10.65
Total number of cores: 3

Hole 1270D
Latitude: 14°43.2702′N
Longitude: 44°53.0839′W
Time on hole: 35.75 (0300 hr, 1 June–1445 hr, 2 June 2003)
Seafloor (drill pipe measurement from rig floor, mbrf): 1828.0
Distance between rig floor and sea level (m): 11.1
Water depth (drill pipe measurement from sea level, m): 1816.9
Total depth (drill pipe measurement from rig floor, mbrf): 1885.3
Total penetration (mbsf): 57.3
Total length of cored section (m): 57.3
Total core recovered (m): 7.68
Core recovery (%): 13.4
Total number of cores: 11

Core	Date (May 2003)	Local time (hr)	Depth (mbsf) Top	Depth (mbsf) Bottom	Length (m) Cored	Length (m) Recovered	Recovery (%)	Remarks
209-1270A-								
1R	29	0930	0.0	11.4	11.4	1.50	13.2	
2R	29	1140	11.4	17.4	6.0	0.96	16.0	
3R	29	1320	17.4	21.9	4.5	0.40	8.9	
4R	29	1515	21.9	26.9	5.0	0.42	8.4	
			Cored totals:		26.9	3.28	12.2	
209-1270B-								
1R	30	0810	0.0	12.4	12.4	1.36	11.0	
2R	30	1000	12.4	17.4	5.0	1.33	26.6	
3M	30	1200	17.4	17.5	0.1	1.28	1280.0	Clean out to total depth. "Miscellaneous" type core, redrilled interval (sidetrack). No advance (10 cm).
4M	30	1555	17.5	22.0	4.5	3.00	66.7	Washed 4.5 m to bottom. "Miscellaneous" type core due to partially redrilled interval (sidetrack). 4.5-m advance (17.5–22.0 mbsf).

Table T1 (continued).

Core	Date (May 2003)	Local time (hr)	Depth (mbsf) Top	Depth (mbsf) Bottom	Length (m) Cored	Length (m) Recovered	Recovery (%)	Remarks
5R	30	1745	22.0	27.0	5.0	0.15	3.0	Core catcher jam.
6R	30	2110	27.0	31.5	4.5	0.45	10.0	
7R	31	0200	31.5	36.5	5.0	3.16	63.2	
8R	31	0445	36.5	40.8	4.3	3.10	72.1	
9R	31	0850	40.8	45.8	5.0	1.36	27.2	Drop deplugger.
10M	31	1300	45.8	45.9	0.1	1.98	1980.0	Attempted to get to bottom. No joy. Unable to drill to bottom. "Miscellaneous" type core. No advance (10 cm).
			Cored totals:		45.9	17.17	37.4	
209-1270C-								
1R	31	2205	0.0	12.5	12.5	0.79	6.3	
2R	31	2355	12.5	18.5	6.0	0.71	11.8	
3M	31	0230	18.5	18.6	0.1	0.48	480.0	No advance (10 cm).
			Cored totals:		18.6	1.98	10.7	
209-1270D-								
1R	1	1135	0.0	13.9	13.9	0.95	6.8	
2R	1	1415	13.9	18.9	5.0	0.35	7.0	
3R	1	1735	18.9	23.4	4.5	2.17	48.2	
4R	1	2135	23.4	28.4	5.0	2.00	40.0	
5R	2	0035	28.4	32.9	4.5	0.36	8.0	
6R	2	0250	32.9	37.9	5.0	0.59	11.8	
7R	2	0430	37.9	42.4	4.5	0.22	4.9	
8R	2	0525	42.4	47.4	5.0	0.12	2.4	
9R	2	0625	47.4	51.6	4.2	0.40	9.5	
10R	2	0750	51.6	56.6	5.0	0.25	5.0	
11R	2	1000	56.6	57.3	0.7	0.27	38.6	
			Cored totals:		57.3	7.68	13.4	

Table T2. XRD results, Holes 1270A, 1270B, 1270C, and 1270D.

Core, section, interval (cm)	Depth (mbsf)	Piece	Rock type	Mineralogy			ICP-AES analyses	Thin section
				Major	Minor	Trace		
209-1270A-								
1R-1, 104–107	1.0	19	Harzburgite	Lizardite	Magnetite		Yes	Yes
1R-2, 34–37	1.8	6	Harzburgite	Lizardite	Magnetite		Yes	Yes
209-1270B-								
1R-1, 101–104	1.0	16	Gabbro	Plagioclase	Amphibole	Cpx	Yes	Yes
4M-2, 54–57	19.5	9	Gabbro	Plagioclase	Amphibole	Cpx	Yes	Yes
4M-2, 121–124	20.2	18	Gabbro	Plagioclase	Amphibole	Cpx	Yes	Yes
7R-1, 104–106	32.5	17	Gabbro	Plagioclase	Chlorite, amphibole		Yes	Yes
8R-2, 116–118	39.0	13	Gabbro	Plagioclase	Magnetite, cpx	Ilmenite	Yes	Yes
9R-1, 56–60	41.4	8A	Gabbro	Plagioclase	Magnetite, cpx	Ilmenite	Yes	Yes
10M-1, 23–25	46.0	6	Gabbro	Plagioclase	Magnetite, cpx		Yes	Yes
209-1270C-								
1R-1, 32–36	0.3	7B	Harzburgite	Lizardite	Magnetite		Yes	Yes
3M-1, 52–55	19.0	10	Vein	Talc	Lizardite	Opx	—	—
209-1270D-								
1R-1, 70–74	0.7	16	Dunite/Harzburgite	Lizardite	Magnetite		Yes	Yes
3R-1, 63–66	19.5	8B	Harzburgite/Gabbro	Chlorite	Amphibole, lizardite	Magnetite	Yes	Yes
3R-1, 93–97	19.8	11	Harzburgite	Lizardite	Magnetite		Yes	Yes
6R-1, 29–32	33.2	4B	Harzburgite	Lizardite	Magnetite		Yes	Yes
10R-1, 7–11	51.7	1	Harzburgite	Lizardite	Magnetite		Yes	Yes

Notes: Cpx = clinopyroxene, opx = orthopyroxene. Due to peak overlap, samples with identified lizardite may also contain chrysotile. Qualifiers "major, minor, and trace" indicate relative abundances based on peak heights and do not necessarily reflect true relative proportions. ICP-AES = inductively coupled plasma–atomic emission spectrometry. ICP-AES data are available in Table **T4,** p. 177. This table is also available in **ASCII.**

Table T3. Vein mineralogy, Holes 1270A, 1270B, 1270C, and 1270D.

Hole	1270A	1270B	1270C	1270D
Penetration depth (mbsf)	26.9	45.9	18.6	57.3
Recovery (%)	12.0	37.4	10.6	13.4
Length recovered (m)	3.2	17.2	2.0	7.7
Volume recovered (cm^3)	8,093	43,040	4,943	19,251
Veins in hole (cm^3/m)	31.0	12.3	50.8	47.1
Veins in hole (%)	1.23	0.49	2.03	1.88
Vein minerals in hole (cm^3/m):				
Serpentine	24.2	2.1	43.8	39.3
Talc	5.88	6.38	0.56	2.53
Chlorite	0.02	2.51	—	—
Amphibole	0.02	1.28	—	0.09
Secondary plagioclase		0.01	—	—
Magnetite	0.87	0.00	—	0.10
Iron oxides (other)	—	0.02	6.35	4.57
Sulfides	—	—	—	0.23
Carbonates		0.01	0.08	2.03
Vein minerals in hole (%):				
Serpentine	0.96	0.08	1.75	1.57
Talc	0.23	0.25	0.00	0.10
Chlorite	0.001	0.10	—	—
Amphibole	0.001	0.05	—	0.004
Secondary plagioclase	—	0.0003	—	—
Magnetite	0.03	0.0001		0.004
Iron oxides (other)	—	—	0.02	0.18
Sulfides	—	—		0.01
Carbonates	—	—	0.25	0.01
Vein minerals in veins (%):				
Serpentine	78.07	17.02	86.31	83.48
Talc	18.98	51.90	1.10	5.37
Chlorite	0.08	20.42	—	
Amphibole	0.08	10.40	—	0.19
Secondary plagioclase		0.00	—	
Magnetite	2.80	0.00		0.22
Iron oxides (other)			12.51	9.70
Sulfides		0.00		0.49
Carbonates			0.08	0.56

Notes: The volume of veins is based on macroscopic observations of vein mineralogy and estimates of vein percentages by pieces. We computed volume percentage of veins by using the volume weighted average of the macroscopic estimates using the relative curated length and assuming a constant core radius throughout the site. This table is also available in **ASCII.**

Table T4. Major and trace element compositions of rocks, Holes 1270A, 1270B, 1270C, and 1270D. (Continued on next page.)

Core, section, interval (cm)	Depth (mbsf)	Piece	Unit	Lithology	Major element oxides (wt%)											Volatiles (wt%)	
					SiO_2	TiO_2	Al_2O_3	Fe_2O_3	MgO	MnO	CaO	Na_2O	K_2O	Total	LOI	CO_2	H_2O
209-1270A-																	
1R-1, 104–107	1.04	19		Harzburgite	44.55	<0.01	0.75	8.15	44.47	0.06	0.06	0.08	0.01	98.14	13.04	0.25	14.13
1R-2, 34–37	1.80	6		Harzburgite	44.96	<0.01	0.73	9.44	44.62	0.06	0.18	0.06	<0.01	100.05	13.32	0.09	15.82
209-1270B-																	
1R-1, 101–104	1.01	18	I	Oxide gabbro	43.01	6.53	12.95	18.52	6.06	0.25	10.86	2.26	0.05	100.48	–0.07	0.08	1.11
4M-2, 54–57	19.54	9	I	Oxide gabbro	43.20	4.04	10.76	23.90	7.64	0.31	10.72	1.65	0.04	102.27	–0.11	0.08	1.16
4M-2, 121–124	20.21	18	II	Microgabbro	49.15	0.73	15.51	10.09	10.69	0.17	12.28	1.54	0.05	100.22	0.57	0.08	1.21
7R-1, 104–106	32.54	17	VI	Microgabbro	46.21	0.88	17.54	13.17	12.53	0.27	7.34	1.57	0.05	99.57	5.42	0.14	7.67
8R-2, 116–118	39.02	13	VII	Oxide gabbro	43.68	2.94	10.82	21.11	8.35	0.23	11.60	1.71	0.05	100.49	0.07	0.08	1.10
9R-1, 56–60	41.36	8A	VII	Oxide gabbro	47.72	1.84	15.82	14.31	6.24	0.17	12.16	2.57	0.07	100.89	0.13	0.09	0.74
10M-1, 23–25	46.03	6	VII	Oxide gabbro	45.27	2.64	12.94	20.04	7.95	0.22	11.67	1.81	0.04	102.56	–0.02	0.06	0.93
209-1270C-																	
1R-1, 32–36	0.32	7B		Harzburgite	46.85	0.02	0.62	8.67	44.49	0.10	0.04	0.07	0.01	100.87	13.60	0.22	15.91
209-1270D-																	
1R-1, 70–74	0.70	16		Harzburgite/Dunite	45.44	0.01	0.48	9.29	41.39	0.13	3.49	0.15	0.02	100.40	14.42	2.21	13.98
3R-1, 63–66	19.53	8B		Harzburgite/vein	49.43	0.13	4.13	7.40	35.06	0.12	3.48	0.27	0.07	100.09	8.51	0.15	9.29
3R-1, 93–97	19.83	11		Harzburgite	46.17	0.01	0.85	8.13	42.70	0.12	0.11	0.08	0.02	98.19	13.40	0.20	15.15
6R-1, 29–32	33.19	4B		Harzburgite	45.99	0.01	0.52	9.29	43.90	0.08	<0.06	0.10	0.01	99.90	13.03	0.38*	12.99*
10R-1, 7–11	51.67	1		Harzburgite	46.31	<0.01	0.33	9.57	42.74	0.10	0.25	0.07	0.01	99.39	12.64	0.16*	12.93*

Notes: * = analyzed using smaller sample sizes for improved H_2O calibration. NA = not analyzed, BDL = below detection limit. This table is also available in **ASCII.**

Table T4 (continued).

Core, section, interval (cm)	Depth (mbsf)	Piece	Unit	Trace elements (ppm)									
				S	Cr	Ni	Ba	Sr	V	Y	Zr	Sc	Co
209-1270A-													
1R-1, 104–107	1.04	19		NA	2824	2001	<39	<5	28.5	<2	4	9	61
1R-2, 34–37	1.80	6		NA	2932	2421	<39	<5	25.1	<2	2	8	70
209-1270B-													
1R-1, 101–104	1.01	18	I	NA	<41	<165	<39	165	644	17	48	64	122
4M-2, 54–57	19.54	9	I	NA	95	<165	<39	117	1299	15	30	68	129
4M-2, 121–124	20.21	18	II	NA	766	240	<39	159	200	13	34	39	63
7R-1, 104–106	32.54	17	VI	NA	742	208	<39	122	241	11	22	36	57
8R-2, 116–118	39.02	13	VII	NA	<41	<165	<39	112	1540	12	20	68	117
9R-1, 56–60	41.36	8A	VII	NA	<41	<165	<39	172	1006	11	17	54	82
10M-1, 23–25	46.03	6	VII	NA	121	<165	<39	138	1335	9	15	58	111
209-1270C-													
1R-1, 32–36	0.32	7B		NA	2237	2395	<39	<5	31.2	<2	3	6	110
209-1270D-													
1R-1, 70–74	0.70	16		NA	1902	2354	<39	530	45.7	<2	<2	9	99
3R-1, 63–66	19.53	8B		NA	2127	1728	<39	10	31.0	20	96	10	68
3R-1, 93–97	19.83	11		NA	2753	2235	<39	<5	34.5	<2	4	9	112
6R-1, 29–32	33.19	4B		BDL	1601	2595	<39	<5	25.4	<2	3	5	96
10R-1, 7–11	51.67	1		BDL	1752	2945	<39	6	21.5	<2	2	6	121

Table T5. Thermal conductivity measurements, Holes 1270A, 1270B, 1270C, and 1270D.

Core, section, interval (cm)	Depth (mbsf)	Piece	Thermal conductivity* (W/[m·K])	Standard deviation	Standard error	Needle orientation	Apparent anisotropy (%)	Primary lithology
209-1270A-								
1R-1, 104–114	1.04	19	3.05	0.020	0.010	0	4.9	Harzburgite
1R-1, 104–114	1.04	19	2.90	0.034	0.017	1		Harzburgite
209-1270B-								
1R-1, 120–128	1.20	18	2.27	0.027	0.013	0	8.4	Gabbro
1R-1, 120–128	1.20	18	2.22	0.007	0.004	1		Gabbro
1R-1, 120–128	1.20	18	2.08	0.007	0.003	2		Gabbro
2R-1, 75–86	13.15	14	2.27	0.017	0.008	0	3.6	Gabbro
2R-1, 75–86	13.15	14	2.19	0.025	0.013	1		Gabbro
2R-1, 75–86	13.15	14	2.23	0.024	0.012	2		Gabbro
4M-1, 49–58	17.99	9	2.41	0.206	0.103	0	1.7	Gabbro
4M-1, 49–58	17.99	9	2.37	0.014	0.007	1		Gabbro
4M-1, 49–58	17.99	9	2.38	0.047	0.024	2		Gabbro
7R-1, 98–110	32.48	17	2.01	0.017	0.008	0	0.9	MicroGabbro
7R-1, 98–110	32.48	17	2.00	0.011	0.005	1		MicroGabbro
7R-1, 98–110	32.48	17	2.02	0.014	0.007	2		MicroGabbro
7R-3, 1–12	34.41	1	2.42	0.033	0.017	0	12.6	Gabbro
7R-3, 1–12	34.41	1	2.13	0.055	0.028	1		Gabbro
7R-3, 1–12	34.41	1	2.38	0.017	0.009	2		Gabbro
9R-1, 44–54	41.24	7	2.17	0.004	0.002	0	7.4	Gabbro
9R-1, 44–54	41.24	7	2.34	0.032	0.016	1		Gabbro
9R-1, 44–54	41.24	7	2.24	0.011	0.005	2		Gabbro
10M-1, 19–29	45.99	6	2.32	0.026	0.013	0	1.7	MicroGabbro
10M-1, 19–29	45.99	6	2.32	0.039	0.020	1		MicroGabbro
10M-1, 19–29	45.99	6	2.28	0.003	0.001	2		MicroGabbro
209-1270C-								
1R-1, 70–80	0.70	11	2.39	0.025	0.013	0	0.2	Harzburgite
1R-1, 70–80	0.70	11	2.39	0.006	0.003	2		Harzburgite
209-1270D-								
4R-1, 39–52	23.79	8	2.52	0.022	0.011	0	7.3	Harzburgite
4R-1, 39–52	23.79	8	2.59	0.010	0.005	1		Harzburgite
4R-1, 39–52	23.79	8	2.41	0.010	0.005	2		Harzburgite
6R-1, 29–41	33.19	4B	2.79	0.014	0.007	0	5.8	Harzburgite
6R-1, 29–41	33.19	4B	2.63	0.018	0.009	1		Harzburgite
6R-1, 29–41	33.19	4B	2.77	0.019	0.010	2		Harzburgite

Notes: * = average of four measurements. 0 = parallel to core axis, 1 = oblique to core axis (~35°), 2 = oblique to core axis (~35°) in opposite direction. This table is also available in **ASCII.**

Table T6. Apparent thermal conductivity anisotropy in Sample 209-1270B-1R-1, 120–128 cm.

Thermal conductivity (W/[m·K])											Standard deviation	Standard error	Angle with core axis (°)
1	2	3	4	5	6	7	8	9	10	Average			
2.272	2.293	2.292	2.284	2.250	2.268	2.268	2.322	2.282	2.239	2.28	0.023	0.007	–40
2.308	2.225	2.215	2.306	2.327	2.220	2.321	2.290	2.314	2.291	2.28	0.044	0.014	–30
2.295	2.287	2.257	2.263	2.331	2.317	2.319	2.309	—	—	2.30	0.027	0.009	–20
2.265	2.250	2.239	2.252	2.286	2.265	—	—	—	—	2.26	0.016	0.007	–10
2.229	2.209	2.232	2.228	2.314	2.230	2.286	—	—	—	2.25	0.038	0.014	0
2.221	2.196	2.219	2.219	2.154	2.176	—	—	—	—	2.20	0.028	0.011	10
2.141	2.135	2.127	2.143	2.082	—	—	—	—	—	2.13	0.025	0.011	20
2.121	2.121	2.123	2.131	2.154	2.021	2.147	—	—	—	2.12	0.044	0.017	30
2.146	2.143	2.140	2.152	2.020	2.190	2.192	—	—	—	2.14	0.057	0.022	40

Note: This table is also available in **ASCII.**

Table T7. Porosity, density, and velocity on discrete samples, Holes 1270A, 1270B, 1270C, and 1270D.

Core, section, interval (cm)	Depth (mbsf)	Volume measured in pycnometer			Sample size	Volume measured with caliper				Primary lithology
		Density (Mg/m³)		Porosity (%)		Density (Mg/m³)		Porosity (%)	V_P (km/s)	
		Bulk	Grain			Bulk	Grain			
209-1270A-										
1R-1, 108–110	1.08	2.50	2.61	6.9	Chip	—	—	—	—	Harzburgite
209-1270B-										
1R-1, 115–117	1.15	3.14	3.16	0.8	Minicore	3.18	3.18	0.02	5.86	Gabbro
1R-1, 115–117	1.15	3.13	3.16	1.1	Chip	—	—	—	—	Gabbro
4M-1, 104–106	18.54	3.01	3.03	0.6	Minicore	2.99	2.99	0.02	5.48	Gabbro
4M-1, 104–106	18.54	3.03	3.05	1.3	Chip	—	—	—	—	Gabbro
4M-2, 125–127	20.25	3.03	3.05	1.0	Chip	—	—	—	—	Microgabbro
4M-3, 6–8	20.49	3.07	3.08	0.4	Minicore	3.05	3.05	0.01	—	Microgabbro
4M-3, 6–8	20.49	3.01	3.03	1.1	Chip	—	—	—	—	Microgabbro
7R-2, 122–124	34.12	3.11	3.12	0.7	Chip	—	—	—	—	Gabbro
8R-1, 127–129	37.77	2.61	2.97	18.7	Chip	—	—	—	—	Gabbro
10M-1, 27–29	46.07	3.02	3.06	2.0	Chip	—	—	—	—	Microgabbro
209-1270C-										
1R-1, 50–52	0.50	2.48	2.56	5.3	Chip	—	—	—	—	Harzburgite
1R-1, 71–73	0.71	2.55	2.61	3.9	Chip	—	—	—	—	Harzburgite
209-1270D-										
3R-1, 59–61	19.49	2.43	2.52	6.2	Chip	—	—	—	—	Harzburgite
3R-2, 49–51	20.65	2.45	2.54	6.0	Minicore	2.47	2.50	0.2	4.18	Harzburgite
3R-2, 49–51	20.65	2.50	2.59	5.5	Chip	—	—	—	—	Harzburgite
4R-1, 91–93	24.31	2.54	2.61	4.5	Chip	—	—	—	—	Dunite/Harzburgite
6R-1, 33–35	33.23	2.55	2.64	5.9	Chip	—	—	—	—	Harzburgite

Note: This table is also available in **ASCII.**

Table T8. Bulk density and velocity measured on cube samples, Holes 1270A, 1270B, 1270C, and 1270D.

Core, section, interval (cm)	Depth (mbsf)	Bulk density (Mg/m^3)	V_P (km/s)				V_P apparent anisotropy (%)	Primary lithology
			x	y	z	Mean		
209-1270A-								
1R-1, 108–110	1.08	2.48	3.73	3.69	3.55	3.65	4.95	Harzburgite
209-1270B-								
1R-1, 98–100	0.98	3.15	6.10	5.66	5.65	5.80	7.72	Gabbro
4M-2, 57–59	19.57	3.19	5.57	5.52	5.55	5.55	0.81	Gabbro
4M-2, 125–127	20.25	3.04	5.76	5.76	5.83	5.78	1.35	Microgabbro
7R-1, 105–107	32.55	2.76	4.52	4.64	4.64	4.60	2.76	Microgabbro
7R-2, 122–124	34.12	3.17	5.70	5.88	5.88	5.82	3.01	Gabbro
8R-1, 127–129	37.77	3.23	5.75	5.35	5.49	5.53	7.25	Gabbro
10M-1, 27–29	46.07	3.19	5.72	5.70	5.67	5.70	0.77	Microgabbro
209-1270C-								
1R-1, 50–52	0.50	2.57	4.40	4.50	4.50	4.47	2.22	Harzburgite
1R-1, 71–73	0.71	2.58	4.47	4.27	4.26	4.33	4.75	Harzburgite
2R-1, 67–69	13.17	2.81	3.66	3.62	3.65	3.64	1.13	Harzburgite
209-1270D-								
3R-1, 59–61	19.49	2.54	4.32	4.36	4.20	4.29	3.73	Harzburgite
3R-2, 53–55	20.69	2.53	4.34	4.21	4.25	4.27	3.05	Harzburgite
4R-1, 91–93	24.31	2.55	4.13	4.13	4.10	4.12	0.80	Dunite/Harzburgite
6R-1, 33–35	33.23	2.50	3.89	3.76	3.64	3.76	6.67	Harzburgite

Note: This table is also available in **ASCII.**

Table T9. Summary of discrete sample data, Holes 1270A, 1270B, 1270C, and 1270D.

Core, section, interval (cm)	Depth (mbsf)	Piece	Lithology	PCA polarity	*N*	Decay type	MAD (°)	Remanence direction (°)		Demagnetization (mT)		*J* (A/m)	PCA (%)
								Declination	Inclination	Low	High		
209-1270A-													
1R-1, 108	1.08	19	2	I	5	+	6.5	276.8	45.6	40	80	0.1386	3.1
209-1270B-													
1R-1, 98	0.98	16	10	R	9	+	2.3	174.9	–1.2	25	80	0.3955	6.0
1R-1, 115	1.15	17	10	R	7	+	1.7	201.4	–6.7	35	100	0.4809	2.9
4M-1, 104	18.54	14	10	R	8	+	2.8	155.3	–8.4	20	60	0.4628	4.8
4M-2, 57	19.57	9	10	R	8	+	4.7	163.8	–23.4	20	60	0.7258	4.8
4M-2, 125	20.25	19	16	R	10	+	7.8	51.7	2.9	10	60	0.3968	13.7
4M-3, 6	20.49	1	16	R	8	+	4.1	170.9	–17.8	25	80	0.2650	4.0
7R-1, 105	32.55	17	16	R	7	F	3.7	328.4	–27.9	20	60	0.1250	16.7
7R-2, 122	34.12	13	10	R	9	+	6.7	310.7	–7	20	70	0.3701	2.0
8R-1, 127	37.77	20B	10	R	6	+	3.3	221.6	–17	15	35	1.060	7.0
10M-1, 27	46.07	6	16	R	9	+	4.0	84.8	–31	25	100	0.4021	0.8
209-1270C-													
1R-1, 50	0.50	9	2	I	8	F	1.5	332.2	9.5	8	40	1.472	80.4
1R-1, 63	0.63	10	2	I	8	F	1.0	357.3	8.4	10	50	1.924	73.1
1R-1, 71	0.71	11	2	I	10	F	1.7	8.2	–8.9	10	80	2.271	76.5
2R-1, 67	13.17	12	2	I	10	F	1.9	153.3	–12.5	6	50	1.036	85.6
209-1270D-													
3R-1, 59	19.49	8B	2	I	9	F	3.5	16.8	–2.7	8	40	0.2050	39.4
3R-2, 49	20.65	3	2	I	7	F	1.4	344.2	3.6	20	60	0.3811	47.0
3R-2, 53	20.69	3	2	I	8	F	1.1	346.9	0.9	15	60	1.209	66.8
4R-1, 91	24.31	12A	1.5	I	9	F	1.3	332.3	4.9	15	80	3.015	74.6
4R-1, 101	24.41	12B	1.5	I	9	F	1.7	328.0	4.7	15	80	2.880	67.8
6R-1, 33	33.23	4B	2	I	6	F	5.0	92.5	–41.3	15	40	0.6965	109.5

Notes: Lithology: 1.5 = dunite/harzburgite, 2 = harzburgite, 10 = gabbro, 16 = microgabbro. PCA (principal component analysis) polarity = polarity for reorientation studies: R = rotate to 180°, N = rotate to 360°, I = indeterminate. *N* = number of points. Decay type: F = free of origin, + = includes origin as point. MAD = maximum angular deviation. PCA (%) = percentage of natural remanent magnetization intensity. This table is also available in **ASCII.**

Table T10. Piece orientations from archive-half data, Holes 1270A, 1270B, 1270C, and 1270D. (**See table notes.** Continued on next page.)

Core, section, interval (cm)	Depth (mbsf)	Piece	Lithology	PCA polarity	*N*	Decay type	MAD (°)	Remanence direction (°)		Demagnetization (mT)		*J* (A/m)	PCA (%)
								Declination	Inclination	Low	High		
209-1270A-													
1R-1, 108	1.08	19	2	I	5	+	6.5	276.8	45.6	40	80	0.1386	3.1
209-1270B-													
1R-1, 20	0.20	4	10	R	3	F	8.5	200.6	12.2	60	80	0.0368	0.2
1R-1, 38	0.38	6	10	R	4	+	2.2	182.1	3.6	60	80	0.0200	1.1
1R-1, 86	0.86	15	10	R	4	+	2.2	213.7	–5.9	60	80	0.0909	4.2
1R-1, 96	0.96	16	10	R	4	+	2.2	169.2	–10.4	60	80	0.1389	4.5
1R-1, 98	0.98	16	10	R	9	+	2.3	174.9	–1.2	25	80	0.3955	6.0
1R-1, 114	1.14	17	10	R	4	+	1.6	209.2	–4.4	60	80	0.1539	2.3
1R-1, 115	1.15	17	10	R	7	+	1.7	201.4	–6.7	35	100	0.4809	2.9
1R-1, 126	1.26	17	10	R	4	+	3.9	167.3	–7	60	80	0.1766	1.2
1R-1, 144	1.44	21	10	R	4	+	1.2	242.0	–4.2	60	80	0.1470	1.3
1R-2, 4	1.54	1	10	R	3	+	2.8	233.9	–9.5	60	80	0.0628	1.0
2R-1, 38	12.78	8	10	R	5	+	1.9	286.8	8.9	15	40	0.4580	15.5
2R-1, 60	13.00	12	10	R	3	+	4.1	205.5	10.1	60	80	0.0731	0.6
2R-1, 84	13.24	14	10	R	3	+	5.8	228.4	8.2	60	80	0.1017	0.9
2R-1, 100	13.40	16	10	R	6	+	4.6	357.9	22.1	20	80	0.9136	7.9
2R-1, 118	13.58	18	10	R	3	+	6.0	256.5	0.2	60	80	0.1186	1.1
2R-1, 130	13.70	19	10	R	4	+	6.0	175.3	5.6	40	80	0.1225	3.3
3M-1, 46	17.86	9	10	R	3	+	6.7	180.8	–1.8	60	80	0.0825	0.9
3M-1, 62	18.02	11	10	R	3	+	3.8	232.9	7.4	60	80	0.0689	0.8
3M-1, 72	18.12	12	10	R	3	+	4.6	210.7	9.1	60	80	0.0703	0.6
3M-1, 114	18.54	16	10	R	3	+	3.0	197.0	0.4	60	80	0.0729	1.3
3M-1, 118	18.58	18	10	R	3	+	1.3	198.3	–2.9	60	80	0.0940	1.7
3M-1, 134	18.74	20	10	R	3	+	3.5	245.4	–13.6	60	80	0.0744	0.9
4M-1, 52	18.02	9	10	R	3	+	1.6	269.3	–7.5	60	80	0.1530	2.0
4M-1, 66	18.16	10	10	R	3	+	4.9	165.6	–1.9	60	80	0.0943	0.6
4M-1, 80	18.30	11	10	R	3	+	2.2	235.8	–9	60	80	0.1189	1.5
4M-1, 96	18.46	13	10	R	3	+	3.8	177.5	–0.6	60	80	0.0439	1.2
4M-1, 104	18.54	14	10	R	8	+	2.8	155.3	–8.4	20	60	0.4628	4.8
4M-1, 108	18.58	15	10	R	5	+	25.2	145.1	37.6	30	80	0.2434	1.7
4M-2, 14	19.14	3	10	R	3	+	2.3	128.7	0.0	60	80	0.0701	2.8
4M-2, 22	19.22	4	10	R	3	+	3.9	127.4	–30.9	60	80	0.0291	0.9
4M-2, 48	19.48	8	10	R	3	+	2.7	221.4	–7	60	80	0.1049	1.3
4M-2, 57	19.57	9	10	R	8	+	4.7	163.8	–23.4	20	60	0.7258	4.8
4M-2, 60	19.60	9	10	R	4	+	11.5	204.4	–9.6	40	80	0.1108	2.3
4M-2, 100	20.00	15	16	R	4	+	9.1	188.4	–5.5	40	80	0.0181	5.1
4M-2, 120	20.20	18	16	R	3	+	4.4	206.4	–7.4	60	80	0.0231	1.8
4M-2, 125	20.25	19	16	R	10	+	7.8	51.7	2.9	10	60	0.3968	13.7
4M-2, 138	20.38	20	16	R	3	+	1.7	115.3	0.6	60	80	0.0348	1.8
4M-3, 6	20.49	1	16	R	8	+	4.1	170.9	–17.8	25	80	0.2650	4.0
4M-3, 8	20.51	1	16	R	3	+	1.4	190.6	–5.5	60	80	0.0488	1.8
7R-1, 86	32.36	15	16	R	4	+	6.9	153.1	8.3	40	80	0.0396	6.8
7R-1, 94	32.44	16	16	R	4	F	8.5	228.7	–30.8	30	80	0.0075	17.7
7R-1, 105	32.55	17	16	R	7	F	3.7	328.4	–27.9	20	60	0.1250	16.7
7R-1, 106	32.56	17	16	R	4	F	1.2	333.9	–17.3	30	80	0.0520	28.1
7R-2, 50	33.40	8	16	R	3	+	3.7	166.9	–11	60	80	0.1318	1.9
7R-2, 66	33.56	9	16	R	3	+	1.0	167.3	–15.4	60	80	0.1980	2.3
7R-2, 98	33.88	11	10	R	3	+	1.6	293.0	–21.5	60	80	0.2149	2.3
7R-2, 112	34.02	12	10	R	5	+	1.6	345.1	–14.3	30	80	0.1220	10.5
7R-2, 122	34.12	13	10	R	9	+	6.7	310.7	–7	20	70	0.3701	2.0
7R-2, 134	34.24	13	10	R	3	+	5.8	281.2	–8.1	60	80	0.1375	0.7
7R-3, 4	34.44	1	10	R	3	+	1.2	286.3	–10.7	60	80	0.1770	1.7
7R-3, 30	34.70	2	10	R	3	+	0.6	236.4	–8.1	60	80	0.1730	1.2
8R-1, 126	37.76	20	10	R	3	+	2.8	274.3	–7.8	60	80	0.2298	1.5
8R-1, 127	37.77	20B	10	R	6	+	3.3	221.6	–17	15	35	1.0595	7.0
8R-2, 8	37.94	1	10	R	3	+	5.1	226.2	–17.1	60	80	0.0957	1.1
8R-2, 58	38.44	6	10	R	3	+	2.2	145.5	–0.9	60	80	0.1259	1.2
8R-2, 70	38.56	7	10	R	3	+	4.3	147.1	–15.2	60	80	0.0951	1.0
8R-2, 80	38.66	8	10	R	3	+	2.0	235.1	–9.9	60	80	0.1639	1.4
8R-2, 120	39.06	13	10	R	3	+	1.6	201.1	–11.6	60	80	0.2129	2.2
8R-2, 138	39.24	14	10	R	3	+	1.8	250.7	–0.1	60	80	0.1320	1.3
8R-3, 4	39.36	1	10	R	4	+	4.4	207.1	–14	50	80	0.0765	1.0
8R-3, 14	39.46	2	10	R	3	+	3.5	235.9	0.8	60	80	0.0470	1.2
8R-3, 50	39.82	7	10	R	5	+	5.4	265.4	–17.1	40	80	0.0837	1.7
9R-1, 38	41.18	6	10	R	3	+	1.8	88.5	–48.7	40	60	0.0684	2.3
9R-1, 50	41.30	7	10	R	3	+	3.1	204.0	10.0	40	60	0.1868	1.3

Table T10 (continued).

Core, section, interval (cm)	Depth (mbsf)	Piece	Lithology	PCA polarity	*N*	Decay type	MAD (°)	Remanence direction (°)		Demagnetization (mT)		*J* (A/m)	PCA (%)
								Declination	Inclination	Low	High		
9R-1, 64	41.44	8	10	R	3	+	0.5	285.3	5.6	40	60	0.1880	1.2
9R-1, 86	41.66	10	10	R	3	+	4.3	286.8	25.7	40	60	0.1975	1.3
9R-1, 106	41.86	12	10	R	4	+	1.9	219.6	6.3	30	60	0.1959	2.1
10M-1, 26	46.06	6	16	R	3	+	8.6	101.5	7.8	40	60	0.1624	2.5
10M-1, 27	46.07	6	16	R	9	+	4.0	84.8	–31	25	100	0.4021	0.8
10M-1, 34	46.14	7	16	R	3	+	4.8	7.9	–2.1	40	60	0.2035	4.9
10M-1, 100	46.80	18	10	R	3	+	2.4	49.1	–0.7	40	60	0.0832	7.5
10M-2, 6	47.36	1	10	R	4	+	1.3	286.4	–1.2	30	60	0.1770	13.8
10M-2, 22	47.52	3	10	R	4	+	5.3	297.4	–1.6	30	60	0.2551	12.1
209-1270C-													
1R-1, 28	0.28	6	2	I	3	+	4.3	357.3	20.9	30	40	0.0625	9.2
1R-1, 36	0.36	7	2	I	6	F	2.2	352.6	26.0	10	40	2.3133	48.4
1R-1, 50	0.50	9	2	I	4	+	3.2	333.1	16.1	25	40	0.3147	7.0
1R-1, 50	0.50	9	2	I	8	F	1.5	332.2	9.5	8	40	1.4717	80.4
1R-1, 62	0.62	10	2	I	4	+	3.1	358.9	15.7	25	40	0.2938	9.7
1R-1, 63	0.63	10	2	I	8	F	1.0	357.3	8.4	10	50	1.9235	73.1
1R-1, 71	0.71	11	2	I	10	F	1.7	8.2	–8.9	10	80	2.2714	76.5
1R-1, 76	0.76	11	2	I	7	+	3.4	2.4	28.7	10	40	3.2191	43.6
2R-1, 44	12.94	8	2	I	5	+	0.9	24.1	5.7	20	40	0.5719	27.4
2R-1, 67	13.17	12	2	I	10	F	1.9	153.3	–12.5	6	50	1.0360	85.6
2R-1, 68	13.18	12	2	I	3	F	0.4	159.9	–3.5	25	40	0.1177	21.5
2R-1, 84	13.34	14	2	I	3	A	2.5	145.8	0.6	25	40	0.0939	16.6
209-1270D-													
3R-1, 54	19.44	8	2	I	4	F	2.5	30.6	21.9	20	40	0.1848	19.5
3R-1, 59	19.49	8B	2	I	9	F	3.5	16.8	–2.7	8	40	0.2050	39.4
3R-1, 98	19.88	11	2	I	4	F	0.8	84.3	–10.7	20	40	0.2500	43.2
3R-1, 110	20.00	12	2	I	4	F	2.1	0.2	18.8	20	40	0.8137	28.5
3R-2, 12	20.28	1	2	I	5	F	1.4	20.9	22.8	10	40	3.6260	67.1
3R-2, 44	20.60	3	2	I	5	F	1.8	343.2	27.1	10	40	2.2584	66.8
3R-2, 49	20.65	3	2	I	7	F	1.4	344.2	3.6	20	60	0.3811	47.0
3R-2, 53	20.69	3	2	I	8	F	1.1	346.9	0.9	15	60	1.2088	66.8
3R-2, 72	20.88	4	2	I	3	+	2.4	32.9	15.3	30	40	0.0942	14.3
3R-2, 86	21.02	5	2	I	5	F	3.0	2.1	23.5	10	40	1.2745	53.6
4R-1, 46	23.86	8	2	I	6	F	1.2	336.7	19.7	10	40	2.2843	63.1
4R-1, 68	24.08	10	2	I	6	F	3.1	359.3	20.5	10	40	1.3766	56.9
4R-1, 100	24.40	12	1.5	I	4	F	2.4	338.8	17.3	20	40	1.2218	25.0
4R-1, 91	24.31	12A	1.5	I	9	F	1.3	332.3	4.9	15	80	3.0146	74.6
4R-1, 101	24.41	12B	1.5	I	9	F	1.7	328.0	4.7	15	80	2.8799	67.8
4R-2, 16	25.06	3	2	I	4	F	4.1	7.8	16.5	20	40	0.3484	24.0
4R-2, 38	25.28	5	1	I	5	F	2.5	347.3	19.9	15	40	1.1336	45.5
4R-2, 54	25.44	6	1	I	5	F	2.4	18.3	21.6	15	40	1.6320	43.2
5R-1, 26	28.66	5	2	I	5	F	2.0	332.8	42.8	15	40	1.0887	46.1
6R-1, 28	33.18	4	2	R	4	+	1.7	114.1	–38	25	40	0.4149	25.3
6R-1, 33	33.23	4B	2	R	6	F	5.0	92.5	–41.3	15	40	0.6965	109.5

Notes: Lithology: 1.5 = harzburgite/dunite, 2 = harzburgite, 10 = gabbro, 16 = microgabbro. Principal component analysis (PCA) polarity: R = rotate to 180°, I = indeterminate. *N* = number of points. Decay type: A = anchored to origin, F = free of origin, + = includes origin as point. MAD = maximum angular deviation. PCA (%) = percentage of natural remanent magnetization intensity. This table is also available in **ASCII.**

Table T11. Anisotropy of magnetic susceptibility, Holes 1270A, 1270B, 1270C, and 1270D.

Core, section, interval (cm)	Depth (mbsf)	Piece	Susceptibility (SI)	1 σ	Maximum*			Intermediate*			Minimum*		
					Value	Dec (°)	Inc (°)	Value	Dec (°)	Inc (°)	Value	Dec (°)	Inc (°)
209-1270A-													
1R-1, 108	1.08	19	8.707E–02	0.00036	0.3527	287.6	56.6	0.3409	137.9	29.6	0.3064	39.7	13.9
209-1270B-													
1R-1, 98	0.98	16	3.826E–02	0.00011	0.3410	150.0	25.5	0.3380	29.7	46.7	0.3210	257.6	32.3
1R-1, 115	1.15	17	9.497E–02	0.00028	0.3513	104.3	73.2	0.3425	14.2	0.0	0.3062	284.2	16.8
4M-1, 104	18.54	14	9.387E–02	0.00022	0.3486	124.6	21.8	0.3361	28.2	15.6	0.3153	265.4	62.7
4M-2, 57	19.57	9	9.233E–02	0.00024	0.3419	130.6	42.4	0.3372	10.8	28.6	0.3210	259.0	34.2
4M-2, 125	20.25	19	2.067E–02	0.00031	0.3558	240.4	22.3	0.3319	107.2	59.1	0.3123	339.1	20.3
4M-3, 6	20.49	1	5.506E–02	0.00095	0.3512	143.2	42.4	0.3417	15.9	33.6	0.3071	264.0	29.3
7R-1, 105	32.55	17	4.909E–03	0.00024	0.3450	236.8	0.7	0.3342	329.2	73.5	0.3208	146.6	16.5
7R-2, 122	34.12	13	1.358E–01	0.00019	0.3579	73.5	8.9	0.3392	341.2	14.3	0.3029	194.5	73.1
8R-1, 127	37.77	20B	1.571E–01	0.00032	0.3672	355.5	8.3	0.3236	265.3	1.4	0.3092	165.8	81.5
10M-1, 27	46.07	6	1.879E–01	0.00119	0.3439	329.8	47.9	0.3371	103.8	32.1	0.3190	210.1	24.1
209-1270C-													
1R-1, 50	0.50	9	2.760E–02	0.00029	0.3505	110.9	5.1	0.3308	18.3	26.6	0.3187	210.9	62.8
1R-1, 63	0.63	10	3.469E–02	0.00027	0.3462	52.5	33.0	0.3389	145.1	4.1	0.3149	241.4	56.7
1R-1, 71	0.71	11	3.989E–02	0.00013	0.3403	27.5	59.3	0.3339	288.2	5.5	0.3258	195.0	30.1
2R-1, 67	13.17	12	2.724E–02	0.00031	0.3537	126.2	30.6	0.3330	19.3	26.1	0.3133	256.8	47.7
209-1270D-													
3R-1, 59	19.49	8B	7.012E–03	0.0005	0.3487	53.7	34.9	0.3392	317.4	9.0	0.3121	215.1	53.6
3R-2, 49	20.65	3	1.207E–02	0.00034	0.3453	109.0	46.8	0.3344	199.7	0.7	0.3203	290.3	43.1
3R-2, 53	20.69	3	2.147E–02	0.00015	0.3406	136.8	8.0	0.3372	41.9	31.2	0.3221	239.6	57.5
4R-1, 91	24.31	12A	4.414E–02	0.0002	0.3374	138.4	19.6	0.3334	28.3	44.0	0.3292	245.5	39.5
4R-1, 101	24.41	12B	4.351E–02	0.00012	0.3386	70.8	25.4	0.3348	163.1	4.9	0.3266	263.2	64.1
6R-1, 33	33.23	4B	3.731E–02	0.00043	0.3443	224.8	33.2	0.3400	321.0	9.4	0.3157	64.8	55.1

Notes: σ = 1 standard deviation for normalized eigenvalues. Total anisotropy critical value = 3.4817. * = unrotated core coordinates (double line on working half = 360°, inclination positive down). Dec = declination, inc = inclination. F12 = max, min eigenvalues, F23 = int, min eigenvalues (critical value = 4.2565 for F12 and F23). *P* (degree of anisotropy) = max/min eigenvalues, *F* (magnetic foliation) = int/min eigenvalues, *L* (magnetic lineation) = max/int eigenvalues. AMS = anisotropy of magnetic susceptibility. † = core coordinates rotated to 180°. This table is also available in **ASCII.**

Table T11 (continued).

Core, section, interval (cm)	Depth (mbsf)	Piece	Total anisotropy	F12	F23	*P*	*F*	*L*	Minimum†		Maximum†	
									Dec (°)	Inc (°)	Dec (°)	Inc (°)
209-1270A-												
1R-1, 108	1.08	19	3535.8	536.2	4534.3	1.151	1.112	1.035	302.9	13.9	190.8	56.6
209-1270B-												
1R-1, 98	0.98	16	7309.0	347.8	9999.9	1.062	1.053	1.009	262.7	32.3	155.1	25.5
1R-1, 115	1.15	17	5948.1	510.2	8553.5	1.147	1.118	1.026	262.8	16.8	82.9	73.2
4M-1, 104	18.54	14	4820.6	1682.8	4579.7	1.106	1.066	1.037	290.1	62.7	149.3	21.8
4M-2, 57	19.57	9	1647.7	189.5	2247.2	1.065	1.050	1.014	275.2	34.2	146.8	42.4
4M-2, 125	20.25	19	4042.4	3036.9	2048.5	1.139	1.063	1.072	107.4	20.3	8.7	22.3
4M-3, 6	20.49	1	477.7	50.6	662.1	1.143	1.112	1.028	273.1	29.3	152.3	42.4
7R-1, 105	32.55	17	1973.8	982.6	1503.1	1.075	1.042	1.032	358.2	16.5	88.4	0.7
7R-2, 122	34.12	13	9999.9	5067.0	9999.9	1.182	1.120	1.055	63.8	73.1	302.8	8.9
8R-1, 127	37.77	20B	6958.1	9082.7	980.1	1.188	1.046	1.135	124.2	81.5	313.9	8.3
10M-1, 27	46.07	6	93.1	16.1	115.2	1.078	1.057	1.020	305.3	24.1	65.0	47.9
209-1270C-												
1R-1, 50	0.50	9	2376.6	2225.4	853.0	1.100	1.038	1.059	58.7	62.8	318.7	5.1
1R-1, 63	0.63	10	2995.7	371.0	4024.1	1.099	1.076	1.021	64.1	56.7	235.2	33.0
1R-1, 71	0.71	11	2391.0	1152.2	1865.0	1.044	1.025	1.019	6.8	30.1	199.3	59.3
2R-1, 67	13.17	12	3366.3	2209.0	2000.6	1.129	1.063	1.062	283.5	47.7	152.9	30.6
209-1270D-												
3R-1, 59	19.49	8B	1180.4	185.2	1500.8	1.118	1.087	1.028	18.3	53.6	216.9	34.9
3R-2, 49	20.65	3	1070.8	499.8	854.4	1.078	1.044	1.032	126.1	43.1	304.8	46.8
3R-2, 53	20.69	3	3613.8	274.2	5296.4	1.057	1.047	1.010	72.7	57.5	329.9	8.0
4R-1, 91	24.31	12A	326.8	195.5	213.1	1.025	1.013	1.012	93.2	39.5	346.1	19.6
4R-1, 101	24.41	12B	2063.0	478.2	2333.5	1.037	1.025	1.011	115.2	64.1	282.8	25.4
6R-1, 33	33.23	4B	1049.9	50.8	1630.3	1.091	1.077	1.013	152.3	55.1	312.3	33.2

Table T12. GC analysis of PFT contamination, Hole 1270D.

Standard PFT curve					Samples			
Dilution (vol:vol)	PFT (g)	Peak area (counts)	Log (PFT)	Log (area counts)	Location	Peak area (counts)	Log (PFT)	Log (area counts)
1×10^{-2}	8.80×10^{-7}	5.29×10^{7}	–2	7.72	Core 1	30,900	–8	4.49
1×10^{-3}	8.80×10^{-8}	5.33×10^{6}	–3	6.73	Core 2	3,960	–9.5	3.60
1×10^{-7}	8.80×10^{-12}	2.87×10^{4}	–7	4.46	Interior	105	–14	2.02
1×10^{-9}	8.80×10^{-14}	5.32×10^{4}	–9	4.73	Blank	1,933	–10	3.29

Notes: GC = gas chromatography. PFT = perfluorocarbon tracer. Sample from Section 209-1270D-4R-1 (Piece 14) run on 3 June 2003.

Table T13. Surface water and atmospheric microbiology results, 29 May–4 June 2003.

Sample	Date (2003)	Surface water (counts/mL)		Air growth* (CFU)		
		Bacteria	Virus	Bacteria	Fungi	Atmospheric condition†
a	29 May	5.67×10^5	5.21×10^6	0/0	0/0	No data
b	30 May	5.09×10^5	5.70×10^6	0/0	0/0	7.0: light cloud
c	31 May	3.58×10^5	5.32×10^6	0/0	0/0	3.6: Clear
d	1 June	4.33×10^5	5.55×10^6	0/1	0/0	No data
e	2 June	6.04×10^5	5.83×10^6	0/0	0/0	7.6: light cloud
f	3 June	5.85×10^5	4.74×10^6	0/0	0/0	8.0: light cloud
g	4 June	5.09×10^5	6.06×10^6	0/0	0/0	7.5: light cloud

Notes: * = colony-forming units (CFU) growth is measured at 48/96 hr. † = SeaWiFS image values.